43800

AN APPROXIMATE VISCOUS SHOCK LAYER TECHNIQUE FOR CALCULATING CHEMICALLY REACTING HYPERSONIC FLOWS ABOUT BLUNT-NOSED BODIES

F. McNeil Cheatwood and Fred R. DeJarnette

NORTH CAROLINA STATE UNIVERSITY
Raleigh, North Carolina

Summary

An approximate axisymmetric method has been developed which can reliably calculate fully viscous hypersonic flows over blunt-nosed bodies. By substituting Maslen's second order pressure expression for the normal momentum equation, a simplified form of the viscous shock layer (VSL) equations is obtained. This approach can solve both the subsonic and supersonic regions of the shock layer without a starting solution for the shock shape. The approach is applicable to perfect gas, equilibrium, and nonequilibrium flowfields. Since the method is fully viscous, the problems associated with coupling a boundary-layer solution with an inviscid-layer solution are avoided. This procedure is significantly faster than the parabolized Navier-Stokes (PNS) or VSL solvers and would be useful in a preliminary design environment. Problems associated with a previously developed approximate VSL technique are addressed before extending the method to nonequilibrium calculations. Perfect gas (laminar and turbulent), equilibrium, and nonequilibrium solutions have been generated for air flows over several analytic body shapes. Surface heat transfer, skin friction, and pressure predictions are comparable to VSL results. In addition, computed heating rates are in good agreement with experimental data. The present technique generates its own shock shape as part of its solution, and therefore could be used to provide more accurate initial shock shapes for higher-order procedures which require starting solutions.

Table of Contents

List of Figures

List of Tables

Nomenclature

A^+	Damping factor (turbulence model)
A_m	Coefficients of parabolic equation in standard form, Eq. (2.1.13); $m = 0, 1, 2, 3, 4$
b_b	Shape parameter for conic body
b_s	Subsonic shock shape parameter
c_i	Mass fraction of species i; $c_i = \rho_i / \rho$
C_f	Skin friction coefficient, defined by Eq. (3.4.1)
C_p	Specific heat at constant pressure
C_s	Subsonic shock shape parameter; $C_s = 1/\kappa_{s_0}$
$\mathcal{D}_{i,m}$	Multicomponent diffusion coefficient
$\mathcal{D}_{12}$	Binary diffusion coefficient
h	Static enthalpy
Δh_i^f	Heat of formation of species i
h_1, h_3	Metrics (shape factors) for generalized orthogonal curvilinear coordinate system
H	Total enthalpy; $H = h + V^2/2$
j_s	Number of points across the shock layer
$\mathcal{J}_i$	Diffusion mass flux of species i
$\tilde{\mathcal{J}}_i$	Component of diffusion mass flux of species i; $\mathcal{J}_i = \tilde{\mathcal{J}}_i \dfrac{\partial c_i}{\partial n}$
k	Thermal conductivity
k_r	Reactive conductivity (due to diffusion)
k_T	Total conductivity; $k_T = k + k_r$
k_b	Backward rate coefficient
k_f	Forward rate coefficient
K_B	Boltzmann's constant; $K_B = 1.38066 \times 10^{-16} erg/K$
l	Prandtl mixing length (turbulence model)
Le_{12}	Binary Lewis number; $Le_{12} = \dfrac{\rho C_{p_f} \mathcal{D}_{12}}{k}$
$Le_{i,m}$	Lewis number; $Le_{i,m} = \dfrac{\rho C_{p_f} \mathcal{D}_{i,m}}{k}$
M	Mach number
M_r	Catalytic third body for reaction r
$\mathcal{M}$	Molecular weight
n	Normal distance from the shock to a point within the shock layer
n^+	Normal coordinate parameter (turbulence model)
n_b	Shock standoff distance at current station
N_c	Number of catalytic third bodies

N_e	Electron number density
N_r	Number of chemical reactions
N_s	Number of reacting species
N_t	Number of reacting species and catalytic third bodies; $N_t = N_s + N_c$
p	Pressure
Pr	Prandtl number; $Pr = \dfrac{\mu C_p}{k}$
q	Heat transfer rate
q_c	Energy flux in the normal direction due to conduction
q_d	Energy flux in the normal direction due to diffusion
r	Radius measured from axis of symmetry
R	Radius of curvature
Re	Reynolds number; $Re = \dfrac{\rho u R_{nose}}{\mu}$
$\tilde{\mathcal{R}}$	Specific gas constant; $\tilde{\mathcal{R}} = \mathcal{R}_u / \mathcal{M}$
$\mathcal{R}_u$	Universal gas constant
s	Distance measured along the shock wave
t	Time
T	Temperature
T_r	Reference temperature for enthalpy and heat of formation
u	Velocity component tangent to the shock wave
v	Velocity component normal to the shock wave
V	Total velocity; $V^2 = u^2 + v^2$
$\dot{w}_i$	Mass rate of formation of species i
W	Dependent variable in parabolic equation of standard form
x_i	Mole fraction of species i
X_i	Concentration of species i (or catalytic body $i - N_s$)
z	Axial distance, measured from shock origin
Z	Compressibility factor (equilibrium gas)
$Z_{n,i}$	Third body catalytic efficiencies relative to argon, $n = N_s + 1, N_j$
$\alpha_{r,n}$	Stoichiometric coefficients for reactants, $n = 1, N_j$
$\beta_{r,n}$	Stoichiometric coefficients for products, $n = 1, N_j$
γ	Ratio of specific heats
γ_{ij}	Klebanoff's intermittency factor (turbulence model)
$\gamma_{i,\xi}$	Streamwise transition intermittency factor (turbulent flow)
γ_i	Mole mass ratio of species i
Γ_b	Body angle
Γ_s	Shock angle
δ	Value of η_n at boundary layer edge
δ_k	Boundary layer displacement thickness (turbulence model)
ϵ	Reynolds number parameter; $\epsilon = \sqrt{\dfrac{\mu_{ref}}{\rho_\infty u_\infty R_{nose}}}$

ϵ^+	Ratio of eddy viscosity to dynamic viscosity; $\epsilon^+ = \mu_t/\mu$
ϵ_i^+	Prandtl mixing length value of ϵ^+, inner layer (turbulence model)
ϵ_o^+	Clauser-Klebanoff value of ϵ^+, outer layer (turbulence model)
η	Ratio of local stream function to shock value; $\eta = \Psi/\Psi_s$
η_n	Computational n coordinate; $\eta_n = 1 - n/n_b$
κ	Curvature; $\kappa = 1/R$
μ	Dynamic viscosity
ξ	Computational s coordinate; $\xi = s$
ρ	Density
τ	Shear stress tensor
Ψ	Stream function

Superscripts

$^-$	Quantity normalized by shock value at current station
$\star$	Dimensional quantity

Subscripts

air	Value for standard air
b	Body value
e	Boundary layer edge
eq	Chemical equilibrium value
f	Chemically frozen value
i	Value for species i
j	Denotes j-th point within shock layer along a shock normal
k	Denotes k-th streamwise station
nose	Nose value
n	Denotes n-th reactant or product
N	Monatomic nitrogen
N_2	Diatomic nitrogen
NO	Nitrous oxide
O	Monatomic oxygen
O_2	Diatomic oxygen
p	Previous iteration
pg	Perfect gas value
r	Denotes r-th reaction
ref	Reference condition (see Appendix A)
s	Shock value

t	Turbulent value
w	Wall value
0	Stagnation point value
298.15	Referenced to $T = 298.15K$
∞	Freestream condition

1 Introduction

Ongoing investigations into configurations such as the Aeroassist Space Transfer Vehicle (ASTV), the National Aero-Space Plane (NASP), and the Personnel Launch System (PLS), with their associated high altitude, high speed environments, have sparked renewed interest in hypersonic aerodynamics [1]. Since extensive computer run times prevent more exact approaches from being used in the preliminary design environment, there is a continued interest in developing improved engineering methods.

For large Reynolds numbers, the shock layer consists of a large inviscid region and a thin boundary layer near the body. Typically, an inviscid solution to this outer region is coupled with a boundary-layer technique (e.g., Ref. [2]). For flows about blunt-nose bodies, the shock slope changes rapidly in the streamwise direction creating strong entropy gradients in the inviscid flow which must be accounted for when coupling the inviscid-layer and boundary-layer solutions.

The viscous region encompasses a significant portion of the shock layer at the lower Reynolds numbers encountered by hypersonic vehicles at high altitude. Most inviscid-layer/boundary-layer approaches neglect the boundary-layer effect on the outer layer, so in some cases a simple coupling technique may not give satisfactory results. Accurate predictions of the flowfield properties may be obtained from solutions to the Navier-Stokes [3], the parabolized Navier-Stokes [4, 5, 6], or the viscous shock layer [7, 8, 9, 10] equations. The full Navier-Stokes equations are typically solved using a time-marching procedure in order to properly model their elliptic behavior (a very costly computation). The parabolized Navier-Stokes (PNS) and viscous shock layer (VSL) equations are derived from the steady compressible Navier-Stokes equations. Both equation sets have been parabolized in the streamwise direction so that a solution may be advanced downstream using spatial marching techniques. These formulations account, among other things, for the nonzero normal pressure gradients which are neglected in a classical boundary-layer approach. Unfortunately, the computational requirements of existing methods for solving these equations exceed that which can be tolerated in preliminary parametric design studies.

For high energy flows, the assumption of perfect gas behavior is not valid since chemical reactions occur. Using the perfect gas assumption results in much higher post-shock temperature predictions than are realized in the flight environment. This reduced temperature is due to energy being absorbed by endothermic chemical reactions. The classical approach is to assume that these reactions occur at a fast enough rate, relative to the time scales of the flow, that an equilibrium composition has been achieved everywhere in the shock layer [8, 11].

Chemical reactions are a result of sufficiently high energy molecular collisions which, in air for example, cause the dissociation of O_2 and N_2 into O and N, along

with the production of NO. Such reactions require a finite amount of time to occur. Thus, a finite amount of time is required for the related chemical changes to take place. For equilibrium flows, the assumption is made that the residence time of the fluid in the shock layer is large relative to the time scales of the chemical reactions. Hence, the reactions occur nearly instantaneously. The assumption of equilibrium flow is not correct for many cases of interest, particularly with reentry trajectories. This is evident from the Catalytic Surface Experiment [12] flight data, which illustrate the nonequilibrium phenomenon via the rather noncatalytic nature of the Space Shuttle surface. Thus, consideration of these nonequilibrium effects in the design process is desirable. VSL solutions with finite-rate chemistry have been documented in a number of references [8, 13, 14, 15, 16, 17]. Unfortunately, the restrictive central processing unit (CPU) requirements cited earlier are intensified when nonequilibrium effects are included. Therefore, a more approximate approach which accounts for the effects of finite-rate chemistry would be useful.

In 1964, Maslen [18] published a simple inverse method (shock shape prescribed, body shape to be determined) for calculating the inviscid flowfield within the shock layer surrounding a smooth axisymmetric body. The direct problem, which is the more straightforward application, requires iterating the shock wave shape until the desired body shape is obtained. A closed-form expression for the local pressure in terms of the stream function is obtained by approximating the integral of the normal momentum equation. With the original approximations, the effects of the velocity normal to the shock are neglected. Using this first-order expression, Grose [19, 20] developed an inviscid, nonequilibrium method for calculating flows in Earth, Martian, and Venusian atmospheres.

In a later effort, Maslen approximated the normal velocity's contribution to the pressure relation to obtain a second order approximate integral of the normal momentum equation [21]. This expression better accounts for the recompression across the shock layer. Zoby and Graves [22] coupled this improved relation with the iterative scheme of Jackson [23] to solve the direct problem for a variety of blunt bodies. Later this approach was extended [24, 25] to include an approximate technique for calculating heating rates for bodies at angle of attack. Ref. [26] provides a review of additional approximate heating methods.

In a more recent work, Grantz and DeJarnette [27, 28, 29] employ the second order Maslen pressure relation, along with a simple linear expression for the normal component of velocity, in an approximate VSL approach. Boundary-layer-like viscous terms are added to the inviscid streamwise momentum and energy equations to obtain a parabolic equation set analogous to the full VSL equations. The viscous terms are retained across the entire shock layer, thus avoiding the problems which can be encountered in the coupled inviscid-layer/boundary-layer approach. Furthermore, since the shock shape is part of the solution, no initial shock shape or smoothing of intermediate shock shapes (both required for the VSL technique) is necessary.

The method of Ref. [29] did not fully yield the anticipated reductions in CPU

requirements as compared with the full VSL equations. Based on a review of the algorithm, several areas of concern in the original technique were recognized: 1) too many iterations are required for shock shape convergence; 2) the solution is inconsistent near the stagnation line; 3) the grid-point spacing across the shock layer may yield oscillations in the shock layer property profiles. Thus, it became apparent that a different approximate VSL approach should be explored.

The first portion of this paper discusses that effort, and details the differences between Ref. [29] and the new approach [30]. Three major differences between these techniques are: 1) more efficient algorithms than those employed in Ref. [29] are used to generate the shock shape; 2) the governing equations give a consistent limiting form on the stagnation line; 3) and the spacing across the layer is related to physical distance rather than the stream function, as in Ref. [29]. Comparisons of results and run times are made using the current approach, the method of Ref. [29], and a full VSL solver [9]. Comparisons with experiment are also made.

The second part of this document concerns nonequilibrium flowfield calculations. A seven-species finite-rate chemistry model for air [15] has been incorporated in the approximate VSL solver discussed above. Comparisons of results and run times are made using the current approach and a full VSL solver [14]. Comparisons with Space Shuttle flight data [31] are also made.

2   General Analysis

Ref. [29] discusses the development of an approximate viscous shock layer technique which is solved in a shock-normal coordinate system. The approach begins with an approximate inviscid flowfield solution based on the second-order pressure relation of Maslen [18], including an approximate representation for the normal component of velocity. In order to approximate a full VSL solution, boundary-layer-like terms are added to the inviscid energy and streamwise momentum equations.

Since the goal of the present work is to develop an approximate VSL algorithm, the current approach starts with the full VSL equations written in orthogonal curvilinear coordinates. First, the equations are cast in a shock-normal (rather than the traditional body-normal) coordinate system. This step is necessary in order to facilitate the use of Maslen's pressure relation which replaces the normal momentum equation. Since the remaining equations are unchanged, the normal component of velocity is found by solving the continuity equation rather than assuming a profile as was done in Ref. [29]. If the form of the energy and streamwise momentum equations used in Ref. [29] are compared to the full VSL equations in the shock-normal system, it can be noted that several "higher-order" terms (involving the variation of the metrics across the shock layer) have been neglected. These higher-order terms are retained in the present study.

The governing equations (along with their stagnation line formulations), boundary conditions, and surface quantities are presented in this chapter. In addition, key differences between the current approach and Ref. [29] are cited. The subsequent four chapters deal with applying these equations to perfect gas, equilibrium, turbulent, and nonequilibrium flows, respectively. Unless otherwise noted, the governing equations as presented in this chapter are employed in those applications. As a final comment, dimensionless variables (see Appendix A) are employed throughout this paper. Dimensional quantities are denoted by a superscript *, except in the results chapter where this superscript is omitted.

2.1   Viscous Shock Layer Equations

The Navier-Stokes equations written in curvilinear coordinates for axisymmetric flow are presented in Appendix B. If v and n are assumed to be order ϵ (where ϵ is the Reynolds number parameter), and terms greater than order ϵ are neglected, the VSL equations [7] are obtained (see Appendix B for details). They are presented below, excluding the normal momentum equation, in nondimensional form.

continuity:

$$\frac{\partial}{\partial s}(\rho u h_3) + \frac{\partial}{\partial n}(\rho v h_1 h_3) = 0 \tag{2.1.1}$$

s - momentum:

$$\rho\left(\frac{u}{h_1}\frac{\partial u}{\partial s} + v\frac{\partial u}{\partial n} + \frac{uv}{h_1}\frac{\partial h_1}{\partial n}\right) + \frac{1}{h_1}\frac{\partial p}{\partial s} = \qquad (2.1.2)$$

$$\epsilon^2\left\{\frac{\partial}{\partial n}\left[\mu\left(\frac{\partial u}{\partial n} - \frac{u}{h_1}\frac{\partial h_1}{\partial n}\right)\right] + \mu\left(\frac{2}{h_1}\frac{\partial h_1}{\partial n} + \frac{1}{h_3}\frac{\partial h_3}{\partial n}\right)\left[\frac{\partial u}{\partial n} - \frac{u}{h_1}\frac{\partial h_1}{\partial n}\right]\right\}$$

energy:

$$\rho\left(\frac{u}{h_1}\frac{\partial h}{\partial s} + v\frac{\partial h}{\partial n}\right) - \frac{u}{h_1}\frac{\partial p}{\partial s} - v\frac{\partial p}{\partial n} =$$

$$\epsilon^2\left\{\frac{\partial}{\partial n}\left[\frac{\mu}{Pr}\frac{\partial h}{\partial n}\right] + \frac{\mu}{Pr}\frac{\partial h}{\partial n}\left(\frac{1}{h_1}\frac{\partial h_1}{\partial n} + \frac{1}{h_3}\frac{\partial h_3}{\partial n}\right)\right. \qquad (2.1.3)$$

$$\left. + \mu\left(h_1\frac{\partial u}{\partial n} - u\frac{\partial h_1}{\partial n}\right)\left(\frac{1}{h_1}\frac{\partial u}{\partial n} - \frac{u}{h_1^2}\frac{\partial h_1}{\partial n}\right)\right\}$$

where the Reynolds number parameter is defined as

$$\epsilon^2 = \frac{\mu_{ref}^\star}{\rho_\infty^\star u_\infty^\star R_{nose}^\star}$$

and *Pr* is the Prandtl number. The dimensional reference conditions are given in Appendix A.

At this stage, this equation set could be transformed to either a body-normal or shock-normal system. The shock-oriented coordinate system is shown in Figure 2.1. Metrics associated with the shock-oriented coordinate system (where s is the distance along the *shock*) used in this effort are

$$h_1 = 1 - n\kappa_s \qquad\qquad h_3 = r = r_s - n\cos\Gamma_s \qquad (2.1.4)$$

where n is the inward normal distance from the shock and κ_s is the shock curvature. By definition,

$$\kappa_s = -\frac{d\Gamma_s}{ds} \qquad (2.1.5)$$

Note: *In addition to Eqs. (2.1.1) through (2.1.3), the standard VSL equations employ the normal momentum equation:*

$$\rho\left(\frac{u}{h_1}\frac{\partial v}{\partial s} + v\frac{\partial v}{\partial n} - \frac{u^2}{h_1}\frac{\partial h_1}{\partial n}\right) + \frac{\partial p}{\partial n} = 0 \qquad (2.1.6)$$

This set of equations is solved in a body-oriented coordinate system (where s is the distance along the body). The metrics are defined as

$$h_1 = 1 + n\kappa_b \qquad\qquad h_3 = r = r_b + n\cos\Gamma_b$$

where n is the outward normal distance from the body and κ_b is the body curvature (which, by definition, is $-d\Gamma_b/ds$).
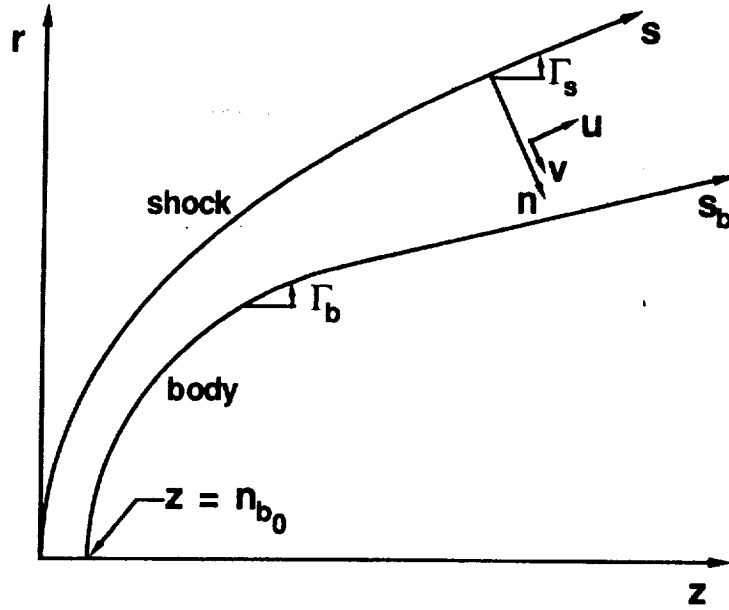
Figure 2.1. Flowfield geometry and curvilinear coordinate system.

In order to facilitate the solution of the governing equations, a transformation to normalized coordinates is performed to yield a constant number of points across the layer from station to station. Using the shock properties, define the following computational variables:

$$\xi = s \qquad\qquad \eta_n = 1 - \frac{n}{n_b}$$

$$\bar{u} = \frac{u}{u_s} \qquad\qquad \bar{\rho} = \frac{\rho}{\rho_s}$$

where n_b and the shock properties are functions of ξ only. From its definition, $\eta_n = 0$ on the body and $\eta_n = 1$ at the shock. The chain rule of differentiation gives

$$\frac{\partial}{\partial s} = \frac{\partial \xi}{\partial s}\frac{\partial}{\partial \xi} + \frac{\partial \eta_n}{\partial s}\frac{\partial}{\partial \eta_n} \qquad\qquad \frac{\partial}{\partial n} = \frac{\partial \xi}{\partial n}\frac{\partial}{\partial \xi} + \frac{\partial \eta_n}{\partial n}\frac{\partial}{\partial \eta_n}$$

Since

$$\frac{\partial \xi}{\partial s} = 1 \qquad\qquad \frac{\partial \eta_n}{\partial s} = \frac{n}{n_b^2}\frac{dn_b}{ds}$$

$$\frac{\partial \xi}{\partial n} = 0 \qquad\qquad \frac{\partial \eta_n}{\partial n} = -\frac{1}{n_b}$$

the derivatives in this coordinate system are

$$\frac{\partial}{\partial s} = \frac{\partial}{\partial \xi} - \frac{\eta_n - 1}{n_b}\frac{dn_b}{d\xi}\frac{\partial}{\partial \eta_n} \qquad\qquad \frac{\partial}{\partial n} = -\frac{1}{n_b}\frac{\partial}{\partial \eta_n} \qquad\qquad (2.1.7)$$

In the transformed coordinate system employed here, the metrics, Eq. (2.1.4), become

$$h_1 = 1 + n_b \left(\eta_n - 1 \right) \kappa_s \qquad\qquad h_3 = r_s + n_b \left(\eta_n - 1 \right) \cos \Gamma_s \qquad (2.1.8)$$

Their partial derivatives in the normal direction are

$$\frac{\partial h_1}{\partial n} = -\kappa_s = -\frac{1}{n_b}\frac{\partial h_1}{\partial \eta_n} \qquad\qquad \frac{\partial h_3}{\partial n} = -\cos \Gamma_s = -\frac{1}{n_b}\frac{\partial h_3}{\partial \eta_n} \qquad (2.1.9)$$

The governing equations in this normalized shock-oriented coordinate system can now be written as
continuity:

$$\frac{\partial}{\partial \xi}\left(\rho_s \bar{\rho} u_s \bar{u} h_3 \right) - \rho_s u_s \frac{\eta_n - 1}{n_b}\frac{dn_b}{d\xi}\frac{\partial}{\partial \eta_n}\left(\bar{\rho}\bar{u}h_3 \right) - \frac{\rho_s}{n_b}\frac{\partial}{\partial \eta_n}\left(\bar{\rho}v h_1 h_3 \right) = 0 \qquad (2.1.10)$$

ξ - *momentum:*

$$\rho_s \bar{\rho} \left(\frac{u}{h_1}\left[u_s \frac{\partial u}{\partial \xi} + \bar{u}\frac{du_s}{d\xi} - u_s \frac{\eta_n - 1}{n_b}\frac{dn_b}{d\xi}\frac{\partial \bar{u}}{\partial \eta_n}\right] - \frac{v}{n_b}\left[\frac{\partial \bar{u}}{\partial \eta_n} + \frac{\bar{u}}{h_1}\frac{\partial h_1}{\partial \eta_n}\right]\right)$$

$$+ \frac{1}{h_1 u_s}\left[\frac{\partial p}{\partial \xi} - \frac{\eta_n - 1}{n_b}\frac{dn_b}{d\xi}\frac{\partial p}{\partial \eta_n}\right] = \frac{\epsilon^2}{n_b^2}\left\{ \frac{\partial}{\partial \eta_n}\left[\mu \left(\frac{\partial \bar{u}}{\partial \eta_n} - \frac{\bar{u}}{h_1}\frac{\partial h_1}{\partial \eta_n}\right)\right]\right.$$

$$\left. + \mu \left(\frac{2}{h_1}\frac{\partial h_1}{\partial \eta_n} + \frac{1}{h_3}\frac{\partial h_3}{\partial \eta_n}\right)\left(\frac{\partial \bar{u}}{\partial \eta_n} - \frac{\bar{u}}{h_1}\frac{\partial h_1}{\partial \eta_n}\right)\right\} \qquad (2.1.11)$$

energy:

$$\rho_s \bar{\rho} \left(\frac{u_s \bar{u}}{h_1}\left[\frac{\partial h}{\partial \xi} - \frac{\eta_n - 1}{n_b}\frac{dn_b}{d\xi}\frac{\partial h}{\partial \eta_n}\right] - \frac{v}{n_b}\frac{\partial h}{\partial \eta_n}\right)$$

$$- \frac{u_s \bar{u}}{h_1}\left[\frac{\partial p}{\partial \xi} - \frac{\eta_n - 1}{n_b}\frac{dn_b}{d\xi}\frac{\partial p}{\partial \eta_n}\right] + \frac{v}{n_b}\frac{\partial p}{\partial \eta_n} = \qquad (2.1.12)$$

$$\frac{\epsilon^2}{n_b^2}\left\{ \frac{\partial}{\partial \eta_n}\left[\frac{\mu}{Pr}\frac{\partial h}{\partial \eta_n}\right] + \frac{\mu}{Pr}\frac{\partial h}{\partial \eta_n}\left(\frac{1}{h_1}\frac{\partial h_1}{\partial \eta_n} + \frac{1}{h_3}\frac{\partial h_3}{\partial \eta_n}\right) + u_s^2 \mu \left(\frac{\partial \bar{u}}{\partial \eta_n} - \frac{\bar{u}}{h_1}\frac{\partial h_1}{\partial \eta_n}\right)^2\right\}$$

Equations Eqs. (2.1.11) and (2.1.12) can be cast in the following standard form for parabolic partial differential equations:

$$A_0 \frac{\partial^2 W}{\partial \eta_n^2} + A_1 \frac{\partial W}{\partial \eta_n} + A_2 W + A_3 + A_4 \frac{\partial W}{\partial \xi} = 0 \qquad (2.1.13)$$

where W represents the dependent variables $\bar{u}$ and h, respectively. The values for the coefficients are listed below:
ξ - *momentum:*

$$A_0 = -\frac{\epsilon^2}{n_b^2}\mu$$

$$A_1 = -\frac{\epsilon^2}{n_b^2}\left[\frac{\partial \mu}{\partial \eta_n} + \mu\left(\frac{1}{h_1}\frac{\partial h_1}{\partial \eta_n} + \frac{1}{h_3}\frac{\partial h_3}{\partial \eta_n}\right)\right] - \rho_s\bar{\rho}\left[\frac{v}{n_b} + \frac{u_s\bar{u}}{h_1}\frac{\eta_n - 1}{n_b}\frac{dn_b}{d\xi}\right]$$

$$A_2 = \frac{\epsilon^2}{n_b^2}\left(\frac{1}{h_1}\frac{\partial h_1}{\partial \eta_n}\right)\left[\frac{\partial \mu}{\partial \eta_n} + \mu\left(\frac{1}{h_1}\frac{\partial h_1}{\partial \eta_n} + \frac{1}{h_3}\frac{\partial h_3}{\partial \eta_n}\right)\right] + \frac{\rho_s\bar{\rho}}{h_1}\left(\bar{u}\frac{du_s}{d\xi} - \frac{v}{n_b}\frac{\partial h_1}{\partial \eta_n}\right)$$

$$A_3 = \frac{1}{h_1}\left[\left\{\frac{1}{u_s}\frac{\partial p}{\partial \xi}\right\} - \frac{\eta_n - 1}{n_b}\frac{\partial p}{\partial \eta_n}\left\{\frac{1}{u_s}\frac{dn_b}{d\xi}\right\}\right] \qquad (2.1.14)$$

$$A_4 = \rho_s u_s\frac{\bar{\rho}\bar{u}}{h_1}$$

energy:

$$A_0 = -\frac{\epsilon^2}{n_b^2}\frac{\mu}{Pr}$$

$$A_1 = -\frac{\epsilon^2}{n_b^2}\left[\frac{\partial}{\partial \eta_n}\left(\frac{\mu}{Pr}\right) + \frac{\mu}{Pr}\left(\frac{1}{h_1}\frac{\partial h_1}{\partial \eta_n} + \frac{1}{h_3}\frac{\partial h_3}{\partial \eta_n}\right)\right] - \rho_s\bar{\rho}\left[\frac{v}{n_b} + \frac{u_s\bar{u}}{h_1}\frac{\eta_n - 1}{n_b}\frac{dn_b}{d\xi}\right]$$

$$A_2 = 0 \qquad (2.1.15)$$

$$A_3 = -\frac{u_s\bar{u}}{h_1}\left[\frac{\partial p}{\partial \xi} - \frac{\eta_n - 1}{n_b}\frac{dn_b}{d\xi}\frac{\partial p}{\partial \eta_n}\right] + \frac{v}{n_b}\frac{\partial p}{\partial \eta_n} - \epsilon^2\mu\frac{u_s^2}{n_b^2}\left(\frac{\partial \bar{u}}{\partial \eta_n} - \frac{\bar{u}}{h_1}\frac{\partial h_1}{\partial \eta_n}\right)^2$$

$$A_4 = \rho_s u_s\frac{\bar{\rho}\bar{u}}{h_1}$$

2.2 Maslen's Pressure Equation

As mentioned in the previous section, the normal momentum equation is solved as part of the standard VSL solution. In the approximate VSL method, Maslen's second-order pressure equation is used in lieu of numerically integrating the n-momentum equation. The derivation of this approximate closed-form expression is presented in Appendix C. The result is repeated here:

$$p(\xi, \eta) = p_s + \frac{\kappa_s r_s u_s}{2}(\eta - 1) - \frac{v_s \sin \Gamma_s}{4}\left[1 + \frac{\kappa_s r_s}{\cos \Gamma_s}\right](\eta^2 - 1) \qquad (2.2.1)$$

where

$$\eta = \frac{\Psi}{\Psi_s}$$

and Ψ is the stream function.

Maslen's pressure expression offers an attractive alternative to numerically integrating the normal momentum equation to solve for p, since it expresses p as a function of the shock properties at the current station and η only. This relation is very simple as compared with the normal momentum equation which it supplants.

The variable η should not be confused with the transformation variable η_n defined previously. The relationship between these distinct quantities is derived in Appendix D, and is repeated below:

$$\Psi_s \eta = n_b^2 \left[\rho_s u_s^2 \int_0^{\eta_n} \bar{\rho}\bar{u} \left(\eta_n - 1 \right) d\eta_n \right] + n_b \left[\rho_s u_s r_s \int_0^{\eta_n} \bar{\rho}\bar{u} d\eta_n \right] \qquad (2.2.2)$$

Maslen's relation fosters analytic relations for the partial derivatives of pressure (which appear in the governing equations) as well. Differentiating Eq. (2.2.1) with respect to η gives

$$\frac{\partial p}{\partial \eta} = \frac{\kappa_s r_s u_s}{2} - \frac{v_s \sin \Gamma_s}{2} \left[1 + \frac{\kappa_s r_s}{\cos \Gamma_s} \right] \eta \qquad (2.2.3)$$

Differentiating Eq. (2.2.1) with respect to ξ gives

$$\left. \frac{\partial p}{\partial \xi} \right|_\eta = \frac{dp_s}{d\xi} + \frac{\eta - 1}{2} \left\{ u_s \kappa_s \sin \Gamma_s + u_s r_s \frac{d\kappa_s}{d\xi} + \kappa_s^2 r_s \sin \Gamma_s \right\}$$

$$- \frac{\eta^2 - 1}{4} \left\{ \frac{v_s \sin \Gamma_s}{\cos \Gamma_s} \left[r_s \frac{d\kappa_s}{d\xi} + \kappa_s \sin \Gamma_s \left(1 - \frac{\kappa_s r_s}{\cos \Gamma_s} \right) \right] \right.$$

$$\left. + \left(1 + \frac{\kappa_s r_s}{\cos \Gamma_s} \right) \left[\sin \Gamma_s \frac{dv_s}{d\xi} - v_s \kappa_s \cos \Gamma_s \right] \right\} \qquad (2.2.4)$$

As noted, Eq. (2.2.4) is the partial derivative of p along lines of constant η. The following expression relates this quantity to the partial derivative of p along lines of constant η_n (see Appendix C):

$$\left. \frac{\partial p}{\partial \xi} \right|_{\eta_n} = \left. \frac{\partial p}{\partial \xi} \right|_\eta + \frac{\partial \eta}{\partial s} \frac{\partial p}{\partial \eta} + \frac{\eta_n - 1}{n_b} \frac{dn_b}{d\xi} \frac{\partial p}{\partial \eta_n} \qquad (2.2.5)$$

where

$$\frac{\partial \eta}{\partial s} = \frac{\rho_s \bar{\rho} u_s \bar{u} h_3}{\Psi_s} \left. \frac{\partial n}{\partial \xi} \right|_\eta \qquad (2.2.6)$$

and

$$\left. \frac{\partial n}{\partial \xi} \right|_\eta = \frac{(1 - \eta)}{2} \frac{v_s}{\cos \Gamma_s} \left[1 - \frac{\kappa_s r_s}{\cos \Gamma_s} \right] \qquad (2.2.7)$$

Further,

$$\frac{\partial p}{\partial \eta_n} = \frac{\rho_s \bar{\rho} u_s \bar{u} h_3 n_b}{\Psi_s} \frac{\partial p}{\partial \eta} \qquad (2.2.8)$$

2.3 Wall Boundary Conditions

The no-slip condition is applied at the wall so that

$$u_w = v_w = 0$$

In addition, the wall temperature (T_w), which can vary along the wall, must be specified.

2.4   Stagnation Line

The stagnation line is a singularity in the standard VSL equations. Typically, this singularity is handled by representing the dependent variables on the stagnation line with a truncated power series of ξ. Substituting these expressions into the governing equations yields a set of ordinary differential equations for the stagnation line. However, since truncated expansions were used in their formulation, these stagnation line equations are not strictly consistent with the general governing equations.

In the shock-oriented system, an explicit limiting form of the governing equations as $\xi \to 0$ can be calculated, since Maslen's relation provides analytic derivatives of the pressure. Thus, a set of ordinary differential equations which is consistent with the general governing equations can be obtained. The form of the streamwise momentum equation used in Ref. [29] contains a group of terms which vanish on the stagnation line provided the normal momentum equation is satisfied. However, Maslen's expression does not satisfy the normal momentum equation, so a correction term must be carried along throughout the shock layer in order to force the solution to smoothly approach its stagnation value. Despite these efforts, the stagnation solution was not consistent with the remainder of the layer. In the current research, the streamwise momentum equation does not contain this group of terms, so no correction terms are required. Results of Chapter 9 show that with the current approach, the problem with the limiting form of the equations as they near the stagnation line is successfully addressed. The governing equations for the stagnation line are presented below.

2.4.1   Viscous Shock Layer Equations

The limiting values of the geometric quantities are given in Appendix E. First consider the continuity equation. Without loss of generality, Eq. (2.1.10) can be rewritten as

$$\frac{\partial}{\partial \xi} \left(\rho_s u_s n_b \bar{\rho}\bar{u} h_3 \right) - \rho_s u_s \frac{dn_b}{d\xi} \frac{\partial}{\partial \eta_n} \left[(\eta_n - 1) \bar{\rho}\bar{u} h_3 \right] - \rho_s \frac{\partial}{\partial \eta_n} \left(\bar{\rho} v h_1 h_3 \right) = 0 \qquad (2.4.1)$$

On the stagnation line,

$$\lim_{\xi \to 0} \left\{ u_s \frac{\partial}{\partial \xi} \left(\rho_s n_b \bar{\rho}\bar{u} h_1 \right) + \frac{\rho_s n_b}{r_s} \bar{\rho}\bar{u} h_1 \frac{\partial}{\partial \xi} \left(u_s r_s \right) - \rho_s u_s \frac{dn_b}{d\xi} \frac{\partial}{\partial \eta_n} \left[(\eta_n - 1) \bar{\rho}\bar{u} h_1 \right] \right\}$$

$$- \rho_{s_0} \frac{\partial}{\partial \eta_n} \left(\bar{\rho} v h_1^2 \right) = 0 \qquad (2.4.2)$$

so that

$$\bar{\rho}\bar{u} h_1 \lim_{\xi \to 0} \left\{ \rho_s n_b \left[\frac{u_s}{r_s} \frac{dr_s}{d\xi} + \frac{du_s}{d\xi} \right] \right\} - \rho_{s_0} \frac{\partial}{\partial \eta_n} \left(\bar{\rho} v h_1^2 \right) = 0 \qquad (2.4.3)$$

Further applying these limits to Eqs. (2.1.11) and (2.1.12) yields the following set of equations which are valid along the stagnation line:

continuity:

$$2\kappa_{s_0} n_{b_0} \rho_{s_0} \bar{\rho} \bar{u} h_1 - \rho_{s_0} \frac{\partial}{\partial \eta_n} \left(\bar{\rho} v h_1^2 \right) = 0 \tag{2.4.4}$$

ξ - *momentum:*

$$\rho_{s_0} \bar{\rho} \left(\frac{\bar{u}^2}{h_1} \frac{du_s}{d\xi} - \frac{v}{n_{b_0}} \left[\frac{\partial \bar{u}}{\partial \eta_n} + \frac{\bar{u}}{h_1} \frac{\partial h_1}{\partial \eta_n} \right] \right) + \frac{1}{h_1} \lim_{\xi \to 0} \left\{ \frac{1}{u_s} \left[\frac{\partial p}{\partial \xi} - \frac{\eta_n - 1}{n_b} \frac{dn_b}{d\xi} \frac{\partial p}{\partial \eta_n} \right] \right\}$$

$$= \frac{\epsilon^2}{n_{b_0}^2} \left\{ \frac{\partial}{\partial \eta_n} \left[\mu \left(\frac{\partial \bar{u}}{\partial \eta_n} - \frac{\bar{u}}{h_1} \frac{\partial h_1}{\partial \eta_n} \right) \right] + 3 \frac{\mu}{h_1} \frac{\partial h_1}{\partial \eta_n} \left(\frac{\partial \bar{u}}{\partial \eta_n} - \frac{\bar{u}}{h_1} \frac{\partial h_1}{\partial \eta_n} \right) \right\} \tag{2.4.5}$$

energy:

$$- \rho_{s_0} \bar{\rho} v \frac{\partial h}{\partial \eta_n} + v \frac{\partial p}{\partial \eta_n} = \frac{\epsilon^2}{n_{b_0}} \left\{ \frac{\partial}{\partial \eta_n} \left[\frac{\mu}{Pr} \frac{\partial h}{\partial \eta_n} \right] + \frac{2}{h_1} \frac{\mu}{Pr} \frac{\partial h_1}{\partial \eta_n} \frac{\partial h}{\partial \eta_n} \right\} \tag{2.4.6}$$

It follows that Eqs. (2.1.14) and (2.1.15) become

ξ - *momentum:*

$$A_0 = -\frac{\epsilon^2}{n_{b_0}^2} \mu$$

$$A_1 = -\frac{\epsilon^2}{n_{b_0}^2} \left[\frac{\partial \mu}{\partial \eta_n} + 2 \frac{\mu}{h_1} \frac{\partial h_1}{\partial \eta_n} \right] - \rho_{s_0} \bar{\rho} \frac{v}{n_{b_0}}$$

$$A_2 = \frac{\epsilon^2}{n_{b_0}^2} \left(\frac{1}{h_1} \frac{\partial h_1}{\partial \eta_n} \right) \left[\frac{\partial \mu}{\partial \eta_n} + 2 \frac{\mu}{h_1} \frac{\partial h_1}{\partial \eta_n} \right] + \frac{\rho_{s_0} \bar{\rho}}{h_1} \left(\bar{u} \frac{du_s}{d\xi} - \frac{v}{n_{b_0}} \frac{\partial h_1}{\partial \eta_n} \right) \tag{2.4.7}$$

$$A_3 = \frac{1}{h_1} \left[\lim_{\xi \to 0} \left\{ \frac{1}{u_s} \frac{\partial p}{\partial \xi} \right\} - \frac{\eta_n - 1}{n_{b_0}} \frac{\partial p}{\partial \eta_n} \lim_{\xi \to 0} \left\{ \frac{1}{u_s} \frac{dn_b}{d\xi} \right\} \right]$$

$$A_4 = 0$$

energy:

$$A_0 = -\frac{\epsilon^2}{n_{b_0}} \frac{\mu}{Pr}$$

$$A_1 = -\frac{\epsilon^2}{n_{b_0}} \left[\frac{\partial}{\partial \eta_n} \left(\frac{\mu}{Pr} \right) + \frac{2}{h_1} \frac{\mu}{Pr} \frac{\partial h_1}{\partial \eta_n} \right] - \rho_{s_0} \bar{\rho} v$$

$$A_2 = 0 \tag{2.4.8}$$

$$A_3 = v \frac{\partial p}{\partial \eta_n}$$

$$A_4 = 0$$

2.4.2   Maslen's Pressure Equation

On the stagnation line, equation Eq. (2.2.1) reduces to

$$p(\eta) = p_{s_0} - \frac{v_{s_0}}{2}\left(\eta^2 - 1\right) \tag{2.4.9}$$

and Eq. (2.2.2) becomes

$$\frac{1}{2}\eta = n_{b_0}{}^2\left[\rho_{s_0}\kappa_{s_0}{}^2\int_0^{\eta_n}\bar{\rho}\bar{u}\left(\eta_n - 1\right)d\eta_n\right] + n_{b_0}\left[\rho_{s_0}\kappa_{s_0}\int_0^{\eta_n}\bar{\rho}\bar{u}d\eta_n\right] \tag{2.4.10}$$

From Eq. (2.2.3)

$$\frac{\partial p}{\partial \eta} = -v_{s_0}\eta \tag{2.4.11}$$

Further, Eq. (2.2.4) becomes

$$\lim_{\xi \to 0}\left\{\frac{1}{u_s}\left.\frac{\partial p}{\partial \xi}\right|_{\eta}\right\} = \lim_{\xi \to 0}\left\{\frac{1}{u_s}\frac{dp_s}{d\xi}\right\} + \kappa_{s_0}\left(\eta - 1\right) \tag{2.4.12}$$

$$-\frac{\eta^2 - 1}{4}\left\{v_{s_0}\left[\frac{1}{\kappa_{s_0}}\lim_{\xi \to 0}\left\{\frac{1}{u_s}\frac{d\kappa_s}{d\xi}\right\} + \kappa_{s_0}\lim_{\xi \to 0}\left\{\frac{\cos\Gamma_s - r_s\kappa_s}{u_s^3}\right\}\right]\right.$$

$$\left. + 2\left[\lim_{\xi \to 0}\left\{\frac{1}{u_s}\frac{dv_s}{d\xi}\right\} - v_{s_0}\kappa_{s_0}\right]\right\}$$

Utilizing results from Appendix E, this can be written as

$$\lim_{\xi \to 0}\left\{\frac{1}{u_s}\left.\frac{\partial p}{\partial \xi}\right|_{\eta}\right\} = \lim_{\xi \to 0}\left\{\frac{1}{u_s}\frac{dp_s}{d\xi}\right\} + \kappa_{s_0}\left(\eta - 1\right) \tag{2.4.13}$$

$$-\frac{\eta^2 - 1}{2}\left[\frac{2}{3}\frac{v_{s_0}}{\kappa_{s_0}}\lim_{\xi \to 0}\left\{\frac{1}{u_s}\frac{d\kappa_s}{d\xi}\right\} + \lim_{\xi \to 0}\left\{\frac{1}{u_s}\frac{dv_s}{d\xi}\right\} - v_{s_0}\kappa_{s_0}\right]$$

where the terms

$$\lim_{\xi \to 0}\left\{\frac{1}{u_s}\frac{dp_s}{d\xi}\right\} \qquad\qquad \lim_{\xi \to 0}\left\{\frac{1}{u_s}\frac{dv_s}{d\xi}\right\} \qquad\qquad \lim_{\xi \to 0}\left\{\frac{1}{u_s}\frac{d\kappa_s}{d\xi}\right\}$$

are defined elsewhere.

Continuing, from Eq. (2.2.5) the limiting form of the streamwise pressure gradient is

$$\lim_{\xi \to 0}\left\{\frac{1}{u_s}\left.\frac{\partial p}{\partial \xi}\right|_{\eta_n}\right\} = \lim_{\xi \to 0}\left\{\frac{1}{u_s}\left.\frac{\partial p}{\partial \xi}\right|_{\eta}\right\} + \frac{\partial p}{\partial \eta}\lim_{\xi \to 0}\left\{\frac{1}{u_s}\frac{\partial \eta}{\partial s}\right\} + \frac{\eta_n - 1}{n_{b_0}}\frac{\partial p}{\partial \eta_n}\lim_{\xi \to 0}\left\{\frac{1}{u_s}\frac{dn_b}{d\xi}\right\}$$

$$\tag{2.4.14}$$

where

$$\lim_{\xi \to 0} \left\{ \frac{1}{u_s} \frac{\partial \eta}{\partial s} \right\} = 2\rho_{s_0} \bar{\rho} \bar{u} h_1 \lim_{\xi \to 0} \left\{ \frac{1}{r_s} \frac{\partial n}{\partial \xi} \bigg|_\eta \right\} \qquad (2.4.15)$$

Taking the limit of the streamwise derivative of n gives

$$\lim_{\xi \to 0} \left\{ \frac{1}{r_s} \frac{\partial n}{\partial \xi} \bigg|_\eta \right\} = (1 - \eta) \frac{v_{s_0}}{2} \lim_{\xi \to 0} \left\{ \frac{\cos \Gamma_s - r_s \kappa_s}{u_s^2 r_s} \right\}$$

so that (see Appendix E)

$$\lim_{\xi \to 0} \left\{ \frac{1}{r_s} \frac{\partial n}{\partial \xi} \bigg|_\eta \right\} = \frac{(\eta - 1) v_{s_0}}{6 \kappa_{s_0}} \lim_{\xi \to 0} \left\{ \frac{1}{u_s} \frac{d\kappa_s}{d\xi} \right\} \qquad (2.4.16)$$

Further, the derivative of p with respect to η_n is

$$\frac{\partial p}{\partial \eta_n} = 2\rho_{s_0} \kappa_{s_0} n_{b_0} \bar{\rho} \bar{u} h_1 \frac{\partial p}{\partial \eta} \qquad (2.4.17)$$

3 Perfect Gas Analysis

The governing equations given in Chapter 2 must be supplemented by the equation of state. In addition, the thermodynamic and transport properties are required for closure of the equations set. This chapter supplies those quantities for perfect gas flows. In addition, the perfect gas shock jump conditions are given in Section 3.3. Perfect gas results generated using these governing equations are presented in Chapter 9.

3.1 State Equation

In its general form, the equation of state is

$$p^\star = p^\star \left(\rho^\star, h^\star \right)$$

For perfect gas flows,

$$p^\star = \rho^\star \tilde{\mathcal{R}}^\star T^\star \tag{3.1.1}$$

where for standard air (N_2 and O_2 only), $\tilde{\mathcal{R}}^\star = \tilde{\mathcal{R}}^\star_{air}$. Written in nondimensional form (see Appendix A),

$$p = \rho \tilde{\mathcal{R}}_{air} T = \rho \frac{\gamma - 1}{\gamma} T \tag{3.1.2}$$

where γ is the ratio of specific heats.

3.2 Thermodynamic and Transport Properties

For perfect gas flows, the specific heat has a constant value:

$$C_p^\star = \frac{\gamma \tilde{\mathcal{R}}^\star_{air}}{\gamma - 1} \tag{3.2.1}$$

where in nondimensional form (see Appendix A) this becomes

$$C_p = \frac{\gamma \tilde{\mathcal{R}}_{air}}{\gamma - 1} = 1 \tag{3.2.2}$$

As a result, the definition of enthalpy for perfect gas flows is simply

$$h^\star = C_p^\star T^\star \tag{3.2.3}$$

so that nondimensionally

$$h = C_p T = T \tag{3.2.4}$$

Sutherland's law [32] is employed to calculate the viscosity:

$$\mu^* = 2.27 \times 10^{-8} \frac{T^{*1.5}}{T^* + 198.6} \qquad [slug/ft\text{-}s] \qquad (3.2.5)$$

where T^* is in degrees R. The Prandtl number (Pr) is the ratio of viscous diffusivity to thermal diffusivity:

$$Pr = \frac{\mu C_p}{k} \qquad (3.2.6)$$

For a perfect gas, this quantity is constant throughout the shock layer, and in this investigation is assumed to be $Pr = .72$. With C_p, μ, and Pr as defined above, the thermal conductivity, k, can be determined from Eq. (3.2.6).

3.3 Shock Properties

The shock jump conditions are given by the Rankine-Hugoniot relations. For the special case of perfect gas flow, these expressions take the following form (see Appendix F for details):

$$p_s = \frac{2\sin^2 \Gamma_s}{\gamma + 1} - \frac{\gamma - 1}{\gamma(\gamma + 1) M_\infty^2} \qquad (3.3.1)$$

$$\rho_s = \frac{(\gamma + 1) M_\infty^2 \sin^2 \Gamma_s}{2 + (\gamma - 1) M_\infty^2 \sin^2 \Gamma_s} \qquad (3.3.2)$$

$$T_s = \frac{p_s}{\rho_s} \frac{\gamma}{\gamma - 1} \qquad (3.3.3)$$

$$v_s = \frac{\sin \Gamma_s}{\rho_s} \qquad (3.3.4)$$

The streamwise derivative of u_s appears in the ξ-momentum equation. Further, the derivatives of p_s and v_s with respect to ξ are required for Maslen's analytic expression for $dp_s/d\xi$. These gradients are given by (see Appendix F)

$$\frac{du_s}{d\xi} = \kappa_s \sin \Gamma_s \qquad (3.3.5)$$

$$\frac{dv_s}{d\xi} = \kappa_s \cos \Gamma_s \left[\frac{4}{(\gamma + 1) M_\infty^2 \sin^2 \Gamma_s} - \frac{1}{\rho_s} \right] \qquad (3.3.6)$$

$$\frac{dp_s}{d\xi} = -\frac{4}{(\gamma + 1)} \kappa_s \sin \Gamma_s \cos \Gamma_s \qquad (3.3.7)$$

On the stagnation line, the shock jump conditions take the form of the normal shock relations:

$$p_{s_0} = \frac{2}{\gamma + 1} - \frac{\gamma - 1}{\gamma(\gamma + 1) M_\infty^2} \qquad (3.3.8)$$

$$\rho_{s_0} = \frac{(\gamma + 1)\, M_\infty^2}{2 + (\gamma - 1)\, M_\infty^2} \tag{3.3.9}$$

$$T_{s_0} = \frac{p_{s_0}}{\rho_{s_0}} \frac{\gamma}{\gamma - 1} \tag{3.3.10}$$

$$v_{s_0} = \frac{1}{\rho_{s_0}} \tag{3.3.11}$$

In addition, the stagnation line limiting forms of the shock gradients are

$$\frac{du_s}{d\xi} = \kappa_{s_0} \tag{3.3.12}$$

$$\lim_{\xi \to 0} \left\{ \frac{1}{u_s} \frac{dv_s}{d\xi} \right\} = \kappa_{s_0} \left[\frac{4}{(\gamma + 1)\, M_\infty^2} - \frac{1}{\rho_{s_0}} \right] \tag{3.3.13}$$

$$\lim_{\xi \to 0} \left\{ \frac{1}{u_s} \frac{dp_s}{d\xi} \right\} = -\frac{4\kappa_{s_0}}{(\gamma + 1)} \tag{3.3.14}$$

3.4   Surface Quantities

In the design environment, estimates of the lift, drag, and heating rates are desired. Thus, a design tool should provide values for body pressure, skin friction, and heat transfer rate. In this effort, the body pressure is supplied by Maslen's relation. Relations for the skin friction and heating rates are given below. Gradients along the shock-normal lines are used in lieu of body-normal values.

The skin friction coefficient is defined as

$$C_f = \frac{2}{\rho_\infty^\star V_\infty^{\star 2}} \tau_w^\star \tag{3.4.1}$$

where the shear stress at the wall is

$$\tau_w^\star = \mu_w^\star \left(-\frac{\partial u^\star}{\partial n^\star} \right) \bigg|_w \tag{3.4.2}$$

In terms of the nondimensional variables (see Appendix A),

$$\tau_w^\star = \left(\mu_{ref}^\star \frac{V_\infty^\star}{R_{nose}^\star} \right) \frac{\mu_w}{n_b} \frac{\partial u}{\partial \eta_n} \bigg|_w \tag{3.4.3}$$

so that

$$C_f = 2 \frac{\epsilon^2}{n_b} \mu_w \frac{\partial u}{\partial \eta_n} \bigg|_w \tag{3.4.4}$$

The heat transfer rate (see Appendix G) to the body is

$$q_w^\star = -k_w^\star \left. \frac{\partial T^\star}{\partial n^\star} \right|_w \tag{3.4.5}$$

so that in nondimensional form,

$$q_w = -\epsilon^2 k_w \left. \frac{\partial T}{\partial n} \right|_w = \frac{\epsilon^2}{n_b} k_w \left. \frac{\partial T}{\partial \eta_n} \right|_w \tag{3.4.6}$$

Since

$$dh = C_p dT$$

this may be written as

$$q_w = \frac{\epsilon^2}{n_b} \frac{k_w}{C_p} \left. \frac{\partial h}{\partial \eta_n} \right|_w \tag{3.4.7}$$

or

$$q_w = \frac{\epsilon^2}{n_b} \frac{\mu_w}{Pr_w} \left. \frac{\partial h}{\partial \eta_n} \right|_w \tag{3.4.8}$$

4   Equilibrium Analysis

The governing equations as presented in Chapter 2 are readily applicable to equilibrium flowfields. In fact, the form of the continuity equation and Maslen's equation remains unchanged for all flow regimes considered in this paper. The state equation, the thermodynamic and transport properties, and shock jump conditions for equilibrium flows are provided in this chapter. Chapter 9 presents equilibrium results based on these governing equations.

4.1   State Equation

For a nonreacting gas, $\tilde{\mathcal{R}}$ is constant since $\mathcal{M}$ is constant. However, when chemical reactions become important, $\mathcal{M}$ varies within the fluid, and using $\tilde{\mathcal{R}} = \tilde{\mathcal{R}}_{air}$ in Eq. (3.1.2) is no longer valid. There are a variety of approaches for handling equilibrium flows [33, 34] which account for the variation of $\tilde{\mathcal{R}}$. In this study, Eq. (3.1.2) is modified to account for the effects of chemical reactions:

$$p = \rho Z \tilde{\mathcal{R}}_{air} T \qquad (4.1.1)$$

The term Z is the compressibility factor:

$$Z = \frac{\mathcal{M}_{air}}{\mathcal{M}}$$

This factor is evaluated through a table look-up procedure of values calculated using Hansen's expressions [35].

4.2   Thermodynamic and Transport Properties

For equilibrium flows, both the Prandtl number and specific heat of the fluid vary within the shock layer. In addition, Sutherland's viscosity relation is no longer valid. In past efforts (see [36], for example), various techniques [37, 34, 38, 39, 40] have been employed to define the thermodynamic and transport properties of equilibrium flows. The energy equation as written in Chapter 2 requires that the *equilibrium* Prandtl number be used (see Appendix G). Hansen's paper [35] includes expressions for h, T, μ, and Pr_{eq}. This is the model used to define thermodynamic and transport properties for the solutions presented in this paper. As in the calculation of Z, these relations are used to generate a table of data which spans a large range of values for p, h, and T. These tabulated values are then interpolated as needed during the numerical solution of the governing equations. At the body surface (where T_w is known), the table look-up procedure takes the form

$$h_w = h_w(p_w, T_w) \qquad\qquad Z_w = Z_w(p_w, T_w)$$
$$\mu_w = \mu_w(p_w, T_w) \qquad\qquad Pr_{eq_w} = Pr_{eq_w}(p_w, T_w)$$

Elsewhere, since h is known, the implementation is of the form

$$T = T(p, h) \qquad\qquad Z = Z(p, h)$$
$$\mu = \mu(p, h) \qquad\qquad Pr_{eq} = Pr_{eq}(p, h)$$

4.3 Shock Properties

With perfect gas flows, closed-form relations can be used to determine the values of the jump conditions. However, no such simple expressions can be formulated for chemically reacting flows. Therefore, the following set of equations must be solved in an iterative fashion (see Appendix F for details):

$$v_s = \frac{\sin \Gamma_s}{\rho_s} \tag{4.3.1}$$

$$p_s = p_\infty + \sin^2 \Gamma_s \left(1 - \frac{1}{\rho_s}\right) \tag{4.3.2}$$

$$h_s = h_\infty + \frac{\sin^2 \Gamma_s}{2}\left(1 - \frac{1}{\rho_s^2}\right) \tag{4.3.3}$$

$$T_s = T_s(p_s, h_s) \qquad\qquad Z_s = Z_s(p_s, h_s) \tag{4.3.4}$$

$$\rho_s = \frac{p_s}{Z_s \mathcal{R}_{air} T_s} \tag{4.3.5}$$

The iterative procedure is as follows:

1) Begin by setting $\rho_s = 10$.
2) Use Eq. (4.3.2) to calculate p_s.
3) Find h_s from Eq. (4.3.3).
4) For these values of p_s and h_s, find T_s and Z_s from Hansen's model.
5) Determine a new value of ρ_s from Eq. (4.3.5).
6) Steps (2) through (5) are repeated until the relative error between the new and old values for ρ_s is less than the prescribed tolerance.
7) After convergence, compute v_s from Eq. (4.3.1).

The derivatives of u_s, p_s, and v_s with respect to ξ are also required. The definition of the streamwise derivative of u_s as given in Section 3.3 is valid for equilibrium flows. Finding the gradients of p_s and v_s, however, presents a challenge. Fortunately, these gradients only appear in Maslen's streamwise pressure gradient. As will be discussed later, a simple two-point backward-difference representation of this term is employed in the marching region, so analytic forms of these derivatives are only required in the

nose region. The following algorithm is employed. The shock values for p and v in the nose region are fit in a least-squares sense with the following conic

$$A\xi^2 + B\xi\,(S - S_0) + CS\,(S - S_0) + 1 - \frac{S}{S_0} = 0 \qquad (4.3.6)$$

where S is either p_s or v_s. This equation is constrained to pass through the stagnation value with a slope of zero. The shock gradients are supplied by the derivative of this expression:

$$\frac{dS}{d\xi} = -\frac{2A\xi + B\,(S - S_0)}{C\,(2S - S_0) + B\xi - \dfrac{1}{S_0}} \qquad (4.3.7)$$

On the stagnation line, the equilibrium shock jump conditions of Section 4.3 simplify to become

$$v_{s_0} = \frac{1}{\rho_{s_0}} \qquad (4.3.8)$$

$$p_{s_0} = p_\infty + 1 - \frac{1}{\rho_{s_0}} \qquad (4.3.9)$$

$$h_{s_0} = h_\infty + \frac{1}{2}\left(1 - \frac{1}{\rho_{s_0}{}^2}\right) \qquad (4.3.10)$$

$$T_{s_0} = T_{s_0}(p_{s_0}, h_{s_0}) \qquad\qquad Z_{s_0} = Z_{s_0}(p_{s_0}, h_{s_0}) \qquad (4.3.11)$$

$$\rho_{s_0} = \frac{p_{s_0}}{Z_{s_0}\tilde{\mathcal{R}}_{air}T_{s_0}} \qquad (4.3.12)$$

Equations Eqs. (4.3.8) through (4.3.12) are solved using the iterative procedure of Section 4.3. The stagnation line value of the streamwise derivative of u_s is given in Section 3.3. The quantities

$$\lim_{\xi\to 0}\left\{\frac{1}{u_s}\frac{dp_s}{d\xi}\right\} \qquad\qquad \lim_{\xi\to 0}\left\{\frac{1}{u_s}\frac{dv_s}{d\xi}\right\}$$

are required for Eq. (2.4.13). Recall that the gradients are given by

$$\frac{dS}{d\xi} = -\frac{2A\xi + B\,(S - S_0)}{C\,(2S - S_0) + B\xi - \dfrac{1}{S_0}} \qquad (4.3.13)$$

where S is either p_s or v_s. Also note that

$$\lim_{\xi\to 0}\left\{\frac{1}{u_s}\frac{dS}{d\xi}\right\} = \frac{1}{\kappa_{s_0}}\lim_{\xi\to 0}\left\{\frac{1}{r_s}\frac{dS}{d\xi}\right\} \qquad (4.3.14)$$

Since $r_s \to \xi$ and $S \to S_0$ as $\xi \to 0$, the above equation gives

$$\lim_{\xi \to 0} \left\{ \frac{1}{r_s} \frac{dS}{d\xi} \right\} = -\frac{2A}{CS_0 - \dfrac{1}{S_0}} - \left[\frac{B}{CS_0 - \dfrac{1}{S_0}} \right] \frac{\Delta S}{\Delta \xi} \qquad (4.3.15)$$

Further, since $\Delta S / \Delta \xi \to dS/d\xi \to 0$ as $\xi \to 0$,

$$\lim_{\xi \to 0} \left\{ \frac{1}{r_s} \frac{dS}{d\xi} \right\} = -\frac{2A}{CS_0 - \dfrac{1}{S_0}} \qquad (4.3.16)$$

so that

$$\lim_{\xi \to 0} \left\{ \frac{1}{u_s} \frac{dS}{d\xi} \right\} = -\frac{2AC_s}{CS_0 - \dfrac{1}{S_0}} \qquad (4.3.17)$$

4.4 Surface Quantities

The relations given in Section 3.4 for perfect gas flows can be employed for equilibrium flows as well, provided Pr_{eq} is used in Eq. (3.4.8).

5   Nonequilibrium Analysis

In nonequilibrium flows, the characteristic time scales of the chemical reactions are of the same order as the time scales of the mean flow. Thus, species conservation equations must be solved in order to determine the local composition of the fluid. In addition, it is advantageous to rewrite the energy equation in terms of T. The rate of production of each species appears in the energy equation when it is written in this form. These changes to the governing equations presented in Chapter 2 are detailed in the sections that follow. Further, discussions of the thermodynamic and transport properties, state equation, boundary conditions, and surface quantities are presented in this chapter.

5.1   Viscous Shock Layer Equations

The continuity and streamwise momentum equations and Maslen's expression, presented in Chapter 2, are still valid for these flows. However, it is advantageous to recast the energy equation in terms of T (see Appendix G for details), since the chemical rate equations are functions of T:

$$\rho C_{p_f} \left(\frac{u}{h_1} \frac{\partial T}{\partial s} + v \frac{\partial T}{\partial n} \right) - \frac{u}{h_1} \frac{\partial p}{\partial s} - v \frac{\partial p}{\partial n} =$$

$$\epsilon^2 \left\{ \frac{\partial}{\partial n} \left[k \frac{\partial T}{\partial n} \right] + k \frac{\partial T}{\partial n} \left(\frac{1}{h_1} \frac{\partial h_1}{\partial n} + \frac{1}{h_3} \frac{\partial h_3}{\partial n} \right) + \mu \left(\frac{\partial u}{\partial n} - \frac{u}{h_1} \frac{\partial h_1}{\partial n} \right)^2 \right\} \qquad (5.1.1)$$

$$- \epsilon^2 \sum_{i=1}^{N_s} \mathcal{J}_i C_{p_i} \frac{\partial T}{\partial n} - \sum_{i=1}^{N_s} h_i \dot{w}_i$$

The subscript i is the species index for the seven-species air model used here. Table 5.1 provides the key for this indexing, along with the species molecular weights and perfect gas values of specific heat.

Each species present in the mixture is governed by a species conservation equation (see Appendix G):

$$\rho \left(\frac{u}{h_1} \frac{\partial c_i}{\partial s} + v \frac{\partial c_i}{\partial n} \right) = \dot{w}_i - \epsilon^2 \left\{ \frac{\partial \mathcal{J}_i}{\partial n} + \mathcal{J}_i \left(\frac{1}{h_1} \frac{\partial h_1}{\partial n} + \frac{1}{h_3} \frac{\partial h_3}{\partial n} \right) \right\} \qquad (5.1.2)$$

where the binary diffusion mass flux is

$$\mathcal{J}_i = -\frac{k}{C_{p_f}} Le_{12} \frac{\partial c_i}{\partial n} \qquad (5.1.3)$$

Table 5.1. Species Data

i	Species	$\mathcal{M}_i$	$C^{\star}_{p_{i_{pg}}}$
		$[gm/gm\text{-}mole]$	$[cal/gm\text{-}mole\text{-}K]$
1	N_2	28	7.00
2	O_2	32	7.00
3	N	14	4.97
4	O	16	5.44
5	NO	30	7.00
6	NO^+	30	7.00
7	e^-	0.0005486	

and Le_{12} is the binary Lewis number. Binary diffusion assumes that the fluid consists primarily of heavy particles diffusing to light particles, and vice versa. Previous investigations [8, 13] have used this approach successfully (assuming $Le_{12} = 1.4$ everywhere, for example). In keeping with the approximate nature of this approach, a constant Lewis number of 1.4 is used here. The species mass fractions are

$$c_i = \frac{\rho_i}{\rho} \tag{5.1.4}$$

and by definition satisfy the relation

$$\sum_{i=1}^{N_s} c_i = 1 \tag{5.1.5}$$

In the normalized shock-oriented coordinate system (see Chapter 2), Eqs. (5.1.1) and (5.1.2) can be written as

energy:

$$\rho_s \bar{\rho} C_{p_f} \left(\frac{u_s \bar{u}}{h_1} \left[\frac{\partial T}{\partial \xi} - \frac{\eta_n - 1}{n_b} \frac{dn_b}{d\xi} \frac{\partial T}{\partial \eta_n} \right] - \frac{v}{n_b} \frac{\partial T}{\partial \eta_n} \right)$$

$$- \frac{u_s \bar{u}}{h_1} \left[\frac{\partial p}{\partial \xi} - p_s \frac{\eta_n - 1}{n_b} \frac{dn_b}{d\xi} \frac{\partial p}{\partial \eta_n} \right] + \frac{v}{n_b} \frac{\partial p}{\partial \eta_n} =$$

$$\frac{\epsilon^2}{n_b^2} \left\{ \frac{\partial}{\partial \eta_n} \left[k \frac{\partial T}{\partial \eta_n} \right] + k \frac{\partial T}{\partial \eta_n} \left(\frac{1}{h_1} \frac{\partial h_1}{\partial \eta_n} + \frac{1}{h_3} \frac{\partial h_3}{\partial \eta_n} \right) + u_s^2 \mu \left(\frac{\partial \bar{u}}{\partial \eta_n} - \frac{\bar{u}}{h_1} \frac{\partial h_1}{\partial \eta_n} \right)^2 \right\}$$

$$+ \frac{\epsilon^2}{n_b} \sum_{i=1}^{N_s} \mathcal{J}_i C_{p_i} \frac{\partial T}{\partial \eta_n} - \sum_{i=1}^{N_s} h_i \dot{w}_i \tag{5.1.6}$$

species conservation:

$$\rho_s \bar{\rho} \left(\frac{u_s \tilde{u}}{h_1} \left[\frac{\partial c_i}{\partial \xi} - \frac{\eta_n - 1}{n_b} \frac{dn_b}{d\xi} \frac{\partial c_i}{\partial \eta_n} \right] - \frac{v}{n_b} \frac{\partial c_i}{\partial \eta_n} \right) =$$

$$\dot{w}_i + \frac{\epsilon^2}{n_b^2} \left\{ \frac{\partial}{\partial \eta_n} \left[\tilde{\mathcal{J}}_i \frac{\partial c_i}{\partial \eta_n} \right] + \tilde{\mathcal{J}}_i \frac{\partial c_i}{\partial \eta_n} \left(\frac{1}{h_1} \frac{\partial h_1}{\partial \eta_n} + \frac{1}{h_3} \frac{\partial h_3}{\partial \eta_n} \right) \right\} \qquad (5.1.7)$$

with

$$\mathcal{J}_i = \frac{k}{C_{p_f}} \frac{Le_{12}}{n_b} \frac{\partial c_i}{\partial \eta_n} = \frac{\tilde{\mathcal{J}}_i}{n_b} \frac{\partial c_i}{\partial \eta_n} \qquad (5.1.8)$$

where

$$\tilde{\mathcal{J}}_i = \frac{k}{C_{p_f}} Le_{12} = \frac{\mu}{Pr} Le_{12} \qquad (5.1.9)$$

In preparation for numerically integrating the governing equations, the production terms are written in terms of T and c_i in the energy and species conservation equation, respectively. These representations are given in the next section, along with the resulting governing equations.

5.2 Species Rates of Production

In addition to their presence in the species conservation equations, the species rates of production $(\dot{w}_i)$ appear in the energy equation when it is written in the above form. These source terms are functions of both T and c_i (see Appendix H). As such, they should be expressed in terms of c_i for the species continuity equations, and in terms of T for the energy equation [58, 59].

For the species continuity equation, the production term can be linearized [58, 59] to yield

$$\frac{\dot{w}_i}{\rho} = \dot{w}_i^0 - c_i \dot{w}_i^1 \qquad (5.2.1)$$

where

$$\dot{w}_i^0 = \frac{\mathcal{M}_i}{\dot{w}_{ref}^\star} \sum_{r=1}^{N_r} \left[\Gamma_{i,r}^+ R_{f,r}^\star + \Gamma_{i,r}^- R_{b,r}^\star \right]_p \qquad (5.2.2)$$

$$\dot{w}_i^1 = \frac{\mathcal{M}_i}{\dot{w}_{ref}^\star} \sum_{r=1}^{N_r} \left[\frac{\Gamma_{i,r}^+ R_{b,r}^\star + \Gamma_{i,r}^- R_{f,r}^\star}{c_i} \right]_p \qquad (5.2.3)$$

$$\Gamma_{i,r}^+ = \begin{cases} \beta_{i,r} - \alpha_{i,r} & \text{, for } \beta_{i,r} - \alpha_{i,r} > 0 \\ 0 & \text{, for } \beta_{i,r} - \alpha_{i,r} \leq 0 \end{cases} \qquad (5.2.4)$$

$$\Gamma_{i,r}^- = \begin{cases} \alpha_{i,r} - \beta_{i,r} & \text{, for } \alpha_{i,r} - \beta_{i,r} > 0 \\ 0 & \text{, for } \alpha_{i,r} - \beta_{i,r} \leq 0 \end{cases} \qquad (5.2.5)$$

and the remaining quantities are given in Appendix H. The subscript p denotes evaluation at the previous iteration. The quantities $\alpha_{i,r}$ and $\beta_{i,r}$ are the stoichiometric coefficients for reactants and products, respectively.

For the energy equation, the production term can be written as a truncated Taylor's series [58, 59]:

$$\frac{\dot{w}_i}{\rho} = \left.\frac{\dot{w}_i}{\rho}\right|_p + \left.\frac{\partial}{\partial T}\left(\frac{\dot{w}_i}{\rho}\right)\right|_p [T - T_p] \tag{5.2.6}$$

where again the subscript p denotes evaluation at the previous iteration. Thus, the production term in the energy equation can be expressed as

$$\sum_{i=1}^{N_s} h_i \dot{w}_i = \dot{w}_{1_i} + T \dot{w}_{2_i} \tag{5.2.7}$$

where

$$\dot{w}_{1_i} = \left\{ \rho \left[\sum_{i=1}^{N_s} h_i \frac{\dot{w}_i}{\rho} - T \sum_{i=1}^{N_s} h_i \frac{\partial}{\partial T}\left(\frac{\dot{w}_i}{\rho}\right) \right] \right\}_p \tag{5.2.8}$$

and

$$\dot{w}_{2_i} = \left\{ \rho \sum_{i=1}^{N_s} h_i \frac{\partial}{\partial T}\left(\frac{\dot{w}_i}{\rho}\right) \right\}_p \tag{5.2.9}$$

Further,

$$\frac{\partial}{\partial T}\left(\frac{\dot{w}_i}{\rho}\right) = \frac{\mathcal{M}_i}{T} \sum_{r=1}^{N_r} (\beta_{i,r} - \alpha_{i,r}) \tag{5.2.10}$$

$$\times \left[\left(B_{f,r} + \frac{D_{f,r}}{T} - \alpha_r \right) R_{f,r} - \left(B_{b,r} + \frac{D_{b,r}}{T} - \beta_r \right) R_{b,r} \right]$$

Now make use of these expressions in the energy and species continuity equations. For clarity, the entire set of governing equations for nonequilibrium flows is repeated below.

continuity:

$$\frac{\partial}{\partial \xi}(\rho_s \bar{\rho} u_s \bar{u} h_3) - \rho_s u_s \frac{\eta_n - 1}{n_b} \frac{dn_b}{d\xi} \frac{\partial}{\partial \eta_n}(\bar{\rho}\bar{u}h_3) - \frac{\rho_s}{n_b} \frac{\partial}{\partial \eta_n}(\bar{\rho}vh_1h_3) = 0 \tag{5.2.11}$$

ξ - *momentum:*

$$\rho_s \bar{\rho} \left(\frac{\bar{u}}{h_1} \left[u_s \frac{\partial \bar{u}}{\partial \xi} + \bar{u} \frac{du_s}{d\xi} - u_s \frac{\eta_n - 1}{n_b} \frac{dn_b}{d\xi} \frac{\partial \bar{u}}{\partial \eta_n} \right] - \frac{v}{n_b} \left[\frac{\partial \bar{u}}{\partial \eta_n} + \frac{\bar{u}}{h_1} \frac{\partial h_1}{\partial \eta_n} \right] \right)$$

$$+ \frac{1}{h_1 u_s} \left[\frac{\partial p}{\partial \xi} - \frac{\eta_n - 1}{n_b} \frac{dn_b}{d\xi} \frac{\partial p}{\partial \eta_n} \right] = \frac{\epsilon^2}{n_b^2} \left\{ \frac{\partial}{\partial \eta_n} \left[\mu \left(\frac{\partial \bar{u}}{\partial \eta_n} - \frac{\bar{u}}{h_1} \frac{\partial h_1}{\partial \eta_n} \right) \right] \right.$$

$$\left. + \mu \left(\frac{2}{h_1} \frac{\partial h_1}{\partial \eta_n} + \frac{1}{h_3} \frac{\partial h_3}{\partial \eta_n} \right) \left(\frac{\partial \bar{u}}{\partial \eta_n} - \frac{\bar{u}}{h_1} \frac{\partial h_1}{\partial \eta_n} \right) \right\} \tag{5.2.12}$$

energy:

$$\rho_s \bar{\rho} C_{p_f} \left(\frac{u_s \bar{u}}{h_1} \left[\frac{\partial T}{\partial \xi} - \frac{\eta_n - 1}{n_b} \frac{dn_b}{d\xi} \frac{\partial T}{\partial \eta_n} \right] - \frac{v}{n_b} \frac{\partial T}{\partial \eta_n} \right)$$

$$- \frac{u_s \bar{u}}{h_1} \left[\frac{\partial p}{\partial \xi} - \frac{\eta_n - 1}{n_b} \frac{dn_b}{d\xi} \frac{\partial p}{\partial \eta_n} \right] + \frac{v}{n_b} \frac{\partial p}{\partial \eta_n} =$$

$$\frac{\epsilon^2}{n_b^2} \left\{ \frac{\partial}{\partial \eta_n} \left[k \frac{\partial T}{\partial \eta_n} \right] + k \frac{\partial T}{\partial \eta_n} \left(\frac{1}{h_1} \frac{\partial h_1}{\partial \eta_n} + \frac{1}{h_3} \frac{\partial h_3}{\partial \eta_n} \right) + u_s^2 \mu \left(\frac{\partial \bar{u}}{\partial \eta_n} - \frac{\bar{u}}{h_1} \frac{\partial h_1}{\partial \eta_n} \right)^2 \right\}$$

$$+ \frac{\epsilon^2}{n_b} \sum_{i=1}^{N_s} \mathcal{J}_i C_{p_i} \frac{\partial T}{\partial \eta_n} - \dot{w}_{1_i} - T \dot{w}_{2_i} \qquad (5.2.13)$$

species conservation:

$$\rho_s \bar{\rho} \left(\frac{u_s \bar{u}}{h_1} \left[\frac{\partial c_i}{\partial \xi} - \frac{\eta_n - 1}{n_b} \frac{dn_b}{d\xi} \frac{\partial c_i}{\partial \eta_n} \right] - \frac{v}{n_b} \frac{\partial c_i}{\partial \eta_n} \right) =$$

$$\rho \left[\dot{w}_i^0 - c_i \dot{w}_i^1 \right] + \frac{\epsilon^2}{n_b^2} \left\{ \frac{\partial}{\partial \eta_n} \left[\tilde{\mathcal{J}}_i \frac{\partial c_i}{\partial \eta_n} \right] + \tilde{\mathcal{J}}_i \frac{\partial c_i}{\partial \eta_n} \left(\frac{1}{h_1} \frac{\partial h_1}{\partial \eta_n} + \frac{1}{h_3} \frac{\partial h_3}{\partial \eta_n} \right) \right\} \qquad (5.2.14)$$

Maslen's equation:

$$p = p_s + \frac{\kappa_s r_s u_s}{2} (\eta - 1) - \frac{v_s \sin \Gamma_s}{4} \left[1 + \frac{\kappa_s r_s}{\cos \Gamma_s} \right] (\eta^2 - 1) \qquad (5.2.15)$$

with

$$\Psi_s \eta = n_b^2 \left[\rho_s u_s^2 \int_0^{\eta_n} \bar{\rho} \bar{u} (\eta_n - 1) d\eta_n \right] + n_b \left[\rho_s u_s r_s \int_0^{\eta_n} \bar{\rho} \bar{u} d\eta_n \right] \qquad (5.2.16)$$

Eqs. (5.2.12), (5.2.13) and (5.2.14) are cast in the standard form for parabolic partial differential equations to yield the following coefficients (see Appendix G):
ξ - *momentum:*

$$A_0 = -\frac{\epsilon^2}{n_b^2} \mu$$

$$A_1 = -\frac{\epsilon^2}{n_b^2} \left[\frac{\partial \mu}{\partial \eta_n} + \mu \left(\frac{1}{h_1} \frac{\partial h_1}{\partial \eta_n} + \frac{1}{h_3} \frac{\partial h_3}{\partial \eta_n} \right) \right] - \rho_s \bar{\rho} \left[\frac{v}{n_b} + \frac{u_s \bar{u}}{h_1} \frac{\eta_n - 1}{n_b} \frac{dn_b}{d\xi} \right]$$

$$A_2 = \frac{\epsilon^2}{n_b^2} \left(\frac{1}{h_1} \frac{\partial h_1}{\partial \eta_n} \right) \left[\frac{\partial \mu}{\partial \eta_n} + \mu \left(\frac{1}{h_1} \frac{\partial h_1}{\partial \eta_n} + \frac{1}{h_3} \frac{\partial h_3}{\partial \eta_n} \right) \right] + \rho_s \bar{\rho} \left(\bar{u} \frac{du_s}{d\xi} - \frac{v}{n_b} \frac{\partial h_1}{\partial \eta_n} \right)$$

$$A_3 = \frac{1}{h_1} \left[\left\{ \frac{1}{u_s} \frac{\partial p}{\partial \xi} \right\} - \frac{\eta_n - 1}{n_b} \frac{\partial p}{\partial \eta_n} \left\{ \frac{1}{u_s} \frac{dn_b}{d\xi} \right\} \right] \qquad (5.2.17)$$

$$A_4 = \rho_s u_s \frac{\bar{\rho} \bar{u}}{h_1}$$

energy:

$$A_0 = -\frac{\epsilon^2}{n_b^2} k$$

$$A_1 = -\frac{\epsilon^2}{n_b^2} \left[\frac{\partial k}{\partial \eta_n} + k \left(\frac{1}{h_1} \frac{\partial h_1}{\partial \eta_n} + \frac{1}{h_3} \frac{\partial h_3}{\partial \eta_n} \right) + n_b \sum_{i=1}^{N_s} \mathcal{J}_i C_{p_i} \right]$$

$$- \rho_s \bar{\rho} \left[\frac{v}{n_b} + \frac{u_s \bar{u}}{h_1} \frac{\eta_n - 1}{n_b} \frac{dn_b}{d\xi} \right] C_{p_f}$$

$$A_2 = \dot{w}_{2_i} \tag{5.2.18}$$

$$A_3 = -\frac{u_s \bar{u}}{h_1} \left[\frac{\partial p}{\partial \xi} - \frac{\eta_n - 1}{n_b} \frac{dn_b}{d\xi} \frac{\partial p}{\partial \eta_n} \right] + \frac{v}{n_b} \frac{\partial p}{\partial \eta_n}$$

$$- \epsilon^2 \mu \frac{u_s^2}{n_b^2} \left(\frac{\partial \bar{u}}{\partial \eta_n} - \frac{\bar{u}}{h_1} \frac{\partial h_1}{\partial \eta_n} \right)^2 + \dot{w}_{1_i}$$

$$A_4 = \rho_s u_s \frac{\bar{\rho}\bar{u}}{h_1}$$

species conservation:

$$A_0 = \frac{\epsilon^2}{n_b^2} \check{\mathcal{J}}_i$$

$$A_1 = \frac{\epsilon^2}{n_b^2} \left[\frac{\partial}{\partial \eta_n} \left(\hat{\mathcal{J}}_i \right) + \hat{\mathcal{J}}_i \left(\frac{1}{h_1} \frac{\partial h_1}{\partial \eta_n} + \frac{1}{h_3} \frac{\partial h_3}{\partial \eta_n} \right) \right] + \rho_s \bar{\rho} \left[\frac{v}{n_b} + \frac{u_s \bar{u}}{h_1} \frac{\eta_n - 1}{n_b} \frac{dn_b}{d\xi} \right]$$

$$A_2 = -\rho_s \bar{\rho} \dot{w}_i^1 \tag{5.2.19}$$

$$A_3 = \rho_s \bar{\rho} \dot{w}_i^0$$

$$A_4 = -\rho_s u_s \frac{\bar{\rho}\bar{u}}{h_1}$$

All N_s species conservation equations need not be integrated to determine the concentrations of each species. It is possible to use only $N_s - 1$ of the species continuity equations, in conjunction with Eq. (5.1.5). Ref. [16] goes one step further by locally conserving the elemental composition of the fluid. For air, this gives two relations, if binary diffusion assumed:

$$c_{N_2} + c_N + \frac{\mathcal{M}_N}{\mathcal{M}_{NO}} \left(c_{NO} + c_{NO^+} \right) = c_{N_2 \infty} \tag{5.2.20}$$

$$c_{O_2} + c_O + \frac{\mathcal{M}_O}{\mathcal{M}_{NO}} \left(c_{NO} + c_{NO^+} \right) = c_{O_2 \infty} \tag{5.2.21}$$

so that only $N_s - 2$ species continuity equations must be integrated. Numerically integrating fewer equations should reduce CPU requirements, so this latter approach is employed here.

5.3   State Equation

As mentioned in Chapter 4, $\tilde{\mathcal{R}}$ is variable for reacting flows since $\mathcal{M}$ of the mixture is not constant. When finite-rate chemical reactions are considered, the flowfield can be modeled as a mixture of thermally perfect gases. For such a mixture, the equation of state is

$$p = \rho \frac{\mathcal{R}_u}{\mathcal{M}} T \qquad\qquad (5.3.1)$$

where

$$\mathcal{R}_u = \frac{\mathcal{R}_u^*}{C_{p\infty}^{\prime *}}$$

The mixture molecular weight can be written as

$$\mathcal{M} = \frac{1}{\displaystyle\sum_{i=1}^{N_s} \frac{c_i}{\mathcal{M}_i}} \qquad\qquad (5.3.2)$$

5.4   Thermodynamic and Transport Properties

5.4.1   Thermodynamic Properties

The thermodynamic properties are required for each species that is present in the fluid. Expressions from Ref. [60] are used to define C_{p_i} and h_i for the temperature range of $300K \leq T^* \leq 30000K$ (see Appendix I). The thermodynamic properties for the gas mixture are determined in terms of the individual species properties through the relations

$$h = \sum_{i=1}^{N_s} c_i h_i \qquad\qquad (5.4.1)$$

and

$$C_{p_f} = \sum_{i=1}^{N_s} c_i C_{p_i}^{\prime} \qquad\qquad (5.4.2)$$

5.4.2   Transport Properties

Ref. [60] also supplies the species transport properties (μ_i and k_i) with curve fits for the temperature range of $1000K \leq T^* \leq 30000K$ (see Appendix J). While the thermodynamic properties of the fluid are linear combinations of the individual species thermodynamic properties, the transport properties are defined by more complicated expressions. These expressions are referred to as *mixing laws*. Ref. [61] presents a thorough review of mixing laws, and points out several approximate formulations of

them. In the present research, two of these simplified relations are employed. The method of Armaly and Sutton [62] is used to define the mixture viscosity:

$$\mu = \sum_{i=1}^{N_s} \frac{x_i^2}{\mathcal{H}_{ii}}$$

(5.4.3)

where

$$\mathcal{H}_{ii} = \frac{x_i^2}{\mu_i} + \sum_{\substack{j=1 \\ j \neq i}}^{N_s} 2 \frac{x_i x_j}{\mu_{ij}} \frac{\mathcal{M}_i \mathcal{M}_j}{(\mathcal{M}_i + \mathcal{M}_j)^2} \left[\frac{5}{3A_{ij}} + \frac{\mathcal{M}_j}{\mathcal{M}_i} \right]$$

(5.4.4)

and

$$\mu_{ij} = \frac{\sqrt{32 \frac{\mathcal{M}_i \mathcal{M}_j}{\mathcal{M}_i + \mathcal{M}_j}}}{\left[\frac{\mathcal{M}_i^{.25}}{\sqrt{\mu_i}} + \frac{\mathcal{M}_j^{.25}}{\sqrt{\mu_j}} B_{ij} \right]^2}$$

(5.4.5)

The mole fraction for species i is

$$x_i = c_i \frac{\mathcal{M}}{\mathcal{M}_i}$$

(5.4.6)

Further, $A_{ij} = 1.25$ and

$$B_{ij} = \begin{cases} 0.78 &, \text{ for interactions of atoms or molecules with each other} \\ 0.15 &, \text{ for interactions of atoms or molecules with ions} \end{cases}$$

(5.4.7)

For the mixture conductivity, the method of Mason and Saxena [63] is employed:

$$k = \sum_{i=1}^{N_s} \frac{k_i}{\left[1 + \sum_{\substack{j=1 \\ j \neq i}}^{N_s} \Phi_{ij} \frac{x_j}{x_i} \right]}$$

(5.4.8)

where

$$\Phi_{ij} = \frac{1.065}{2\sqrt{2}} \frac{\left(1 + \sqrt{\frac{\mu_i}{\mu_j}} \frac{\mathcal{M}_j^{.25}}{\mathcal{M}_i^{.25}} \right)^2}{\sqrt{1 + \frac{\mathcal{M}_i}{\mathcal{M}_j}}}$$

(5.4.9)

Ref. [61] shows that values from the curve fits approach Sutherland's values as $T^* \to 1000K$. Thus, for temperatures less than $1000K$, Sutherland's viscosity law

$$\mu^* = 1.4584 \times 10^{-5} \frac{T^{*1.5}}{T^* + 110.33} \qquad [gm/cm\text{-}s]$$

(5.4.10)

and Sutherland's law for thermal conductivity [32]

$$k^* = 5.9776 \times 10^{-6} \frac{T^{*1.5}}{T^* + 194.4} \qquad [cal/cm\text{-}s\text{-}K]$$

(5.4.11)

may be used to define the mixture viscosity and conductivity, respectively.

5.5   Boundary Conditions

5.5.1   Wall Values

As in the case of perfect gas and equilibrium flows, the no-slip condition is applied at the wall so that

$$u_w = v_w = 0$$

Further, the wall temperature, $T_w(\xi)$, must be specified. Additional boundary conditions must be supplied for the species continuity equations. For a noncatalytic surface, the boundary condition is

$$\left.\frac{\partial c_i}{\partial \eta_n}\right|_w = 0 \tag{5.5.1}$$

If equilibrium catalytic wall conditions are specified, then

$$c_{i_w} = c_{i_{eq}}(T_w) \tag{5.5.2}$$

In this research, the wall temperature is low enough to produce freestream values for these concentrations:

$$c_{O_2 w} = 0.23456 \qquad\qquad c_{N_2 w} = 0.76544 \tag{5.5.3}$$

$$c_{O_w} = c_{N_w} = c_{NO_w} = c_{NO^+{}_w} = c_{e^-{}_w} = 0$$

5.5.2   Shock Properties

For nonequilibrium calculations, flow through the shock wave is assumed to be chemically frozen. The governing equations for the shock jump conditions are (see Appendix F for details):

$$v_s = \frac{\sin \Gamma_s}{\rho_s} \tag{5.5.4}$$

$$p_s = p_\infty + \sin^2 \Gamma_s \left(1 - \frac{1}{\rho_s} \right) \tag{5.5.5}$$

$$h_s = h_\infty + \frac{\sin^2 \Gamma_s}{2} \left(1 - \frac{1}{\rho_s^2} \right) \tag{5.5.6}$$

$$h_s = c_{O_2\infty} h_{O_2}(T_s) + c_{N_2\infty} h_{N_2}(T_s) \tag{5.5.7}$$

$$C_{p_s} = c_{O_2\infty} C_{p_{O_2}}(T_s) + c_{N_2\infty} C_{p_{N_2}}(T_s) \tag{5.5.8}$$

$$\rho_s = \frac{p_s}{\frac{\mathcal{R}_u}{\mathcal{M}_{air}} T_s} \tag{5.5.9}$$

where the species enthalpies of Eq. (5.5.7), as well as the species specific heats in Eq. (5.5.8), are obtained from the curve fits of Ref. [60].

By substituting Eq. (5.5.9) into Eq. (5.5.5), the following quadratic for p_s is obtained (with T_s as the only unknown):

$$p_s^2 - \left(p_\infty + \sin^2 \Gamma_s\right) p_s + \frac{\mathcal{R}_u}{\mathcal{M}_{air}} T_s \sin^2 \Gamma_s = 0 \qquad (5.5.10)$$

Substitute Eq. (5.5.9) into Eq. (5.5.6) to obtain

$$h_s = h_\infty + \frac{\sin^2 \Gamma_s}{2} \left(1 - \left[\frac{\mathcal{R}_u}{\mathcal{M}_{air}} \frac{T_s}{p_s} \right]^2 \right) \qquad (5.5.11)$$

Differentiating Eq. (5.5.10) with respect to T_s gives

$$\frac{\partial p_s}{\partial T_s} = \frac{\dfrac{\mathcal{R}_u}{\mathcal{M}_{air}} \sin^2 \Gamma_s}{2p_s - \left(p_\infty + \sin^2 \Gamma_s\right)} \qquad (5.5.12)$$

Differentiating Eq. (5.5.11) with respect to T_s gives

$$\frac{\partial h_s}{\partial T_s} = - \sin^2 \Gamma_s \left(\frac{\mathcal{R}_u}{\mathcal{M}_{air}} \right)^2 \frac{T_s}{p_s} \left[\frac{1}{p_s} - \frac{T_s}{p_s^2} \frac{\partial p_s}{\partial T_s} \right] \qquad (5.5.13)$$

Combine Eqs. (5.5.12) and (5.5.13), and rearrange to get

$$\frac{\partial h_s}{\partial T_s} = - \frac{\dfrac{\mathcal{R}_u}{\mathcal{M}_{air}} \sin^2 \Gamma_s}{\rho_s p_s - \sin^2 \Gamma_s} \qquad (5.5.14)$$

As with equilibrium flows, these equations must be solved in an iterative fashion. To speed convergence, Newton's method is employed:

$$T_s = T_{s_p} + \Delta T_s \qquad (5.5.15)$$

where

$$\Delta T_s = - \frac{F}{F'} \qquad (5.5.16)$$

The function F is defined to be the difference in enthalpy values given by Eqs. (5.5.6) and (5.5.7), respectively:

$$F(T_s) = h_{s_{\text{Eq. (5.5.6)}}} - h_{s_{\text{Eq. (5.5.7)}}} \qquad (5.5.17)$$

so that

$$F'(T_s) = \frac{\partial h_s}{\partial T_s} - C_{p_s} \qquad (5.5.18)$$

The solution procedure is as follows:

1) Begin with T_s from the previous shock evaluation.

2) Use Eq. (5.5.10) to calculate p_s.

3) Determine a new value of ρ_s from Eq. (5.5.9).

4) Find h_s from Eq. (5.5.6).

5) Evaluate h_s from Eq. (5.5.7) and C_{p_s} from Eq. (5.5.8).

6) Calculate F and F'' from Eqs. (5.5.17) and (5.5.18), respectively, to determine ΔT_s from Eq. (5.5.16).

7) If $|\Delta T_s|$ is greater than the prescribed tolerance, update T_s using Eq. (5.5.15) and return to (2).

8) After convergence, compute v_s from Eq. (5.5.4).

The derivative of u_s is given in Section 3.3. The derivatives of p_s and v_s with respect to ξ are (see Appendix F)

$$\frac{dp_s}{d\xi} = \frac{\kappa_s \cos \Gamma_s \left\{ \dfrac{(v_s - \rho_s \sin \Gamma_s)}{C_{p_s}} - 2\left[\dfrac{T_s}{v_s^2} + \dfrac{1}{C_{p_s}}\right](v_s - \sin \Gamma_s) \right\}}{\dfrac{\mathcal{M}_{air}}{\mathcal{R}_u} - \left(\dfrac{T_s}{v_s^2} + \dfrac{1}{C_{p_s}}\right)} \qquad (5.5.19)$$

and

$$\frac{dv_s}{d\xi} = 2\kappa_s \cos \Gamma_s \left(\frac{1}{\rho_s} - 1\right) - \frac{1}{\rho_s}\left[\kappa_s \cos \Gamma_s + \frac{1}{v_s}\frac{dp_s}{d\xi}\right] \qquad (5.5.20)$$

respectively.

5.6   Stagnation Line

As mentioned in Chapter 2, a limiting form of the governing equations can be obtained for use on the stagnation line. A limiting form for the energy equation cast in T, as well as the species conservation equations, may be found in the same manner. These ordinary differential equations are given in Section 5.6.1. In addition, the stagnation line jump conditions and their gradients are presented in Section 5.6.2.

5.6.1   Viscous Shock Layer Equations

continuity:

$$2\kappa_{s_0} n_{b_0}\rho_{s_0}\bar{\rho}\bar{u}h_1 - \rho_{s_0}\frac{\partial}{\partial \eta_n}\left(\bar{\rho}v h_1^2\right) = 0 \qquad (5.6.1)$$

ξ - momentum:

$$\rho_{s_0}\bar{\rho}\left(\frac{\bar{u}^2}{h_1}\frac{du_s}{d\xi} - \frac{v}{n_{b_0}}\left[\frac{\partial \bar{u}}{\partial \eta_n} + \frac{\bar{u}}{h_1}\frac{\partial h_1}{\partial \eta_n}\right]\right) + \frac{1}{h_1}\lim_{\xi \to 0}\left\{\frac{1}{u_s}\left[\frac{\partial p}{\partial \xi} - \frac{\eta_n - 1}{n_b}\frac{dn_b}{d\xi}\frac{\partial p}{\partial \eta_n}\right]\right\}$$

$$= \frac{\epsilon^2}{n_{b_0}{}^2} \left\{ \frac{\partial}{\partial \eta_n} \left[\mu \left(\frac{\partial \bar{u}}{\partial \eta_n} - \frac{\bar{u}}{h_1} \frac{\partial h_1}{\partial \eta_n} \right) \right] + 3 \frac{\mu}{h_1} \frac{\partial h_1}{\partial \eta_n} \left(\frac{\partial \bar{u}}{\partial \eta_n} - \frac{\bar{u}}{h_1} \frac{\partial h_1}{\partial \eta_n} \right) \right\} \qquad (5.6.2)$$

energy:

$$- \rho_{s_0} \bar{\rho} C_{p_f} v \frac{\partial T}{\partial \eta_n} + v \frac{\partial p}{\partial \eta_n} = \qquad (5.6.3)$$

$$\frac{\epsilon^2}{n_{b_0}} \left\{ \frac{\partial}{\partial \eta_n} \left[k \frac{\partial T}{\partial \eta_n} \right] + k \frac{\partial T}{\partial \eta_n} \frac{2}{h_1} \frac{\partial h_1}{\partial \eta_n} \right\} + \epsilon^2 \sum_{i=1}^{N_s} \mathcal{J}_i C_{p_i} \frac{\partial T}{\partial \eta_n} - n_{b_0} \left[\dot{w}_{1_i} + T \dot{w}_{2_i} \right]$$

species conservation:

$$- \rho_{s_0} \bar{\rho} v \frac{\partial c_i}{\partial \eta_n} = \rho n_{b_0} \left[\dot{w}_i^0 - c_i \dot{w}_i^1 \right] + \frac{\epsilon^2}{n_{b_0}} \left\{ \frac{\partial}{\partial \eta_n} \left[\tilde{\mathcal{J}}_i \frac{\partial c_i}{\partial \eta_n} \right] + \tilde{\mathcal{J}}_i \frac{\partial c_i}{\partial \eta_n} \frac{2}{h_1} \frac{\partial h_1}{\partial \eta_n} \right\} \qquad (5.6.4)$$

Maslen's equation:

$$p = p_{s_0} - \frac{v_{s_0}}{2} \left(\eta^2 - 1 \right) \qquad (5.6.5)$$

with

$$\frac{1}{2} \eta = n_{b_0}{}^2 \left[\rho_{s_0} \kappa_{s_0}{}^2 \int_0^{\eta_n} \rho \bar{u} \left(\eta_n - 1 \right) d\eta_n \right] + n_{b_0} \left[\rho_{s_0} \kappa_{s_0} \int_0^{\eta_n} \bar{\rho} \bar{u} d\eta_n \right] \qquad (5.6.6)$$

Eqs. (5.6.2), (5.6.3), and (5.6.4) are cast in the standard form for parabolic partial differential equations to yield the following coefficients (see Appendix G):

ξ - *momentum:*

$$A_0 = -\frac{\epsilon^2}{n_{b_0}{}^2} \mu$$

$$A_1 = -\frac{\epsilon^2}{n_{b_0}{}^2} \left[\frac{\partial \mu}{\partial \eta_n} + 2 \frac{\mu}{h_1} \frac{\partial h_1}{\partial \eta_n} \right] - \rho_{s_0} \bar{\rho} \frac{v}{n_{b_0}}$$

$$A_2 = \frac{\epsilon^2}{n_{b_0}{}^2} \left(\frac{1}{h_1} \frac{\partial h_1}{\partial \eta_n} \right) \left[\frac{\partial \mu}{\partial \eta_n} + 2 \frac{\mu}{h_1} \frac{\partial h_1}{\partial \eta_n} \right] + \frac{\rho_{s_0} \bar{\rho}}{h_1} \left(\bar{u} \frac{du_s}{d\xi} - \frac{v}{n_{b_0}} \frac{\partial h_1}{\partial \eta_n} \right) \qquad (5.6.7)$$

$$A_3 = \frac{1}{h_1} \left[\lim_{\xi \to 0} \left\{ \frac{1}{u_s} \frac{\partial p}{\partial \xi} \right\} - \frac{\eta_n - 1}{n_{b_0}} \frac{\partial p}{\partial \eta_n} \lim_{\xi \to 0} \left\{ \frac{1}{u_s} \frac{dn_b}{d\xi} \right\} \right]$$

$$A_4 = 0$$

energy:

$$A_0 = -\frac{\epsilon^2}{n_{b_0}{}^2} k$$

$$A_1 = -\frac{\epsilon^2}{n_{b_0}{}^2} \left[\frac{\partial k}{\partial \eta_n} + 2 \frac{k}{h_1} \frac{\partial h_1}{\partial \eta_n} \right] + \frac{\epsilon^2}{n_{b_0}} \sum_{i=1}^{N_s} \mathcal{J}_i C_{p_i} - \rho_{s_0} \bar{\rho} \frac{v}{n_{b_0}} C_{p_f}$$

$$A_2 = \dot{w}_{2_i} \qquad (5.6.8)$$

$$A_3 = \frac{v}{n_{b_0}} \frac{\partial p}{\partial \eta_n} + \dot{w}_{1_i}$$

$$A_4 = 0$$

species conservation:

$$A_0 = \frac{\epsilon^2}{n_{b_0}^2} \hat{J}_i$$

$$A_1 = \frac{\epsilon^2}{n_{b_0}^2} \left[\frac{\partial}{\partial \eta_n} \left(\hat{J}_i \right) + 2 \frac{\hat{J}_i}{h_1} \frac{\partial h_1}{\partial \eta_n} \right] + \rho_{s_0} \bar{\rho} \frac{v}{n_{b_0}}$$

$$A_2 = -\rho_{s_0} \bar{\rho} \dot{w}_i^1 \qquad \qquad (5.6.9)$$

$$A_3 = \rho_{s_0} \bar{\rho} \dot{w}_i^0$$

$$A_4 = 0$$

5.6.2   Shock Properties

On the stagnation line, the shock jump conditions of Section 5.5.2 simplify to become

$$v_{s_0} = \frac{1}{\rho_{s_0}} \qquad \qquad (5.6.10)$$

$$p_{s_0}^2 - (p_\infty + 1) p_{s_0} + \frac{\mathcal{R}_u}{\mathcal{M}_{air}} T_{s_0} = 0 \qquad \qquad (5.6.11)$$

$$h_{s_0} = h_\infty + \frac{1}{2} \left(1 - \left[\frac{\mathcal{R}_u}{\mathcal{M}_{air}} \frac{T_{s_0}}{p_{s_0}} \right]^2 \right) \qquad \qquad (5.6.12)$$

$$h_{s_0} = c_{O_2 \infty} h_{O_2} \left(T_{s_0} \right) + c_{N_2 \infty} h_{N_2} \left(T_{s_0} \right) \qquad \qquad (5.6.13)$$

$$C_{p_{s_0}} = c_{O_2 \infty} C_{p_{O_2}} \left(T_{s_0} \right) + c_{N_2 \infty} C_{p_{N_2}} \left(T_{s_0} \right) \qquad \qquad (5.6.14)$$

$$\rho_{s_0} = \frac{p_{s_0}}{\dfrac{\mathcal{R}_u}{\mathcal{M}_{air}} T_{s_0}} \qquad \qquad (5.6.15)$$

with

$$\left. \frac{\partial h_s}{\partial T_s} \right|_0 = -\frac{\dfrac{\mathcal{R}_u}{\mathcal{M}_{air}}}{\rho_{s_0} p_{s_0} - 1} \qquad \qquad (5.6.16)$$

Equations Eqs. (4.3.8) through (4.3.12) are solved using the iterative procedure of Section 5.5.2.

Next, the limiting forms of the shock derivatives defined in Section 5.5.2 must be determined. The stagnation line value of the derivative of u_s is given in Section 3.3. The limiting forms of Eqs. (5.5.19) and (5.5.20) are

$$\lim_{\xi \to 0} \left\{ \frac{1}{u_s} \frac{dp_s}{d\xi} \right\} = \frac{\kappa_{s_0} \left\{ \frac{(v_{s_0} - \rho_{s_0})}{C_{ps0}} - 2\left[\frac{T_{s_0}}{v_{s_0}^2} + \frac{1}{C_{ps0}} \right] (v_{s_0} - 1) \right\}}{\frac{\mathcal{M}_{air}}{\mathcal{R}_u} - \left(\frac{T_{s_0}}{v_{s_0}^2} + \frac{1}{C_{ps0}} \right)} \tag{5.6.17}$$

and

$$\lim_{\xi \to 0} \left\{ \frac{1}{u_s} \frac{dv_s}{d\xi} \right\} = 2\kappa_{s_0} \left(\frac{1}{\rho_{s_0}} - 1 \right) - \frac{1}{\rho_{s_0}} \left[\kappa_{s_0} + \frac{1}{v_{s_0}} \lim_{\xi \to 0} \left\{ \frac{1}{u_s} \frac{dp_s}{d\xi} \right\} \right] \tag{5.6.18}$$

respectively.

5.7 Surface Quantities

The relation for skin friction which was defined in Section 3.4 is still valid for nonequilibrium flows. However, for chemically reacting flow, the effect of diffusion, in addition to that of conduction, must be included in the heat flux calculations. The heat transfer to the wall is

$$q_w^\star = [q_c^\star + q_d^\star]_w \tag{5.7.1}$$

where $q_d^\star$ is the energy flux due to diffusion in the normal direction. This term can be expressed as (see Appendix G)

$$q_d^\star = -\rho^\star \mathcal{D}_{12}^\star \sum_{i=1}^{N_s} h_i^\star \frac{\partial c_i}{\partial n^\star} = \sum_{i=1}^{N_s} h_i^\star \mathcal{J}_i^\star \tag{5.7.2}$$

Written in nondimensional form (see Appendix A),

$$q_d = \epsilon^2 \sum_{i=1}^{N_s} h_i \mathcal{J}_i = -\epsilon^2 \sum_{i=1}^{N_s} \frac{\mu Le_{12}}{Pr} h_i \frac{\partial c_i}{\partial n} \tag{5.7.3}$$

From Section 3.4, the heat flux due to conduction is

$$q_c = -\epsilon^2 k \frac{\partial T}{\partial n} = \frac{\epsilon^2}{n_b} k \frac{\partial T}{\partial \eta_n} \tag{5.7.4}$$

Combining these components,

$$q_w = -\epsilon^2 \left[k \frac{\partial T}{\partial n} - \sum_{i=1}^{N_s} h_i \mathcal{J}_i \right]_w \tag{5.7.5}$$

or

$$q_w = -\epsilon^2 \left[k\frac{\partial T}{\partial n} + \sum_{i=1}^{N_s} \frac{\mu Le_{12}}{Pr} h_i \frac{\partial c_i}{\partial n} \right]_w = \frac{\epsilon^2}{n_b} \left[k\frac{\partial T}{\partial \eta_n} + \sum_{i=1}^{N_s} \hat{J}_i h_i \frac{\partial c_i}{\partial \eta_n} \right]_w \qquad (5.7.6)$$

For a noncatalytic surface,

$$\left. \frac{\partial c_i}{\partial \eta_n} \right|_w = 0 \qquad (5.7.7)$$

and the heat transfer rate reduces to the familiar form

$$q_w = -\epsilon^2 \left[k\frac{\partial T}{\partial n} \right]_w = \frac{\epsilon^2}{n_b} \left[k\frac{\partial T}{\partial \eta_n} \right]_w \qquad (5.7.8)$$

6 Turbulence

For turbulent flow, the governing equations are modified [41] using an eddy viscosity model. In various efforts [33, 41, 42, 11, 43, 44] the Cebeci-Smith [45, 46, 47] or Baldwin-Lomax [48] eddy viscosity models have been mated with VSL solvers. Such algebraic (or zero-equation) models are less complicated than more exact approaches, such as the Johnson-King [49] and two-equation [50] models, and as a result are more computationally efficient (although theoretically less accurate). The equations in this chapter may be applied to perfect gas or equilibrium flows.

6.1 Viscous Shock Layer Equations

The VSL equations of Chapter 2 are modified [41] using an eddy viscosity model so that they are applicable to turbulent flows. Simply put, the laminar transport coefficients are supplemented with turbulence terms. Thus, replace

$$\mu \qquad \text{with} \qquad \mu + \mu_t$$

where μ_t is the eddy viscosity, and replace

$$k \qquad \text{with} \qquad k + k_t$$

where k_t is the eddy thermal conductivity.

By definition,

$$Pr = \frac{C_p \mu}{k}$$

so that

$$\frac{\mu}{Pr} = \frac{k}{C_p}$$

The turbulent Prandtl number can be defined as

$$Pr_t = \frac{C_p \mu_t}{k_t}$$

so that

$$\frac{\mu_t}{Pr_t} = \frac{k_t}{C_p}$$

Thus, the thermal conductivity may be rewritten as

$$\frac{k}{C_p} + \frac{k_t}{C_p} = \frac{\mu}{Pr} + \frac{\mu_t}{Pr_t} = \frac{\mu}{Pr}\left(1 + \frac{\mu_t}{\mu}\frac{Pr}{Pr_t}\right)$$

In this study, a value of 0.90 is used for the turbulent Prandtl number [44].

Summarizing, the modifications to the governing equations are

$$\mu \implies \mu\left(1 + \epsilon^+\right) \qquad\qquad \frac{\mu}{Pr} \implies \frac{\mu}{Pr}\left(1 + \epsilon^+\frac{Pr}{Pr_t}\right)$$

where

$$\epsilon^+ = \frac{\mu_t}{\mu}$$

These modifications affect only the energy and streamwise momentum equations. Referring back to Eqs. (2.1.2) and (2.1.3), these equations become

s - momentum:

$$\rho\left(\frac{u}{h_1}\frac{\partial u}{\partial s} + v\frac{\partial u}{\partial n} + \frac{uv}{h_1}\frac{\partial h_1}{\partial n}\right) + \frac{1}{h_1}\frac{\partial p}{\partial s} = \epsilon^2\left\{\frac{\partial}{\partial n}\left[\mu\left(1 + \epsilon^+\right)\frac{\partial u}{\partial n} - \mu\frac{u}{h_1}\frac{\partial h_1}{\partial n}\right]\right.$$

$$\left. + \left(\frac{2}{h_1}\frac{\partial h_1}{\partial n} + \frac{1}{h_3}\frac{\partial h_3}{\partial n}\right)\left[\mu\left(1 + \epsilon^+\right)\frac{\partial u}{\partial n} - \mu\frac{u}{h_1}\frac{\partial h_1}{\partial n}\right]\right\} \qquad (6.1.1)$$

energy:

$$\rho\left(\frac{u}{h_1}\frac{\partial h}{\partial s} + v\frac{\partial h}{\partial n}\right) - \frac{u}{h_1}\frac{\partial p}{\partial s} - v\frac{\partial p}{\partial n} =$$

$$\epsilon^2\left\{\frac{\partial}{\partial n}\left[\frac{\mu}{Pr}\left(1 + \epsilon^+\frac{Pr}{Pr_t}\right)\frac{\partial h}{\partial n}\right] + \frac{\mu}{Pr}\left(1 + \epsilon^+\frac{Pr}{Pr_t}\right)\frac{\partial h}{\partial n}\left(\frac{1}{h_1}\frac{\partial h_1}{\partial n} + \frac{1}{h_3}\frac{\partial h_3}{\partial n}\right)\right. \qquad (6.1.2)$$

$$\left. + \mu\left(1 + \epsilon^+\right)\left[\left(\frac{\partial u}{\partial n}\right)^2 - 2\frac{u}{h_1}\frac{\partial h_1}{\partial n}\frac{\partial u}{\partial n}\right] + \mu\left(\frac{u}{h_1}\frac{\partial h_1}{\partial n}\right)^2\right\}$$

Note: *The described modifications are not performed on the higher order terms.*

Looking in the transformed system, Eqs. (2.1.11) and (2.1.12) become

ξ *- momentum:*

$$\rho_s\bar{\rho}\left(\frac{\bar{u}}{h_1}\left[u_s\frac{\partial\bar{u}}{\partial\xi} + \bar{u}\frac{du_s}{d\xi} - u_s\frac{\eta_n - 1}{n_b}\frac{dn_b}{d\xi}\frac{\partial\bar{u}}{\partial\eta_n}\right] - \frac{v}{n_b}\left[\frac{\partial\bar{u}}{\partial\eta_n} + \frac{\bar{u}}{h_1}\frac{\partial h_1}{\partial\eta_n}\right]\right)$$

$$+ \frac{1}{h_1 u_s}\left[\frac{\partial p}{\partial\xi} - \frac{\eta_n - 1}{n_b}\frac{dn_b}{d\xi}\frac{\partial p}{\partial\eta_n}\right] = \frac{\epsilon^2}{n_b^2}\left\{\frac{\partial}{\partial\eta_n}\left[\mu\left(1 + \epsilon^+\right)\frac{\partial\bar{u}}{\partial\eta_n} - \mu\frac{\bar{u}}{h_1}\frac{\partial h_1}{\partial\eta_n}\right]\right.$$

$$\left. + \left(\frac{2}{h_1}\frac{\partial h_1}{\partial\eta_n} + \frac{1}{h_3}\frac{\partial h_3}{\partial\eta_n}\right)\left[\mu\left(1 + \epsilon^+\right)\frac{\partial\bar{u}}{\partial\eta_n} - \mu\frac{\bar{u}}{h_1}\frac{\partial h_1}{\partial\eta_n}\right]\right\} \qquad (6.1.3)$$

energy:

$$\rho_s\bar{\rho}\left(\frac{u_s\bar{u}}{h_1}\left[\frac{\partial h}{\partial\xi} - \frac{\eta_n - 1}{n_b}\frac{dn_b}{d\xi}\frac{\partial h}{\partial\eta_n}\right] - \frac{v}{n_b}\frac{\partial h}{\partial\eta_n}\right)$$

$$-\frac{u_s \bar{u}}{h_1}\left[\frac{\partial p}{\partial \xi} - \frac{\eta_n - 1}{n_b}\frac{dn_b}{d\xi}\frac{\partial p}{\partial \eta_n}\right] + \frac{v}{n_b}\frac{\partial p}{\partial \eta_n} = \tag{6.1.4}$$

$$\frac{\epsilon^2}{n_b^2}\left\{\frac{\partial}{\partial \eta_n}\left[\frac{\mu}{Pr}\left(1 + \epsilon^+\frac{Pr}{Pr_t}\right)\frac{\partial h}{\partial \eta_n}\right] + \frac{\mu}{Pr}\left(1 + \epsilon^+\frac{Pr}{Pr_t}\right)\frac{\partial h}{\partial \eta_n}\left(\frac{1}{h_1}\frac{\partial h_1}{\partial \eta_n} + \frac{1}{h_3}\frac{\partial h_3}{\partial \eta_n}\right)\right.$$

$$\left. + u_s^2\left[\mu\left(1 + \epsilon^+\right)\left\{\left(\frac{\partial \bar{u}}{\partial \eta_n}\right)^2 - 2\frac{\bar{u}}{h_1}\frac{\partial h_1}{\partial \eta_n}\frac{\partial \bar{u}}{\partial \eta_n}\right\} + \mu\left(\frac{\bar{u}}{h_1}\frac{\partial h_1}{\partial \eta_n}\right)^2\right]\right\}$$

As a result, Eqs. (2.1.14) and (2.1.15) become

ξ - *momentum:*

$$A_0 = -\frac{\epsilon^2}{n_b^2}\mu\left(1 + \epsilon^+\right)$$

$$A_1 = -\frac{\epsilon^2}{n_b^2}\left[\frac{\partial}{\partial \eta_n}\left\{\mu\left(1 + \epsilon^+\right)\right\} + \mu\left(1 + \epsilon^+\right)\left(\frac{2}{h_1}\frac{\partial h_1}{\partial \eta_n} + \frac{1}{h_3}\frac{\partial h_3}{\partial \eta_n}\right) - \frac{\mu}{h_1}\frac{\partial h_1}{\partial \eta_n}\right]$$

$$- \rho_s\bar{\rho}\left[\frac{v}{n_b} + \frac{u_s\bar{u}}{h_1}\frac{\eta_n - 1}{n_b}\frac{dn_b}{d\xi}\right] \tag{6.1.5}$$

$$A_2 = \frac{\epsilon^2}{n_b^2}\left(\frac{1}{h_1}\frac{\partial h_1}{\partial \eta_n}\right)\left[\frac{\partial \mu}{\partial \eta_n} + \mu\left(\frac{1}{h_1}\frac{\partial h_1}{\partial \eta_n} + \frac{1}{h_3}\frac{\partial h_3}{\partial \eta_n}\right)\right] + \frac{\rho_s\bar{\rho}}{h_1}\left(\bar{u}\frac{du_s}{d\xi} - \frac{v}{n_b}\frac{\partial h_1}{\partial \eta_n}\right)$$

$$A_3 = \frac{1}{h_1}\left[\left\{\frac{1}{u_s}\frac{\partial p}{\partial \xi}\right\} - \frac{\eta_n - 1}{n_b}\frac{\partial p}{\partial \eta_n}\left\{\frac{1}{u_s}\frac{dn_b}{d\xi}\right\}\right]$$

$$A_4 = \rho_s u_s\frac{\bar{\rho}\bar{u}}{h_1}$$

energy:

$$A_0 = -\frac{\epsilon^2}{n_b^2}\frac{\mu}{Pr}\left(1 + \epsilon^+\frac{Pr}{Pr_t}\right)$$

$$A_1 = -\frac{\epsilon^2}{n_b^2}\left(1 + \epsilon^+\frac{Pr}{Pr_t}\right)\left[\frac{\partial}{\partial \eta_n}\left(\frac{\mu}{Pr}\right) + \frac{\mu}{Pr}\left(\frac{1}{h_1}\frac{\partial h_1}{\partial \eta_n} + \frac{1}{h_3}\frac{\partial h_3}{\partial \eta_n}\right)\right]$$

$$- \rho_s\bar{\rho}\left[\frac{v}{n_b} + \frac{u_s\bar{u}}{h_1}\frac{\eta_n - 1}{n_b}\frac{dn_b}{d\xi}\right] - \frac{\epsilon^2}{n_b^2}\frac{\mu}{Pr}\frac{\partial}{\partial \eta_n}\left(1 + \epsilon^+\frac{Pr}{Pr_t}\right)$$

$$A_2 = 0 \tag{6.1.6}$$

$$A_3 = -\frac{u_s\bar{u}}{h_1}\left[\frac{\partial p}{\partial \xi} - \frac{\eta_n - 1}{n_b}\frac{dn_b}{d\xi}\frac{\partial p}{\partial \eta_n}\right] + \frac{v}{n_b}\frac{\partial p}{\partial \eta_n}$$

$$- \epsilon^2\frac{u_s^2}{n_b^2}\left\{\mu\left(\frac{\bar{u}}{h_1}\frac{\partial h_1}{\partial \eta_n}\right)^2 + \mu\left(1 + \epsilon^+\right)\left[\left(\frac{\partial \bar{u}}{\partial \eta_n}\right)^2 - 2\frac{\bar{u}}{h_1}\frac{\partial h_1}{\partial \eta_n}\frac{\partial \bar{u}}{\partial \eta_n}\right]\right\}$$

$$A_4 = \rho_s u_s\frac{\bar{\rho}\bar{u}}{h_1}$$

Note: *For $\epsilon^+ = 0$, the laminar expressions of Eqs. (2.1.11), (2.1.12), (2.1.14), and (2.1.15) are recovered from Eqs. (6.1.3) through (6.1.6), respectively.*

6.2 Stagnation Line

If fully turbulent flow is to be considered, the limiting forms of the governing equations are needed in order to calculate stagnation line solution. As $\xi \to 0$, Eqs. (6.1.3) and (6.1.4) reduce to

ξ - *momentum:*

$$\rho_{s_0}\bar{\rho}\left(\frac{\bar{u}^2}{h_1}\frac{du_s}{d\xi} - \frac{v}{n_{b_0}}\left[\frac{\partial\bar{u}}{\partial\eta_n} + \frac{\bar{u}}{h_1}\frac{\partial h_1}{\partial\eta_n}\right]\right) + \frac{1}{h_1}\lim_{\xi\to 0}\left\{\frac{1}{u_s}\left[\frac{\partial p}{\partial\xi} - \frac{\eta_n - 1}{n_b}\frac{dn_b}{d\xi}\frac{\partial p}{\partial\eta_n}\right]\right\} \quad (6.2.1)$$

$$= \frac{\epsilon^2}{n_{b_0}^2}\left\{\frac{\partial}{\partial\eta_n}\left[\mu\left(1 + \epsilon^+\right)\frac{\partial\bar{u}}{\partial\eta_n} - \mu\frac{\bar{u}}{h_1}\frac{\partial h_1}{\partial\eta_n}\right] + \frac{3}{h_1}\frac{\partial h_1}{\partial\eta_n}\left[\mu\left(1 + \epsilon^+\right)\frac{\partial\bar{u}}{\partial\eta_n} - \mu\frac{\bar{u}}{h_1}\frac{\partial h_1}{\partial\eta_n}\right]\right\}$$

energy:

$$-\rho_{s_0}\rho v\frac{\partial h}{\partial\eta_n} + v\frac{\partial p}{\partial\eta_n} = \quad (6.2.2)$$

$$\frac{\epsilon^2}{n_{b_0}}\left\{\frac{\partial}{\partial\eta_n}\left[\frac{\mu}{Pr}\left(1 + \epsilon^+\frac{Pr}{Pr_t}\right)\frac{\partial h}{\partial\eta_n}\right] + \frac{2}{h_1}\frac{\partial h_1}{\partial\eta_n}\frac{\mu}{Pr}\left(1 + \epsilon^+\frac{Pr}{Pr_t}\right)\frac{\partial h}{\partial\eta_n}\right\}$$

It follows that Eqs. (6.1.5) and (6.1.6) become

ξ - *momentum:*

$$A_0 = -\frac{\epsilon^2}{n_{b_0}^2}\mu\left(1 + \epsilon^+\right)$$

$$A_1 = -\frac{\epsilon^2}{n_{b_0}^2}\left[\frac{\partial}{\partial\eta_n}\left\{\mu\left(1 + \epsilon^+\right)\right\} + \mu\left(1 + \epsilon^+\right)\frac{3}{h_1}\frac{\partial h_1}{\partial\eta_n} - \frac{\mu}{h_1}\frac{\partial h_1}{\partial\eta_n}\right] - \rho_{s_0}\bar{\rho}\frac{v}{n_{b_0}}$$

$$A_2 = \frac{\epsilon^2}{n_{b_0}^2}\left(\frac{1}{h_1}\frac{\partial h_1}{\partial\eta_n}\right)\left[\frac{\partial\mu}{\partial\eta_n} + 2\frac{\mu}{h_1}\frac{\partial h_1}{\partial\eta_n}\right] + \frac{\rho_{s_0}\bar{\rho}}{h_1}\left(\bar{u}\frac{du_s}{d\xi} - \frac{v}{n_{b_0}}\frac{\partial h_1}{\partial\eta_n}\right) \quad (6.2.3)$$

$$A_3 = \frac{1}{h_1}\left[\lim_{\xi\to 0}\left\{\frac{1}{u_s}\frac{\partial p}{\partial\xi}\right\} - \frac{\eta_n - 1}{n_{b_0}}\frac{\partial p}{\partial\eta_n}\lim_{\xi\to 0}\left\{\frac{1}{u_s}\frac{dn_b}{d\xi}\right\}\right]$$

$$A_4 = 0$$

energy:

$$A_0 = -\frac{\epsilon^2}{n_{b_0}}\frac{\mu}{Pr}\left(1 + \epsilon^+\frac{Pr}{Pr_t}\right)$$

$$A_1 = -\frac{\epsilon^2}{n_{b_0}}\left(1 + \epsilon^+\frac{Pr}{Pr_t}\right)\left[\frac{\partial}{\partial\eta_n}\left(\frac{\mu}{Pr}\right) + \frac{3}{h_1}\frac{\partial h_1}{\partial\eta_n}\frac{\mu}{Pr}\right]$$

$$-\rho_{s_0}\bar{\rho}v - \frac{\epsilon^2}{n_{b_0}}\frac{\mu}{Pr}\frac{\partial}{\partial\eta_n}\left(1 + \epsilon^+\frac{Pr}{Pr_t}\right)$$

$$A_2 = 0 \quad (6.2.4)$$

$$A_3 = v\frac{\partial p}{\partial\eta_n}$$

$$A_4 = 0$$

6.3 Turbulence Model

A turbulence model must be employed to define ϵ^+, and the Cebeci-Smith model is used here. It is a two-layer eddy viscosity formulation whose inner layer value, ϵ_i^+, is based on Prandtl's mixing length concept [51]. The outer layer value, ϵ_o^+, is given by the Clauser-Klebanoff [52, 53] expression. The inner layer expression is used from the wall outward until $\epsilon_i^+ > \epsilon_o^+$.

Note: *The Cebeci-Smith model was developed for a body-normal system, however it is being applied here in a shock-normal environment.*

In the laminar to turbulent transition region, the composite eddy viscosity is modified using the Dhawan and Narashima [54] method.

6.3.1 Inner Layer

The inner layer eddy viscosity is based on Prandtl's mixing length theory:

$$\epsilon_i^+ = \frac{\rho l^2}{\epsilon^2 \mu} \frac{1}{n_b} \left| \frac{\partial u}{\partial \eta_n} - \frac{u}{h_1} \frac{\partial h_1}{\partial \eta_n} \right| \tag{6.3.1}$$

The mixing length for the inner layer according to Van Driest [51] is

$$l = K_v n_b \eta_n \left[1 - exp\left(-n^+/A^+ \right) \right] \tag{6.3.2}$$

where the von Karman constant is

$$K_v = 0.4$$

and the normal coordinate parameter is

$$n^+ = \frac{n_b \eta_n \rho}{\epsilon \mu} \left[\frac{\mu_w}{\rho n_b} \left| \frac{\partial u}{\partial \eta_n} \right|_w \right]^{1/2} \tag{6.3.3}$$

In Ref. [44], the damping factor is defined as

$$A^+ = 26 \left(\left| \frac{\tau}{\tau_w} \right| \right)^{-1/2} \tag{6.3.4}$$

where the local shear stress is

$$\tau = \mu \left(1 + \epsilon^+ \right) \left| \frac{\partial u}{\partial \eta_n} - \frac{u}{h_1} \frac{\partial h_1}{\partial \eta_n} \right| \tag{6.3.5}$$

The subscript w indicates that quantity is evaluated at the wall.

6.3.2 Outer Layer

The outer layer eddy viscosity is approximated by the Clauser-Klebanoff [52, 53] expression:

$$\epsilon_o^+ = 0.0168\frac{\rho u_e \delta_k \gamma_{ij}}{\epsilon^2 \mu} \tag{6.3.6}$$

The displacement thickness is

$$\delta_k = n_b \int_0^\delta \left(1 - \frac{u}{u_e}\right) d\eta_n \tag{6.3.7}$$

where δ is the value of η_n at the boundary layer edge. Klebanoff's intermittency factor [55] is

$$\gamma_{ij} = \left[1 + 5.5 \left(\frac{\eta_n}{\delta}\right)^6\right]^{-1} \tag{6.3.8}$$

6.3.3 Boundary Layer Edge

By definition, at the boundary layer edge,

$$\frac{H}{H_\infty} \to 1$$

where the total enthalpy (H) is

$$H = h + \frac{u^2 + v^2}{2}$$

Numerically, this can be approximated as the first grid point where

$$\frac{H}{H_\infty} > 0.995$$

This approach can lead to oscillations at the boundary-layer edge. Reference [56] proposes a different criteria, which is based on another characteristic of the boundary layer edge:

$$\frac{d}{d\eta_n}\left(\frac{H}{H_\infty}\right) \to 0$$

Numerically, this is approximated as

$$\frac{d}{d\eta_n}\left(\frac{H}{H_\infty}\right) \le 0.5$$

This is the criteria which is employed in the present work.

6.3.4 Transition

Transition from laminar to turbulent flow is modeled through the definition of a streamwise transition intermittency factor [54]:

$$\gamma_{i,\xi} = 1 - \exp(-0.412\bar{\xi}^2) \qquad (6.3.9)$$

where

$$\bar{\xi} = 2.96 \frac{(\xi - \xi_0)}{[\xi_0(\bar{X} - 1)]} \qquad (6.3.10)$$

Before transition begins, the flow is laminar and $\gamma_{i,\xi} = 0$. As $\bar{\xi} \to \infty$, it can be seen that $\gamma_{i,\xi} \to 1$. In practical applications, this value of unity is essentially achieved at $\bar{\xi} = 5$. Thus, transition begins at $\xi = \xi_0$ (as prescribed by the user) and continues until $\bar{\xi} = 5$. Within the transition region, the local value of eddy viscosity is modified by

$$\epsilon^+ = \epsilon^+ \gamma_{i,\xi} \qquad (6.3.11)$$

The value of $\bar{X}$ is dependent on the flow conditions and body geometry under consideration [57]. It is usually determined empirically. In the results presented later, a value of $\bar{X} = 2$ is chosen for the purposes of comparison.

7 Shock Layer Geometry

This chapter discusses the relations which define the shock and body shapes, and the resultant shock layer thickness. Sections 7.1 and 7.2 discuss the analytic expressions used to describe the body and shock shapes, respectively. Relations for the shock layer thickness and its streamwise gradient are presented in Section 7.3. The final section contrasts three coordinate transformations which have been investigated as a part of this research.

7.1 Body Geometry

7.1.1 Forebody

For many configurations of interest, the body shape can be defined by an axisymmetric conic equation:

$$r_b^2 = 2\left(z_b - n_{b_0}\right) - b_b \left(z_b - n_{b_0}\right)^2 \tag{7.1.1}$$

where n_{b_0} is the stagnation standoff distance and the nondimensional nose radius of curvature has a value of unity. This is the equation of an axisymmetric conic body whose nose is at $(z_b = n_{b_0}, r_b = 0)$.

The character of the conic is dictated by b_b:

$$b_b \begin{cases} < 0 & , \text{ hyperboloid} \\ = 0 & , \text{ paraboloid} \\ > 0 & , \text{ ellipsoid} \\ = 1 & , \text{ sphere} \end{cases}$$

For a hyperboloid, the value of the cone angle, Γ_b, that the hyperboloid asymptotically approaches is specified so that

$$b_b = -\tan^2 \Gamma_b \tag{7.1.2}$$

For $b_b \geq 0$, the value of b_b is a required input. By setting $b_b > 0$, Eq. (7.1.1) can be used to define the forebody of an elliptic-cone, where $b_b = 1$ is the special case of a sphere-cone.

For the blunted body described by Eq. (7.1.1), the slope is

$$\frac{dr_b}{dz_b} = \frac{1 - b_b\left(z_b - n_{b_0}\right)}{r_b} \tag{7.1.3}$$

7.1.2 Stagnation Line

From Eq. (2.1.4), the body radius is

$$r_b = h_{3_b} = r_s - n_b \cos \Gamma_s = r_s \left[1 - n_b \frac{\cos \Gamma_s}{r_s} \right] \qquad (7.1.4)$$

On the stagnation line this becomes

$$r_b = r_s \left[1 - n_b \kappa_{s_0} \right] = r_s h_{1_b}$$

so that Eq. (7.1.3) can be rewritten as

$$\frac{dr_b}{dz_b} = \frac{1 - b_b \left(z_b - n_{b_0} \right)}{r_s h_{1_b}} = \frac{1}{r_s h_{1_b}} \qquad (7.1.5)$$

7.1.3 Ellipsoid-Cone Juncture

At the juncture between the ellipsoidal forebody and cone afterbody, both the position and slope of the body are continuous. Thus, the coordinates of this juncture may be determined by equating Eqs. (7.1.3) and (7.1.11). Solving for $z_b = z_{junct}$ (after some manipulation) gives

$$z_{junct} = n_{b_0} + \frac{1}{b_b} \left\{ 1 - \frac{\sin \Gamma_b}{\sqrt{b_b \cos^2 \Gamma_b + \sin^2 \Gamma_b}} \right\} \qquad (7.1.6)$$

Now the corresponding value for r_{junct} can be found from Eq. (7.1.1):

$$r_{junct}^2 = 2 \left(z_{junct} - n_{b_0} \right) - b_b \left(z_{junct} - n_{b_0} \right)^2 \qquad (7.1.7)$$

For the special case of a sphere-cone ($b_b = 1$):

$$z_{junct} = n_{b_0} + 1 - \sin \Gamma_b \qquad (7.1.8)$$

and

$$r_{junct} = \cos \Gamma_b \qquad (7.1.9)$$

For $z_b < z_{junct}$, the body is defined by the equations of Section 7.1.1. After this juncture, the body shape is described by the equations of Section 7.1.4.

7.1.4 Afterbody

The cone afterbody is given by

$$r_b = r_{junct} + \left(z_b - z_{junct} \right) \tan \Gamma_b \qquad (7.1.10)$$

where r_{junct} and z_{junct} are the coordinates of the ellipsoid-cone juncture, defined in Section 7.1.3. The slope of the cone is

$$\frac{dr_b}{dz_b} = \tan \Gamma_b \qquad (7.1.11)$$

7.2   Shock Shape

7.2.1   Subsonic-Transonic Region

The body shape in the nose region is described by a conic equation (see Section 7.1.1). Van Dyke and Gordon [64] suggest that a conic body generates a conic shock shape, so the subsonic-transonic region is described by a conic equation:

$$r_s^2 = 2C_s z_s - b_s z_s^2 \tag{7.2.1}$$

where C_s is the value of the shock radius of curvature on the stagnation line and b_s determines the conic's character.

Since the shock shape is defined analytically, closed-form expressions for the quantities listed below may be determined. (see Appendix K for details). The shock angle can be found from

$$\sin \Gamma_s = (C_s - b_s z_s) \frac{\cos \Gamma_s}{r_s} \tag{7.2.2}$$

The curvature is given by

$$\kappa_s = \frac{\cos \Gamma_s}{r_s} \left(\sin^2 \Gamma_s + b_s \cos^2 \Gamma_s \right) \tag{7.2.3}$$

Further, the gradient of the curvature is

$$\frac{d\kappa_s}{d\xi} = 3\kappa_s \sin \Gamma_s \frac{\cos^2 \Gamma_s}{r_s} (b_s - 1) \tag{7.2.4}$$

Referring to Eq. (2.2.4), the streamwise pressure derivative can be rewritten as

$$\left. \frac{\partial p}{\partial \xi} \right|_\eta = \frac{dp_s}{d\xi} + \frac{\eta - 1}{2} \kappa_s \sin \Gamma_s \left\{ u_s + 3u_s \cos^2 \Gamma_s (b_s - 1) + \kappa_s r_s \right\} \tag{7.2.5}$$

$$-\frac{\eta^2 - 1}{4} \left\{ 2v_s \kappa_s \sin^2 \Gamma_s \cos \Gamma_s (b_s - 1) + \left(1 + \frac{\kappa_s r_s}{\cos \Gamma_s} \right) \left[\sin \Gamma_s \frac{dv_s}{d\xi} - v_s \kappa_s \cos \Gamma_s \right] \right\}$$

In addition, from Eq. (2.2.7), the streamwise derivative of n becomes

$$\left. \frac{\partial n}{\partial \xi} \right|_\eta = (\eta - 1) \frac{v_s}{2} \cos \Gamma_s (b_s - 1) \tag{7.2.6}$$

On the stagnation line, Eq. (7.2.4) has the following limiting form:

$$\lim_{\xi \to 0} \left\{ \frac{1}{\cos \Gamma_s} \frac{d\kappa_s}{d\xi} \right\} = 3\kappa_{s_0}^2 (b_s - 1) \tag{7.2.7}$$

Thus, Eq. (2.4.12) becomes

$$\lim_{\xi \to 0} \left\{ \frac{1}{u_s} \frac{\partial p}{\partial \xi} \right\} = \lim_{\xi \to 0} \left\{ \frac{1}{u_s} \frac{dp_s}{d\xi} \right\} + \kappa_{s_0} (\eta - 1) \qquad (7.2.8)$$

$$- \frac{\eta^2 - 1}{2} \left[v_{s_0} \kappa_{s_0} (b_s - 2) + \lim_{\xi \to 0} \left\{ \frac{1}{u_s} \frac{dv_s}{d\xi} \right\} \right]$$

and Eq. (2.4.16) becomes

$$\lim_{\xi \to 0} \left\{ \frac{1}{r_s} \left. \frac{\partial n}{\partial \xi} \right|_\eta \right\} = (\eta - 1) \frac{v_{s_0}}{2} \kappa_{s_0} (b_s - 1) \qquad (7.2.9)$$

7.2.2 Supersonic Region

Since the supersonic region is hyperbolic-parabolic in nature, a marching procedure is employed. The shock shape segment between the previous $(k-1)$ and current (k) stations is described by a truncated Taylor's series (see Appendix L for details):

$$r_s = \tilde{r}_0 + \tilde{r}_1 (\Delta z_s) + \frac{\tilde{r}_2}{2!} (\Delta z_s)^2 + \frac{\tilde{r}_3}{3!} (\Delta z_s)^3 \qquad (7.2.10)$$

where

$$\Delta z_s = z_s - z_{s_{k-1}}$$

The shock angle can be found from

$$\tan \Gamma_s = \frac{dr_s}{dz_s} = \tilde{r}_1 + \tilde{r}_2 (\Delta z_s) + \frac{\tilde{r}_3}{2} (\Delta z_s)^2 \qquad (7.2.11)$$

The curvature is given by

$$\kappa_s = - \cos^3 \Gamma_s \frac{d^2 r_s}{dz_s^2} \qquad (7.2.12)$$

where

$$\frac{d^2 r_s}{dz_s^2} = \tilde{r}_2 + \tilde{r}_3 (\Delta z_s) \qquad (7.2.13)$$

In this marching region, a simple backward difference representation of the pressure derivative is employed. Thus, at a given point k on station j,

$$\left. \frac{\partial p}{\partial \xi} \right|_{\eta_n} = \frac{p_{k,j} - p_{k-1,j}}{\Delta \xi_k} \qquad (7.2.14)$$

where

$$\Delta \xi_k = \xi_k - \xi_{k-1}$$

7.3 Shock Layer

With each iteration in the solution of the governing equations, a calculated value of the shock layer thickness may be determined from the continuity equation. In addition, the analytic expressions for the shock and body shape provide the means of calculating a geometric value of the thickness. If the equation used for the shock shape is reasonable, then these two values should match. This observation serves as the criteria for shock-shape convergence at a given station (see Chapter 8). Expressions for the calculated and geometric thickness values are given below. In addition, an analytic expression for the gradient of the shock layer thickness (a term which appears in the governing equations) is presented.

7.3.1 Calculated Thickness

The continuity equation can be used to determine the shock layer thickness based on the conservation of mass. This *calculated* thickness (see Appendix D) is defined by the following quadratic for n_b:

$$n_b^2 \left[\rho_s u_s \cos \Gamma_s \int_0^1 \bar{\rho}\bar{u} \left(\eta_n - 1 \right) d\eta_n \right] + n_b \left[\rho_s u_s r_s \int_0^1 \bar{\rho}\bar{u} d\eta_n \right] - \Psi_s = 0 \qquad (7.3.1)$$

Dividing by Ψ_s, Eq. (7.3.1) can be written as

$$n_b^2 \left[2\rho_s \frac{u_s \cos \Gamma_s}{r_s^2} \int_0^1 \bar{\rho}\bar{u} \left(\eta_n - 1 \right) d\eta_n \right] + n_b \left[2\rho_s \frac{u_s}{r_s} \int_0^1 \bar{\rho}\bar{u} d\eta_n \right] - 1 = 0 \qquad (7.3.2)$$

As $\xi \to 0$, Eq. (7.3.2) becomes (see Appendix E)

$$n_b^2 \left[2\rho_s \kappa_s^2 \int_0^1 \bar{\rho}\bar{u} \left(\eta_n - 1 \right) d\eta_n \right] + n_b \left[2\rho_s \kappa_s \int_0^1 \bar{\rho}\bar{u} d\eta_n \right] - 1 = 0 \qquad (7.3.3)$$

This expression is used to define the stagnation standoff distance, n_{b_0}.

7.3.2 Geometric Thickness

Through geometric considerations,

$$r_b = r_s - n_{b_g} \cos \Gamma_s \qquad (7.3.4)$$

where

$$n_{b_g} = \sqrt{\left(z_s - z_b \right)^2 + \left(r_s - r_b \right)^2} \qquad (7.3.5)$$

is the *geometric* shock layer thickness (measured along a shock normal).

Differentiating with respect to ξ gives

$$\frac{dr_b}{d\xi} = h_{1_b} \sin \Gamma_s - \frac{dn_b}{d\xi} \cos \Gamma_s \qquad (7.3.6)$$

Similarly,

$$z_b = z_s + n_{b_g} \sin \Gamma_s \tag{7.3.7}$$

Differentiating with respect to ξ gives

$$\frac{dz_b}{d\xi} = h_{1_b} \cos \Gamma_s + \frac{dn_b}{d\xi} \sin \Gamma_s \tag{7.3.8}$$

However,

$$\frac{dr_b}{d\xi} = \frac{dr_b}{dz_b} \frac{dz_b}{d\xi} \tag{7.3.9}$$

where dr_b/dz_b is the local slope of the body geometry. Combine Eqs. (7.3.6), (7.3.8), and (7.3.9) to get

$$\frac{dn_b}{d\xi} = \frac{h_{1_b} \left[\sin \Gamma_s - \dfrac{dr_b}{dz_b} \cos \Gamma_s \right]}{\cos \Gamma_s + \dfrac{dr_b}{dz_b} \sin \Gamma_s} \tag{7.3.10}$$

which is valid for any body geometry.

A shock normal has a slope of

$$m = -\left(\frac{dr_s}{dz_s}\right)^{-1}$$

Thus, the equation of the shock normal line passing through the shock point (z_b, r_b) and intersecting the body at point (z_b, r_b) is

$$r_b = mz_b + (r_s - mz_s) \tag{7.3.11}$$

Forebody

Combining Eqs. (7.1.1) and (7.3.11) gives

$$\left(m^2 + b_b\right) z_b^2 + 2\left[(r_s - mz_s) m - b_b n_{b_0} - 1 \right] z_b + (r_s - mz_s)^2 + b_b n_{b_0}^2 + 2n_{b_0} = 0 \tag{7.3.12}$$

This quadratic can be solved for z_b, and then r_b is found from Eq. (7.1.1). With dr_b/dz_b defined by Eq. (7.1.3), the gradient of the shock layer thickness can be determined from Eq. (7.3.10).

Stagnation Line

The limit of Eq. (7.3.10) as $\xi \to 0$ is

$$\lim_{\xi \to 0} \left\{ \frac{1}{\cos \Gamma_s} \frac{dn_b}{d\xi} \right\} = \frac{h_{1_b}}{\cos \Gamma_s} \frac{\left[1 - \dfrac{dr_b}{dz_b} \cos \Gamma_s \right]}{\dfrac{dr_b}{dz_b}} \tag{7.3.13}$$

Now combine Eq. (7.1.5) with this result to get

$$\lim_{\xi \to 0} \left\{ \frac{1}{\cos \Gamma_s} \frac{dn_b}{d\xi} \right\} = \frac{h_{1_b}}{\cos \Gamma_s} \frac{\left[1 - \frac{\kappa_s}{h_{1_b}} \right]}{\frac{1}{r_s h_{1_b}}} = \frac{r_s}{\cos \Gamma_s} h_{1_b} \left[h_{1_b} - \kappa_s \right] \qquad (7.3.14)$$

so that

$$\lim_{\xi \to 0} \left\{ \frac{1}{\cos \Gamma_s} \frac{dn_b}{d\xi} \right\} = h_{1_b} \left[C_s h_{1_b} - 1 \right] \qquad (7.3.15)$$

Afterbody

Combining Eqs. (7.1.10) and (7.3.11) gives

$$z_b = \frac{r_{junct} - z_{junct} \tan \Gamma_b - (r_s - m z_s)}{m - \tan \Gamma_b} \qquad (7.3.16)$$

Substitute into Eq. (7.1.10) to get r_b. Utilizing Eq. (7.1.11), the shock layer thickness gradient is determined from Eq. (7.3.10).

7.4 Spacing Across Layer

At the beginning of this investigation, a considerable effort went into the development of an inviscid nonequilibrium algorithm. In this early work, the governing equations were transformed to a streamline coordinate system (Figure 7.1). In this transformed space, the solution was advanced by marching along streamlines. At each new station, the shock streamline is added to the grid. Thus, if a constant number of points is desired, an automated procedure for dropping streamlines is required.

In Ref. [29], η (where $\eta = \Psi / \Psi_s$) was found to be a better transformation coordinate since it allowed more control of the spacing than the streamline method. In addition, this transformation gives a constant number of points across the layer for each station. Since viscous effects were to be included eventually in the nonequilibrium algorithm, a switch from the streamline approach seemed inevitable. Unfortunately, this decision meant abandoning the explicit approach under development by this author.

In Ref. [29], the solution is advanced along lines of constant η (Figure 7.2). The spacing is still based on mass flow through the layer, rather than on physical distance across the layer. While this transformation to η is an improvement over Ψ, it still yields a grid-point distribution which is less than optimal in the near-wall region of the shock layer. In fact, the points cluster near the shock, rather than near the wall. As will be shown in Chapter 9, the shock layer profiles from the method of Ref. [29] exhibit oscillations as a result of this spacing.
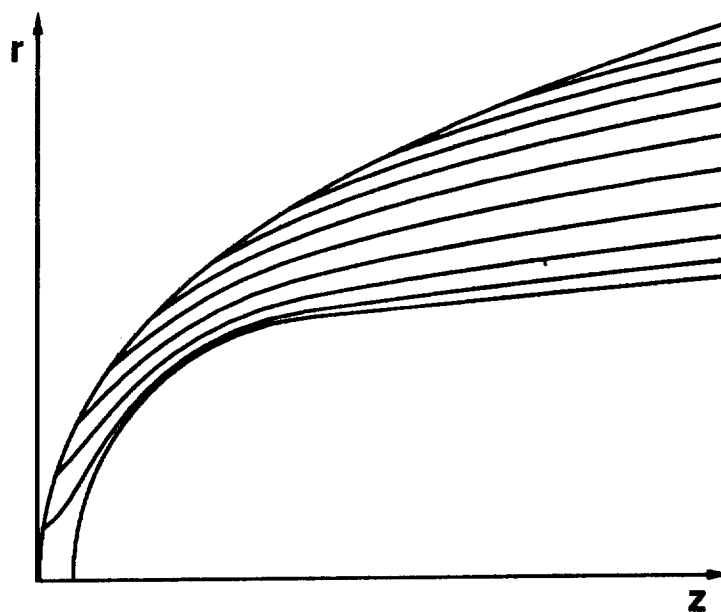
Figure 7.1. Equally-spaced lines of constant Ψ (streamlines).
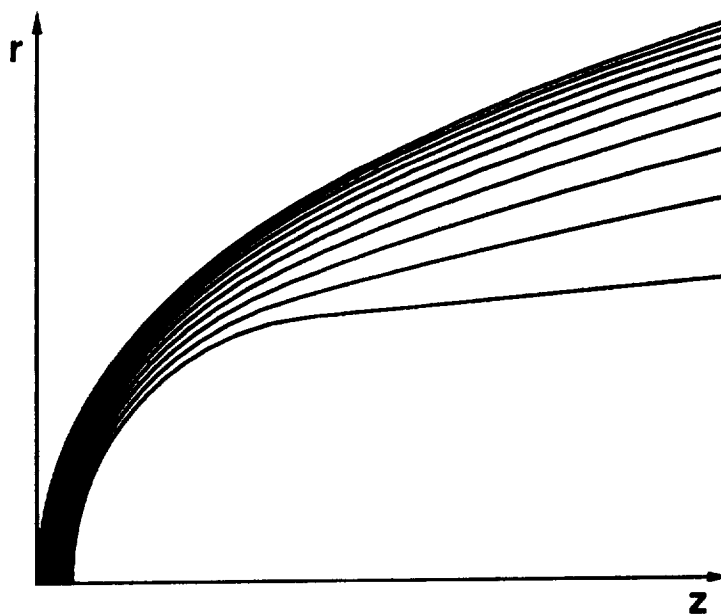
Figure 7.2. Equally-spaced lines of constant η.
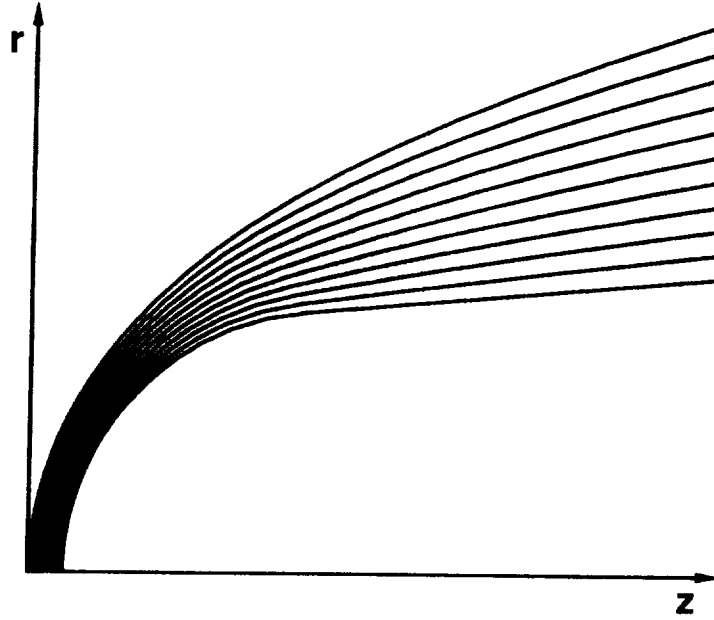
Figure 7.3. Equally-spaced lines of constant η_n.

In order to better control the spacing across the layer in the present technique, a transformation to normalized coordinates as described in Châpter 2 is used. Recall the definition of the following computational variables:

$$\xi = s \qquad \eta_n = 1 - \frac{n}{n_b}$$

This normal spacing based on η_n (Figure 7.3) is analogous to the spacing used in Ref. [9]. Although Figures 7.2 and 7.3 show equally-spaced lines, these spacing functions lend themselves to clustering. However, since the physical distance to which η corresponds varies in the streamwise direction, determining a distribution which will work well for the duration of a given solution can be difficult. On the other hand, since there is no streamwise variation in the normalized distance that η_n represents, finding a suitable distribution is more straightforward in the present approach.

The following distribution function [9] may be used to define the spacing across the shock layer:

$$\eta_{n_j} = f_0 + \frac{f_2 - f_0}{1 + exp\left\{\eta_{slp}\left[\eta_{n_{brk}} - (j - 1)\right]\right\}}$$

(7.4.1)

where

$$f_0 = \frac{\eta_{n_{fac}}{}^{j-1} - 1}{\eta_{n_{fac}}{}^{j_s-1} - 1}$$

(7.4.2)

$$f_2 = \frac{j - 1}{j_s - 1} + \left[1 - \frac{j - 1}{j_s - 1}\right]\eta_{n_{int}}$$

(7.4.3)

In addition, j_s is the total number of grid points, $\eta_{n_{brk}}$ is the point through which the exponential fit passes, $\eta_{n_{fac}}$ is the geometric stretching factor, $\eta_{n_{int}}$ is the intercept on the axis which determines the slope of the linear distribution near the shock, and $\eta_{n_{slp}}$ is the slope of the fit at $\eta_{n_{brk}}$. This function clusters points according to a geometric progression near the wall, a linear distribution near the shock, and an exponential fit for the interior of the shock layer. If $\eta_{n_{int}} \leq 0$ is specified, a simple geometric progression is used so that

$$d\eta_{n_j} = \eta_{n_{fac}} d\eta_{n_{j-1}} \qquad (7.4.4)$$

$$\eta_{n_j} = \eta_{n_{j-1}} + d\eta_{n_j} \qquad (7.4.5)$$

and

$$d\eta_{n_2} = \frac{\eta_{n_{fac}} - 1}{\eta_{n_{fac}}^{j_s-1} - 1} \qquad (7.4.6)$$

This relation clusters points near the wall, but not at the shock.

For the perfect gas and equilibrium solutions presented in Chapter 9, $j_s = 101$, while for the nonequilibrium solutions, $j_s = 51$. The factors corresponding to these values of j_s are

$j_s = 51$	$j_s = 101$
$\eta_{n_{brk}} = 30$	$\eta_{n_{brk}} = 60$
$\eta_{n_{fac}} = 1.17$	$\eta_{n_{fac}} = 1.13$
$\eta_{n_{int}} = 0.$	$\eta_{n_{int}} = 0.$
$\eta_{n_{slp}} = 0.13$	$\eta_{n_{slp}} = 0.1$

8   Method of Solution

The procedure for solving the equations presented in the preceding chapters is outlined here. First, an introduction to the issue of generating the shock shape is given. Next, the quasi-linearization of the streamwise momentum equation is discussed. The procedure for numerically integrating the equations of standard parabolic form is presented in Section 8.3. The chapter concludes with a discussion on the advancement of the solution from one station to the next.

8.1   Shock Shape

The full VSL approach requires the user to input an initial shock shape, which is used to calculate a first iteration solution. The shock shape calculated in the first-iteration solution must then be smoothed and used as the input shape for a second iteration. This user-controlled process is continued until the new calculated shock shape varies little from the input shape (usually 2 to 4 iterations). In the design environment, such requirements of the user are undesirable.

Automating this process was addressed in Ref. [29] by incorporating a shock iteration technique in the solution. Since the subsonic-transonic region is elliptic in nature, this portion of the flowfield must be solved in a global fashion. The derivative of shock layer thickness is described in terms of a cubic equation involving the body radius where an iterative procedure is applied to determine its coefficients. This process typically requires ten to twenty iterations to obtain a converged shock shape.

A marching technique is employed aft of the subsonic-transonic region, since the inviscid layer is supersonic. For this region, the shock shape at the current station is extrapolated from the previous station using a cubic equation for the shock radius as a function of axial location. Requirements that this expression match the position, slope, and curvature at the previous station leaves one free coefficient (essentially the shock curvature derivative). An iterative technique is employed to determine this value based on comparisons between the shock standoff distance obtained from the flowfield solution and the geometric distance between the shock and body curves. When these two values agree to within the prescribed tolerance, the solution is advanced downstream to the next station. The iterative procedure used in Ref. [29] is sensitive, so this marching technique is often slow to converge.

The current technique also generates its shock shape as part of the solution. The details are given in Section 8.4. Before discussing that topic, the linearization procedure is given in Section 8.2. Then, an outline of the solution of the governing equations is presented in Section 8.3.

8.2 Streamwise Momentum Linearization

The usual approach to handling the nonlinearities in the VSL equations is to evaluate the A_m coefficients ($m = 0, 1, 2, 3, 4$) from the most recent information available. For example, the value of u obtained in the most recent solution of the streamwise momentum equation is used in loading the coefficients for solving the energy equation. This approach, which essentially treats all such quantities as knowns, still leaves the following nonlinear terms in the streamwise momentum equation:

$$\bar{u}\frac{\partial \bar{u}}{\partial \eta_n} \qquad\qquad \bar{u}\frac{\partial \bar{u}}{\partial \xi} \qquad\qquad \bar{u}^2$$

For the energy equation, the nonlinearities are handled through a simple lagging technique. However, in order to speed convergence, the streamwise momentum equation is quasi-linearized [65]. This process involves expressing $\bar{u}$ as

$$\bar{u} = \bar{u}_p + \Delta\bar{u} \tag{8.2.1}$$

where the subscript p denotes evaluation at the previous iteration and $\Delta\bar{u}$ is the change in $\bar{u}$ from the previous iteration. Differentiating Eq. (8.2.1) with respect to η_n gives

$$\frac{\partial \bar{u}}{\partial \eta_n} = \left.\frac{\partial \bar{u}}{\partial \eta_n}\right|_p + \Delta\left(\frac{\partial \bar{u}}{\partial \eta_n}\right) \tag{8.2.2}$$

and differentiating Eq. (8.2.1) with respect to ξ gives

$$\frac{\partial \bar{u}}{\partial \xi} = \left.\frac{\partial \bar{u}}{\partial \xi}\right|_p + \Delta\left(\frac{\partial \bar{u}}{\partial \xi}\right) \tag{8.2.3}$$

Using these representations,

$$\bar{u}\frac{\partial \bar{u}}{\partial \eta_n} = (\bar{u}_p + \Delta\bar{u})\left[\left.\frac{\partial \bar{u}}{\partial \eta_n}\right|_p + \Delta\left(\frac{\partial \bar{u}}{\partial \eta_n}\right)\right]$$

so that if the higher order term is dropped, then

$$\bar{u}\frac{\partial \bar{u}}{\partial \eta_n} = \bar{u}_p\left.\frac{\partial \bar{u}}{\partial \eta_n}\right|_p + \left.\frac{\partial \bar{u}}{\partial \eta_n}\right|_p \Delta\bar{u} + \bar{u}_p\Delta\left(\frac{\partial \bar{u}}{\partial \eta_n}\right) \tag{8.2.4}$$

Using Eqs. (8.2.1) and (8.2.2) this can be rewritten as

$$\bar{u}\frac{\partial \bar{u}}{\partial \eta_n} = \left\{\left.\frac{\partial \bar{u}}{\partial \eta_n}\right|_p \bar{u}\right\} + \bar{u}_p\frac{\partial \bar{u}}{\partial \eta_n} - \bar{u}_p\left.\frac{\partial \bar{u}}{\partial \eta_n}\right|_p \tag{8.2.5}$$

Similarly,

$$\bar{u}\frac{\partial \bar{u}}{\partial \xi} = \left\{\left.\frac{\partial \bar{u}}{\partial \xi}\right|_p \bar{u}\right\} + \bar{u}_p\frac{\partial \bar{u}}{\partial \xi} - \bar{u}_p\left.\frac{\partial \bar{u}}{\partial \xi}\right|_p \qquad (8.2.6)$$

and finally,

$$\bar{u}^2 = 2\left\{\bar{u}_p\bar{u}\right\} - \bar{u}_p^2 \qquad (8.2.7)$$

The "bracketed" portions of these three expressions are the terms which would be present without linearization. Eqs. (8.2.5) through (8.2.7) are substituted back into the ξ-momentum equation to obtain the linearized form of the equation.

This linearization process only affects the A_2 and A_3 coefficients of the streamwise momentum equation. Based on Eq. (6.1.5), the coefficients for the streamwise momentum equation become

ξ - *momentum:*

$$A_0 = -\frac{\epsilon^2}{n_b^2}\mu\left(1 + \epsilon^+\right)$$

$$A_1 = -\frac{\epsilon^2}{n_b^2}\left[\frac{\partial}{\partial \eta_n}\left\{\mu\left(1 + \epsilon^+\right)\right\} + \mu\left(1 + \epsilon^+\right)\left(\frac{2}{h_1}\frac{\partial h_1}{\partial \eta_n} + \frac{1}{h_3}\frac{\partial h_3}{\partial \eta_n}\right) - \frac{\mu}{h_1}\frac{\partial h_1}{\partial \eta_n}\right]$$

$$- \rho_s\bar{\rho}\left[\frac{v}{n_b} + \frac{u_s\bar{u}}{h_1}\frac{\eta_n - 1}{n_b}\frac{dn_b}{d\xi}\right] \qquad (8.2.8)$$

$$A_2 = \frac{\epsilon^2}{n_b^2}\left(\frac{1}{h_1}\frac{\partial h_1}{\partial \eta_n}\right)\left[\frac{\partial \mu}{\partial \eta_n} + \mu\left(\frac{1}{h_1}\frac{\partial h_1}{\partial \eta_n} + \frac{1}{h_3}\frac{\partial h_3}{\partial \eta_n}\right)\right]$$

$$+ \frac{\rho_s\bar{\rho}}{h_1}\left[2\bar{u}\frac{du_s}{d\xi} - \frac{v}{n_b}\frac{\partial h_1}{\partial \eta_n} + u_s\left(\frac{\partial \bar{u}}{\partial \xi} - \frac{\eta_n - 1}{n_b}\frac{dn_b}{d\xi}\frac{\partial \bar{u}}{\partial \eta_n}\right)\right]$$

$$A_3 = \frac{1}{h_1}\left[\left\{\frac{1}{u_s}\frac{\partial p}{\partial \xi}\right\} - \frac{\eta_n - 1}{n_b}\frac{\partial p}{\partial \eta_n}\left\{\frac{1}{u_s}\frac{dn_b}{d\xi}\right\}\right]$$

$$- \frac{\rho_s\bar{\rho}\bar{u}}{h_1}\left[\bar{u}\kappa_s\sin\Gamma_s + u_s\left(\frac{\partial \bar{u}}{\partial \xi} - \frac{\eta_n - 1}{n_b}\frac{dn_b}{d\xi}\frac{\partial \bar{u}}{\partial \eta_n}\right)\right]$$

$$A_4 = \rho_s u_s\frac{\bar{\rho}\bar{u}}{h_1}$$

On the stagnation line, these become
ξ - *momentum:*

$$A_0 = -\frac{\epsilon^2}{n_b^2}\mu\left(1 + \epsilon^+\right)$$

$$A_1 = -\frac{\epsilon^2}{n_b^2}\left[\frac{\partial}{\partial \eta_n}\left\{\mu\left(1 + \epsilon^+\right)\right\} + \mu\left(1 + \epsilon^+\right)\frac{3}{h_1}\frac{\partial h_1}{\partial \eta_n} - \frac{\mu}{h_1}\frac{\partial h_1}{\partial \eta_n}\right] - \rho_s\bar{\rho}\frac{v}{n_b}$$

$$A_2 = \frac{\epsilon^2}{n_b^2}\frac{1}{h_1}\frac{\partial h_1}{\partial \eta_n}\left[\frac{\partial \mu}{\partial \eta_n} + 2\frac{\mu}{h_1}\frac{\partial h_1}{\partial \eta_n}\right] + \frac{\rho_s\bar{\rho}}{h_1}\left[2\bar{u}\frac{du_s}{d\xi} - \frac{v}{n_b}\frac{\partial h_1}{\partial \eta_n}\right] \qquad (8.2.9)$$

$$A_3 = \frac{1}{h_1}\left[\lim_{\xi\to 0}\left\{\frac{1}{u_s}\frac{\partial p}{\partial \xi}\right\} - \frac{\eta_n - 1}{n_b}\frac{\partial p}{\partial \eta_n}\lim_{\xi\to 0}\left\{\frac{1}{u_s}\frac{dn_b}{d\xi}\right\}\right] - \frac{\rho_s\bar{\rho}\bar{u}^2}{h_1}\kappa_{s_0}$$

$$A_4 = 0$$

8.3 Equations of Standard Parabolic Form

A finite-difference approach is used to solve the ξ-momentum, energy, and species conservation equations (for nonequilibrium flow). As mentioned earlier, the first step is to write these equations in the standard parabolic form:

$$A_0\frac{\partial^2 W}{\partial \eta_n^2} + A_1\frac{\partial W}{\partial \eta_n} + A_2 W + A_3 + A_4\frac{\partial W}{\partial \xi} = 0 \tag{8.3.1}$$

where W represents the dependent variables $\bar{u}$, h, and c_i. Next, finite-difference representations are substituted for the partial derivatives. A two-point backward difference is used for the partial derivatives with respect to ξ. For a fully implicit scheme, a three-point central-difference of values at the *current* station is used for the partial derivatives with respect to η_n. Thus, for an arbitrary point j at station k

$$\frac{\partial^2 W}{\partial \eta_n^2} = \frac{2\left[W_{k,j+1} - (1+\beta)W_{k,j} + \beta W_{k,j-1}\right]}{\Delta\eta_{n_{j+1}}^2 + \beta\Delta\eta_{n_j}^2} \tag{8.3.2}$$

$$\frac{\partial W}{\partial \eta_n} = \frac{W_{k,j+1} - (1-\beta^2)W_{k,j} - \beta^2 W_{k,j-1}}{\Delta\eta_{n_{j+1}} + \beta^2\Delta\eta_{n_j}} \tag{8.3.3}$$

$$\frac{\partial W}{\partial \xi} = \frac{W_{k,j} - W_{k-1,j}}{\Delta\xi_k} \tag{8.3.4}$$

where

$$\Delta\eta_{n_j} = \eta_{n_j} - \eta_{n_{j-1}}$$

$$\beta = \frac{\Delta\eta_{n_{j+1}}}{\Delta\eta_{n_j}}$$

and

$$\Delta\xi_k = \xi_k - \xi_{k-1}$$

In a more general approach, the η_n-derivatives are differenced about point $(k-1+\Theta, j)$ where

$$\Theta = \begin{cases} 0 & , \text{ fully explicit} \\ \frac{1}{2} & , \text{ Crank Nicholson} \\ 1 & , \text{ fully implicit} \end{cases}$$

The derivatives now become

$$\frac{\partial^2 W}{\partial \eta_n^2} = \alpha_1\left\{\left[W_{k,j+1} - (1+\beta)W_{k,j} + \beta W_{k,j-1}\right]\Theta \right. \tag{8.3.5}$$

$$+ \left[W_{k-1,j+1} - (1+\beta) W_{k-1,j} + \beta W_{k-1,j-1} \right] (1 - \Theta) \}$$

and

$$\frac{\partial W}{\partial \eta_n} = \alpha_2 \left\{ \left[W_{k,j+1} - \left(1 - \beta^2 \right) W_{k,j} - \beta^2 W_{k,j-1} \right] \Theta \right. \tag{8.3.6}$$

$$\left. + \left[W_{k-1,j+1} - \left(1 - \beta^2 \right) W_{k-1,j} - \beta^2 W_{k-1,j-1} \right] (1 - \Theta) \right\}$$

where

$$\alpha_1 = \frac{2}{\Delta \eta_{n_{j+1}}^2 + \beta \Delta \eta_{n_j}^2} \qquad\qquad \alpha_2 = \frac{1}{\Delta \eta_{n_{j+1}} + \beta^2 \Delta \eta_{n_j}}$$

In addition, the quantity W is evaluated at point $(k - 1 + \Theta, j)$:

$$W = W_{k,j} \Theta + W_{k-1,j} (1 - \Theta) \tag{8.3.7}$$

Making use of these expressions, Eq. (8.3.1) takes the form

$$\tilde{A}_j W_{k,j-1} + \tilde{B}_j W_{k,j} + \tilde{C}_j W_{k,j+1} = \tilde{D}_j \tag{8.3.8}$$

where

$$\tilde{A}_j = \left[\alpha_1 \beta A_0 - \alpha_2 \beta^2 A_1 \right] \Theta$$

$$\tilde{B}_j = \left[-\alpha_1 (1 + \beta) A_0 - \alpha_2 \left(1 - \beta^2 \right) A_1 + A_2 \right] \Theta + \frac{A_4}{\Delta \xi_k}$$

$$\tilde{C}_j = \left[\alpha_1 A_0 + \alpha_2 A_1 \right] \Theta$$

$$\tilde{D}_j = -A_3 + \frac{W_{k-1,j}}{\Delta \xi_k} A_4 - \left\{ A_0 \left. \frac{\partial^2 W}{\partial \eta_n^2} \right|_{k-1,j} + A_1 \left. \frac{\partial W}{\partial \eta_n} \right|_{k-1,j} + A_2 W_{k-1,j} \right\} (1 - \Theta)$$

On the stagnation line (since $A_4 = 0$ for the streamwise momentum, energy, and species conservation equations), the coefficients reduce to

$$\tilde{A}_j = \left[\alpha_1 \beta A_0 - \alpha_2 \beta^2 A_1 \right] \Theta$$

$$\tilde{B}_j = \left[-\alpha_1 (1 + \beta) A_0 - \alpha_2 \left(1 - \beta^2 \right) A_1 + A_2 \right] \Theta$$

$$\tilde{C}_j = \left[\alpha_1 A_0 + \alpha_2 A_1 \right] \Theta$$

$$\tilde{D}_j = -A_3 - \left\{ A_0 \left. \frac{\partial^2 W}{\partial \eta_n^2} \right|_{k-1,j} + A_1 \left. \frac{\partial W}{\partial \eta_n} \right|_{k-1,j} + A_2 W_{k-1,j} \right\} (1 - \Theta)$$

The results presented in Chapter 9 were generated with the fully-implicit approach $(\Theta = 1)$.

Evaluating the coefficients of Eq. (8.3.8) at discrete points across the shock layer yields a tri-diagonal system of equations which may be solved using Thomas' algorithm [66]. The general solution is

$$W_{k,j} = \tilde{E}_j W_{k,j+1} + \tilde{F}_j \tag{8.3.9}$$

where

$$\tilde{E}_j = -\frac{\tilde{C}_j}{\tilde{B}_j + \tilde{A}_j \tilde{E}_{j-1}}$$

$$\tilde{F}_j = \frac{\tilde{D}_j - \tilde{A}_j \tilde{F}_{j-1}}{\tilde{B}_j + \tilde{A}_j \tilde{E}_{j-1}}$$

The boundary condition at the shock is

$$W_{k,j_s} = W_s \tag{8.3.10}$$

On the body, the general boundary condition is

$$\theta_0 \left.\frac{\partial W}{\partial \eta_n}\right|_{k,1} + \theta_1 W_{k,1} + \theta_2 = 0$$

In finite difference form, this can be written as

$$\theta_0 \left[\frac{W_{k,2} - W_{k,1}}{\Delta \eta_n}\right] + \theta_1 W_{k,1} + \theta_2 = 0$$

or

$$W_{k,1} = \tilde{E}_1 W_{k,2} + \tilde{F}_1 \tag{8.3.11}$$

where

$$\tilde{E}_1 = \frac{\theta_0}{\theta_0 - \Delta \eta_n \theta_1} \qquad \text{and} \qquad \tilde{F}_1 = \frac{\theta_2 \eta_n}{\theta_0 - \Delta \eta_n \theta_1}$$

If the wall condition is specified,

$$W_{k,1} = W_w \tag{8.3.12}$$

so that

$$\tilde{E}_1 = 0 \qquad\qquad \tilde{F}_1 = W_w \tag{8.3.13}$$

If the wall gradient is specified,

$$\left.\frac{\partial W}{\partial \eta_n}\right|_{k,1} = \left.\frac{\partial W}{\partial \eta_n}\right|_w \tag{8.3.14}$$

and

$$\tilde{E}_1 = 1 \qquad\qquad \tilde{F}_1 = \left.\frac{\partial W}{\partial \eta_n}\right|_w \eta_n \tag{8.3.15}$$

In the special case of

$$\left.\frac{\partial W}{\partial \eta_n}\right|_{k,1} = 0 \tag{8.3.16}$$

this gives

$$\tilde{E}_1 = 1 \qquad\qquad \tilde{F}_1 = 0 \tag{8.3.17}$$

Implementation of the algorithm involves first evaluating $\tilde{E}_j$ and $\tilde{F}_j$ from $j = 2$ up to $j = j_s - 1$, and then solving Eq. (8.3.9) for $W_{k,j}$ from $j = j_s - 1$ down to $j = 1$.

For a given station and shock shape, the governing equations are solved in the following order. The streamwise momentum and energy equations are solved for $\bar{u}$ and h, respectively. The equation of state gives ρ. From the continuity equation, the shock layer thickness is determined. The pressure distribution is found directly from Maslen's expression. The normal velocity distribution is extracted from the continuity equation after the standoff distance has been determined.

8.4   Advancing the Solution

The previous sections in this chapter explain the solution procedure of the governing equations for a known shock shape at a given station. More precisely, holding the shock geometry (and the resulting jump conditions) constant, the fluid equations may be satisfied in an iterative fashion. From this solution, a calculated shock layer thickness for the current station is determined. This value is compared to the geometric shock standoff distance, with the difference between the two dictating the adjustment of the shock shape. After convergence of the shock shape for a given station, the solution is advanced to the next station, using the current profiles to initialize the new station. The discussion now turns to how the shock shape is actually determined.

Maslen's original method [18, 21] is an inverse technique. That is, a shock shape is prescribed and the resulting calculated body shape is compared with the desired body shape. The shock shape is then adjusted in an iterative fashion until the desired body shape is obtained. Riley and DeJarnette [67, 68, 69] automate this process for blunt bodies where separate approaches must be used for the nose region and the remainder of the flowfield.

The current approach parallels that of Ref. [29] in that the shock shape is generated as part of the solution, rather than being an input required of the user. However, the approach of Riley and DeJarnette serves as a model for the technique employed here, since it provides a smooth shock shape within relatively few iterations. In the subsonic region, a conic equation is used to describe the shock radius as a function of axial position. The marching procedure again utilizes a cubic equation with one parameter to be determined iteratively. The details of the iterative procedures used to determine the shock shapes for the subsonic and marching regions are presented in Sections 8.4.1 and 8.4.2, respectively.

8.4.1   Subsonic-Transonic Region

Since the subsonic-transonic region is elliptic in nature, this portion of the flowfield must be solved in a global fashion. As discussed in Section 7.2.1, the shock shape for

the subsonic-transonic region is described by

$$r_s^2 = 2C_s z_s - b_s z_s^2 \qquad (8.4.1)$$

where C_s is the value of the shock radius of curvature on the stagnation line and b_s determines the conic's character. For a given body shape, three parameters (b_s, C_s, and n_{b_0}) constrain the geometry of the shock-body tandem (and hence, the shock layer). The value of n_{b_0} is the shock layer thickness (standoff distance) calculated from the stagnation line solution (see Section 7.3.1).

The quantities b_s and C_s are determined through a quasi-Newton iterative procedure. With each variation of these two parameters, the flowfield is solved for the entire subsonic region. The fluid equations are solved at eleven discrete stations beginning on the stagnation line (giving n_{b_0}). The values for the calculated shock layer thickness at two stations near the end of the subsonic region are compared with the values dictated by the geometry (see Section 7.3). Shock iterations are continued until the calculated values of n_b at these two stations match the geometric values. Typically only four to six iterations are required to converge the shock shape.

8.4.2 Supersonic Region

Since the supersonic region is hyperbolic-parabolic in nature, a marching procedure is employed. Recall from Section 7.2.2, the shock shape for the region between the previous and current stations is described by a truncated Taylor's series (see Appendix L for details):

$$r_s = r_{s_{k-1}} + \Delta z_s \left.\frac{dr_s}{dz_s}\right|_{k-1} + \frac{\Delta z_s^2}{6} \left[2 \left.\frac{d^2 r_s}{dz_s^2}\right|_{k-1} + \left.\frac{d^2 r_s}{dz_s^2}\right|_k \right] \qquad (8.4.2)$$

where the shock derivative is given by

$$\frac{dr_s}{dz_s} = \left.\frac{dr_s}{dz_s}\right|_{k-1} + \frac{\Delta z_s}{2} \left[\left.\frac{d^2 r_s}{dz_s^2}\right|_{k-1} + \left.\frac{d^2 r_s}{dz_s^2}\right|_k \right] \qquad (8.4.3)$$

and

$$\Delta z_s = z_s - z_{s_{k-1}}$$

Written in this form, the only unknown is the second derivative of r_s with respect to z_s (which is proportional to the shock curvature) at the current station. This parameter is determined through the iterative process described in the next paragraph. Note that Ref. [29] iterates about the *derivative* of the shock curvature, which is a more sensitive procedure.

The position, slope, and curvature of the shock at the previous station are known. Thus, the curvature at the current station is the only unknown in Eqs. 8.4.2 and 8.4.3. As a first guess, the $d^2 r_s/dz_s^2$ term at station k is extrapolated from its values at the

previous two stations. With the shock geometry (and corresponding jump conditions) constrained, the fluid equations are solved. Then the calculated and geometric values of n_b are compared to determine an error (δ_{err}). After perturbing the guess for d^2r_s/dz_s^2 (which alters the shock position and slope), the governing equations are solved to determine a new value for δ_{err}. Now the second derivative at station k may be updated using the secant method:

$$\frac{d^2r_s}{dz_s^2} = \left.\frac{d^2r_s}{dz_s^2}\right|_p - \frac{\delta_{err}}{\delta_{err} - \delta_{err}|_p}\left\{\frac{d^2r_s}{dz_s^2} - \left.\frac{d^2r_s}{dz_s^2}\right|_p\right\} \qquad (8.4.4)$$

The subscript p denotes a value from the previous iteration. Through successive applications of the secant method (accompanied by a solution to the fluid equations), $\delta_{err} \to 0$, with shock shape convergence typically obtained in three to four iterations per station.

9   Results and Discussion

Results generated with the present algorithm are given in this chapter, which is divided into three sections: perfect gas, equilibrium, and nonequilibrium solutions. In an effort to evaluate the accuracy of this new approach, the comparisons outlined below are made. Heating rates are shown alongside experimental or flight data, where available. In addition, the perfect gas solutions are compared with the results of the VSL [9] and Grantz [29] approaches. Comparisons with the VSL solver of Ref. [9] are also made for equilibrium flows. The nonequilibrium results are compared with those of Ref. [14]. Specific areas to be addressed are:

1) surface properties, including examination of the stagnation region;
2) shock shapes;
3) shock layer profiles of dependent variables;
4) run times.

The algorithms employed here are fully-implicit (see Section 8.3). For the perfect gas and equilibrium results, 101 points across the layer are used by each of the methods (see Section 7.4). The nonequilibrium solutions are based on 51 points across the layer for the VSL and present method. The results are plotted in nondimensional form (see Appendix A), with the dependent variable on a logarithmic scale in most cases. Note that in this chapter, the superscript * is omitted on the dimensional quantities.

9.1   Perfect Gas

Two cases are presented in this section. The first case is a $5°$ sphere-cone with a length of approximately 140 ft. Two solutions with different nose radii are calculated in Ref. [70] in a study of bluntness effects. Comparisons with those results are made here. The geometry of the second case is a $15°$ sphere-cone with a length of approximately 20 in. Again the solutions are obtained for two different nose radii, and the results are compared with experimental data [71]. For each case, analysis of the second radius is limited to surface properties in the interest of brevity.

Case 1

For Case 1, Mach 15 flow over a $5°$ sphere-cone is calculated using the VSL [9], Grantz [29], and present approaches. The freestream conditions are $p_\infty = 0.018919$ psi and $T_\infty = 478°R$, with a wall temperature of $T_w = 2259.69°R$. Fully-laminar solutions are calculated, as well as solutions where the flow transitions to turbulence. The beginning of transition is an input for all three approaches. The VSL heating results are from Ref. [70].

First, the solution for $R_{nose} = 1.5$ in is calculated for a body length of $s_{b_{end}} = 1125$. The transition point is specified to be $s_b = 192$. Figure 9.1 shows the body shape along with the shock shapes (fully-laminar) calculated with the three methods. The approximate (Grantz and present) techniques agree with the VSL results as the sharp cone solution is approached. However, from the close-up given in Figure 9.2, note that the two approximate approaches yield a thinner shock layer than the VSL algorithm in the pressure overexpansion region.

In Figure 9.3, the computed heating results from the three solutions are presented for both laminar and turbulent flows. The laminar results of the VSL and present method are in excellent agreement overall, while those of Ref. [29] are at an approximately ten to fifteen percent higher level. Downstream of the nose region (for s_b between approximately 10 and 100), both approximate techniques over-predict the VSL heating results. It is believed that Maslen's pressure relation is the source of this deviation, as will be discussed in the next paragraph. The turbulent results of the VSL and present method are in excellent agreement overall, with those of Ref. [29] approximately twenty percent higher. The transition heating results (see Figure 9.3) of Grantz [29] reflect an error in the application of the transition model.

Figure 9.4 shows the body pressure distributions from the three methods for the fully-laminar solution. The computed pressure distributions are in excellent agreement (within five percent) except in the pressure overexpansion/recompression region. In this region, the shock and body angles are quite different (see Figure 9.2) for slender cones, violating one of Maslen's assumptions. Apparently, this poor pressure prediction feeds back into the shock shape which is generated as part of the solution, to give the shock shape deviation mentioned earlier. As a result, the VSL shock layer
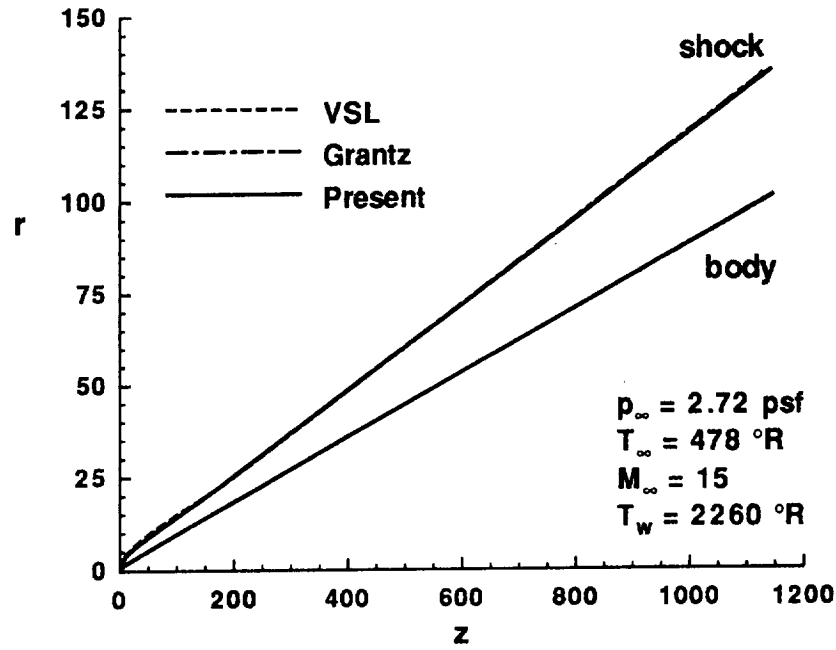
Figure 9.1. Shock shape comparison for $5°$ sphere-cone, $R_{nose} = 1.5$ *in.*
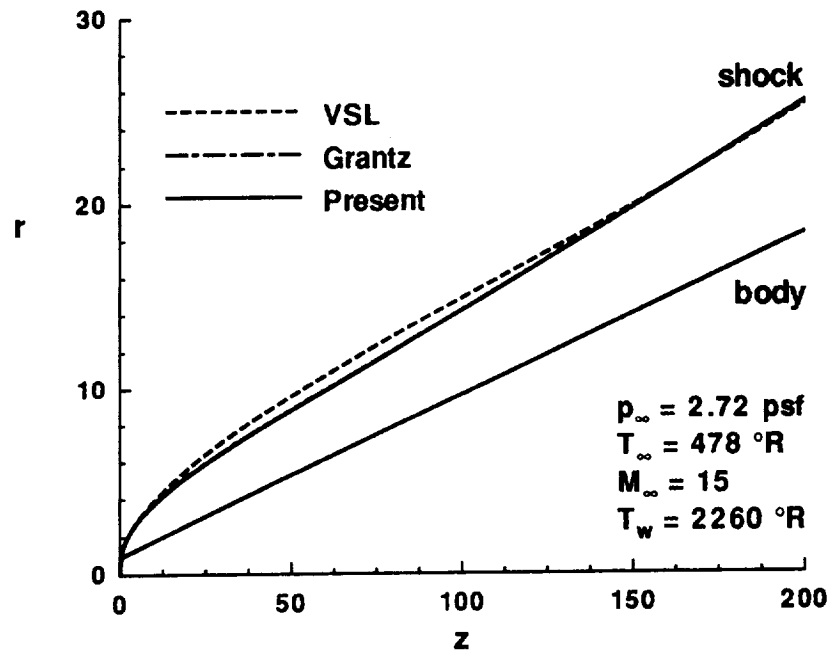

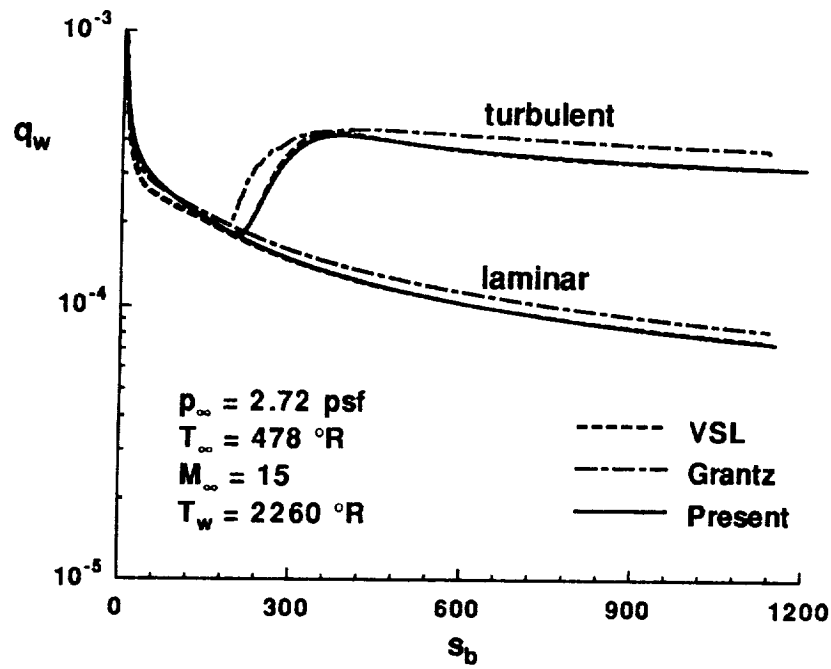**Figure 9.2.** Shock shape comparison for $5°$ sphere-cone, $R_{nose} = 1.5$ *in* (overexpansion region).

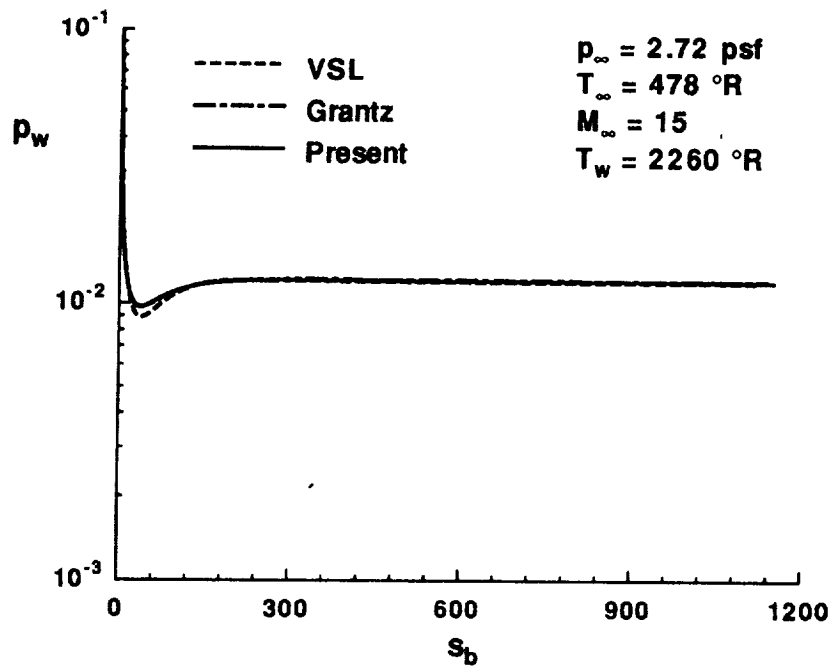**Figure 9.3.** Heat transfer comparison for 5° sphere-cone, $R_{nose} = 1.5$ *in.*

Figure 9.4. Body pressure comparison for 5° sphere-cone, $R_{nose} = 1.5$ *in.*

thickness (and also the thickness gradient) in this region differs from the values given by the approximate methods. Since the thickness gradient plays a prominent role in the governing equations, this deviation is reflected in the shock layer profiles, as well as the surface properties. The effect of the differences in the overexpansion region diminishes further downstream, as can be seen in the figures. A similar phenomena has been seen in the inviscid technique of Riley and DeJarnette [68], which also employs Maslen's pressure relation.

Figures 9.5 and 9.6 provide more detailed information on the stagnation region results. As the stagnation line is approached ($s_b \to 0$), $dq_w/ds_b \to 0$ and $dp_w/ds_b \to 0$. Note that the heating results from the current method approach the stagnation line more smoothly than those of either Ref. [29] or the VSL method. This is a direct result of the limiting form of the governing equations used here (see Section 2.4). Note also that the results of Ref. [29] are approximately twenty percent higher than the other two solutions in this region, and do not approach a zero gradient at the stagnation line. In Figure 9.6, the stagnation region pressure distribution is reasonably smooth for all three methods.

Skin friction results are presented in Figures 9.7 and 9.8. The method of Ref. [29] does not compute this parameter, hence it is excluded from this comparison. Both the laminar and turbulent results are in excellent agreement, (generally within five percent). This result is not surprising since Reynolds analogy relates the skin friction to the heat transfer. Therefore, good agreement for the skin friction is expected in those areas where the heat transfer is predicted well. As shown in Figure 9.8, the present method has a smoother distribution in the stagnation region.

Now consider the stagnation line profiles. Figure 9.9 shows the pressure predictions to be within 0.5 percent of one another. In Figure 9.10, note that the normal velocity results of the VSL and present method are virtually identical, while the results of Ref. [29] differ from them slightly. The approximate relation for v used in Ref. [29] is the source of this difference. The tangential velocity is zero on the stagnation line, but a finite non-zero value for its normalized form ($\bar{u} = u/u_s$) is calculated from the limiting form of the streamwise momentum equation (see Section 2.4). Profiles of this normalized velocity are shown in Figure 9.11. The approximate results are in close agreement with each other, while the VSL results are different. This difference may be due to the VSL limiting form of the streamwise momentum equation (see Section 2.4). Figures 9.12 and 9.13 show that the enthalpy and density profiles of the three methods are virtually identical on the stagnation line. The density "mirrors" the accuracy of the other results (since it is calculated from the state equation), so in the remainder of this chapter it will be shown only sparingly.

Pressure profiles near the pressure minimum ($s_b \approx 40$) and at the end of the body ($s_b \approx 1125$) are presented in Figures 9.14 and 9.15, respectively. The approximate results are virtually identical. Agreement with the VSL solution is excellent as the sharp cone limit is reached. Even in the pressure minimum region, where the deviation is largest, the Maslen pressures are generally within ten to fifteen percent of the VSL
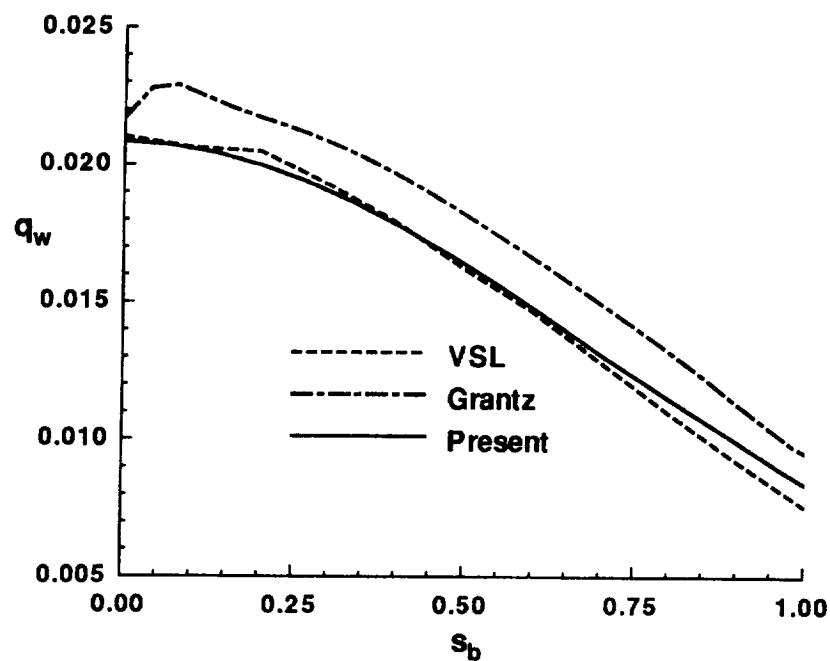
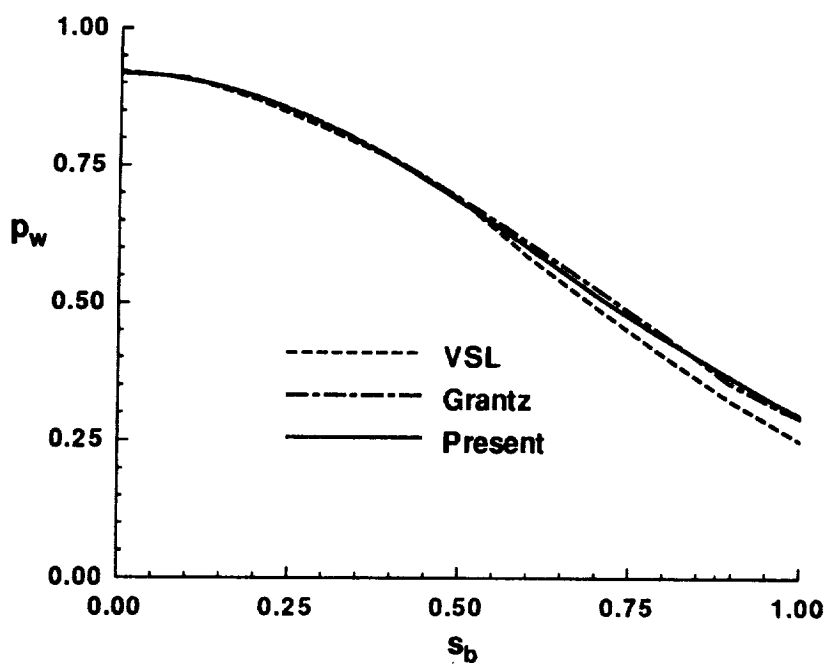**Figure 9.5.** Heat transfer comparison for 5° sphere-cone, $R_{nose} = 1.5$ *in* (stagnation region).

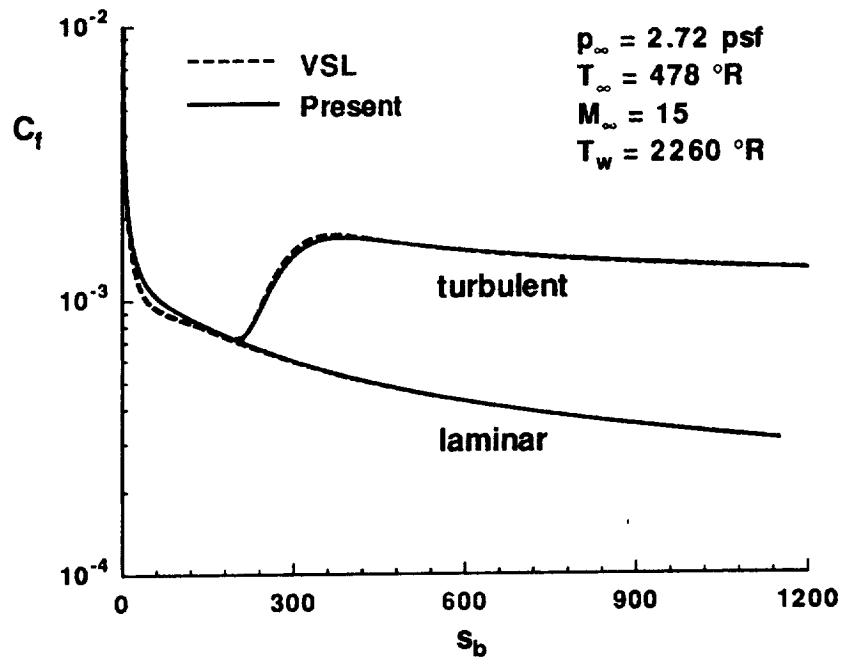**Figure 9.6.** Body pressure comparison for 5° sphere-cone, $R_{nose} = 1.5$ *in* (stagnation region).

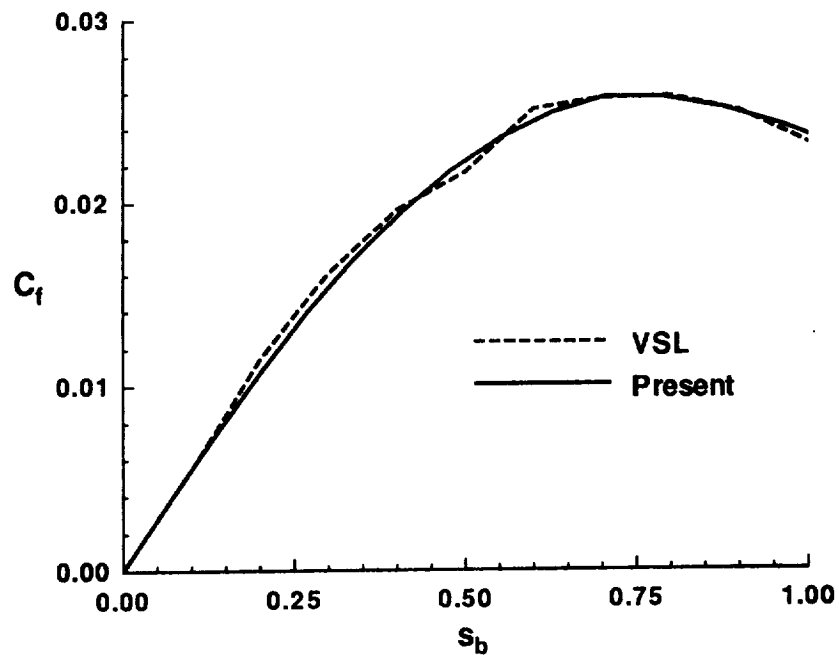**Figure 9.7.** Skin friction comparison for 5° sphere-cone, $R_{nose} = 1.5$ in.

Figure 9.8. Skin friction comparison for 5° sphere-cone, $R_{nose} = 1.5$ in (stagnation region).
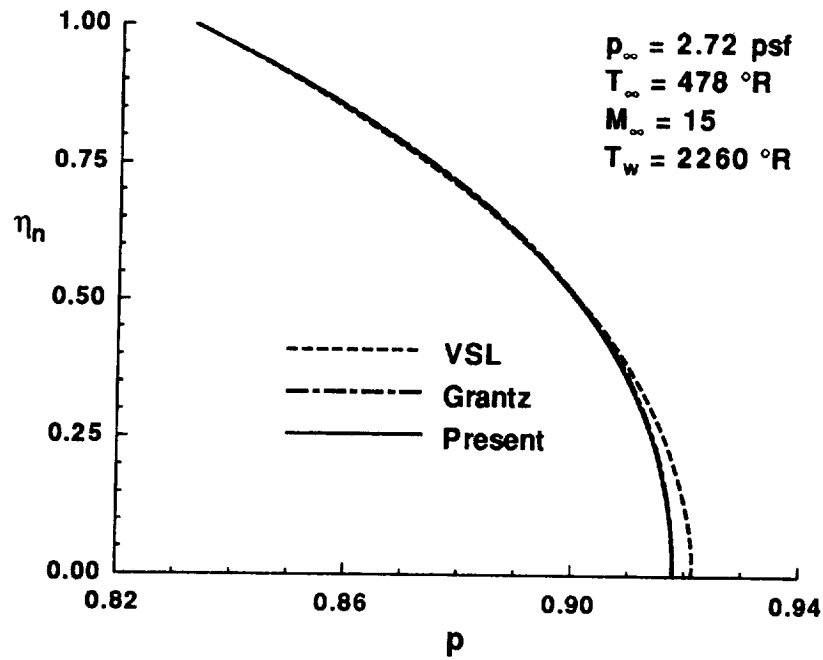
Figure 9.9. Pressure profile comparison for 5° sphere-cone,
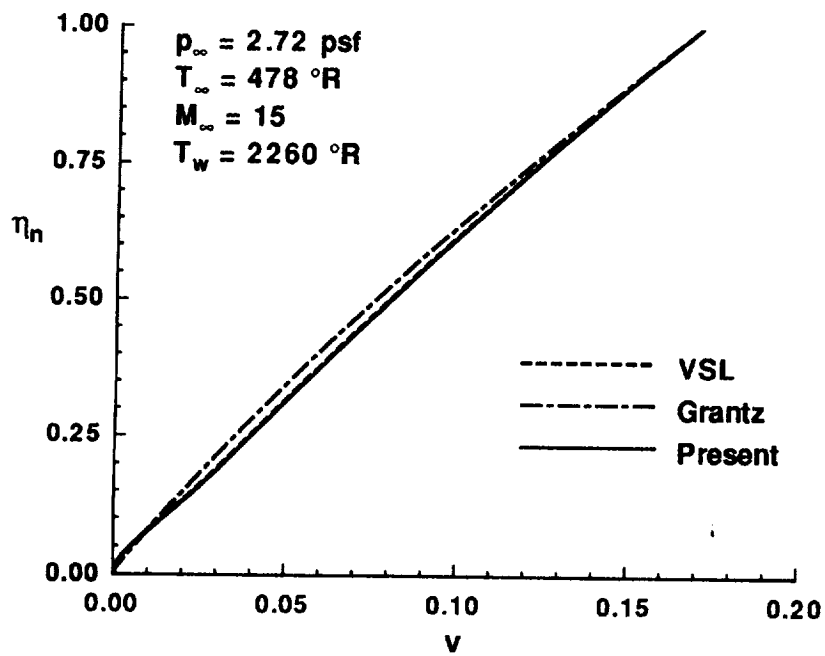$R_{nose} = 1.5$ in (stagnation line).

Figure 9.10. Normal velocity profile comparison for 5° sphere-cone,
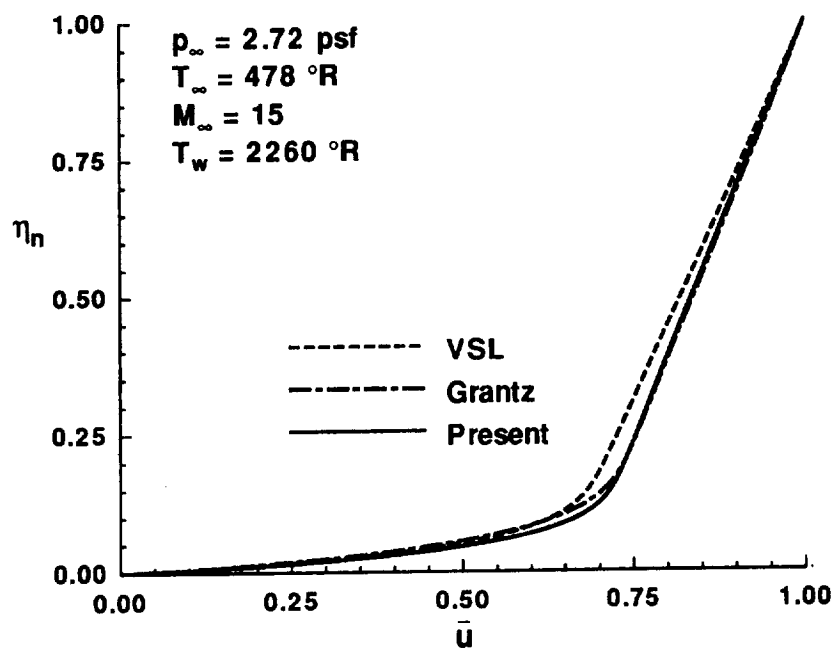$R_{nose} = 1.5$ in (stagnation line).

Figure 9.11. Tangential velocity profile comparison for $5°$ sphere-cone, $R_{nose} = 1.5$ *in* (stagnation line).
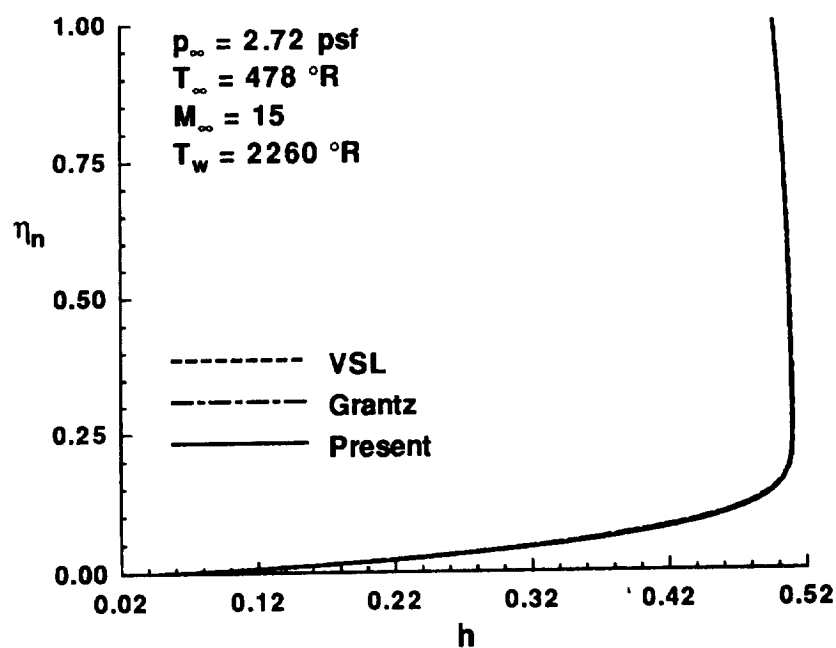

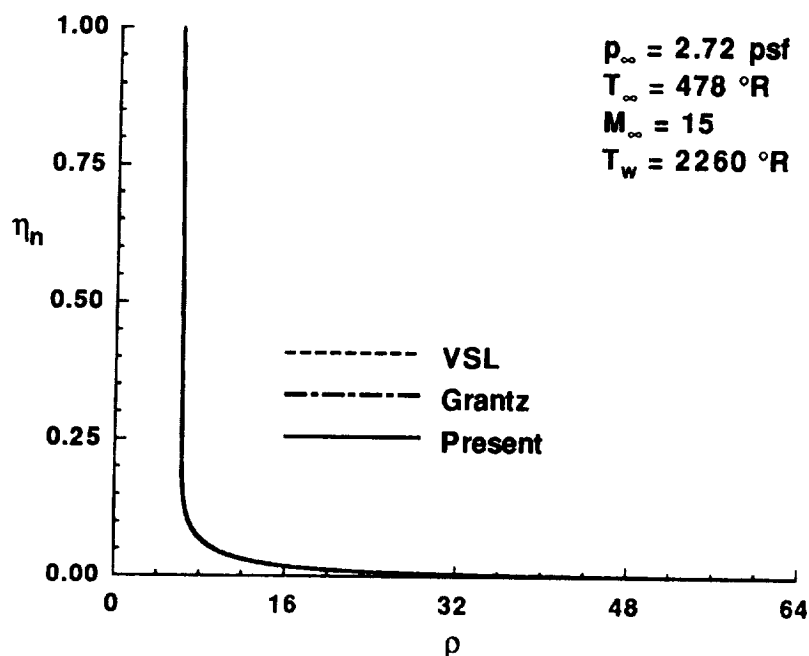**Figure 9.12.** Enthalpy profile comparison for $5°$ sphere-cone, $R_{nose} = 1.5$ *in* (stagnation line).

Figure 9.13. Density profile comparison for 5° sphere-cone,
$R_{nose} = 1.5$ *in* (stagnation line).

results.

For purposes of comparison, the velocities calculated in the two approximate methods (solved in a shock-normal system) are resolved into body-normal components. The velocity component normal to the body is shown in Figures 9.16 and 9.17. The limitations of the approximate expression for v which is used in the method of Ref. [29] are readily apparent. This component is small relative to $\bar{u}$ and h except in the near-wall region. As a result, its poor prediction has minimal effect on the overall shock layer solution outside of the boundary layer. In the pressure minimum region, the other two techniques agree well near the wall. The last station exhibits excellent agreement between the VSL and present approaches.

The body-tangential velocities are shown in Figures 9.18 and 9.19, and the three approaches are in good agreement. The enthalpy profiles of the present and VSL approaches, shown in Figure 9.20 and 9.21, also agree well with one another. At the end station, the results of Ref. [29] differ in the boundary layer. This difference is reflected in the heating rates, and is due to the inaccuracies of the approximate relation for the normal component of velocity. Also at the end station, note the severe oscillations around the boundary-layer edge which are present in the results of Grantz [29]. Figure 9.19 shows wiggles in the tangential velocity profiles as well. This is the result of not having enough points in this region. A grid adjustment is in order, but since the Ref. [29] normal spacing is based on the stream function rather
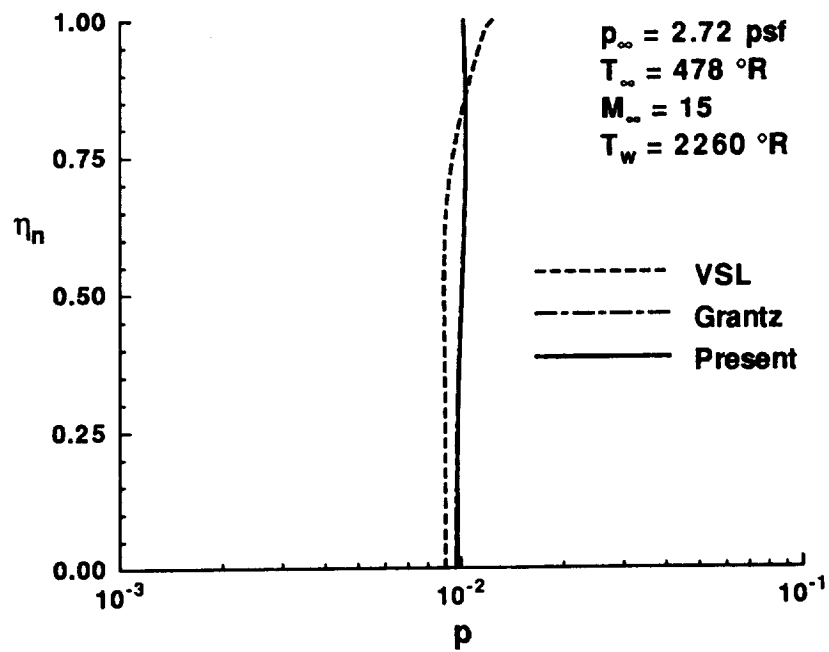
Figure 9.14. Pressure profile comparison for 5° sphere-cone,
$R_{nose} = 1.5$ in $(s_b \approx 40)$.

Figure 9.15. Pressure profile comparison for 5° sphere-cone,
$R_{nose} = 1.5$ in $(s_b \approx 1125)$.

Figure 9.16. Normal velocity profile comparison for $5°$ sphere-cone,
$R_{nose} = 1.5$ in ($s_b \approx 40$).

Figure 9.17. Normal velocity profile comparison for $5°$ sphere-cone,
$R_{nose} = 1.5$ in ($s_b \approx 1125$).

Figure 9.18. Tangential velocity profile comparison for $5°$ sphere-cone, $R_{nose} = 1.5$ *in* $(s_b \approx 40)$.

Figure 9.19. Tangential velocity profile comparison for $5°$ sphere-cone, $R_{nose} = 1.5$ *in* $(s_b \approx 1125)$.
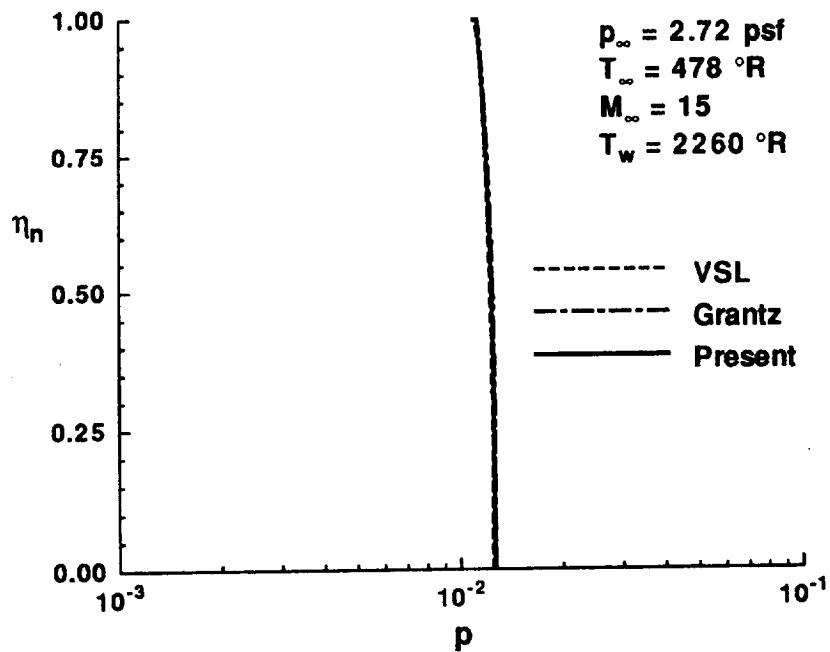
Figure 9.20. Enthalpy profile comparison for $5°$ sphere-cone, $R_{nose} = 1.5$ in $(s_b \approx 40)$.

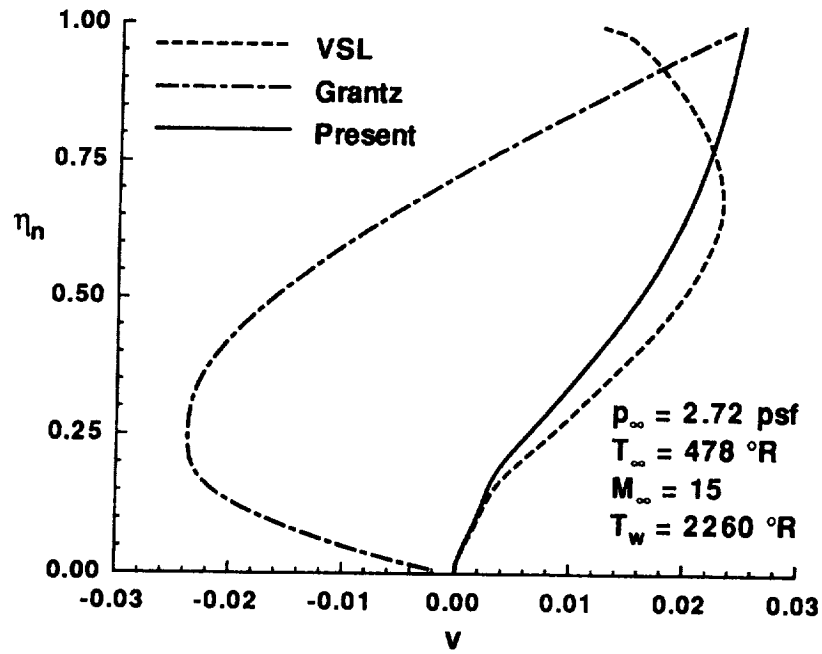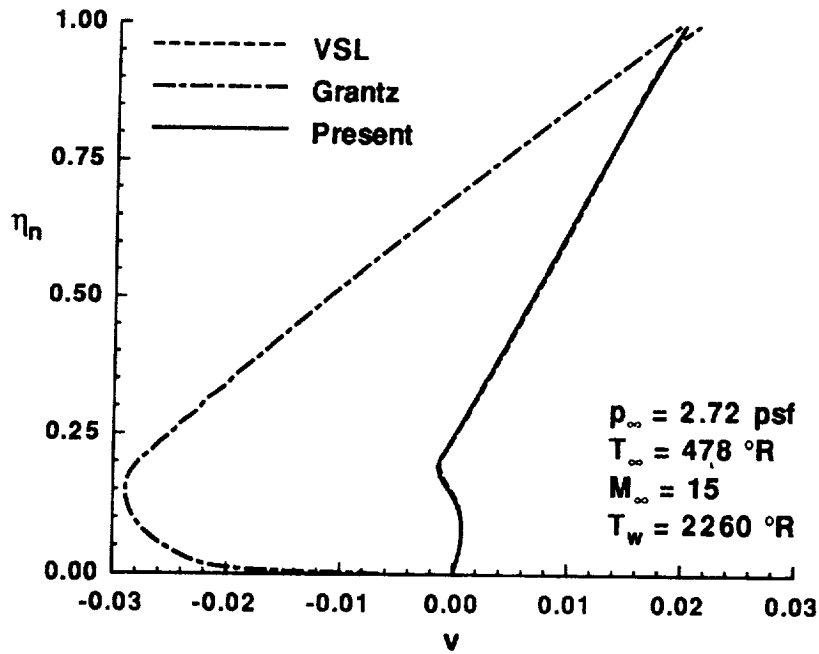**Figure 9.21.** Enthalpy profile comparison for $5°$ sphere-cone, $R_{nose} = 1.5$ in $(s_b \approx 1125)$.
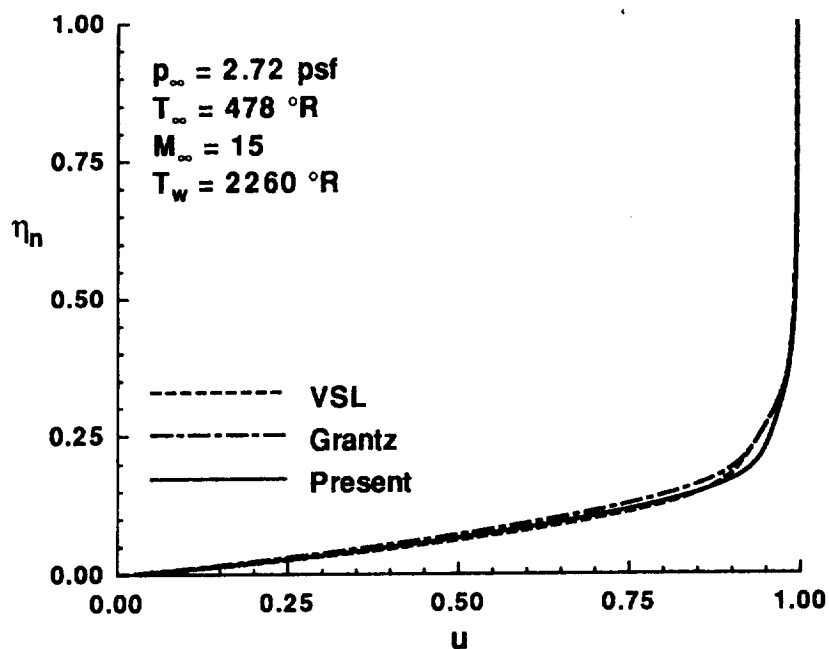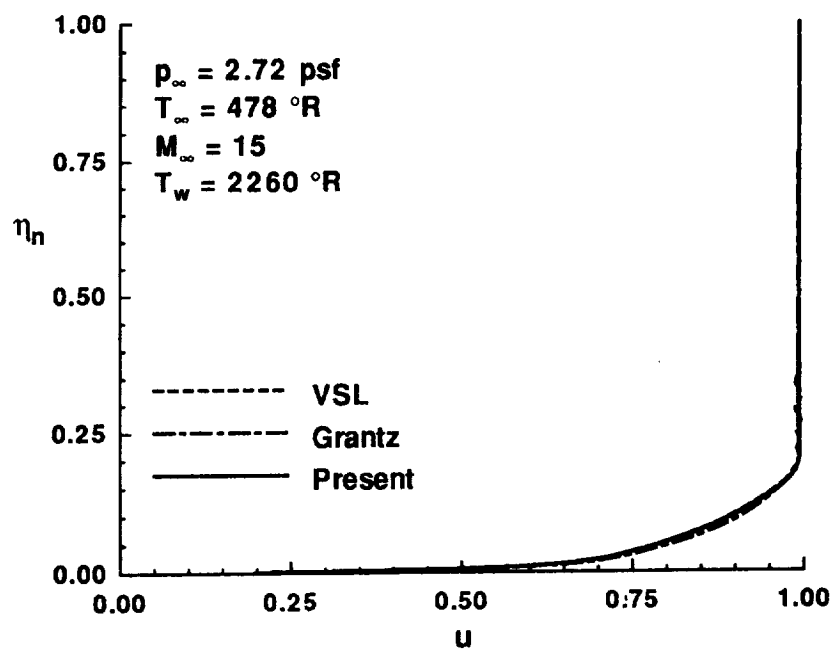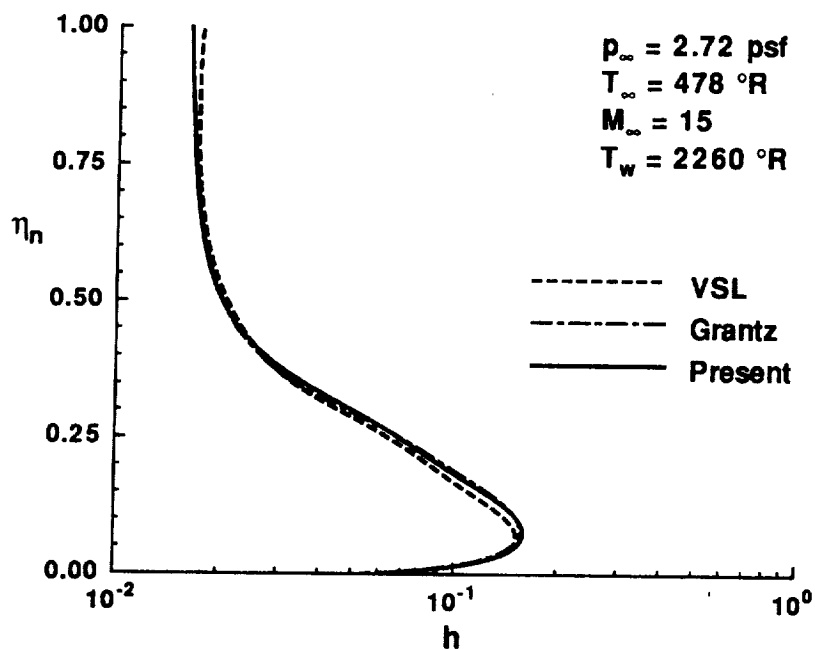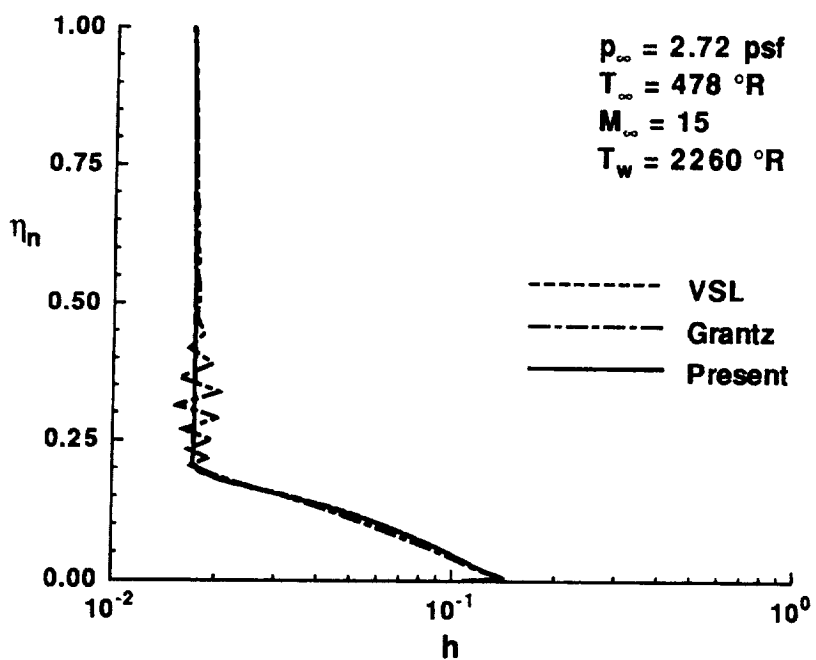
Table 9.1. Run-times[a] for 5° cone, $R_{nose} = 1.5$ in.

	VSL	Ref. [29]	Present
stations	643	333	209
CPU time	4232	867	408
grid pts/sec	15	39	52
shock iterations	3.0	6.5	2.3
grid pts/sec/shock	46	252	121

a – Sun Sparcstation 1+

than a physical distance, an adequate distribution is difficult to determine. These wiggles, which are documented in Ref. [27], were repeatedly observed early on in this research and were the motivation for switching from η- to η_n-spacing, which *is* based on distance across the layer.

Since the nature of this research is to develop an approach for use in preliminary design, where computational speed is an important consideration, some comparisons in run time are presented. Table 9.1 shows the overall run times required to generate the turbulent solution for the 5° sphere-cone. The value shown for the VSL results is the total time required for three shock iterations. However, the CPU requirements to generate the initial and second shock shapes are not included, so this figure is a low estimate for the VSL method. It can be seen that the current algorithm yields a dramatic decrease in total CPU requirements over both the VSL and Ref. [29] techniques. Since varying numbers of streamwise stations are used by each of these approaches, the average number of grid points solved per second is also presented. As shown, three global iterations of the shock shape are required for the VSL solution. The approximate methods iteratively determine the shock shape as the solution is advanced from one station to the next. In this case, for a given station, the method of Grantz [29] requires an average of 6.5 iterations to converge the shock shape, while the present technique averages 2.3 iterations. The last entry in the table takes into account the number of shock shapes calculated, and gives the processing capabilities of each approach for a given shock shape. This illustrates that solving the approximate VSL equations of the present method is inherently 2.5 times as fast as solving the full VSL equations. The method of Ref. [29] is able to process many more grid points/sec/shock shape than the current approach and this can be attributed to its more approximate governing equations.

The solution with a nose radius of $R_{nose} = 9$ *in* and a body length of $s_{b_{end}} = 180$ will now be discussed. The transition point is an input whose value is $s_b = 72$. Because of this larger nose radius, bluntness effects are present for the length of the body. In the interest of brevity, the comparisons are limited to surface properties. The results for this body are similar to the results for the first 200 nose radii of
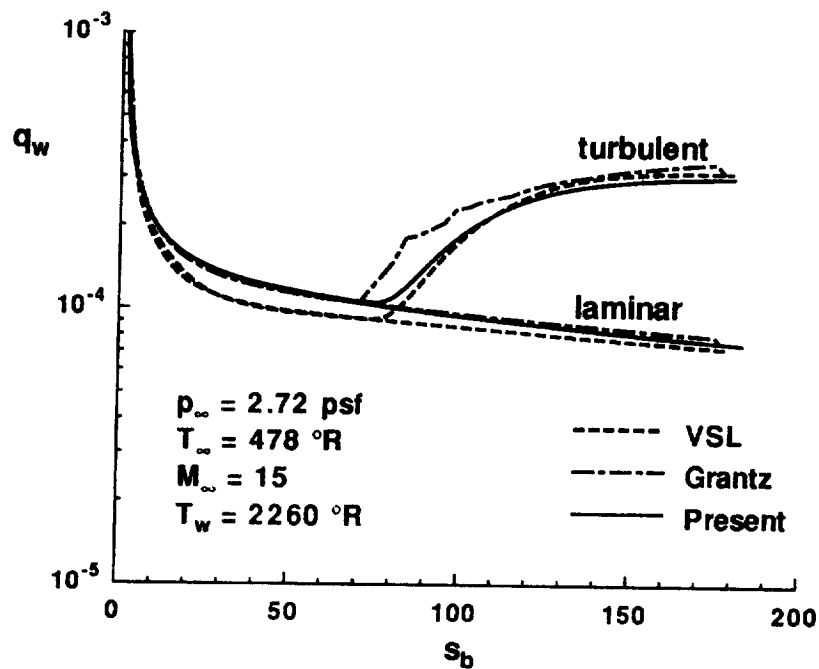
Figure 9.22. Heat transfer comparison for 5° sphere-cone, $R_{nose} = 9$ $in.$

the first body. Figures 9.22 through 9.24 show that the heating rates, laminar body pressures, and skin friction distributions follow the same trends cited above. That is, the results of the approximate approaches are in generally good agreement with the VSL solution. Likewise, the shock-layer profiles (not shown) follow patterns similar to those of the $R_{nose} = 1.5$ in solutions.
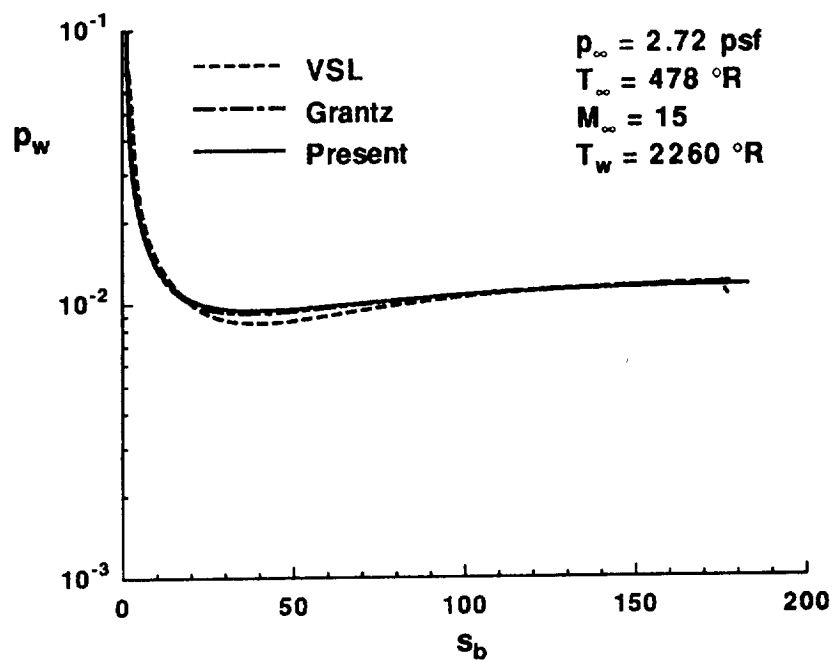
Figure 9.23. Body pressure comparison for $5°$ sphere-cone, $R_{nose} = 9$ *in.*
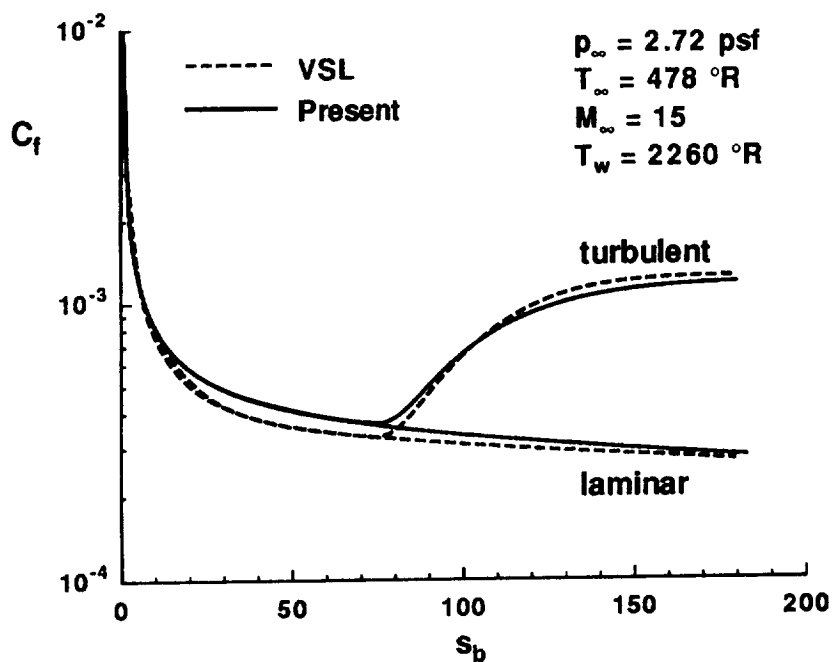
Figure 9.24. Skin friction comparison for $5°$ sphere-cone, $R_{nose} = 9$ *in.*
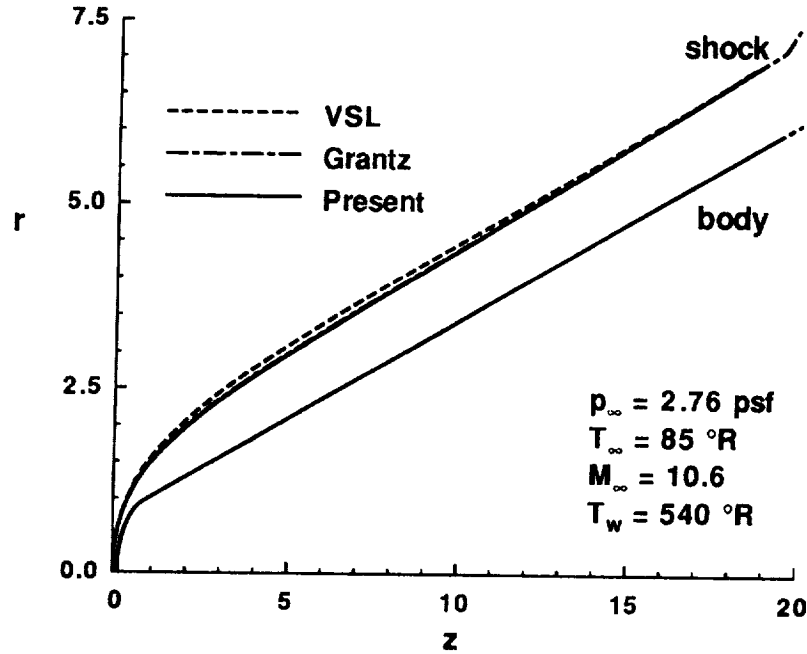
Figure 9.25. Shock shape comparison for 15° sphere-cone, $R_{nose} = 1.1$ *in.*

Case 2

For Case 2, Mach 10.6 flow over a 15° sphere-cone is calculated using the VSL [9], Grantz [29], and present approaches. The freestream conditions are $p_\infty = 0.01915$ *psi* and $T_\infty = 85.2079^o R$, with a wall temperature of $T_w = 540^o R$. Heating rate comparisons are made with Cleary's experimental data [71].

First, the solution for $R_{nose} = 1.1$ *in* is calculated for a body length of $s_{b_{end}} = 20$. Figure 9.25 shows the shock shapes from the three methods. As with the 5° cone, the two approximate techniques yield a thinner shock layer in the pressure overexpansion region than the VSL algorithm. The flare at the end of the shock shape of Ref. [29] reflects an incorrect interpolation for the last computational station.

In Figure 9.26, the heating results from the three solutions are presented and are seen to compare well (generally within fifteen percent) with the experimental data. Figure 9.27 provides more detailed information on the stagnation results. As before, the heating results from the current method approach the stagnation line more smoothly than those of either Ref. [29] or the VSL method.

The computed pressure distributions (Figure 9.28) are in excellent agreement (within five percent) except near the sphere-cone juncture. This deviation is not as large as that seen for the 5° cone, where the difference in shock- and body-angles is greater. As mentioned earlier, Maslen's relation works best when the difference between these two angles is small, so the above improvement is expected. The skin friction comparisons of Figure 9.29 show that the VSL and present method are again in good agreement (generally within fifteen percent).
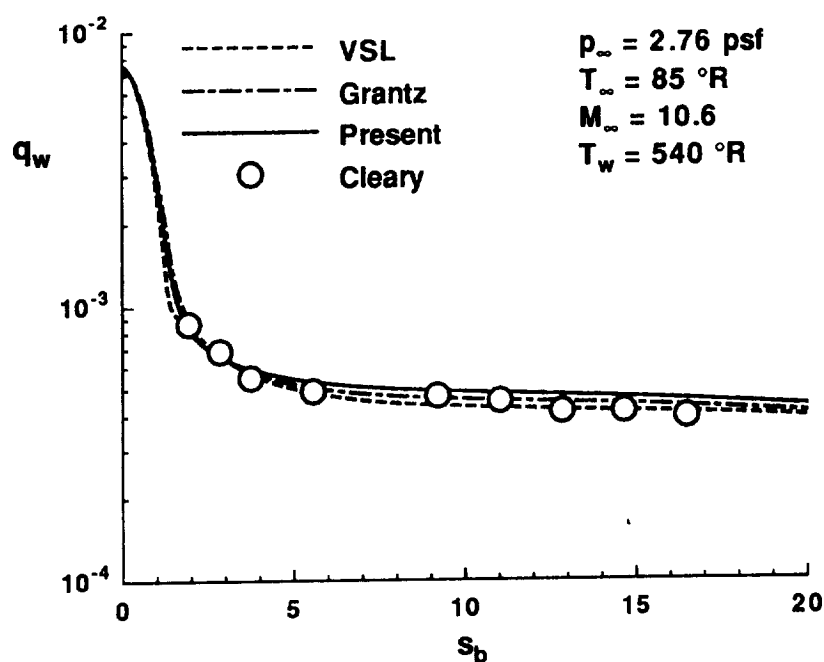
Figure 9.26. Heat transfer comparison for 15° sphere-cone, $R_{nose} = 1.1$ *in.*
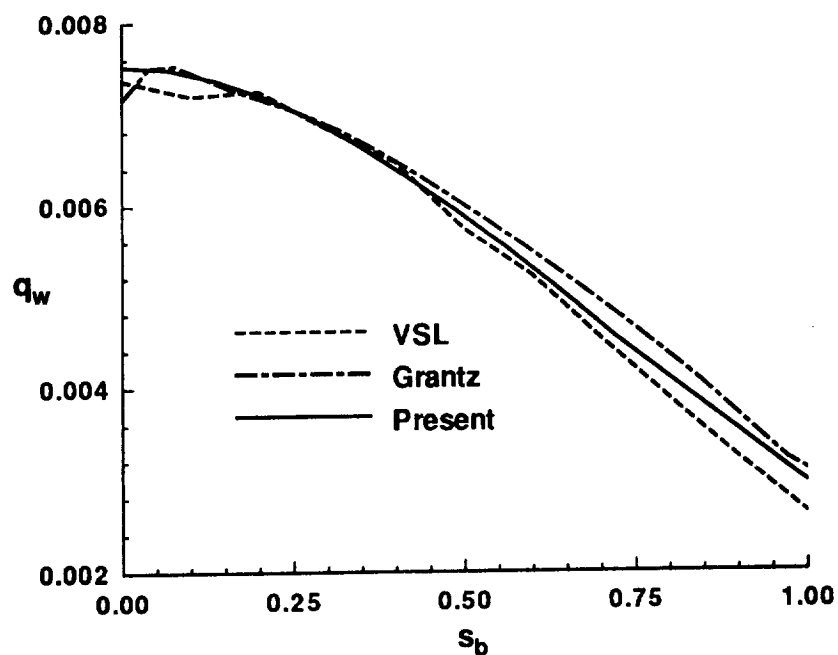

Figure 9.27. Heat transfer comparison for 15° sphere-cone, $R_{nose} = 1.1$ *in* (stagnation region).
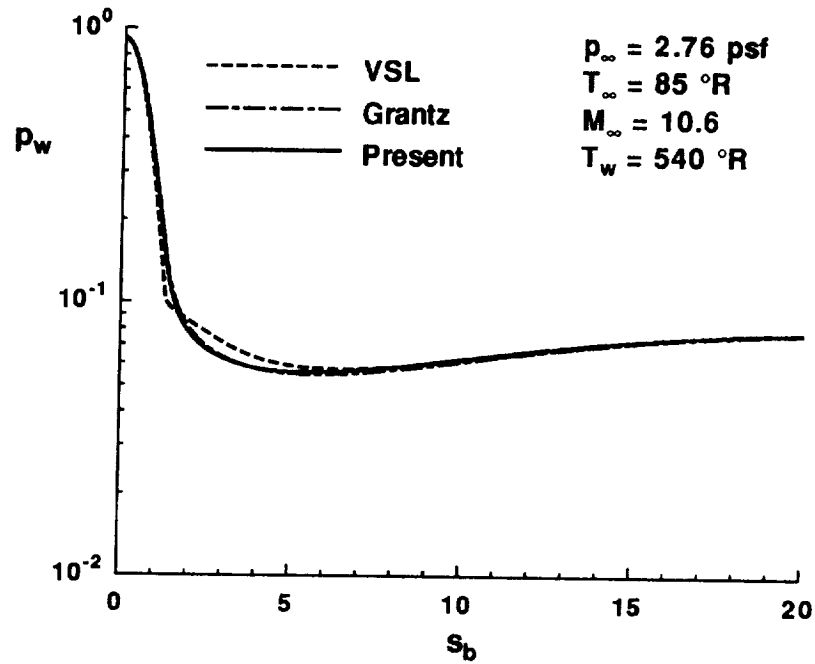
Figure 9.28. Body pressure comparison for $15°$ sphere-cone, $R_{nose} = 1.1$ $in.$
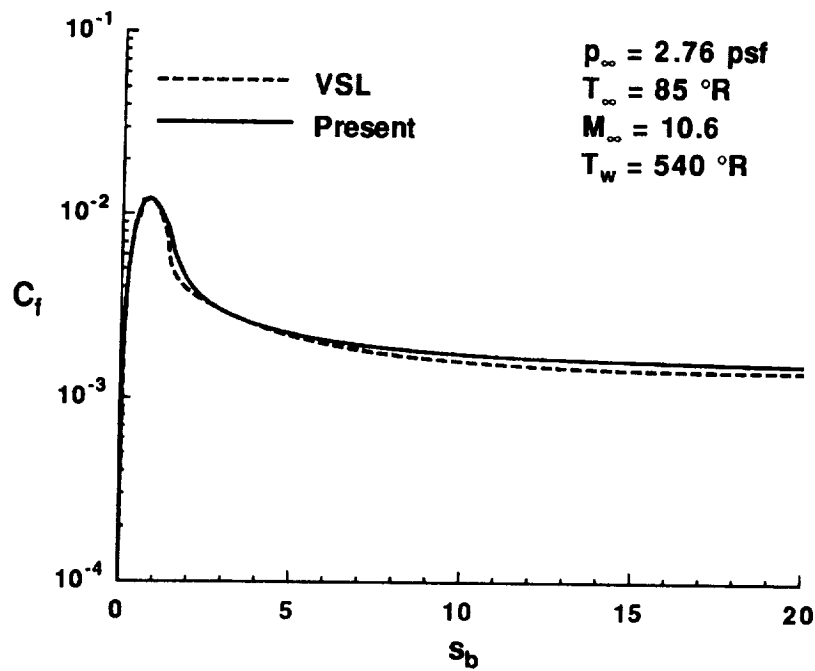

Figure 9.29. Skin friction comparison for $15°$ sphere-cone, $R_{nose} = 1.1$ $in.$

C-2

The stagnation line results are very similar to those given in Figures 9.9 through 9.13, so they are not presented here. As before, profiles near the pressure minimum ($s_b \approx 6$) and at the end of the body ($s_b \approx 20$) are presented. Figures 9.30 and 9.31 show the pressure profiles at these two stations. Figure 9.30 shows the results from the two approximate techniques are similar and generally within five percent of the VSL solution. The agreement is excellent between the approximate results, which are virtually identical, and the VSL solution as the sharp cone limit is reached (Figure 9.31). At the pressure minimum region, the Maslen pressures are generally within five to ten percent of the VSL results.

The velocity components normal to the body are shown in Figures 9.32 and 9.33. The behavior noted for the 5° cone is present here, although the difference between the results of Ref. [29] and the others is not as large as before. The body-tangential velocity (Figures 9.34 and 9.35) and enthalpy profiles (Figure 9.36 and 9.37) also follow the pattern set in the previous case.

The solution with a nose radius of $R_{nose} = 0.375$ *in* and a body length of $s_{b_{end}} = 50$ is now discussed. Because the nose radius is smaller than above, the bluntness effects (which are visible for the length of the body above) are less pronounced at large values of s_b for this case. In the interest of brevity, the comparisons are limited to surface properties. Figures 9.38 through 9.40 show that the heating rates, laminar body pressures, and skin friction distributions follow the same trends cited above: the results of the approximate approaches are in generally good agreement (within five to ten percent) with the VSL solution. Further, the shock-layer profiles (not shown) follow patterns similar to the solutions with $R_{nose} = 1.1$ *in*.

Figure 9.30. Pressure profile comparison for $15°$ sphere-cone,
$R_{nose} = 1.1$ in $(s_b \approx 6.5)$.
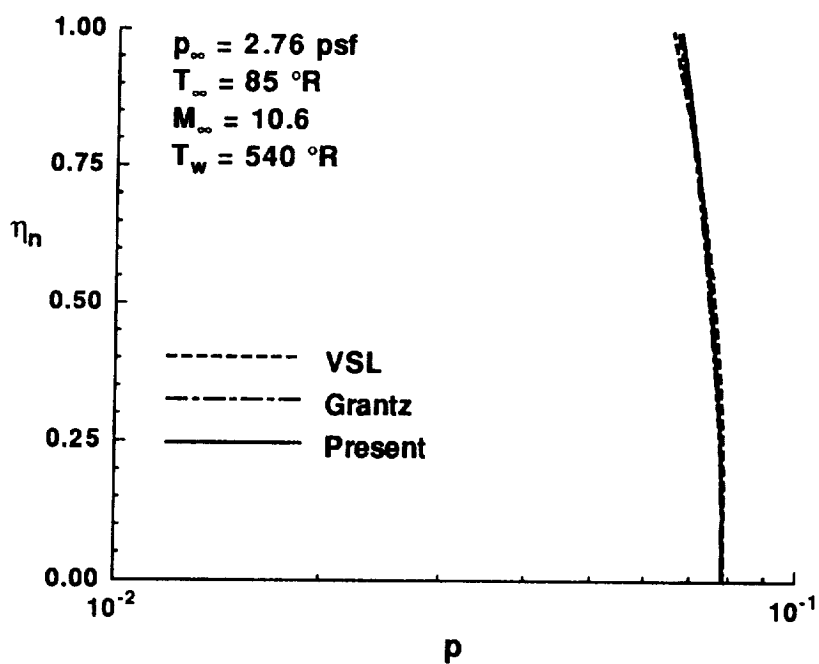
Figure 9.31. Pressure profile comparison for $15°$ sphere-cone,
$R_{nose} = 1.1$ in $(s_b \approx 20)$.

Figure 9.32. Normal velocity profile comparison for 15° sphere-cone, $R_{nose} = 1.1$ in $(s_b \approx 6.5)$.
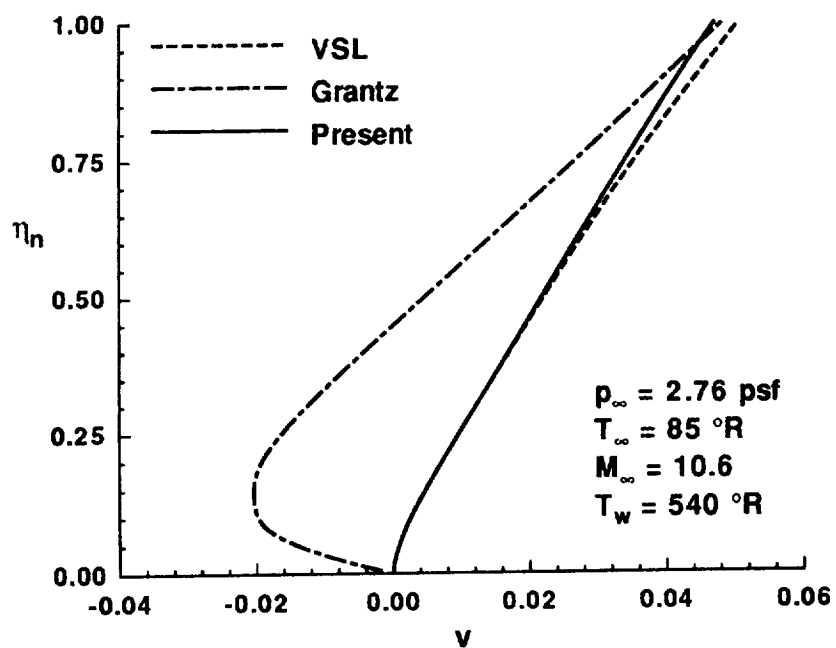
Figure 9.33. Normal velocity profile comparison for 15° sphere-cone, $R_{nose} = 1.1$ in $(s_b \approx 20)$.
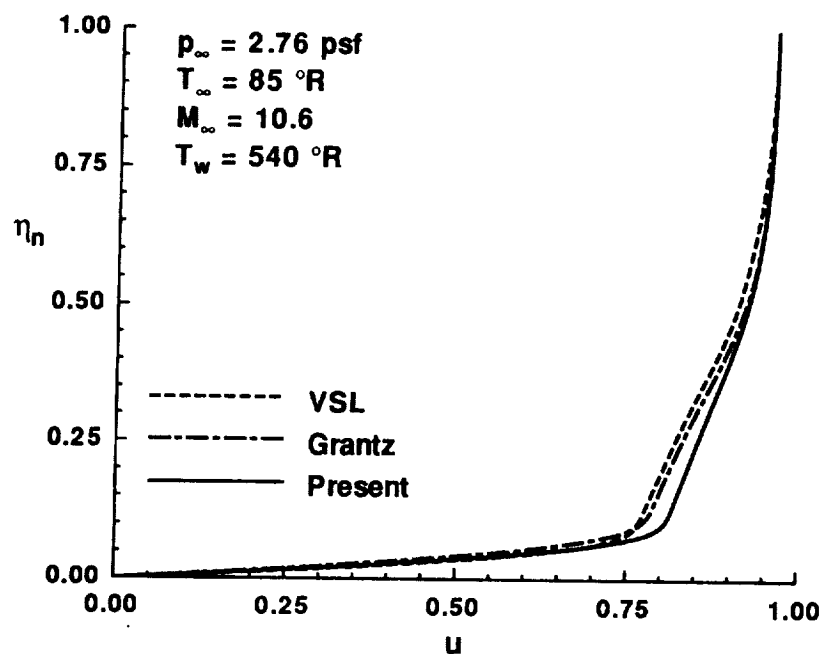
Figure 9.34. Tangential velocity profile comparison for 15° sphere-cone, $R_{nose} = 1.1$ in $(s_b \approx 6.5)$.
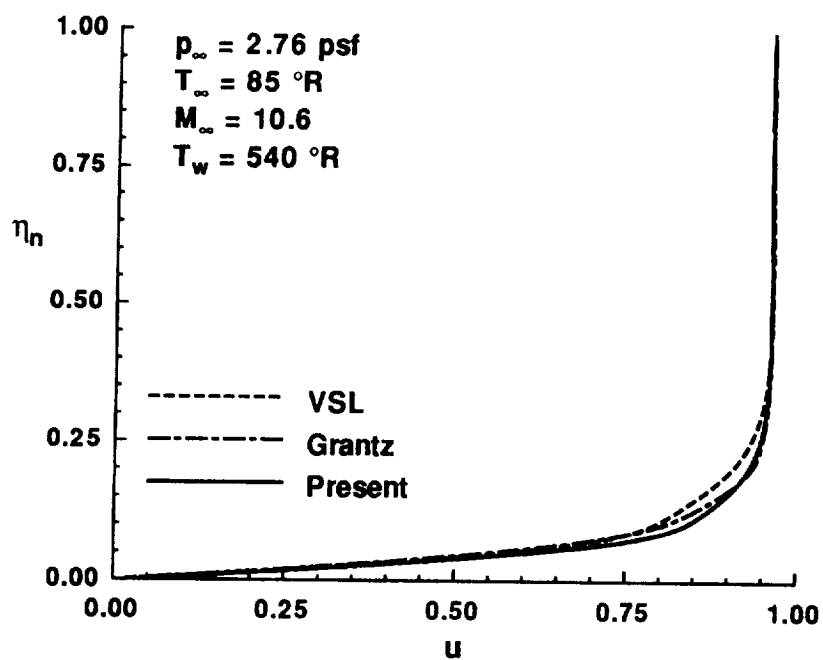
Figure 9.35. Tangential velocity profile comparison for 15° sphere-cone, $R_{nose} = 1.1$ in $(s_b \approx 20)$.
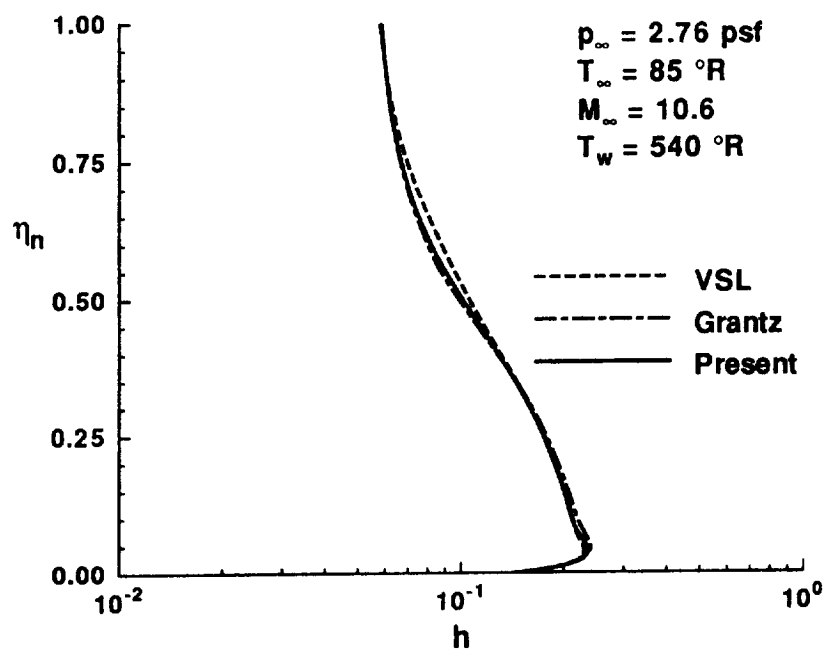
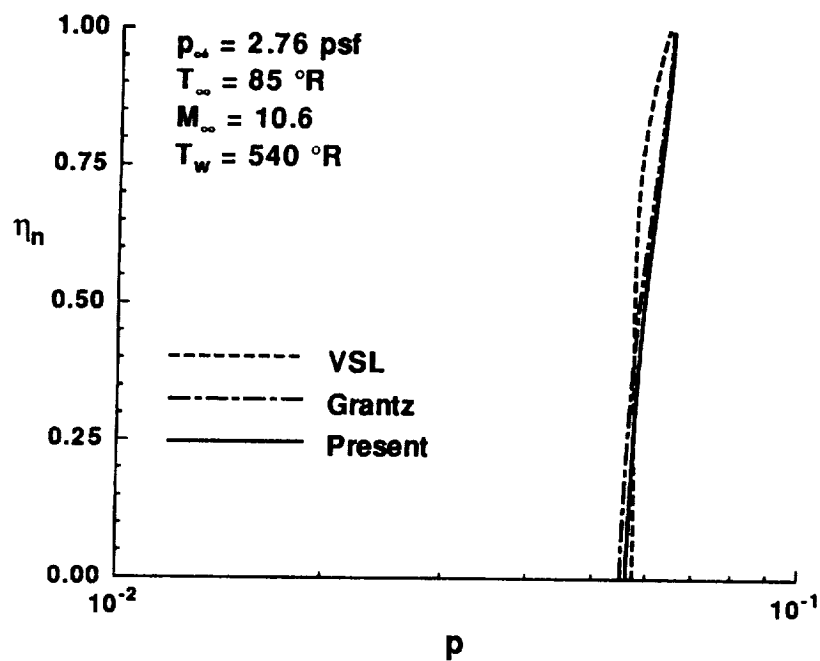**Figure 9.36.** Enthalpy profile comparison for 15° sphere-cone, $R_{nose} = 1.1$ *in* ($s_b \approx 6.5$).

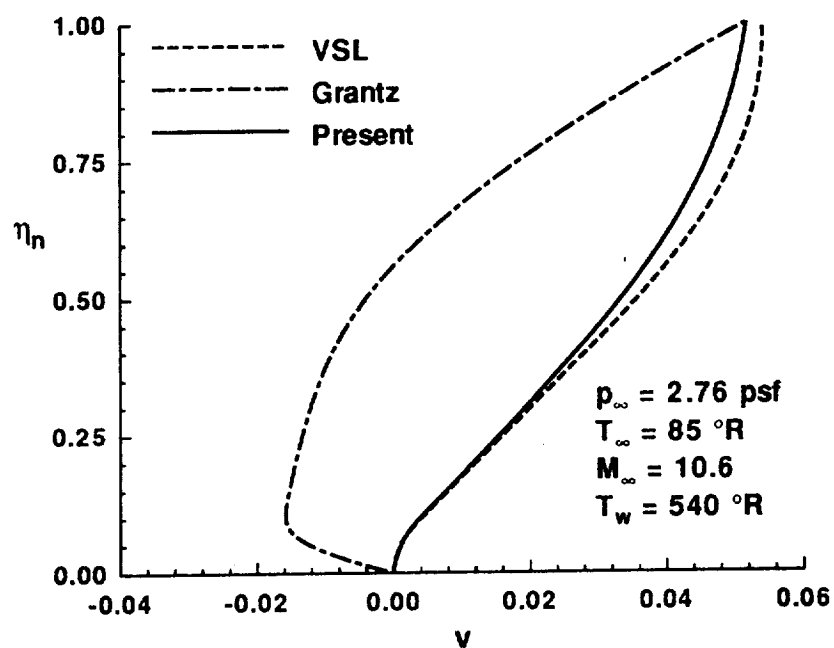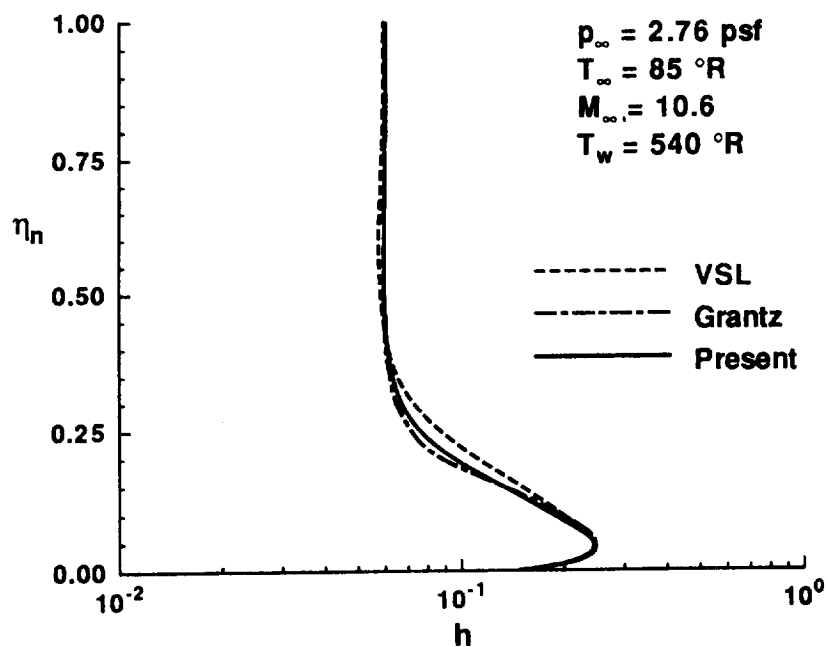**Figure 9.37.** Enthalpy profile comparison for 15° sphere-cone, $R_{nose} = 1.1$ *in* ($s_b \approx 20$).
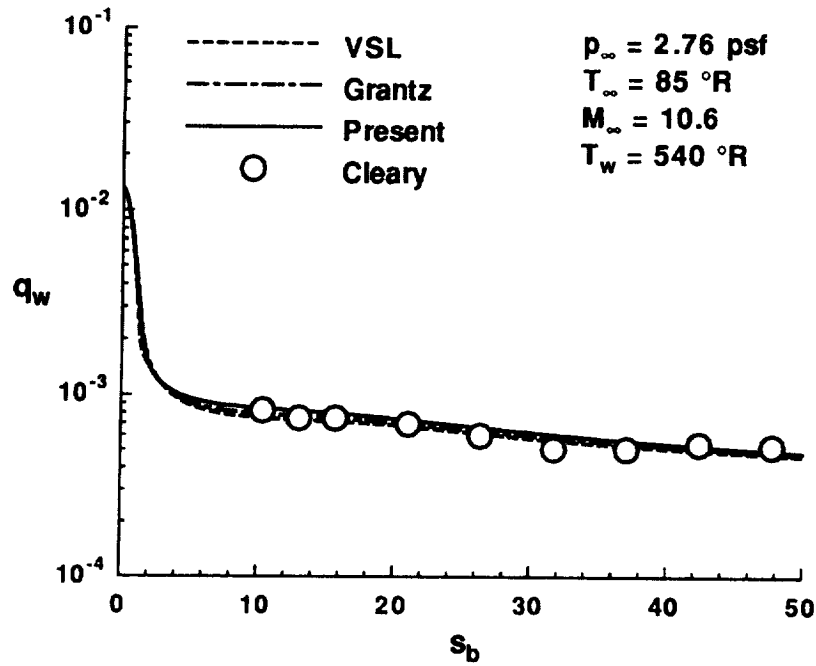
Figure 9.38. Heat transfer comparison for 15° sphere-cone, $R_{nose} = 0.375$ $in.$
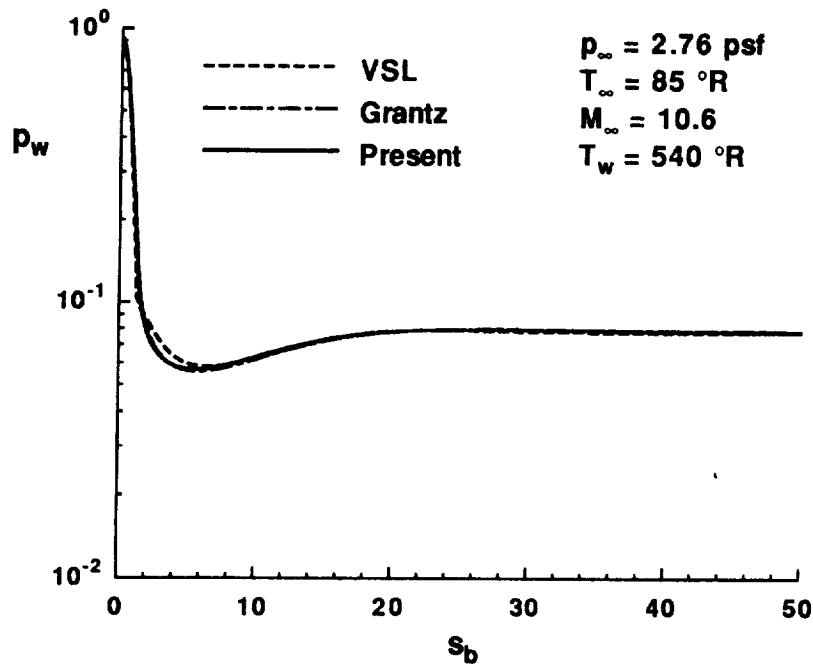
Figure 9.39. Body pressure comparison for 15° sphere-cone, $R_{nose} = 0.375$ $in.$
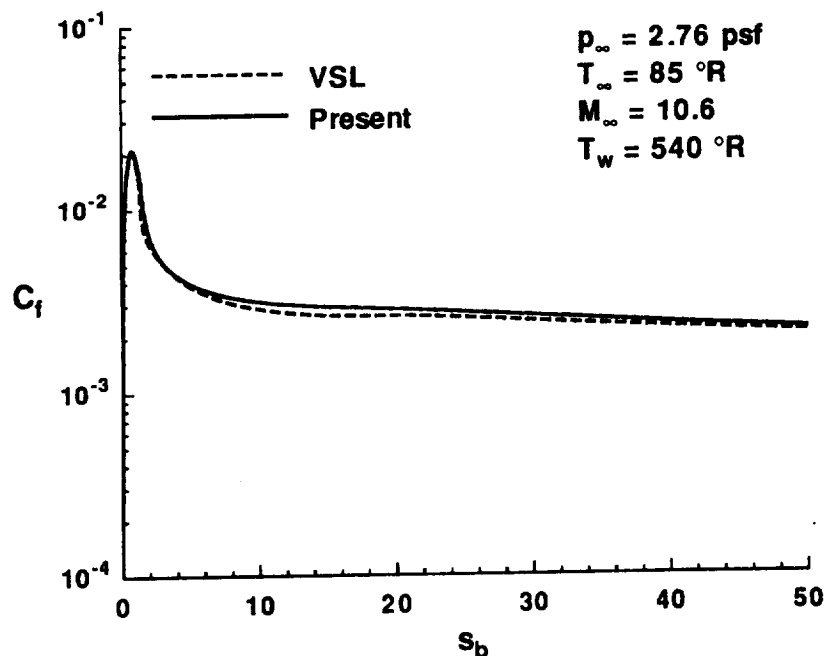
Figure 9.40. Skin friction comparison for 15° sphere-cone, $R_{nose} = 0.375$ $in.$

9.2 Equilibrium

Two sets of results for equilibrium flow are presented in this section. Both cases are for fully-laminar flow. The discussion follows the format of the perfect gas section.

Case 1

As a first case, flow over a 5° sphere-cone ($R_{nose} = 0.114$ in) is calculated using the the VSL [9] and present approaches. Both approaches use Hansen's [35] equilibrium air model. The freestream conditions are $p_\infty = 0.067917$ psi and $T_\infty = 438^o R$, with a variable wall temperature input. Fully-laminar solutions are calculated for a body length of $s_{b_{end}} = 1350$. Heating comparisons are made with the Reentry F flight experiment [72]. The VSL heating results are from Ref. [73].

Figure 9.41 shows the shock shapes from the two methods. The results are analogous to those of the perfect gas, 5° cone solution discussed earlier, although the shock layer is not as thick here. In Figure 9.42, the heating results of the VSL and present method are in very good agreement with each other (within ten percent), although they both underpredict the flight data.

The body pressure distributions are in excellent agreement (within five percent) except in the pressure overexpansion/recompression region, as shown in Figure 9.43. Figures 9.44 and 9.45 provide more detailed information on the stagnation region, and show the results approach the stagnation line in a manner similar to the perfect
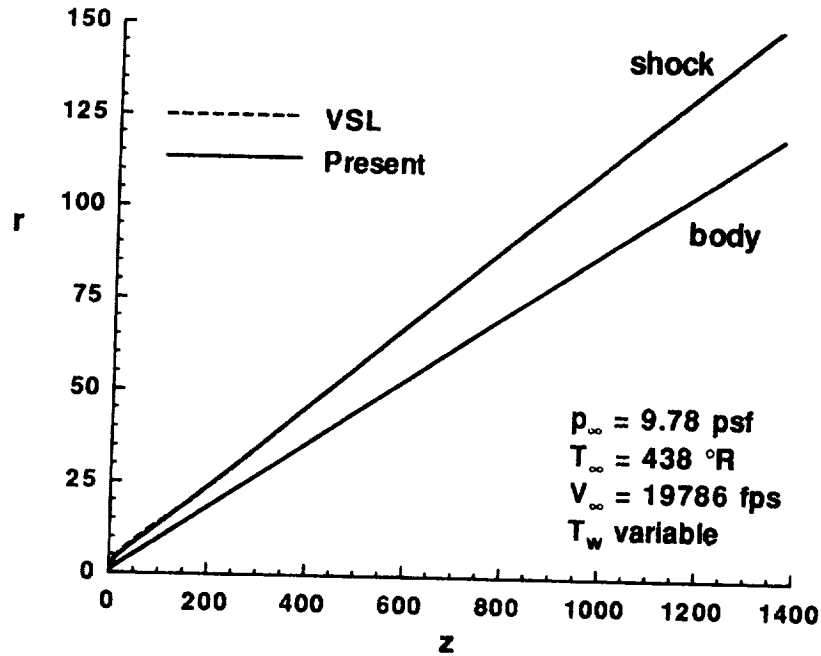
Figure 9.41. Shock shape comparison for 5° sphere-cone, $R_{nose} = 0.114$ *in.*

gas case. The skin friction results of the two methods are presented in Figures 9.46 and 9.47. The two solutions are in good agreement, generally within ten percent.

The stagnation line results for $p, v, \bar{u}, h,$ and ρ are presented in Figures 9.48 through 9.52, respectively. The two sets of results exhibit better agreement than is seen for the perfect gas case. Profiles near the pressure minimum ($s_b \approx 50$) and at the end of the body ($s_b \approx 1350$) are presented in Figures 9.53 and 9.54. The pressure profiles are within ten to fifteen percent of each other at the pressure minimum, while they are nearly indistinguishable (less than five percent apart) at the end of the body. The body-normal velocity components at the pressure minimum (Figure 9.55) are in agreement near the body, although further out in the layer there are noticeable differences. At the end station (Figure 9.56), the agreement is excellent. In fact, the present results are smoother than those of the VSL. The body-tangential velocity (Figures 9.57 and 9.58) and enthalpy profiles (Figures 9.59 and 9.60) agree quite well (within approximately five percent of each other). Again note the oscillations in the VSL results for the end station. These wiggles appear in the present solution as well, and reflect a grid resolution problem at the boundary-layer edge. Since the normal distribution for each method is based on physical distance, this problem can be readily corrected by adjusting the spacing parameters (see Section 7.4).

Table 9.2 shows the overall run times required to generate this solution. The value shown for the VSL results is the total time required for three shock iterations. As with the perfect gas comparison, the approximate algorithm yields a dramatic decrease in total CPU requirements over the VSL technique. Further, the last entry
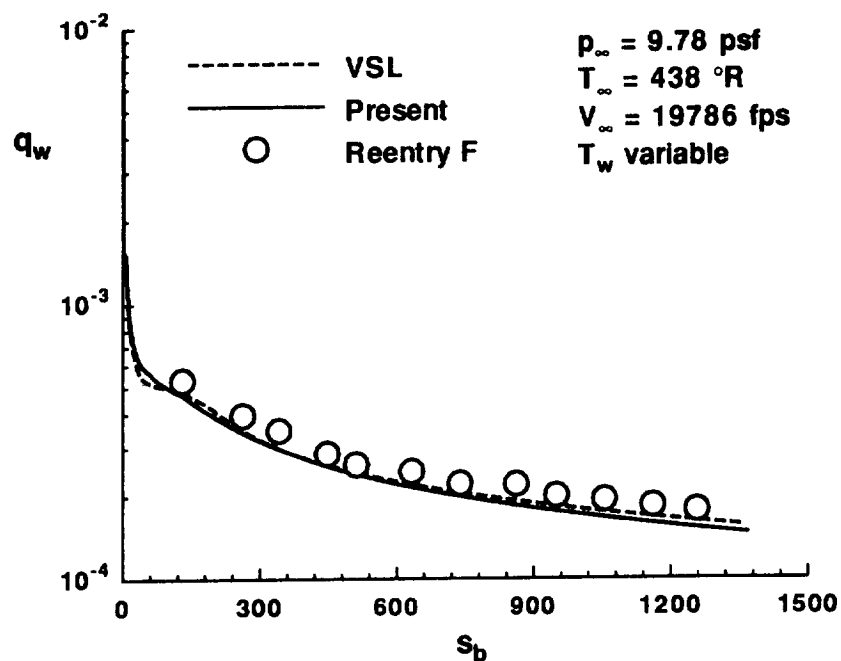
Figure 9.42. Heat transfer comparison for 5° sphere-cone, $R_{nose} = 0.114$ *in.*
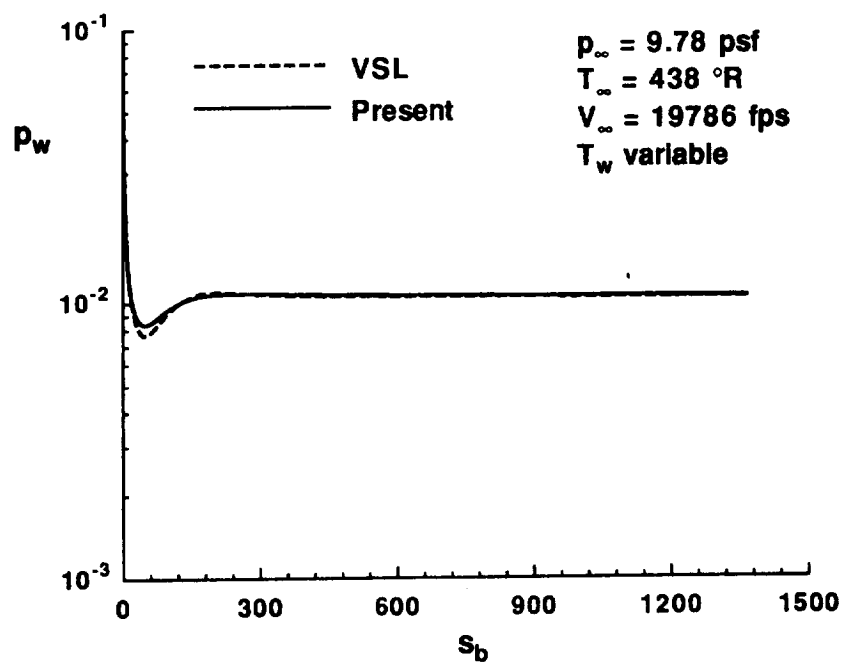
Figure 9.43. Body pressure comparison for 5° sphere-cone, $R_{nose} = 0.114$ *in.*
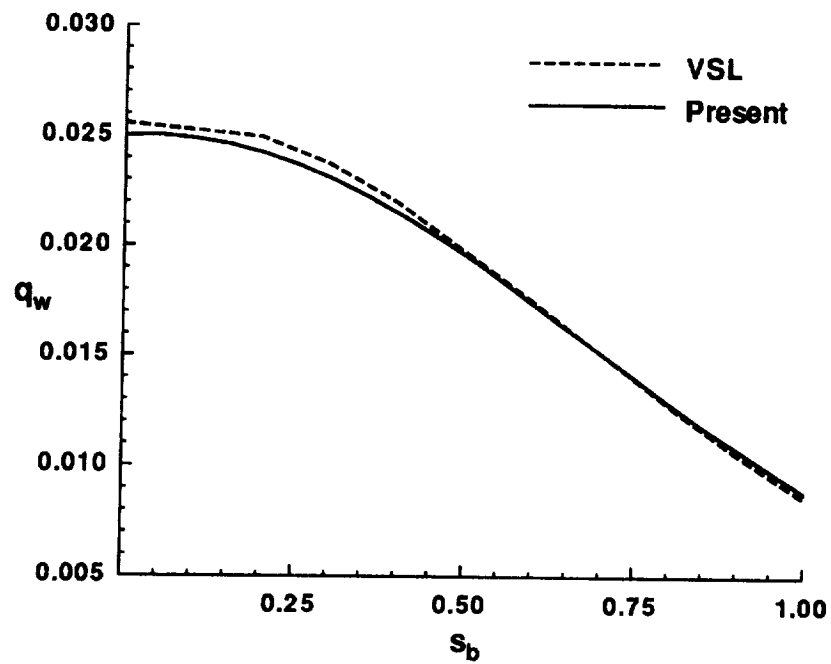
Figure 9.44. Heat transfer comparison for 5° sphere-cone,
$R_{nose} = 0.114$ *in* (stagnation region).
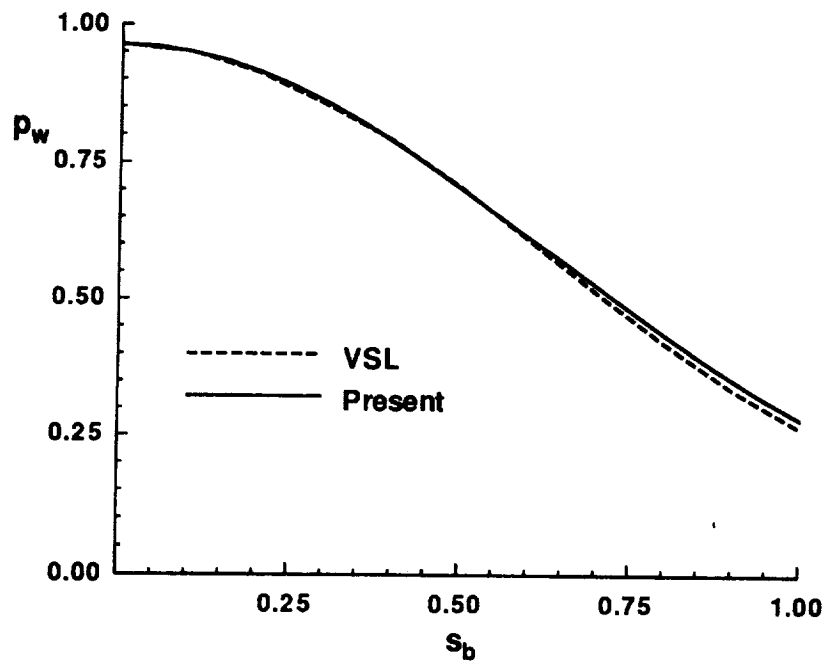
Figure 9.45. Body pressure comparison for 5° sphere-cone,
$R_{nose} = 0.114$ *in* (stagnation region).
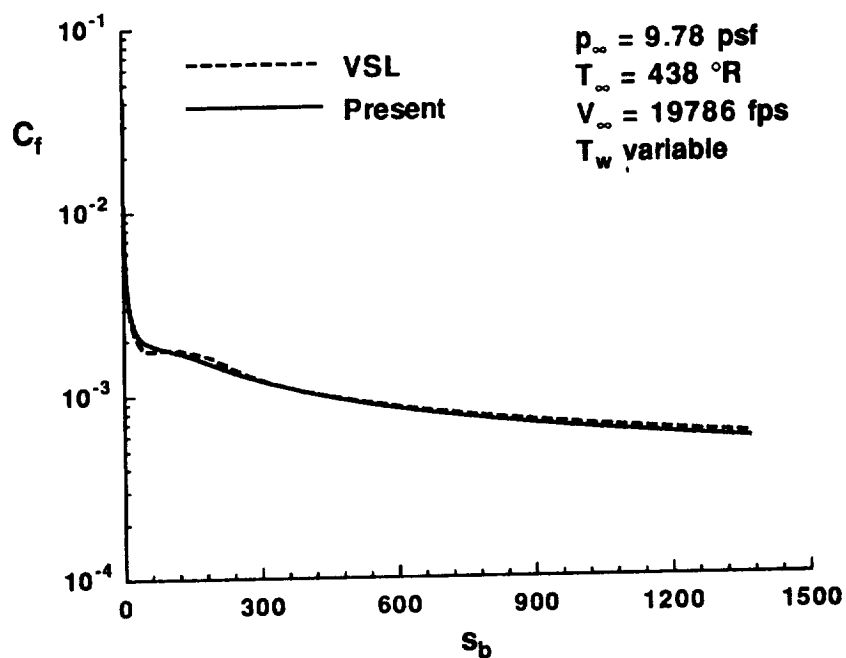
Figure 9.46. Skin friction comparison for 5° sphere-cone, $R_{nose} = 0.114$ *in.*
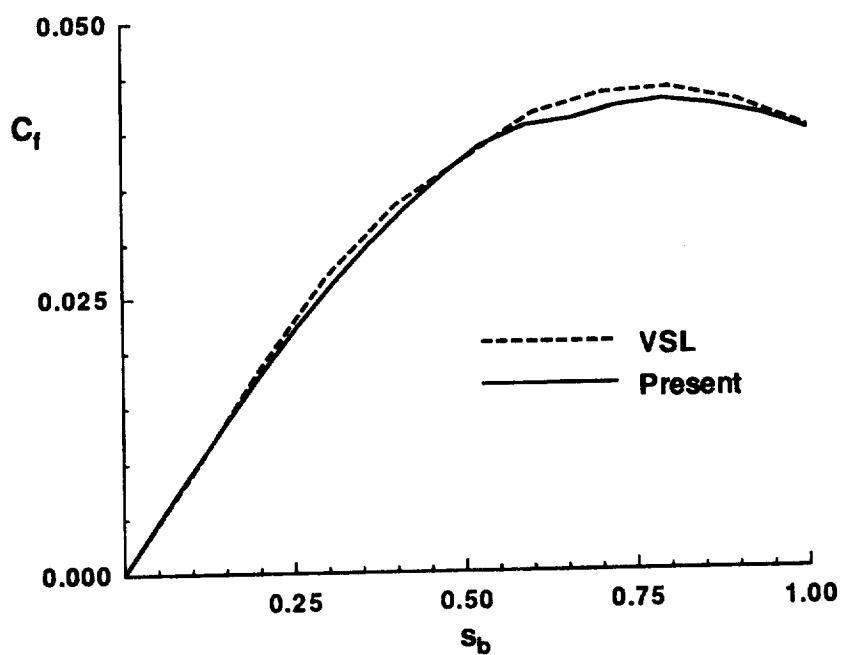
Figure 9.47. Skin friction comparison for 5° sphere-cone, $R_{nose} = 0.114$ *in* (stagnation region).
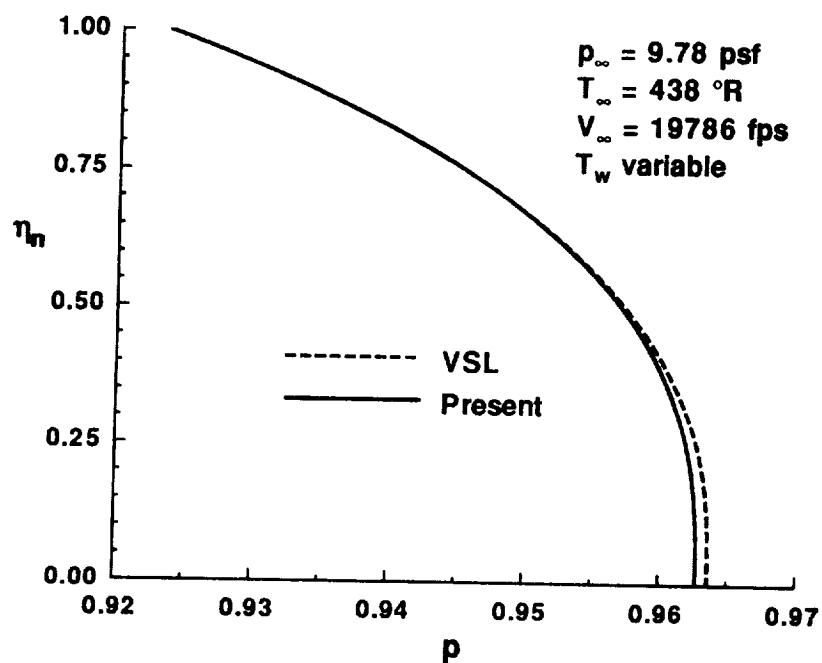
Figure 9.48. Pressure profile comparison for 5° sphere-cone, $R_{nose} = 0.114$ *in* (stagnation line).
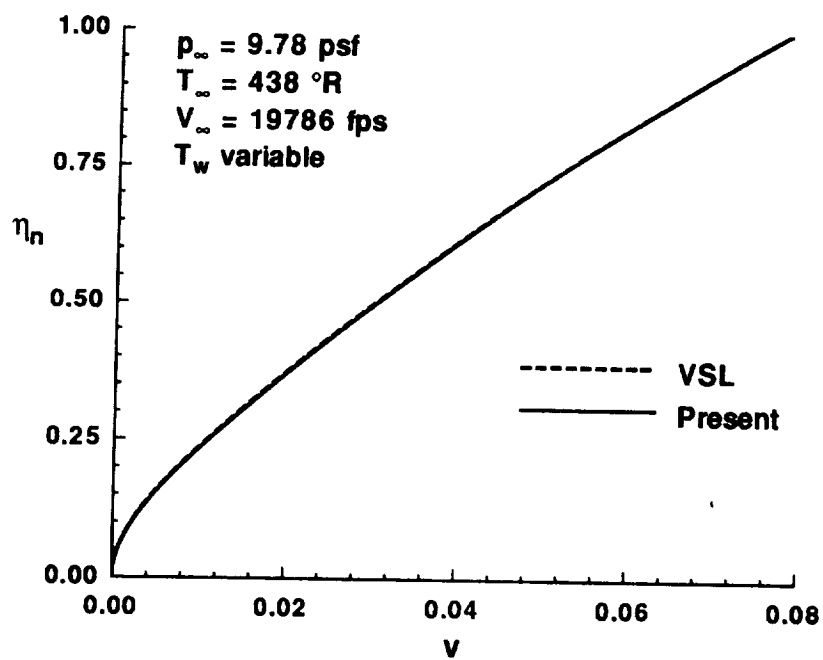
Figure 9.49. Normal velocity profile comparison for 5° sphere-cone, $R_{nose} = 0.114$ *in* (stagnation line).
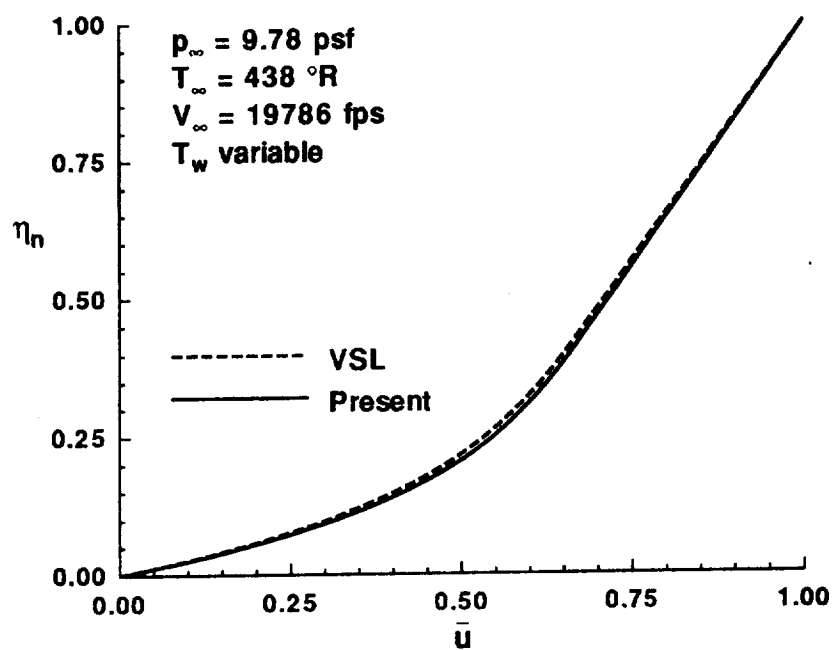
Figure 9.50. Tangential velocity profile comparison for 5° sphere-cone, $R_{nose} = 0.114$ *in* (stagnation line).
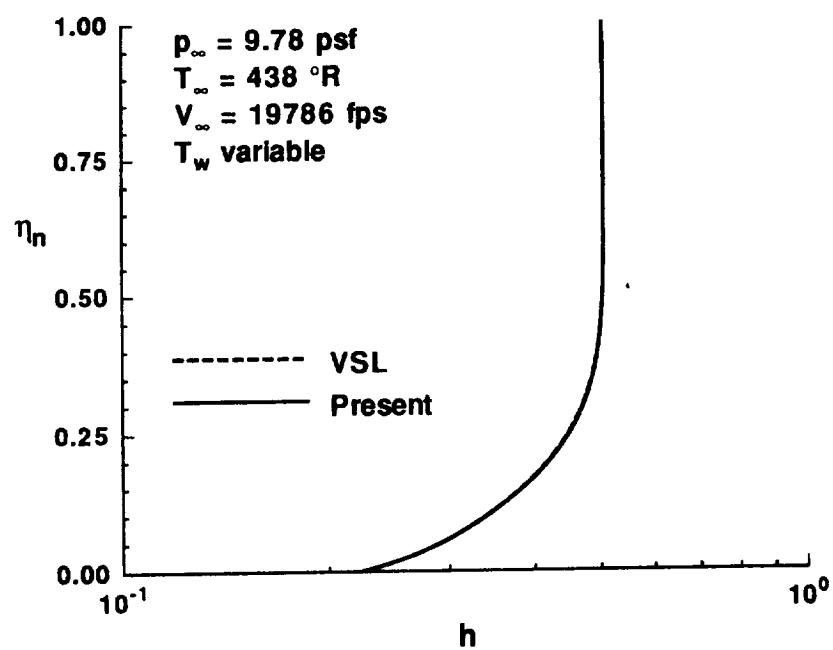
Figure 9.51. Enthalpy profile comparison for 5° sphere-cone, $R_{nose} = 0.114$ *in* (stagnation line).
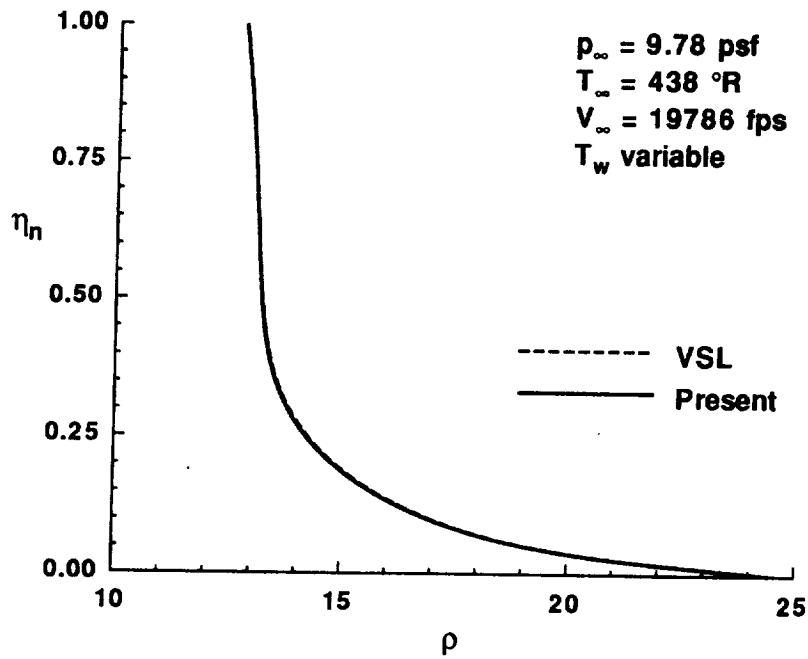
Figure 9.52. Density profile comparison for 5° sphere-cone,
$R_{nose} = 0.114$ *in* (stagnation line).

in the table illustrates that solving the approximate VSL equations for equilibrium flow is inherently about sixty percent faster than solving the full VSL equations. This speed-up is not as large as the perfect gas value, which can be attributed to the complexity of the equilibrium air model relative to the perfect gas relations. This is because a large percentage of the total run time is dedicated to determining thermodynamic and transport properties, which are the same in both methods, so that the benefits of using the time-saving approximate equations are reduced.
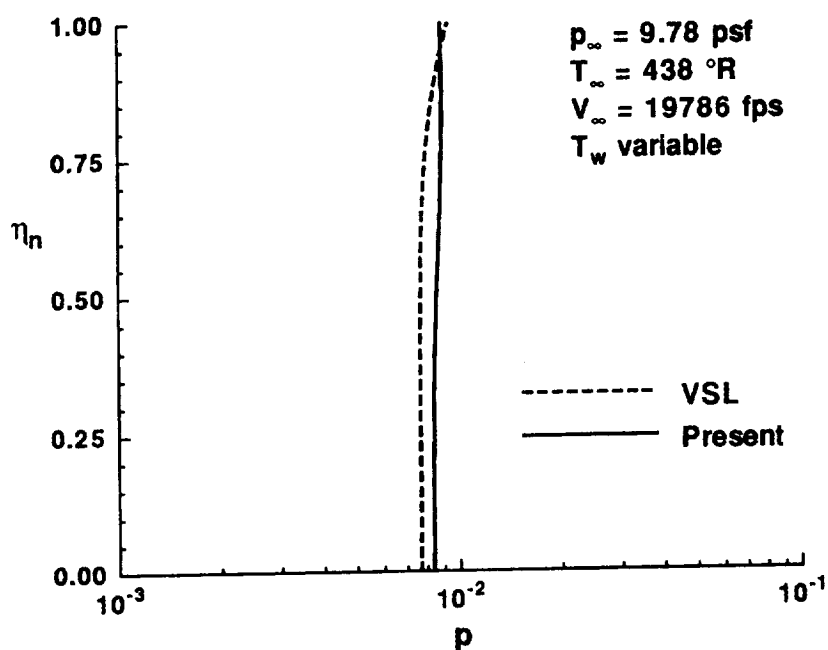
Figure 9.53. Pressure profile comparison for 5° sphere-cone, $R_{nose} = 0.114\ in\ (s_b \approx 50)$.
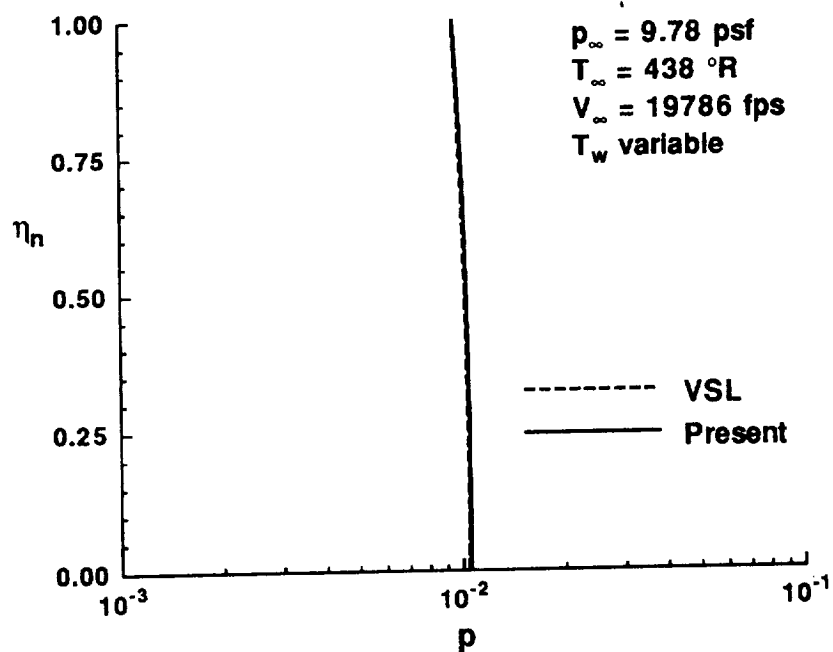
Figure 9.54. Pressure profile comparison for 5° sphere-cone, $R_{nose} = 0.114\ in\ (s_b \approx 1350)$.
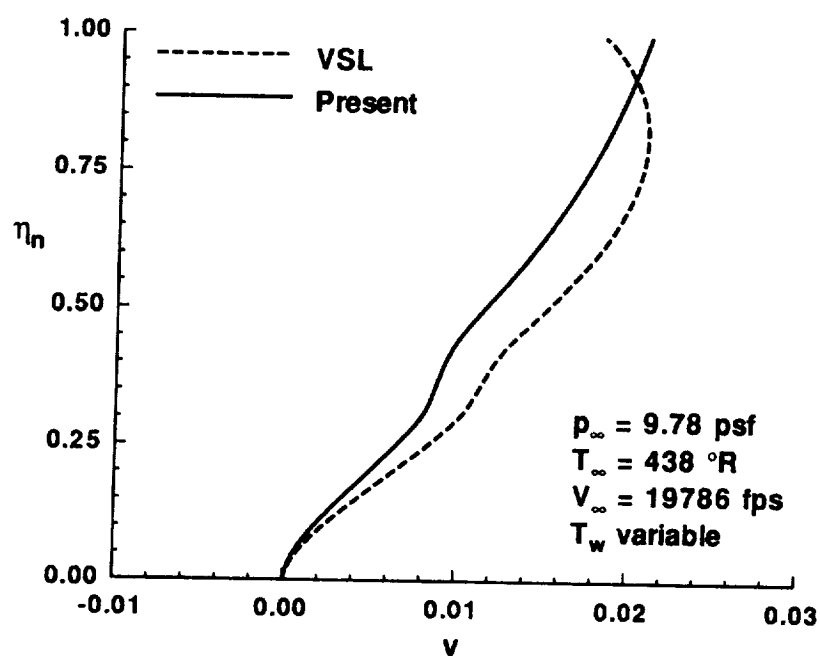
Figure 9.55. Normal velocity profile comparison for $5°$ sphere-cone, $R_{nose} = 0.114$ in $(s_b \approx 50)$.
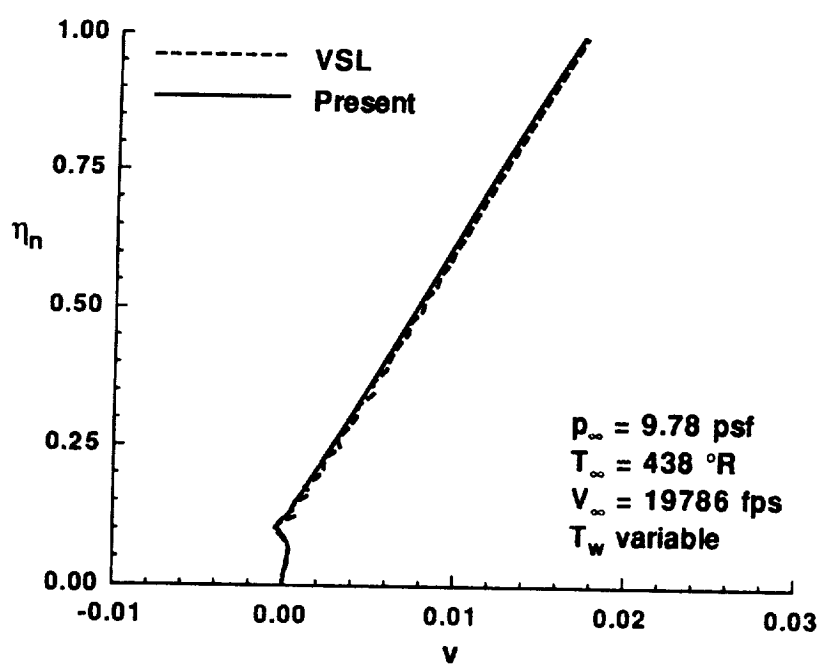
Figure 9.56. Normal velocity profile comparison for $5°$ sphere-cone, $R_{nose} = 0.114$ in $(s_b \approx 1350)$.
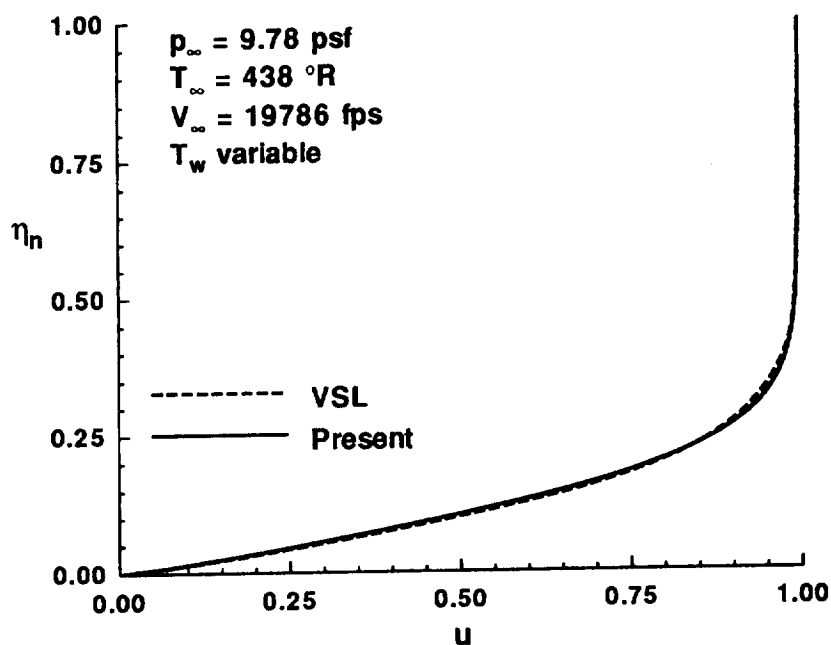
Figure 9.57. Tangential velocity profile comparison for $5°$ sphere-cone, $R_{nose} = 0.114$ in $(s_b \approx 50)$.
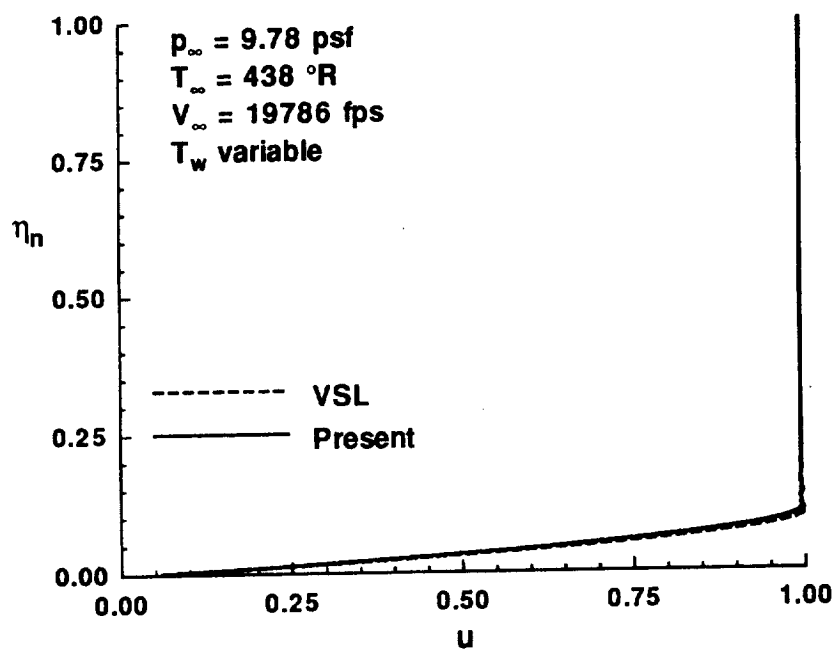
Figure 9.58. Tangential velocity profile comparison for $5°$ sphere-cone, $R_{nose} = 0.114$ in $(s_b \approx 1350)$.
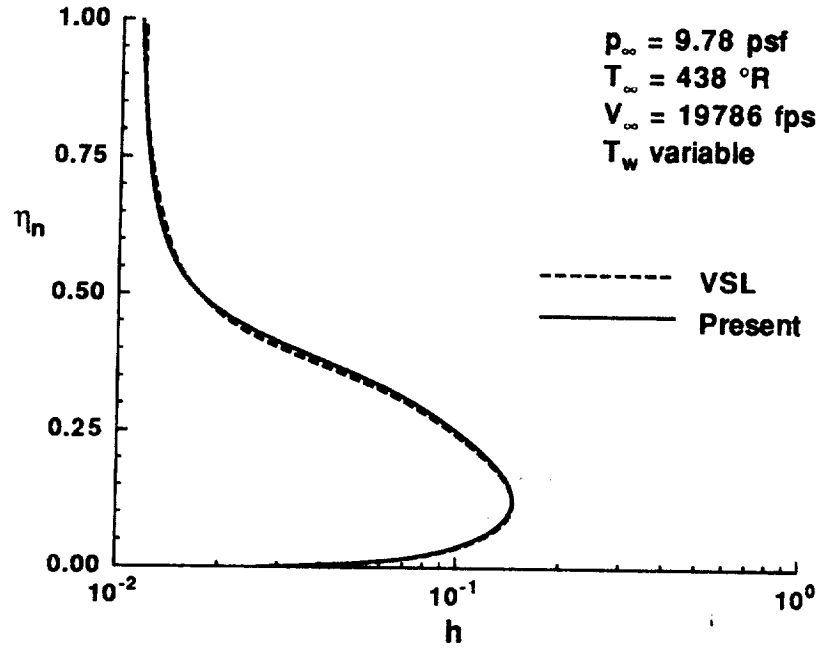
Figure 9.59. Enthalpy profile comparison for 5° sphere-cone,
$R_{nose} = 0.114$ *in* $(s_b \approx 50)$.
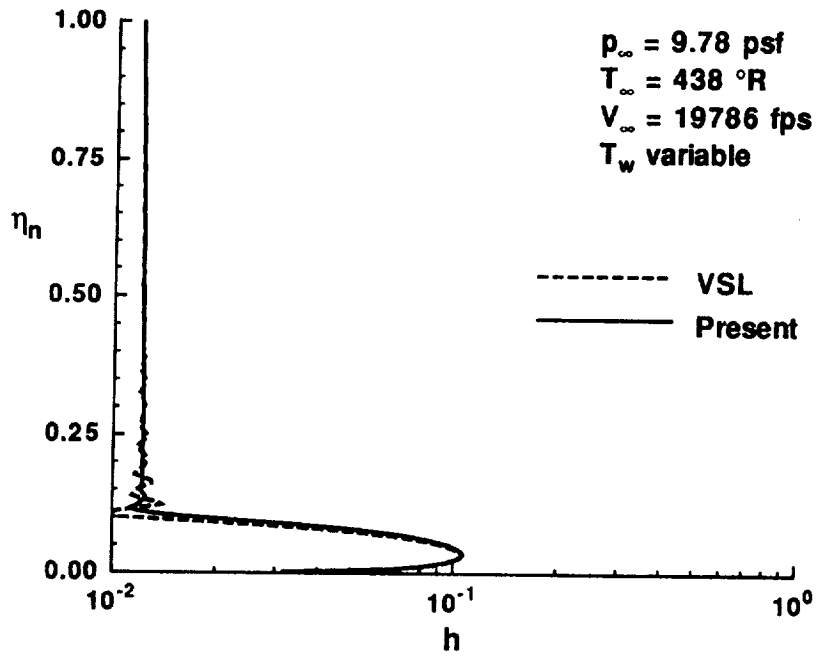
Figure 9.60. Enthalpy profile comparison for 5° sphere-cone,
$R_{nose} = 0.114$ *in* $(s_b \approx 1350)$.

Table 9.2. Run-times[a] for $5°$ cone, $R_{nose} = 0.114$ in.

	VSL	Present
stations	667	206
CPU time	4539	714
grid pts/sec	15	29
shock iterations	3.0	2.5
grid pts/sec/shock	45	72

a – Sun Sparcstation 1+

Case 2

As a second case, comparisons between the VSL [9] and current method are made for Mach 22 flow over a $35.5°$ hyperboloid. The nose radius is $R_{nose} = 3.46457$ *ft* and the fully-laminar solution is computed for a body length of $s_{b_{end}} = 24.5$. The freestream conditions are $p_\infty = 0.00094$ *psi* and $T_\infty = 400°R$, with a wall temperature of $T_w = 1998°R$.

Figure 9.61 shows that the shock shapes from the two methods lie virtually atop one another. In Figure 9.62, the heating rate comparisons are very good (within five to ten percent) for the entire length of the body. Likewise, the computed pressure distributions (Figure 9.63) are in excellent agreement (within two to five percent) everywhere. Referring to Figure 9.61, these excellent results can be attributed to the fact that with the large body angle, the shock- and body-angles are nearly equal for the entire length of the body (which more closely matches Maslen's assumptions). The skin friction comparisons of Figure 9.64 show that the VSL and present method are again in good agreement (generally within ten percent).

Since the stagnation line results are similar to those given in Figures 9.48 through 9.52, and the agreement between the solutions of the two methods is still excellent, they are not presented here. Again, profiles near the pressure minimum ($s_b \approx 15.5$) and at the end of the body ($s_b \approx 25.5$) are presented. Figures 9.65 and 9.66 show that the pressure profiles at these two stations are nearly indistinguishable (less than five percent apart). The only major differences in the body-normal velocity components (Figures 9.67 and 9.68) are near the shock, and thus have minimal impact on the surface properties. Further, the body-tangential velocity profiles (Figures 9.69 and 9.70) and enthalpy profiles (Figures 9.71 and 9.72) are within approximately five percent of each other.
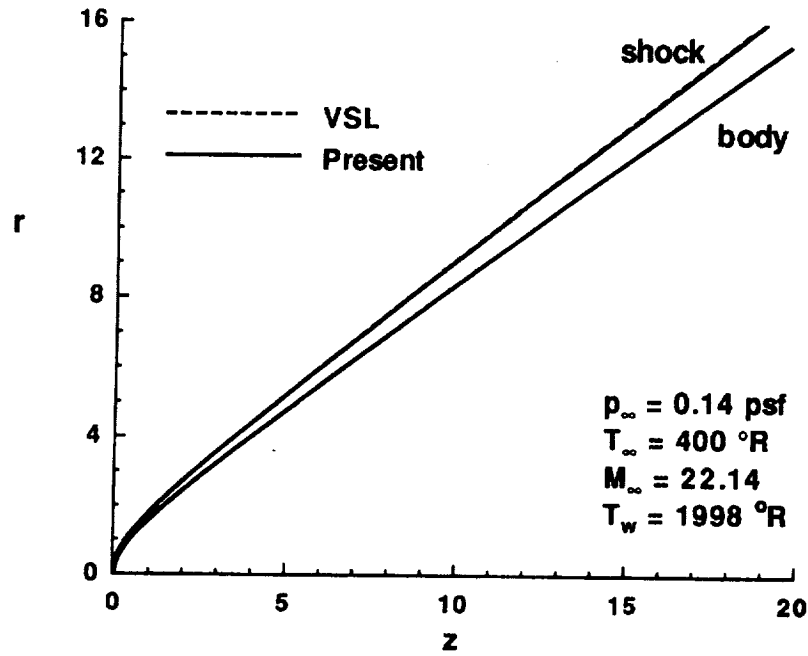
Figure 9.61. Shock shape comparison for $35.5°$ hyperboloid, $R_{nose} = 3.46457$ *ft.*
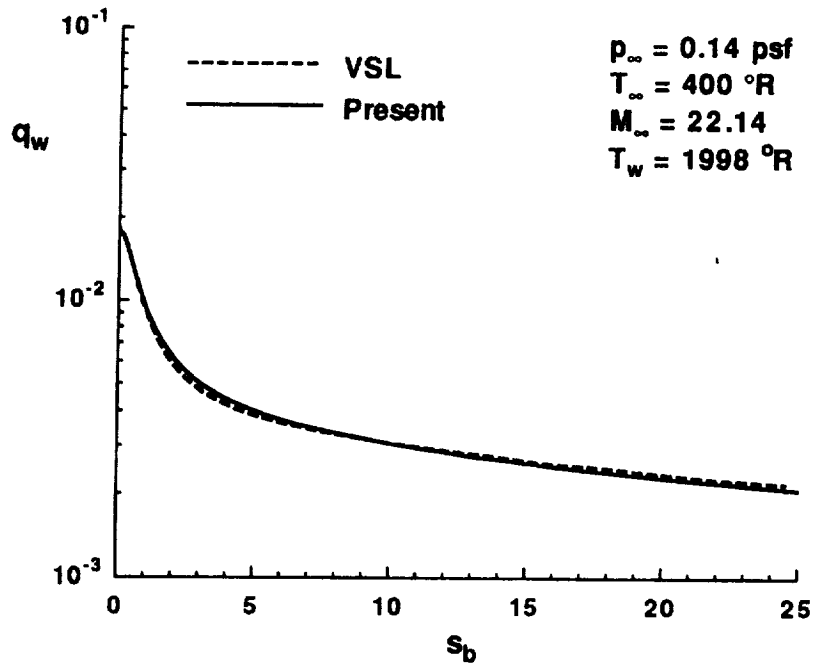
Figure 9.62. Heat transfer comparison for $35.5°$ hyperboloid, $R_{nose} = 3.46457$ *ft.*
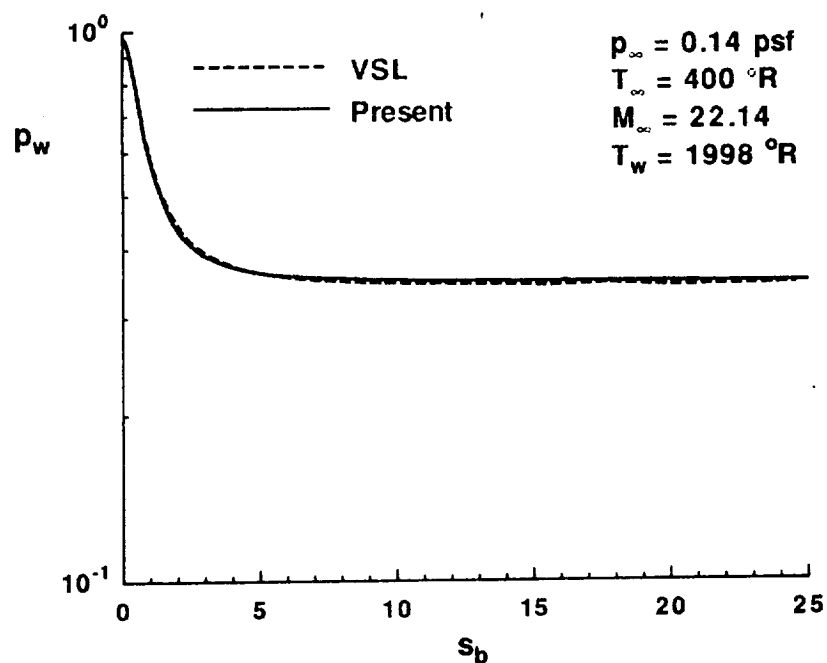
Figure 9.63. Body pressure comparison for $35.5°$ hyperboloid, $R_{nose} = 3.46457\ ft$.
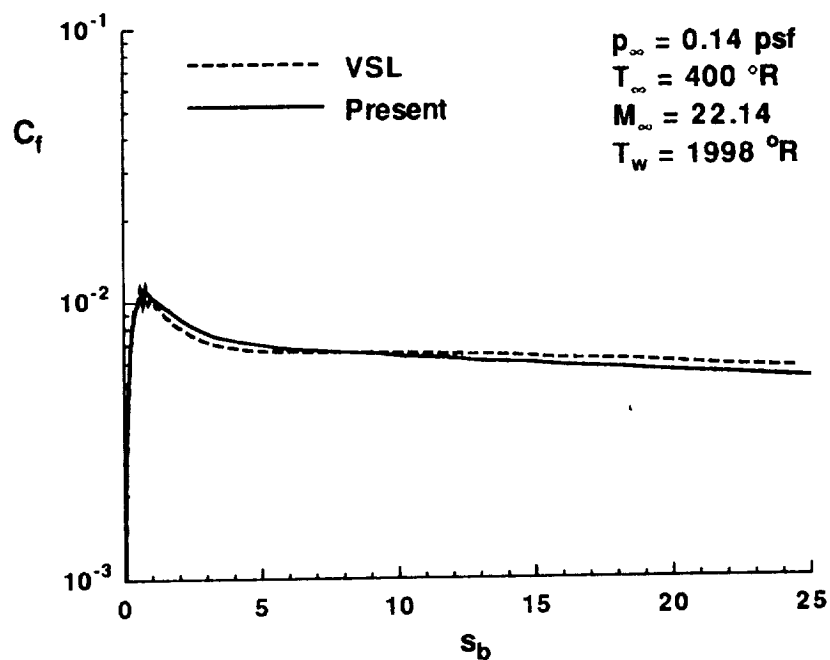
Figure 9.64. Skin friction comparison for $35.5°$ hyperboloid, $R_{nose} = 3.46457\ ft$.
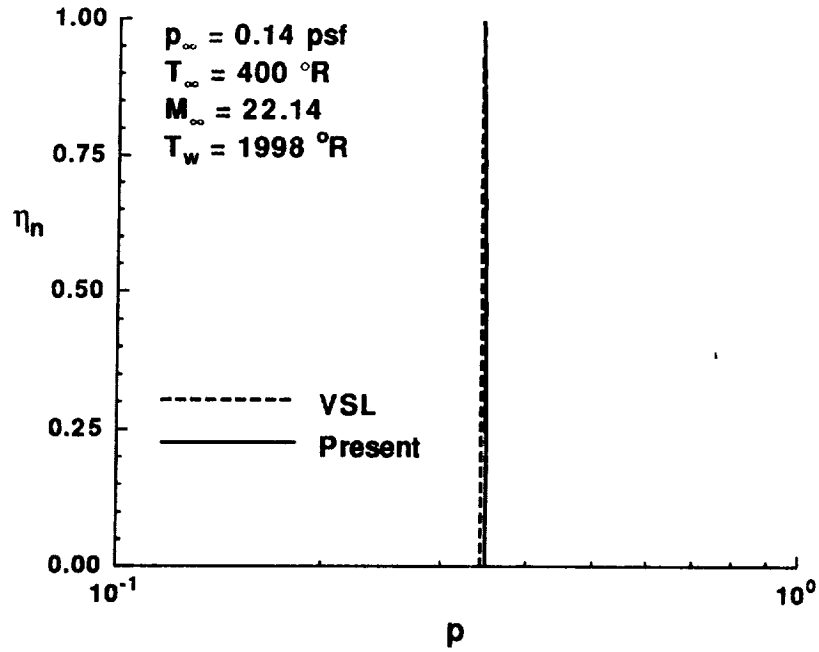
Figure 9.65. Pressure profile comparison for 35.5° hyperboloid,
$R_{nose} = 3.46457$ ft $(s_b \approx 15.5)$.
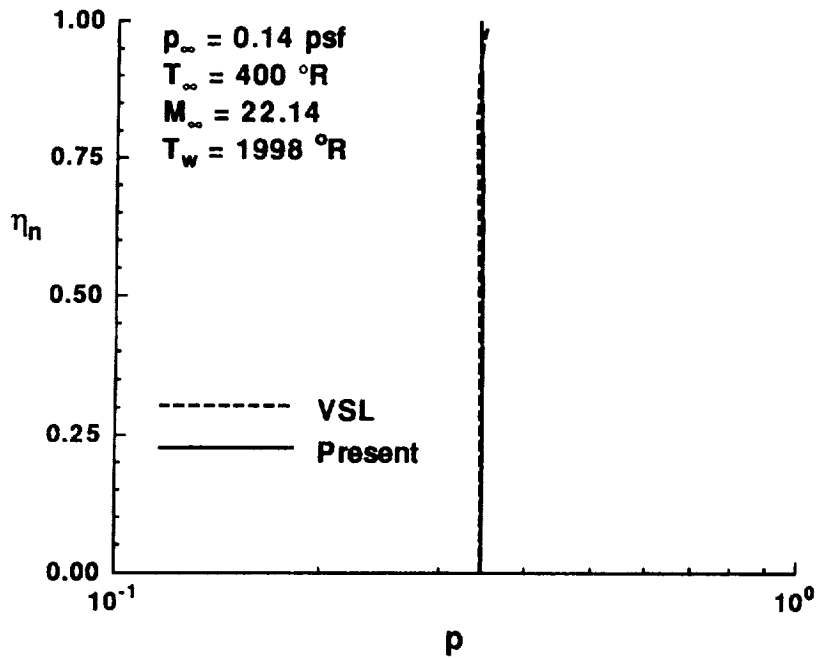
Figure 9.66. Pressure profile comparison for 35.5° hyperboloid,
$R_{nose} = 3.46457$ ft $(s_b \approx 24.5)$.
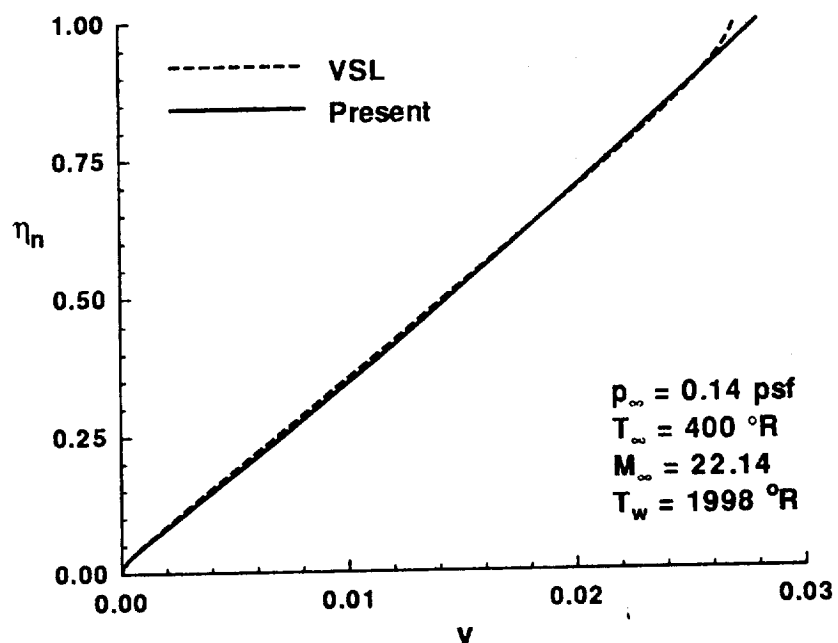
Figure 9.67. Normal velocity profile comparison for 35.5° hyperboloid, $R_{nose} = 3.46457 \ ft \ (s_b \approx 15.5)$.
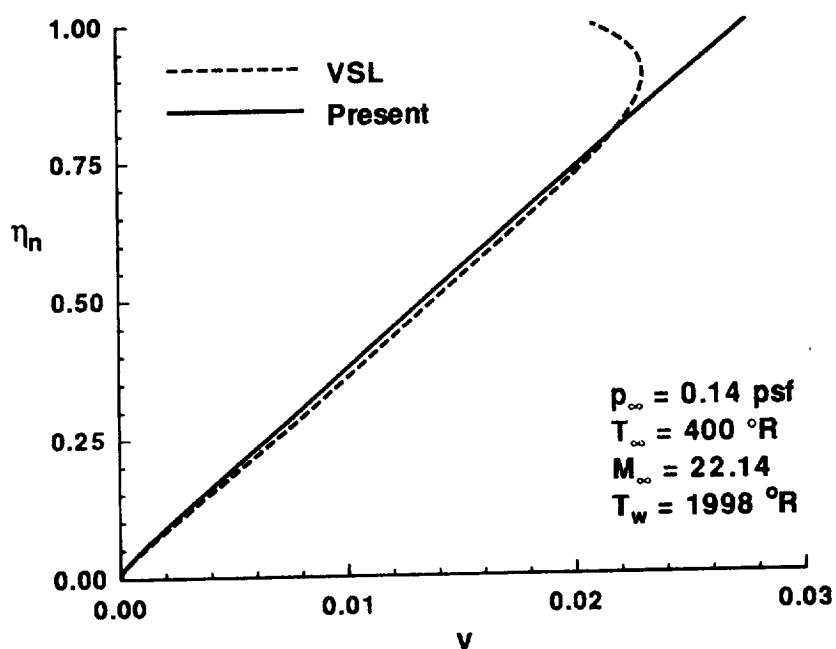
Figure 9.68. Normal velocity profile comparison for 35.5° hyperboloid, $R_{nose} = 3.46457 \ ft \ (s_b \approx 24.5)$.
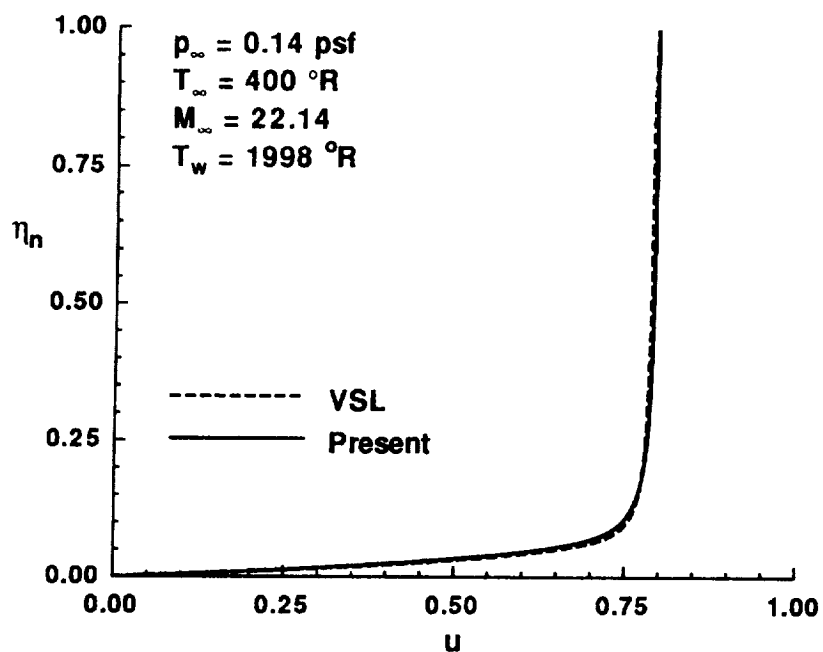
Figure 9.69. Tangential velocity profile comparison for $35.5°$ hyperboloid, $R_{nose} = 3.46457$ ft ($s_b \approx 15.5$).
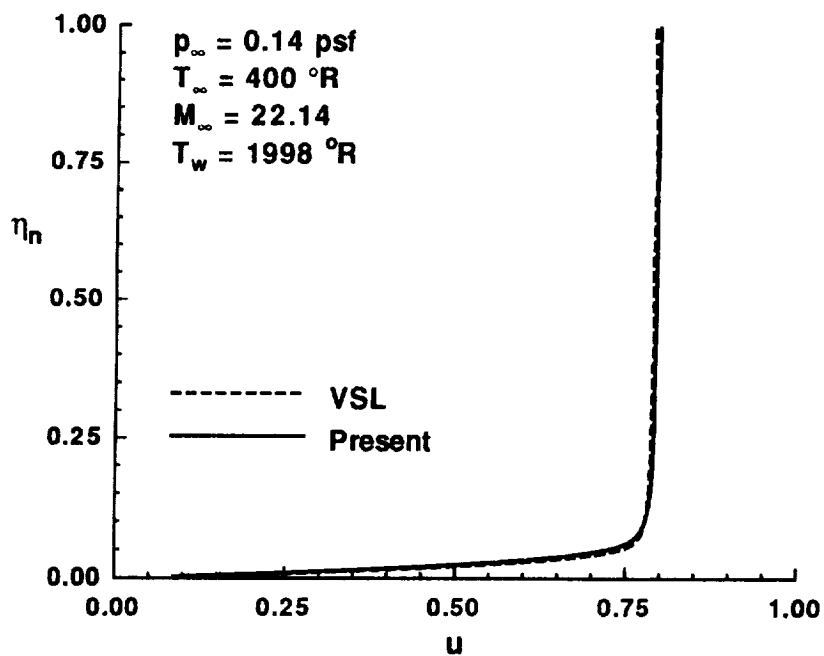
Figure 9.70. Tangential velocity profile comparison for $35.5°$ hyperboloid, $R_{nose} = 3.46457$ ft ($s_b \approx 24.5$).
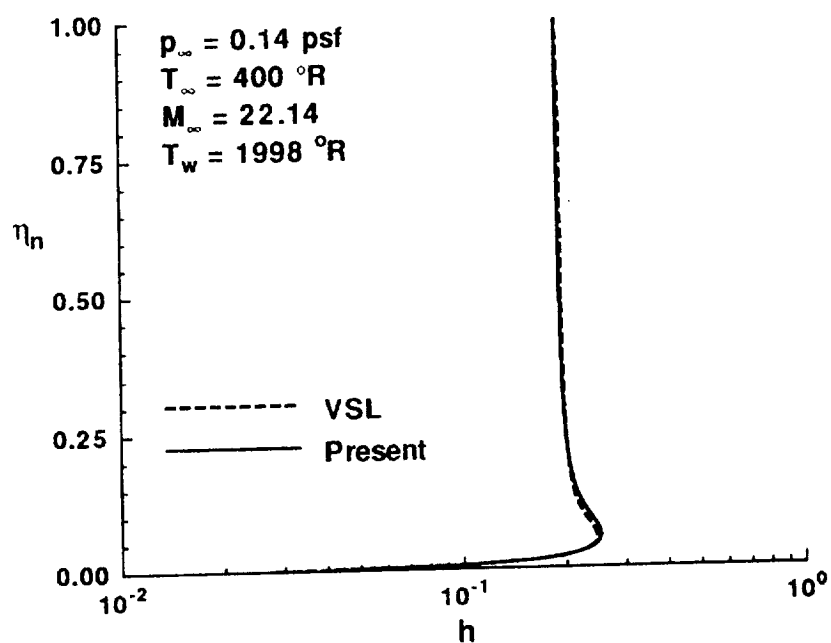
Figure 9.71. Enthalpy profile comparison for 35.5° hyperboloid, $R_{nose} = 3.46457\ ft$ ($s_b \approx 15.5$).
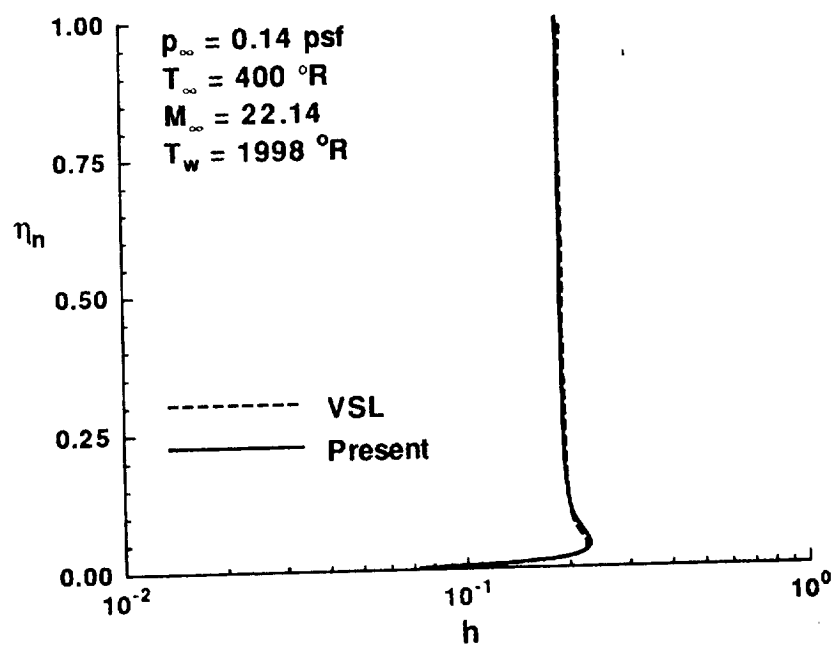
Figure 9.72. Enthalpy profile comparison for 35.5° hyperboloid, $R_{nose} = 3.46457\ ft$ ($s_b \approx 24.5$).
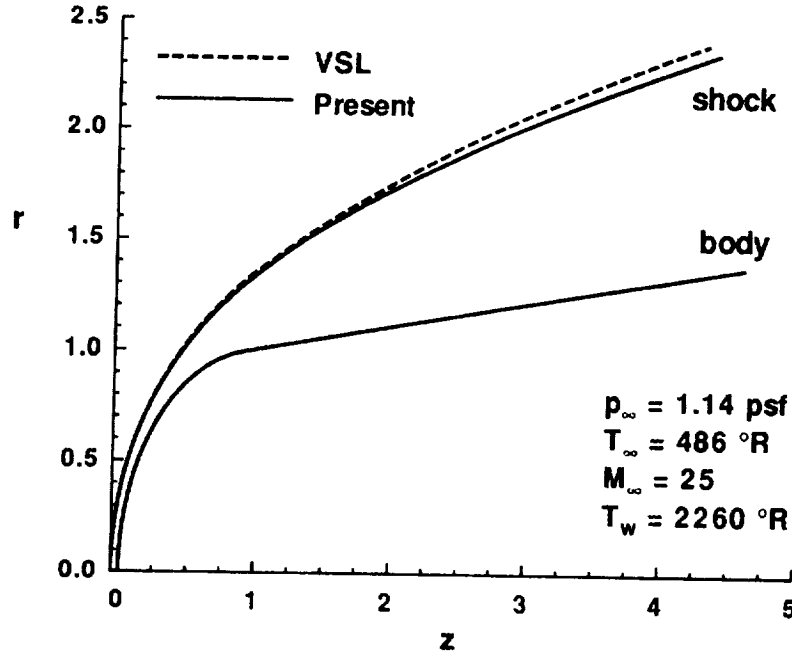
Figure 9.73. Shock shape comparison for 6° sphere-cone, $R_{nose} = 1.5$ in.

9.3 Nonequilibrium

Three sets of results for nonequilibrium flow are presented in this section. The first is flow over a 5° sphere-cone with a noncatalytic wall. The next case is a longer 20° cone, where two solutions are computed: noncatalytic wall and fully-catalytic wall. The VSL [14] and current method are employed for this analysis. The discussion follows the format of the previous sections, although additional profile comparisons are made. As a final case, the present method is used to calculate flow over a hyperboloid with both noncatalytic and fully-catalytic wall conditions. The results for this case are compared with Shuttle flight data.

Case 1

As the first case, comparisons between the VSL [14] and current method are made for Mach 25 flow over a 6° sphere-cone. The nose radius is $R_{nose} = 1.5$ in and the solution is computed for a body length of $s_{b_{end}} = 5$. The freestream conditions are $p_\infty = 0.00794$ psi and $T_\infty = 486^\circ R$, with a wall temperature of $T_w = 2260^\circ R$. Nonequilibrium flowfield calculations require additional boundary conditions for the species mass fractions, and a noncatalytic wall boundary condition (see Section 5.5.1) is specified here. The VSL heating results are from Ref. [70].

Figure 9.73 shows the shock shapes from the two methods. As with the perfect gas and equilibrium results, the computed shock shapes begin to deviate from one

another in the overexpansion region. Figures 9.74 and 9.75 show that the surface heating results are within fifteen percent of each other and approach the stagnation value quite smoothly. The pressure expansion is still underway at the end of this body, and Figure 9.76 clearly shows the differences between the VSL and present body pressures. Note that the pressures are approaching each other as the solution progresses. Figure 9.77 displays the same smooth behavior seen previously for stagnation region pressure distributions. The skin friction results of the two methods are presented in Figures 9.78 and 9.79. The two solutions are in good agreement (generally within ten percent).

The stagnation line results for $p, v, \bar{u}, T$, and ρ are presented in Figures 9.80 through 9.84, respectively. The pressure predictions (Figure 9.80) are within approximately one percent of each other, while the normal velocity profiles (Figure 9.81) agree to within five percent. The tangential velocity profiles (Figure 9.82) are not as close, but as explained earlier, this may be due to differences in the streamwise momentum equation on the stagnation line. Agreement between the temperature, as well as density, profiles (Figures 9.83 and 9.84) is excellent. The species mass fraction profiles are presented in Figure 9.85. Note that for this figure, the dependent variables are assigned to the vertical axis, rather than to the horizontal axis as is done for the other profiles. Again the agreement between the two methods is very good. Only trace amounts of NO^+ are present for this case, so its mass fraction profile is not included in the figure.

Since the flow solution does not encompass the pressure minimum (see Figure 9.76), only profiles at the end of the body ($s_b = 5$) are presented. Figure 9.86 shows that the pressure profiles differ by twenty percent of each other at the end of the body. The body-normal velocity components (Figure 9.87) are in good agreement throughout the shock layer at this station. Notice that this velocity component is negative at this station, which is indicative of the streamlines spreading away from the body surface (see Figure 7.1). Although this behavior has not been shown previously, the same situation exists in this region for perfect gas and equilibrium flows about slender cones. The body-tangential velocity (Figure 9.88) profiles are in agreement near the body and shock, but deviate from one another (by as much as ten percent) in the interior of the shock layer. On the other hand, the temperature (Figure 9.89) and mass fraction profiles (Figure 9.90) agree quite well (within approximately five percent of each other).

As a final comparison for this case, the electron density is considered. Figure 9.91 displays the profiles for the stagnation line and the end station. Note the good agreement between the solutions. As the sharp-cone limit is reached, the normal spacing for the two methods are virtually identical. Thus, the oscillations near the shock for the end station (which are present in both solutions) are possibly due to grid resolution. Since they occur far away from the body, they have little effect on the surface properties.

Table 9.3 shows the overall run times required to generate this solution. The value
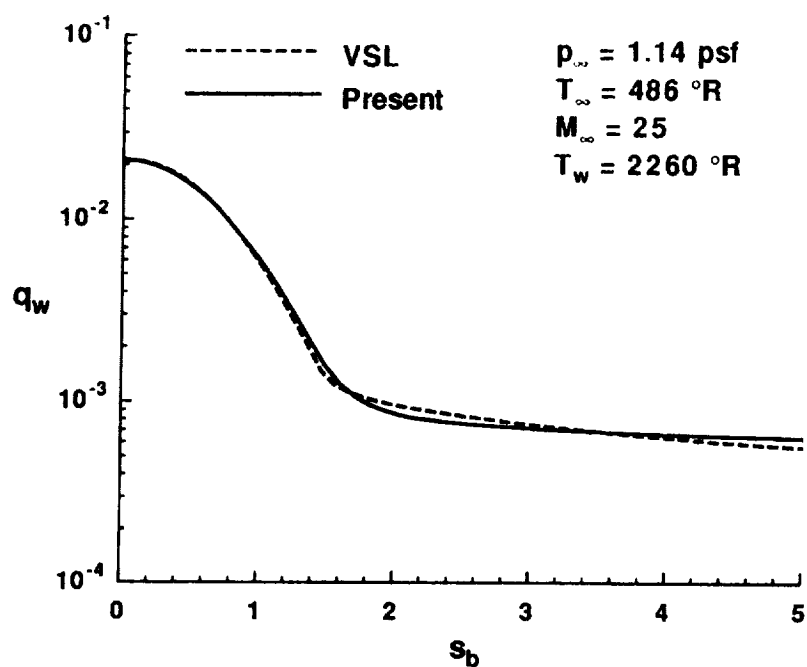
Figure 9.74. Heat transfer comparison for 6° sphere-cone, $R_{nose} = 1.5$ _in._
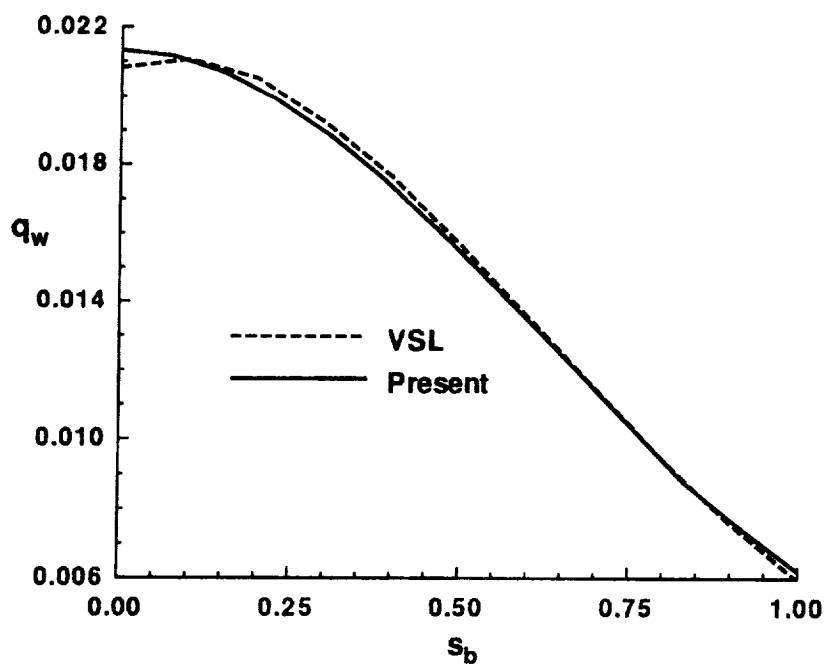
Figure 9.75. Heat transfer comparison for 6° sphere-cone, $R_{nose} = 1.5$ _in_ (stagnation region).
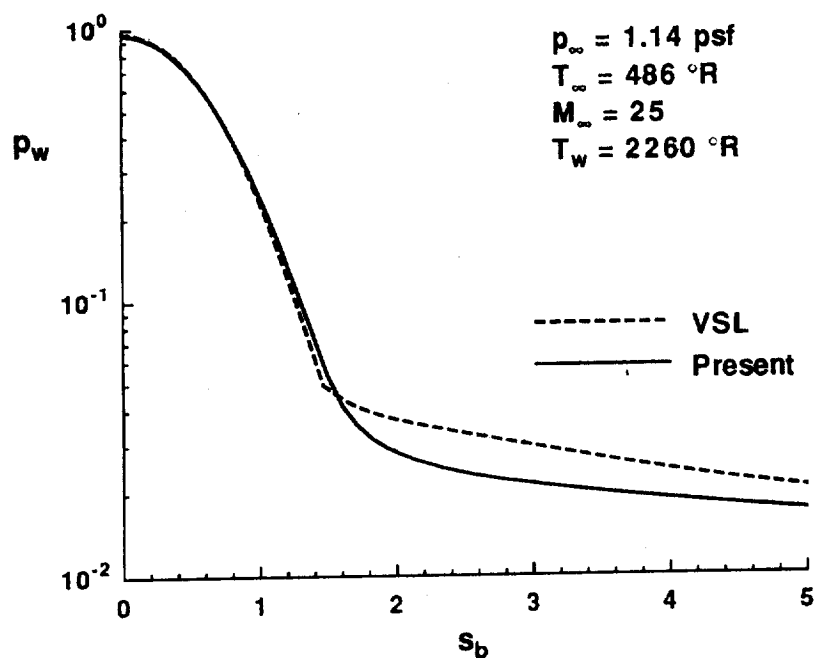
Figure 9.76. Body pressure comparison for 6° sphere-cone, $R_{nose} = 1.5$ $in.$
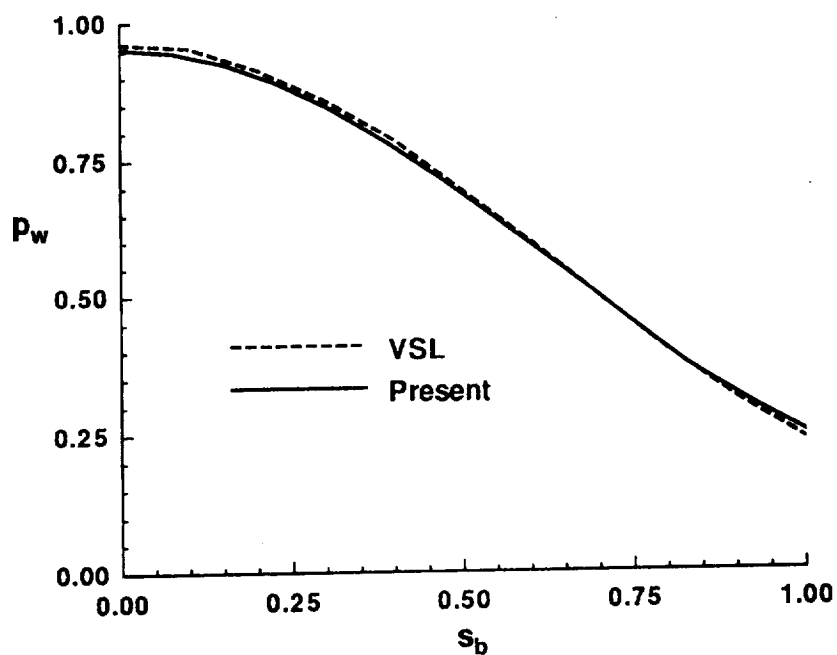
Figure 9.77. Body pressure comparison for 6° sphere-cone, $R_{nose} = 1.5$ in (stagnation region).
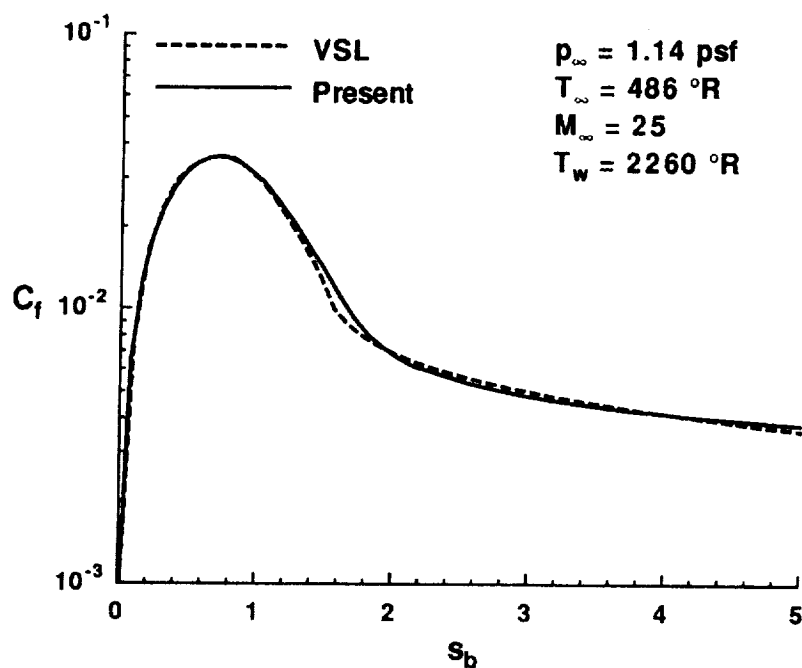
Figure 9.78. Skin friction comparison for $6°$ sphere-cone, $R_{nose} = 1.5$ in.
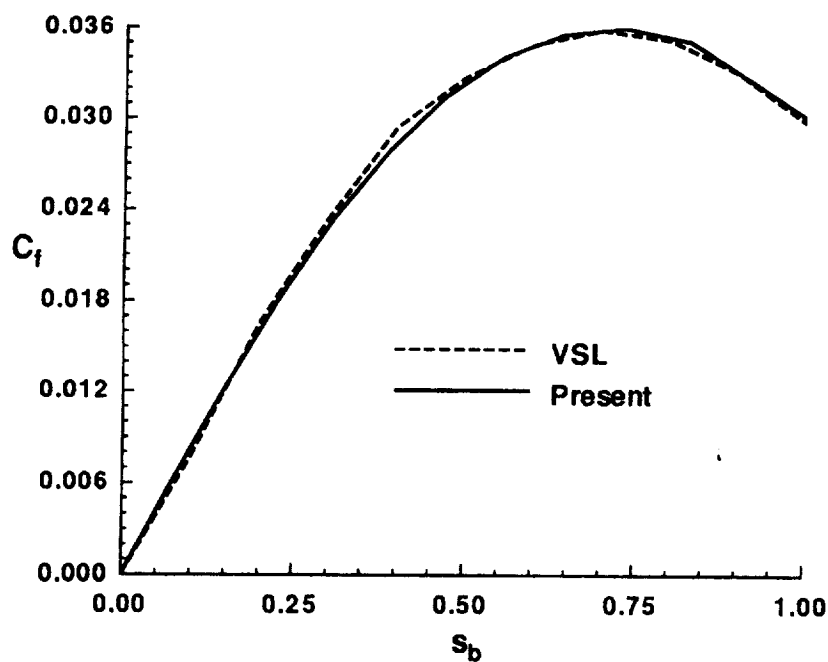
Figure 9.79. Skin friction comparison for $6°$ sphere-cone,
$R_{nose} = 1.5$ in (stagnation region).
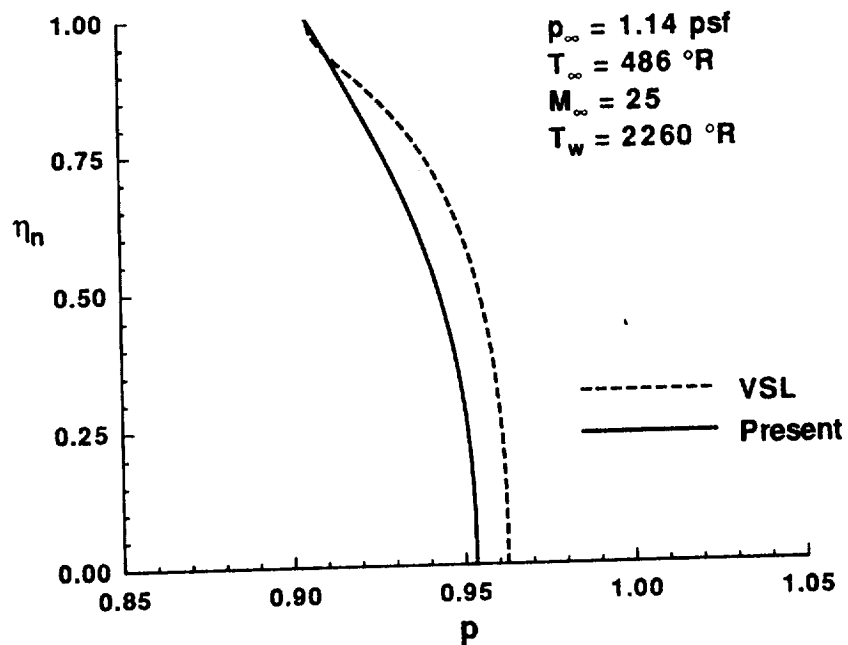
Figure 9.80. Pressure profile comparison for 6° sphere-cone, $R_{nose} = 1.5$ *in* (stagnation line).
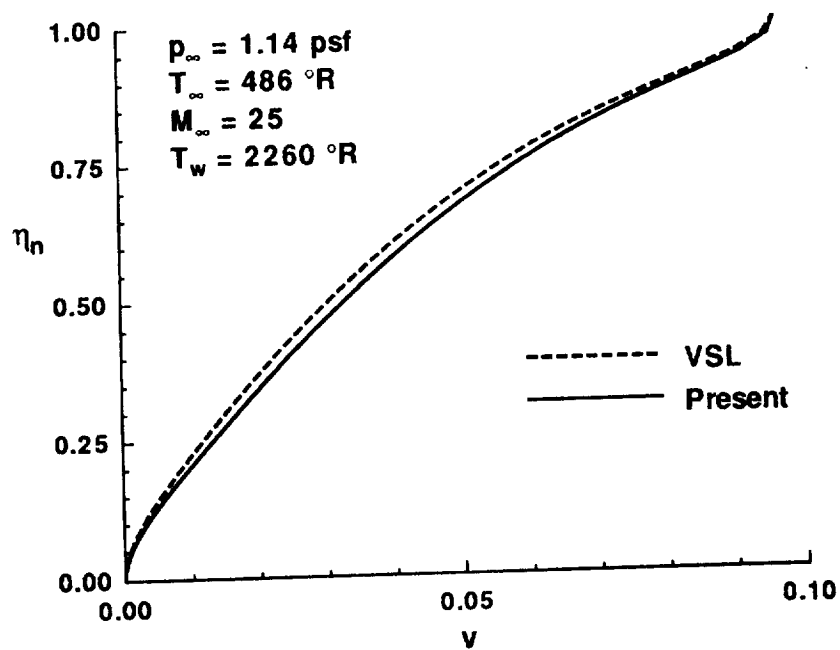
Figure 9.81. Normal velocity profile comparison for 6° sphere-cone, $R_{nose} = 1.5$ *in* (stagnation line).
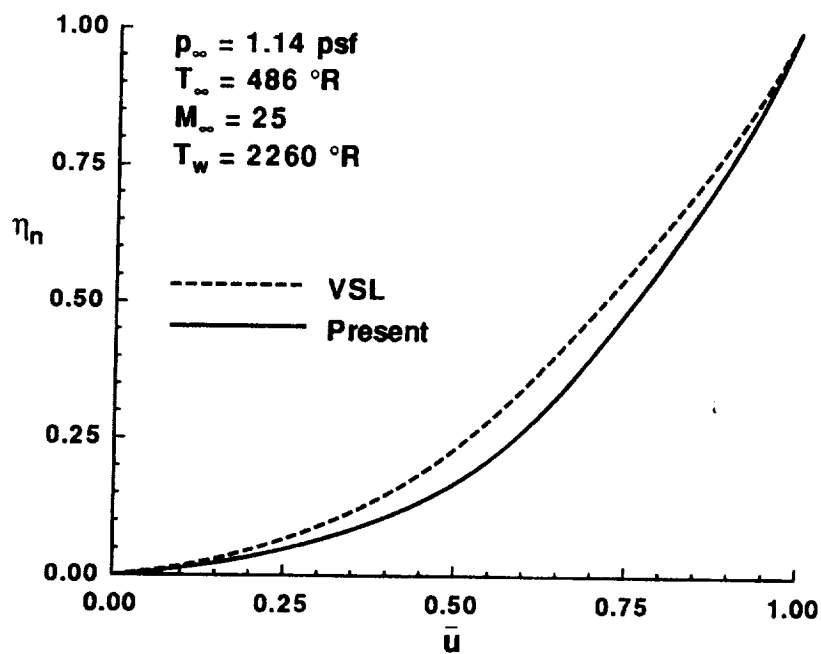
Figure 9.82. Tangential velocity profile comparison for 6° sphere-cone, $R_{nose} = 1.5$ *in* (stagnation line).
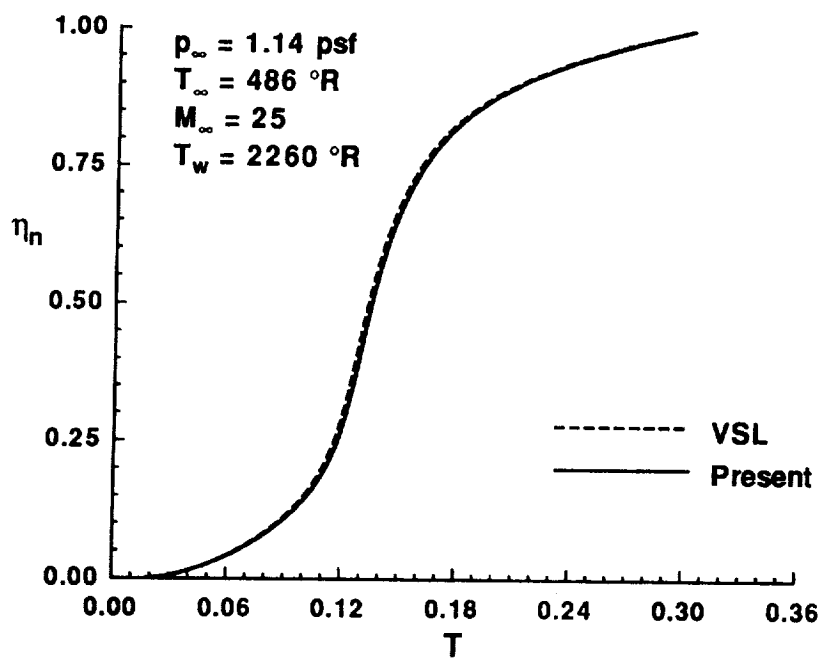
Figure 9.83. Temperature profile comparison for 6° sphere-cone, $R_{nose} = 1.5$ *in* (stagnation line).
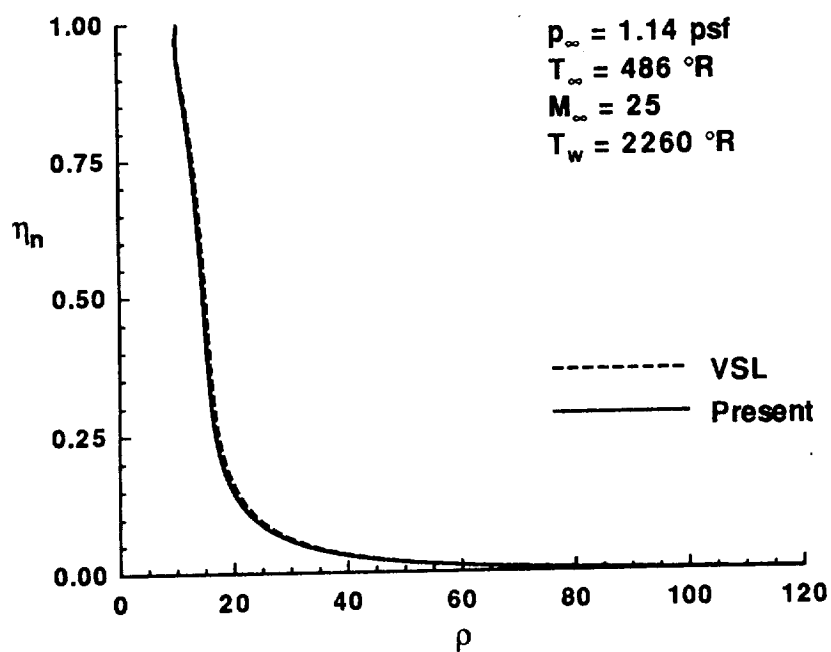
Figure 9.84. Density profile comparison for 6° sphere-cone, $R_{nose} = 1.5$ *in* (stagnation line).
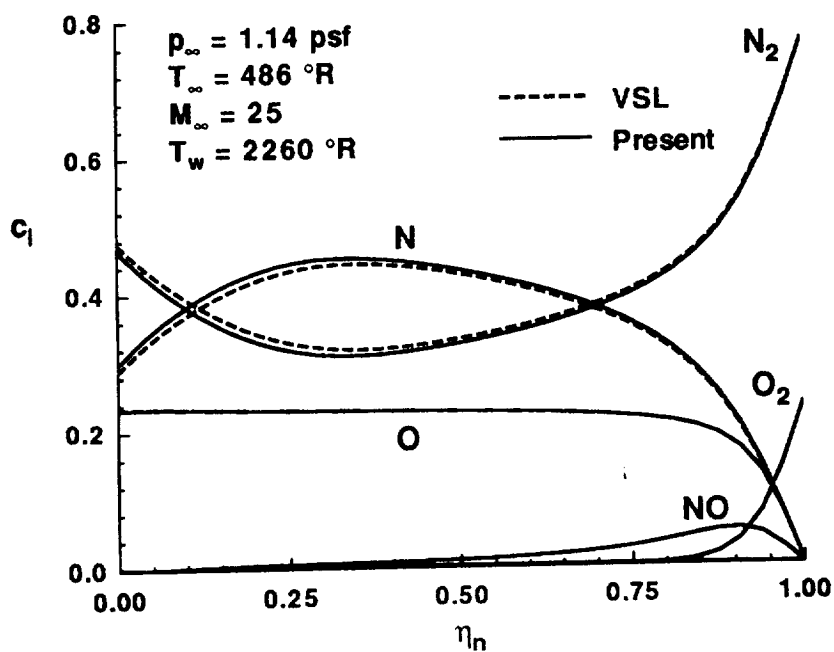
Figure 9.85. Mass fraction profile comparison for 6° sphere-cone, $R_{nose} = 1.5$ *in* (stagnation line).
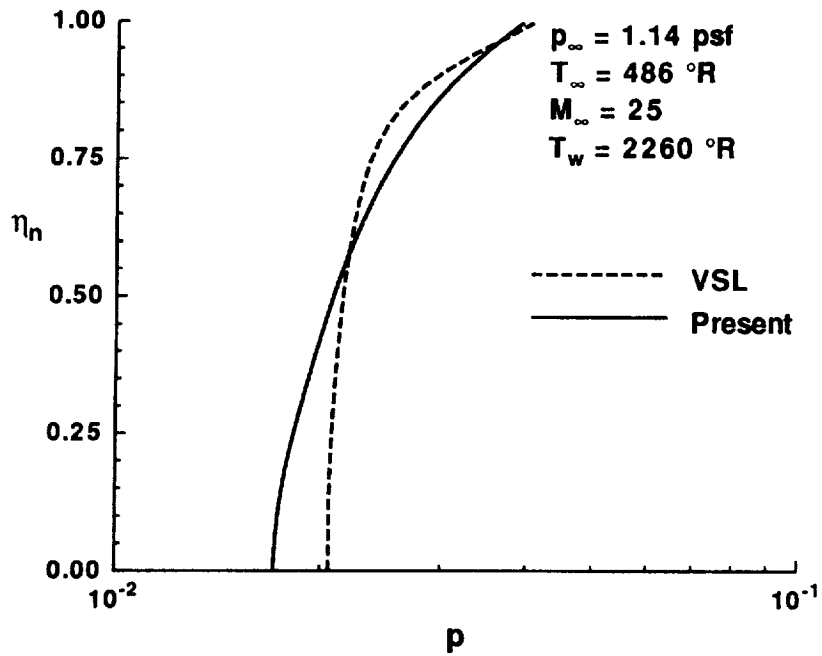
Figure 9.86. Pressure profile comparison for 6° sphere-cone, $R_{nose} = 1.5$ in $(s_b = 5)$.
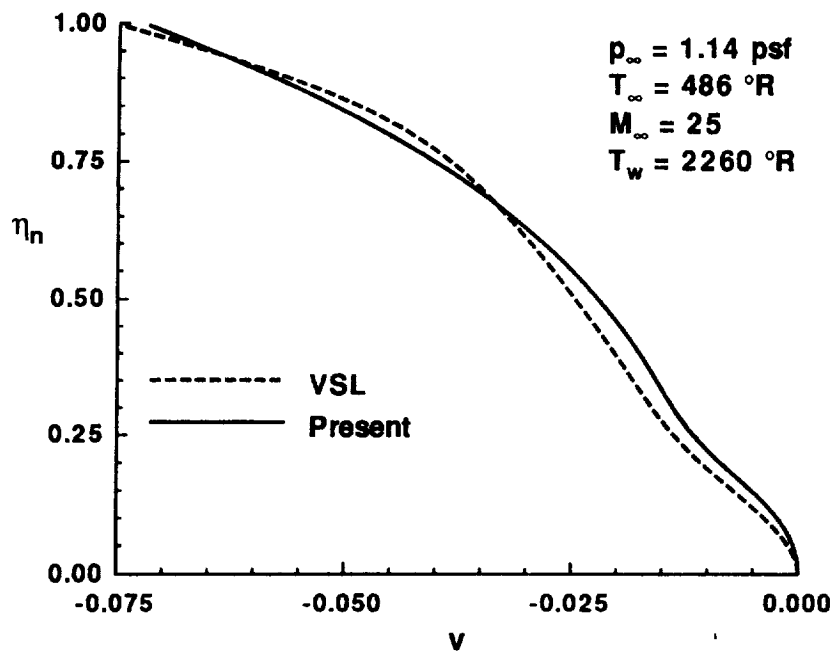
Figure 9.87. Normal velocity profile comparison for 6° sphere-cone, $R_{nose} = 1.5$ in $(s_b = 5)$.
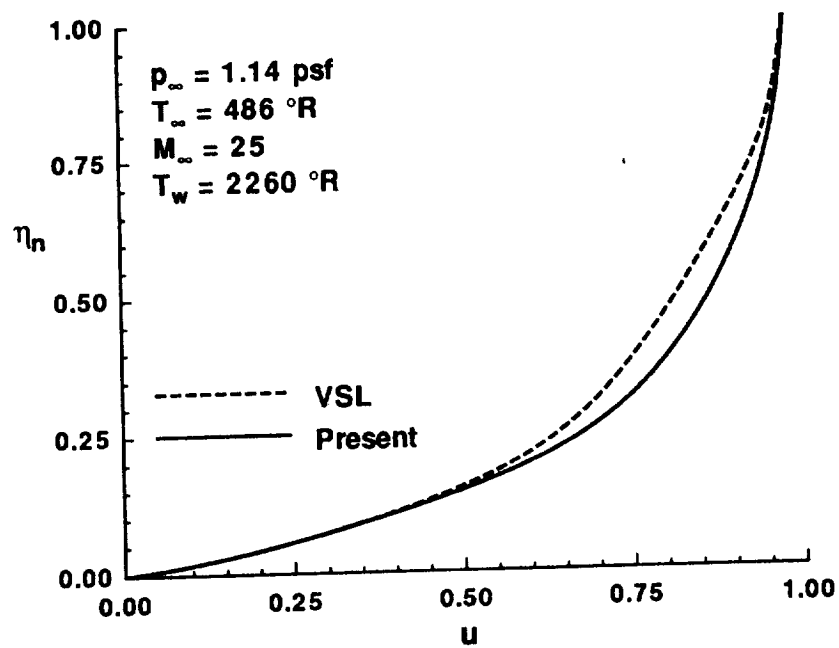
Figure 9.88. Tangential velocity profile comparison for $6°$ sphere-cone, $R_{nose} = 1.5$ *in* $(s_b = 5)$.
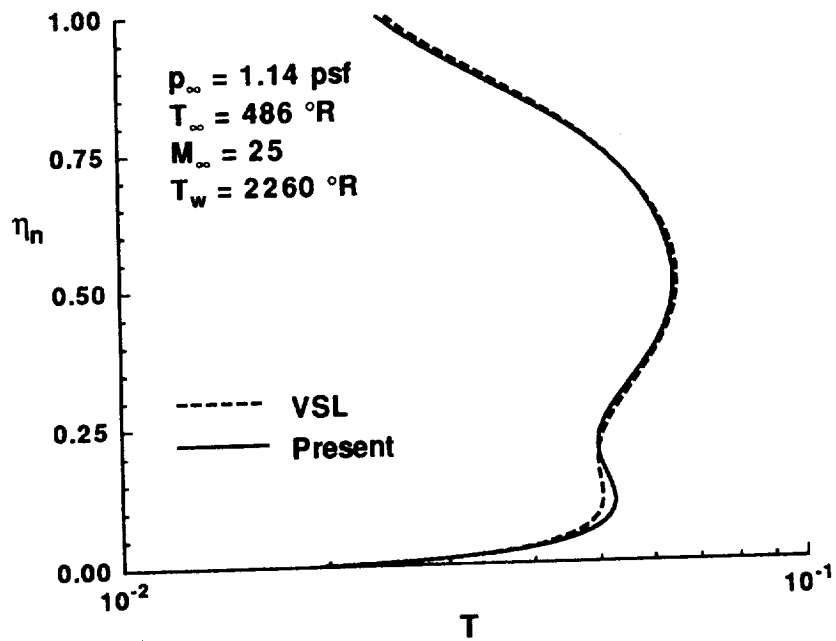
Figure 9.89. Temperature profile comparison for $6°$ sphere-cone, $R_{nose} = 1.5$ *in* $(s_b = 5)$.
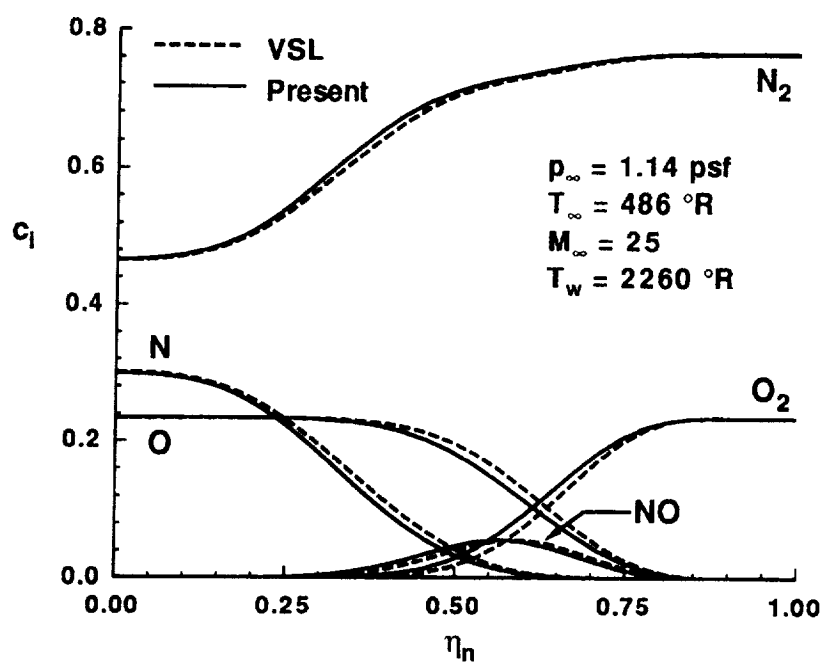
Figure 9.90. Mass fraction profile comparison for 6° sphere-cone,
$R_{nose} = 1.5$ in ($s_b = 5$).
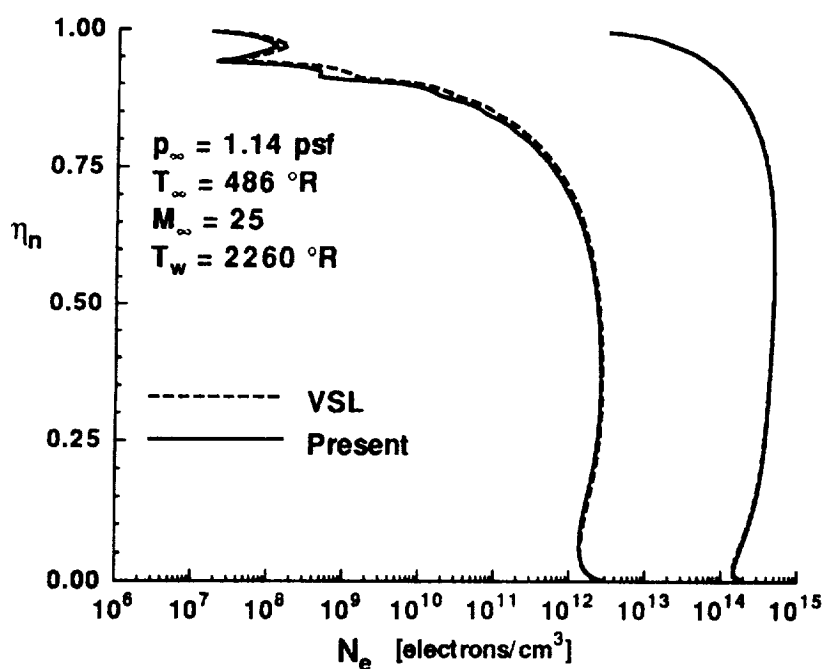
Figure 9.91. Comparison of electron concentration profiles for 6° sphere-cone,
$R_{nose} = 1.5$ in.

Table 9.3. Run-times[a] for 6° cone, $R_{nose} = 1.5$ in.

	VSL	Present
stations	46	38
CPU time	759	273
grid pts/sec	3	7
shock iterations	3.0	4.2
grid pts/sec/shock	9	30

a – Sun Sparcstation 1+

shown for the VSL results is the total time required for three shock iterations. As with the perfect gas comparison, the approximate algorithm yields a dramatic decrease in total CPU requirements relative to the VSL technique. Further, the last entry in the table shows that the the present method can process approximately three times as many grid points per second (for a given shock shape) as the VSL technique.
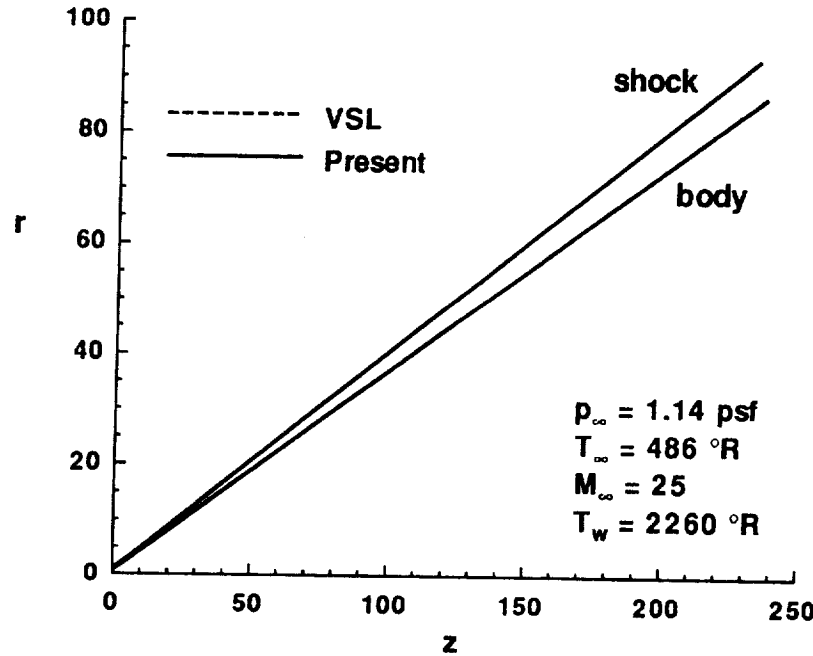
Figure 9.92. Shock shape comparison for 20° sphere-cone, $R_{nose} = 1.5$ in.

Case 2

As a second case, calculations are performed for the Mach 25 flow over a 20° sphere-cone ($R_{nose} = 1.5$ in) with the same freestream conditions as the previous case. Comparisons between the VSL [14] and current method are made for a body length of $s_{b_{end}} = 250$. The freestream conditions are $p_\infty = 0.00794$ psi and $T_\infty = 486^o R$, with a wall temperature of $T_w = 2260^o R$. Solutions are generated for both a noncatalytic and fully-catalytic wall condition (see Section 5.5.1).

Figure 9.92 shows that the shock shapes from the two methods are indistinguishable, once the flow has reached sharp cone conditions. Figure 9.93 shows that with this larger cone angle, the difference between the shock shapes is still very small in the overexpansion region. From Figures 9.94 and 9.95, the approximate and VSL surface heating results are generally within five percent of each other for both wall conditions and approach the stagnation value quite smoothly. Note that in the nose region the effects of wall catalysis are large (more than fifty percent), while further downstream this difference diminishes (to approximately twenty percent). The results of the present method do appear to satisfy $dq_w/ds_b = 0$ at the stagnation line more closely than the VSL approach. The catalytic boundary condition has little effect on the pressure, so only the fully-catalytic results for the body pressure distribution are presented in Figure 9.96. In this figure, the values from the two methods are nearly identical for $s_b > 20$. At the pressure minimum, the difference between results is approximately twenty percent. The behavior of the pressure in the stagnation region is identical to that of the previous case (Figure 9.77). The skin friction results of the
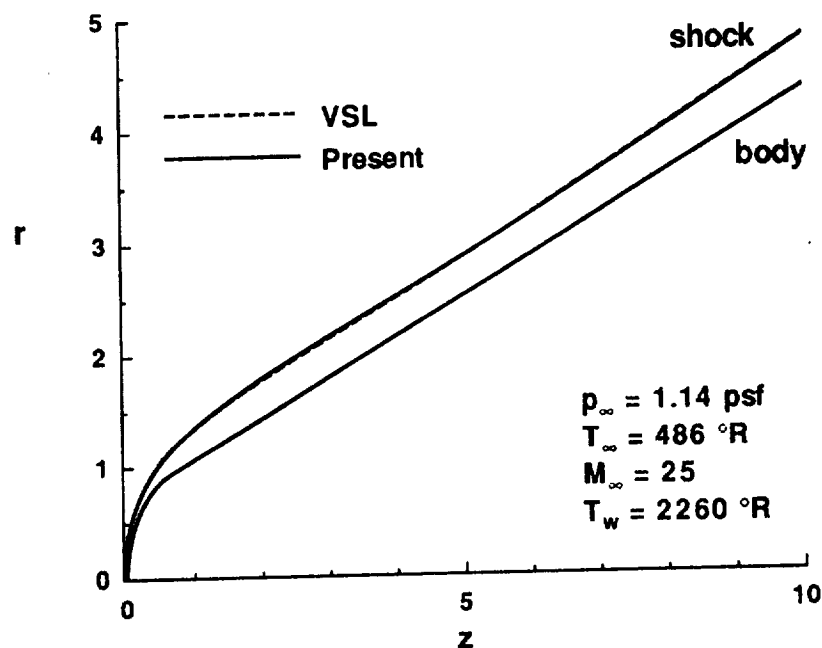
Figure 9.93. Shock shape comparison for $20°$ sphere-cone,
$R_{nose} = 1.5$ in (overexpansion region).

two methods for both catalytic conditions are presented in Figure 9.97. The two solutions are in good agreement for both wall conditions (generally within five percent), and show only a ten percent difference due to the wall catalysis.

Since the freestream conditions are the same as the previous case, and the geometry is still spherically-capped, the noncatalytic wall profiles for the stagnation line are identical to Figures 9.80 through 9.85. For the fully-catalytic wall solution, the profiles of p, v, and $\bar{u}$ are nearly indiscernible from those of Figures 9.80 through 9.82, so they are not shown here. The temperature and mass fractions (Figures 9.98 and 9.99) are visibly different from their noncatalytic-wall counterparts, although agreement between the two methods is still within five to ten percent. The mass fraction profile of NO^+ is not included in Figure 9.99, since only trace amounts are present for this case.

Again, profiles near the pressure minimum ($s_b \approx 3$) and at the end of the body ($s_b \approx 250$) are presented. Because the pressure and velocity profiles are not greatly affected by the wall catalytic condition, only the fully-catalytic wall results for the profiles of p, v, and $\bar{u}$ are presented. Figures 9.100 and 9.101 show that at the pressure minimum the pressure profiles are within ten to fifteen percent of each other while at the end station, the profiles are nearly indistinguishable. At the pressure minimum, the body-normal velocity components differ by twenty percent (Figure 9.102). Figure 9.103 shows these components to be in excellent agreement (within five percent)
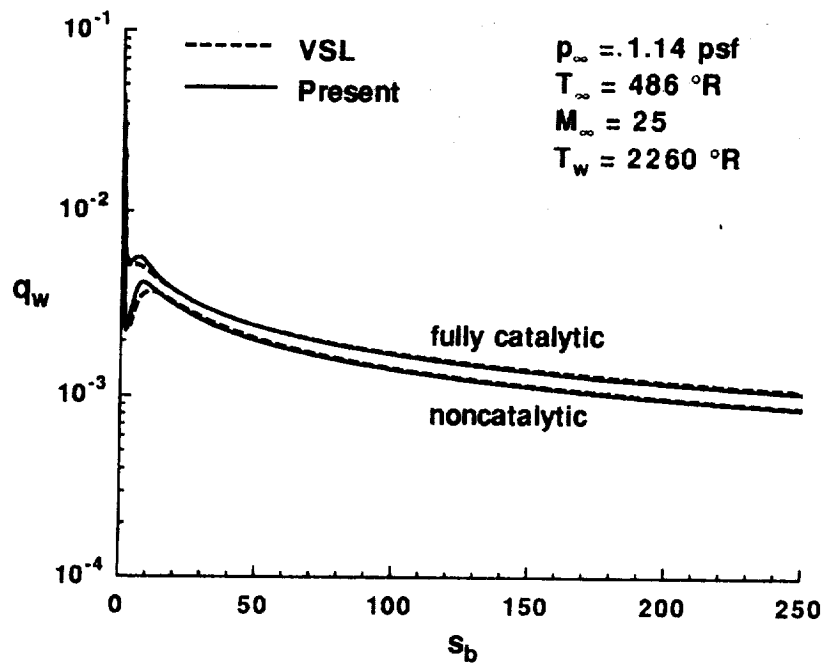
Figure 9.94. Heat transfer comparison for 20° sphere-cone, $R_{nose} = 1.5$ in.
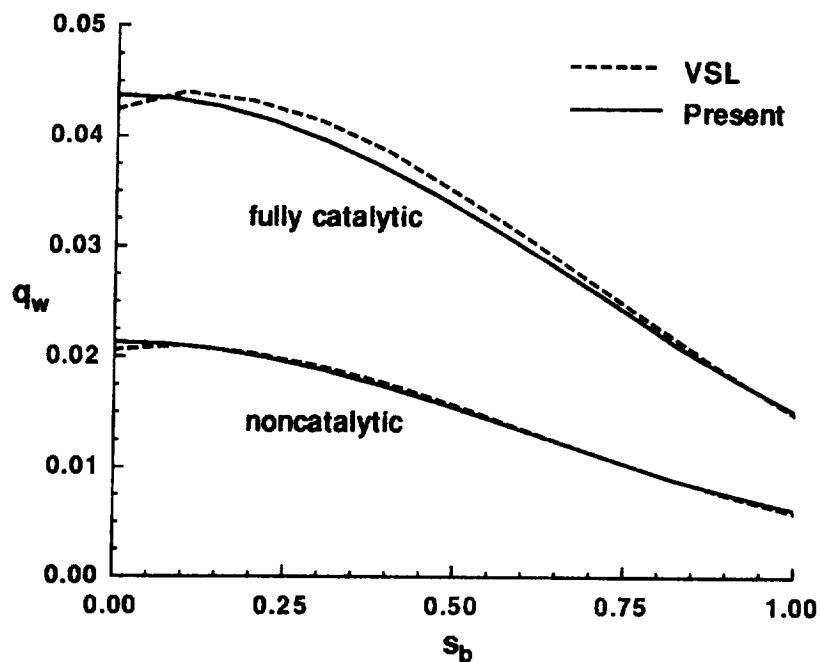
Figure 9.95. Heat transfer comparison for 20° sphere-cone,
$R_{nose} = 1.5$ in (stagnation region).
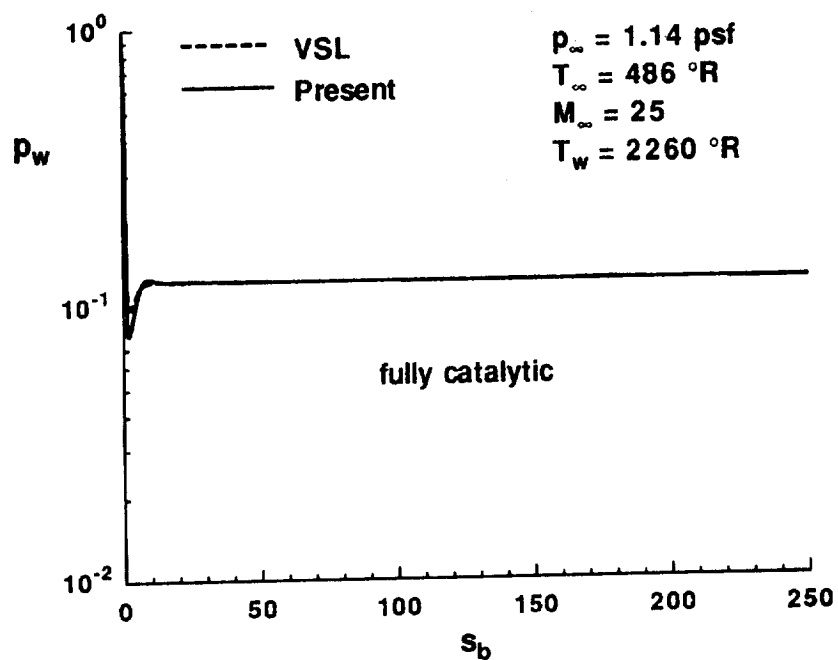
Figure 9.96. Body pressure comparison for 20° sphere-cone, $R_{nose} = 1.5$ *in.*
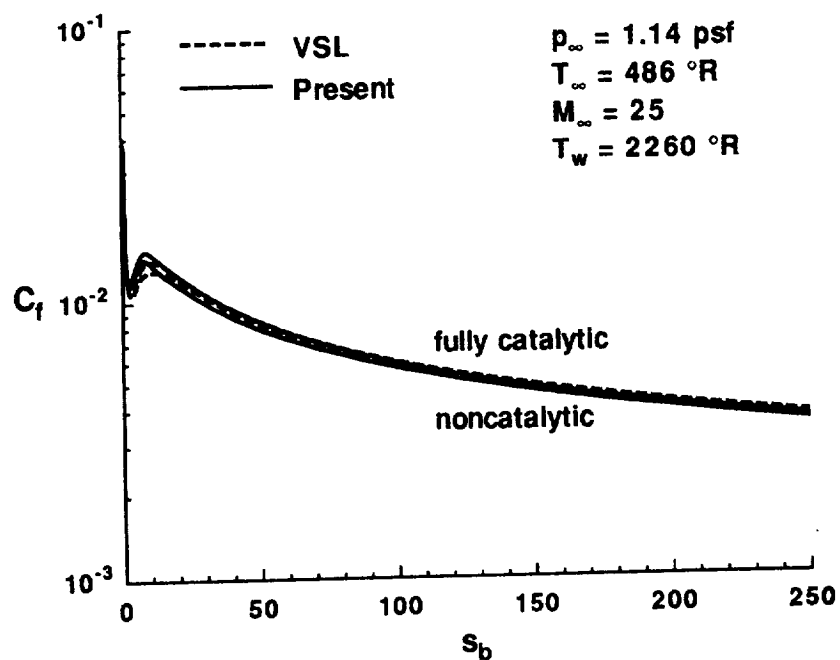
Figure 9.97. Skin friction comparison for 20° sphere-cone, $R_{nose} = 1.5$ *in.*
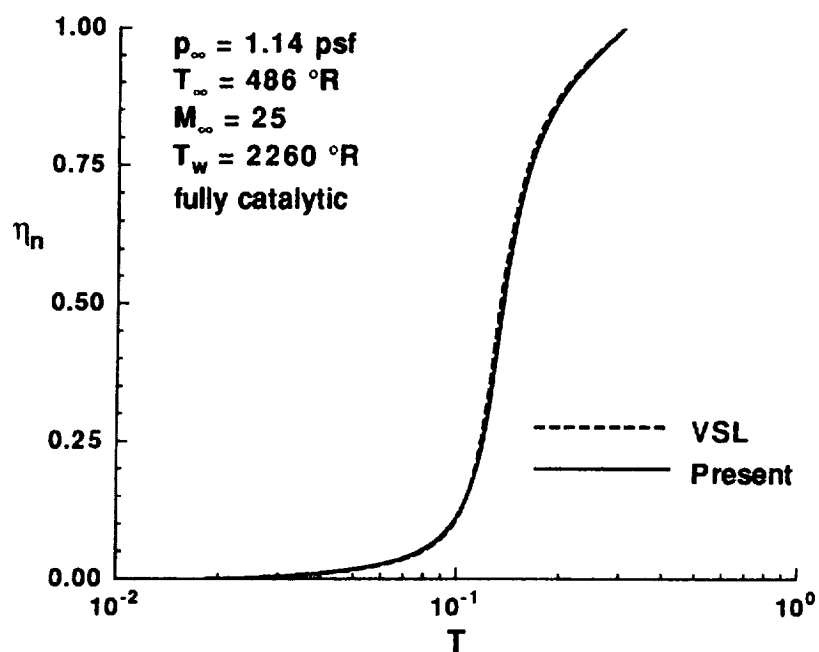
Figure 9.98. Temperature profile comparison for $20°$ sphere-cone, $R_{nose} = 1.5$ *in* (stagnation line).
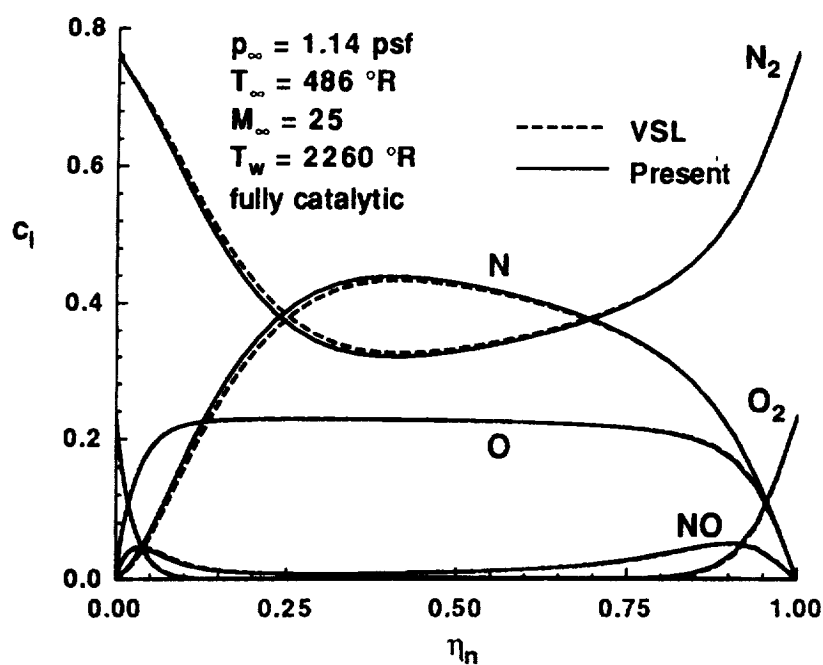
Figure 9.99. Mass fraction profile comparison for $20°$ sphere-cone, $R_{nose} = 1.5$ *in* (stagnation line).
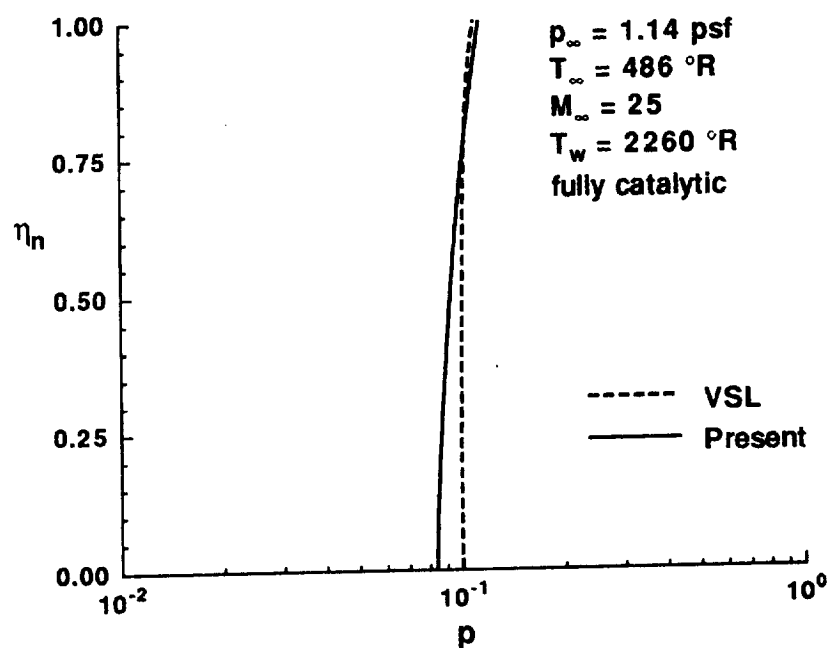
Figure 9.100. Pressure profile comparison for 20° sphere-cone, $R_{nose} = 1.5$ in $(s_b \approx 3)$.
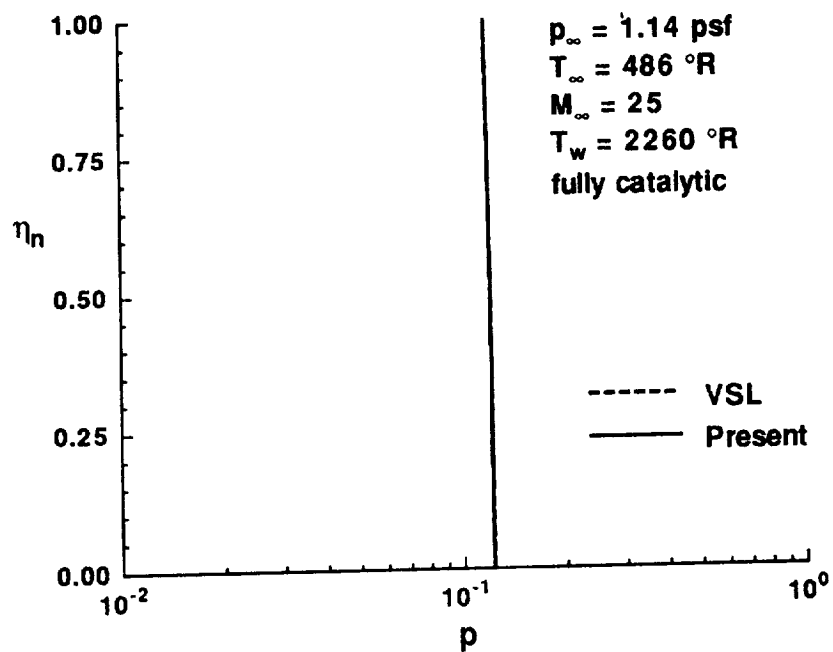
Figure 9.101. Pressure profile comparison for 20° sphere-cone, $R_{nose} = 1.5$ in $(s_b \approx 250)$.

Table 9.4. Run-times[a] for 20° cone, $R_{nose} = 1.5$ in.

	VSL	Present
stations	587	157
CPU time	7961	525
grid pts/sec	4	15
shock iterations	3.0	2.1
grid pts/sec/shock	11	33

a – Sun Sparcstation 1+

at the end station. The body-tangential velocity profiles at the pressure minimum (Figure 9.104) are in agreement near the body and shock, but deviate from one another in the interior of the shock layer. Figure 9.105 shows that at the end station these profiles are virtually identical. Temperature profiles at the two stations given above are shown in Figures 9.106 and 9.107 for the noncatalytic wall, and in Figures 9.108 and 9.109 for the fully-catalytic wall. At the pressure minimum, both sets of profiles are within approximately five percent of one another. The profiles at the end of the body are practically identical.

Mass fraction profiles at these two stations are shown in Figures 9.110 and 9.111 for the noncatalytic wall, and in Figures 9.112 and 9.113 for the fully-catalytic wall. At the pressure minimum, both sets of profiles are within approximately five percent of one another. Differences in the profiles at the end of the body are indistinguishable, with the chemistry effects concentrated in the near-wall region. Only trace amounts of NO^+ are present, so those profiles are excluded from The figures.

As a final comparison for this case, the electron density profiles for the three stations discussed above are considered. Figure 9.114 and 9.115 show generally good agreement between the methods for the noncatalytic and fully-catalytic wall solutions, respectively. The wiggles in the end station profiles at the boundary-layer edge are probably due to poor grid resolution there.

Table 9.4 shows the overall run times required to generate this solution. The value shown for the VSL results is the total time required for three shock iterations. Trends from the previous case are observed again here.
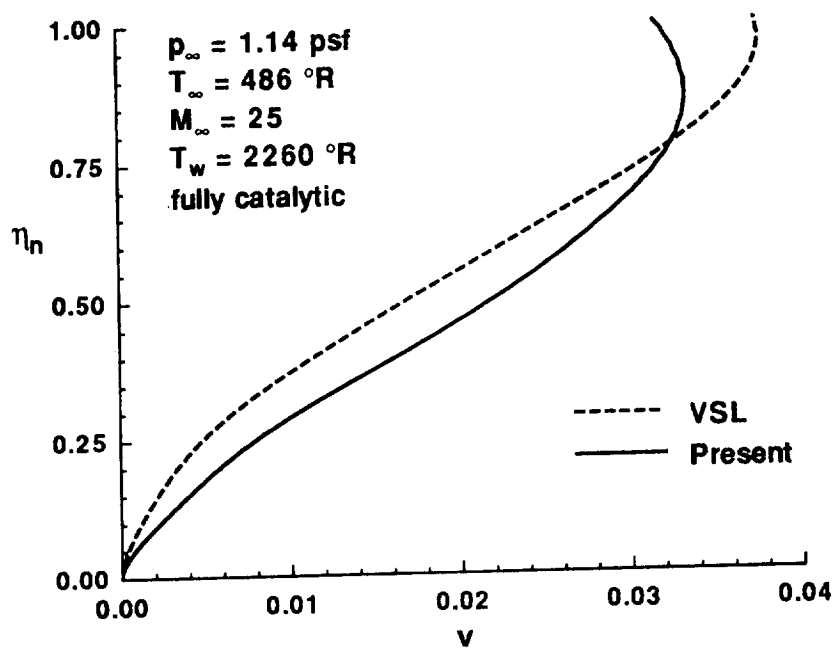
Figure 9.102. Normal velocity profile comparison for $20°$ sphere-cone, $R_{nose} = 1.5$ in $(s_b \approx 3)$.
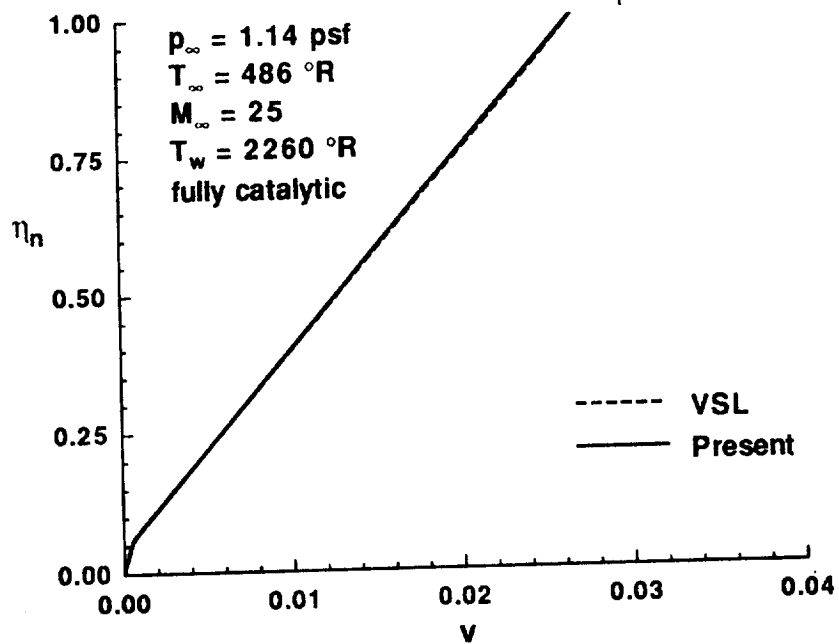
Figure 9.103. Normal velocity profile comparison for $20°$ sphere-cone, $R_{nose} = 1.5$ in $(s_b \approx 250)$.
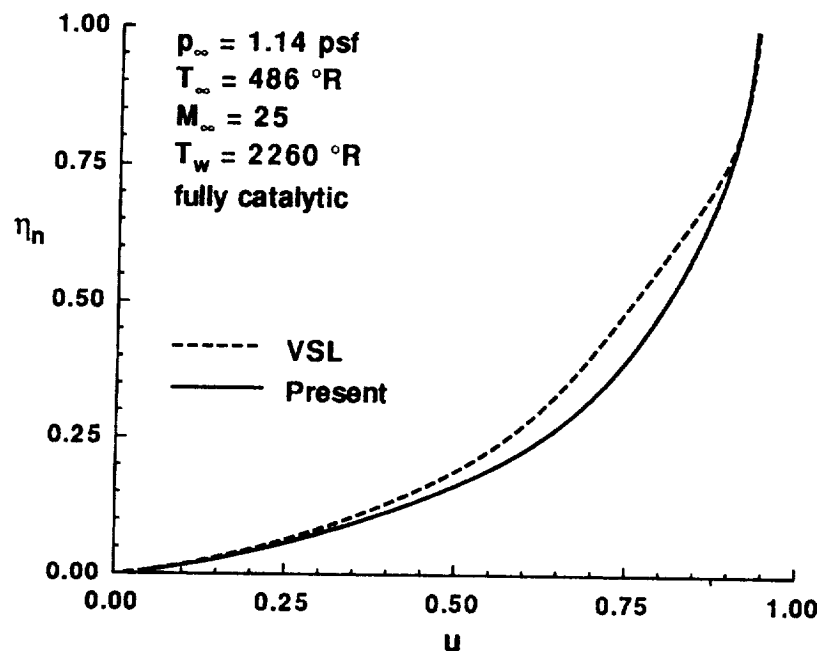
Figure 9.104. Tangential velocity profile comparison for $20°$ sphere-cone, $R_{nose} = 1.5$ in $(s_b \approx 3)$.
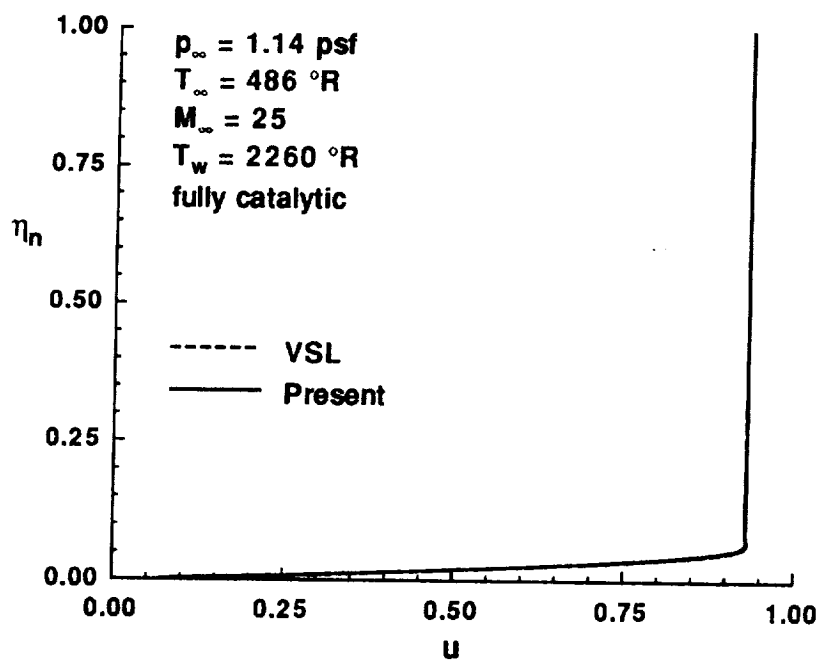
Figure 9.105. Tangential velocity profile comparison for $20°$ sphere-cone, $R_{nose} = 1.5$ in $(s_b \approx 250)$.
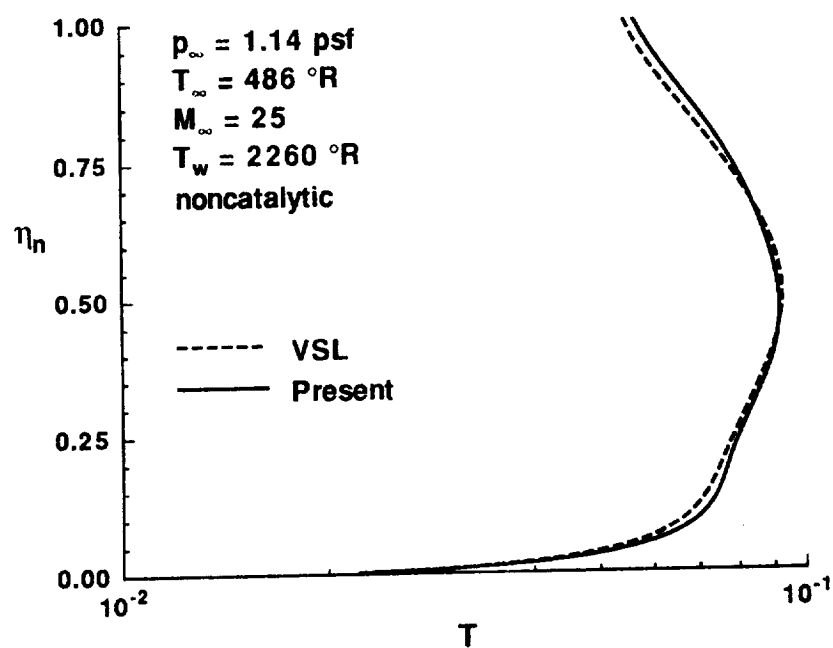
Figure 9.106. Temperature profile comparison for 20° sphere-cone,
$R_{nose} = 1.5$ *in* ($s_b \approx 3$).
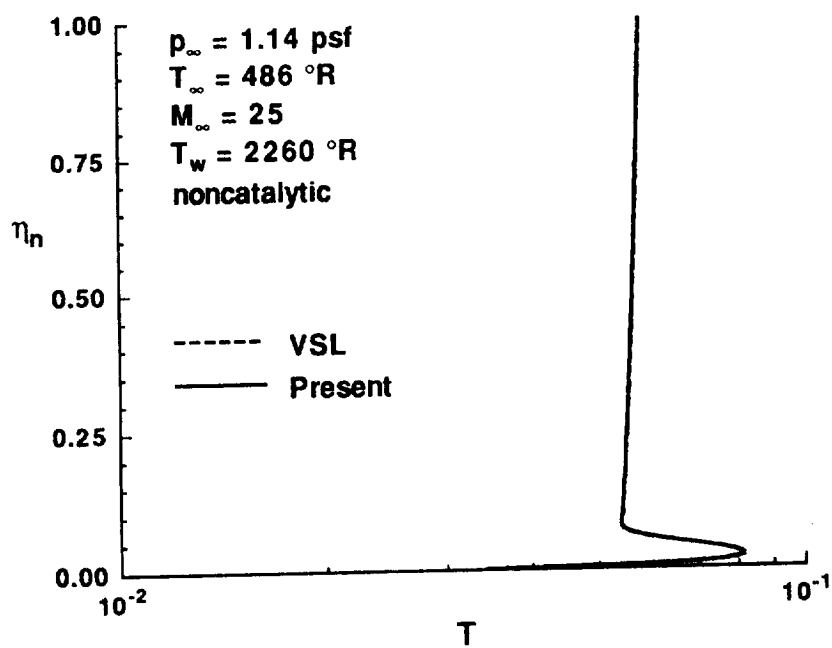
Figure 9.107. Temperature profile comparison for 20° sphere-cone,
$R_{nose} = 1.5$ *in* ($s_b \approx 250$).
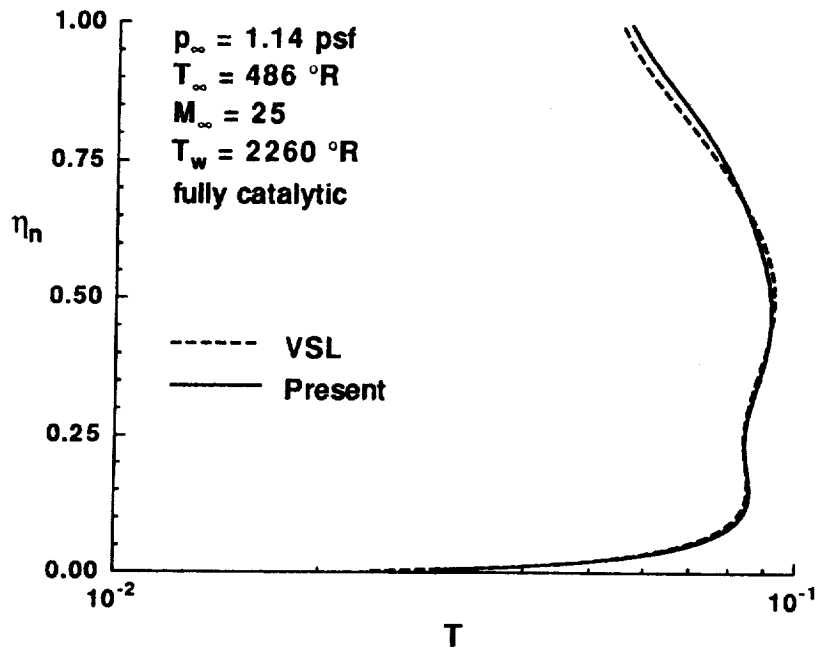
Figure 9.108. Temperature profile comparison for $20°$ sphere-cone, $R_{nose} = 1.5$ in $(s_b \approx 3)$.
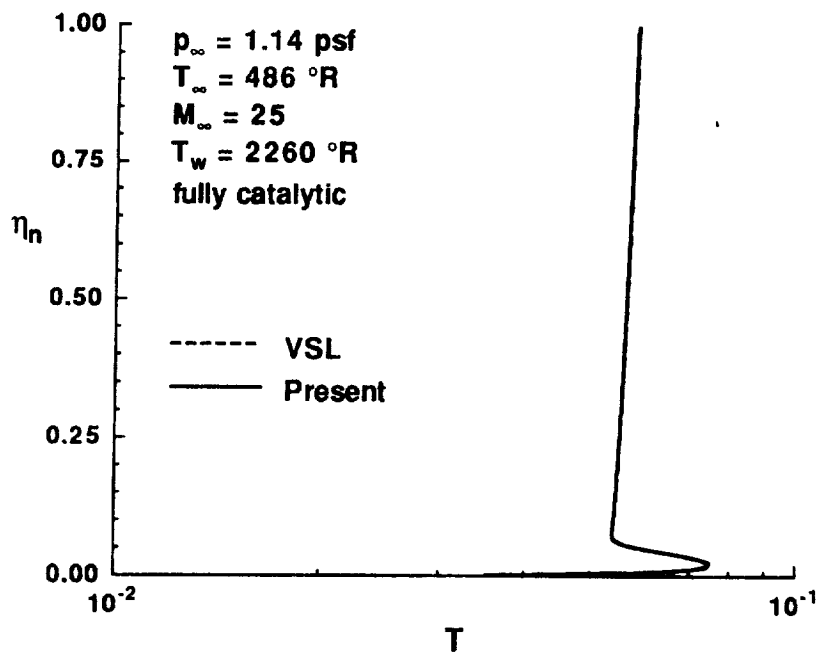
Figure 9.109. Temperature profile comparison for $20°$ sphere-cone, $R_{nose} = 1.5$ in $(s_b \approx 250)$.
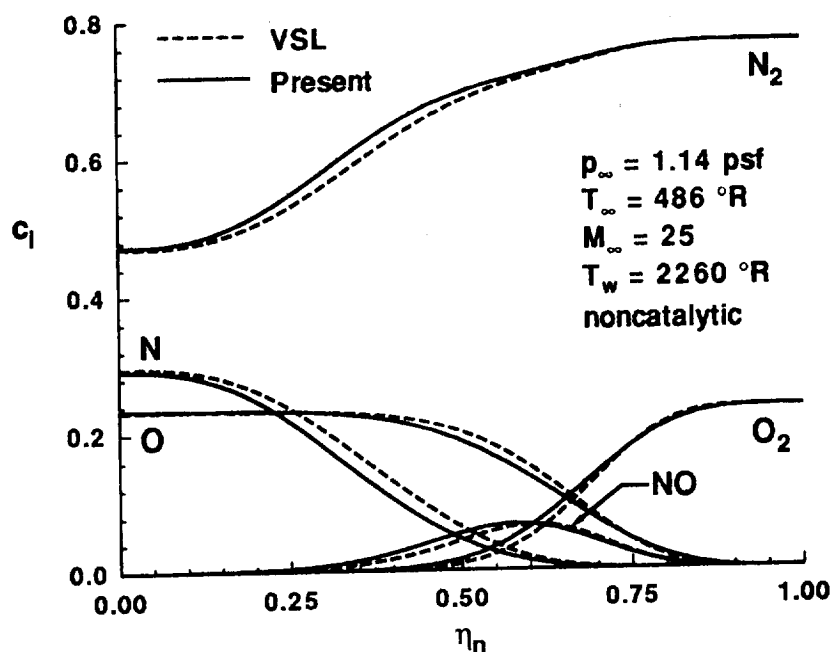
Figure 9.110. Mass fraction profile comparison for $20°$ sphere-cone, $R_{nose} = 1.5$ in $(s_b \approx 3)$.
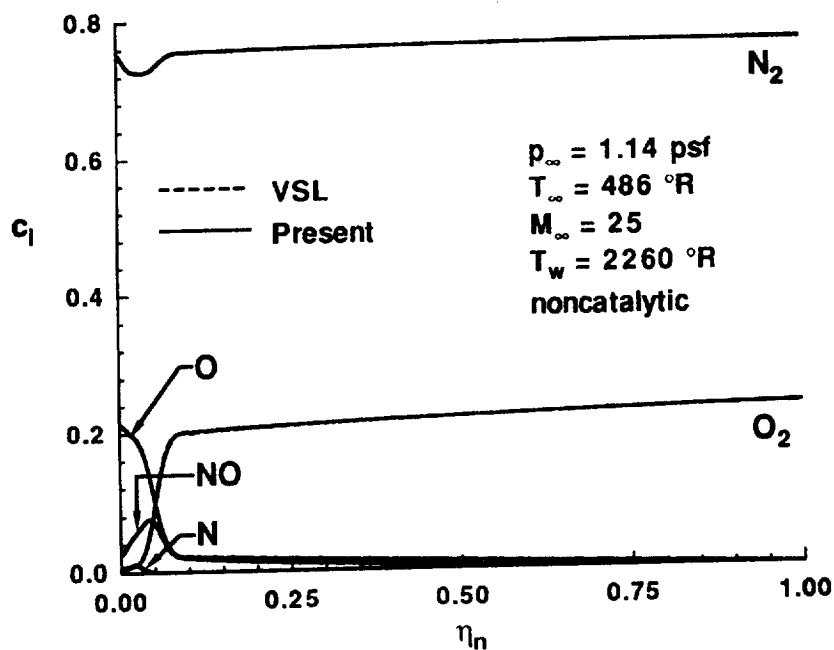
Figure 9.111. Mass fraction profile comparison for $20°$ sphere-cone, $R_{nose} = 1.5$ in $(s_b \approx 250)$.
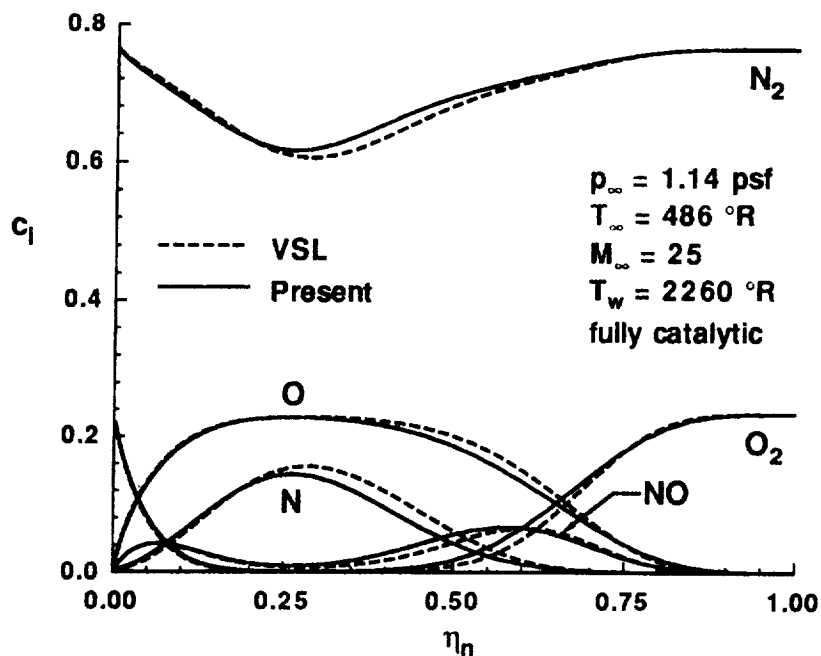
Figure 9.112. Mass fraction profile comparison for $20°$ sphere-cone,
$R_{nose} = 1.5$ in $(s_b \approx 3)$.
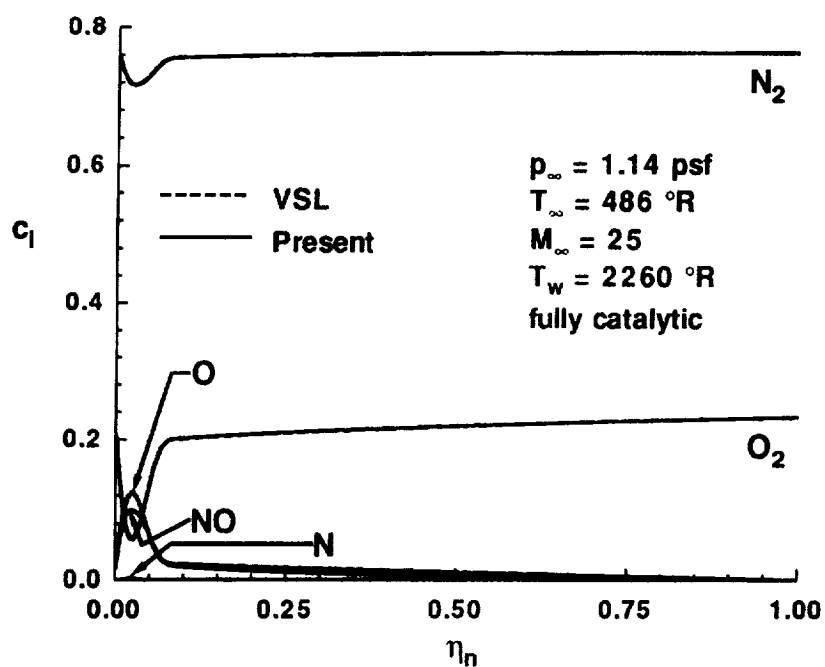
Figure 9.113. Mass fraction profile comparison for $20°$ sphere-cone,
$R_{nose} = 1.5$ in $(s_b \approx 250)$.
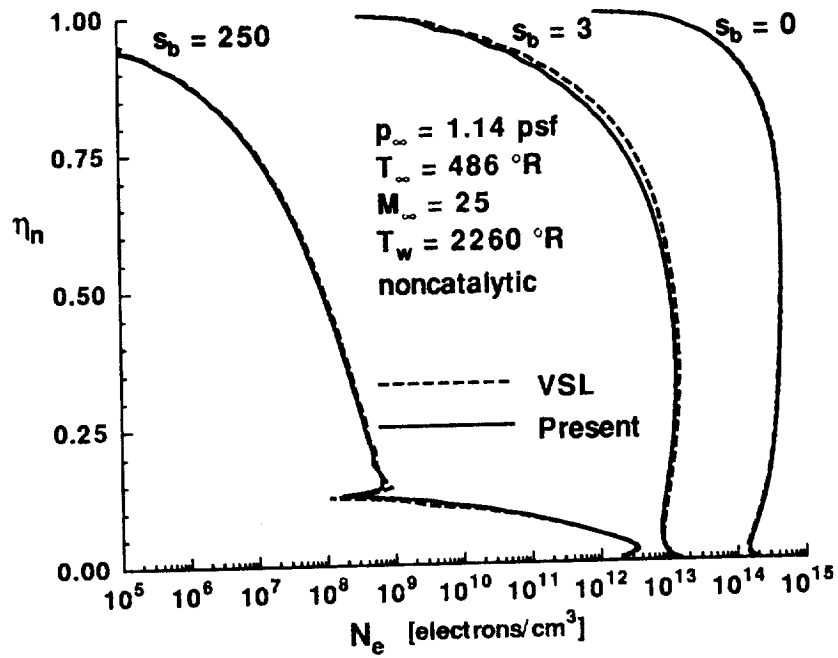
Figure 9.114. Comparison of electron concentration profiles for 20° sphere-cone, $R_{nose} = 1.5$ in.
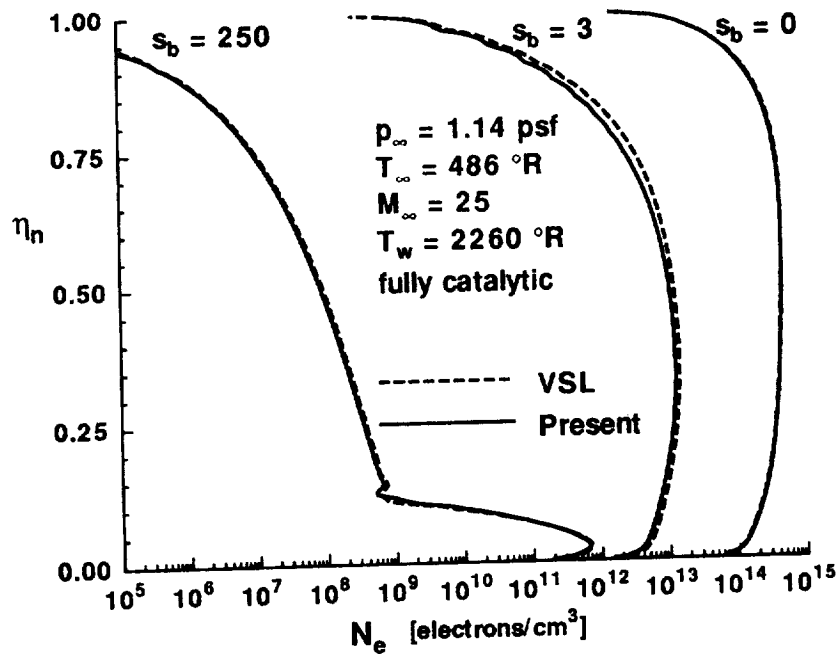
Figure 9.115. Comparison of electron concentration profiles for 20° sphere-cone, $R_{nose} = 1.5$ in.
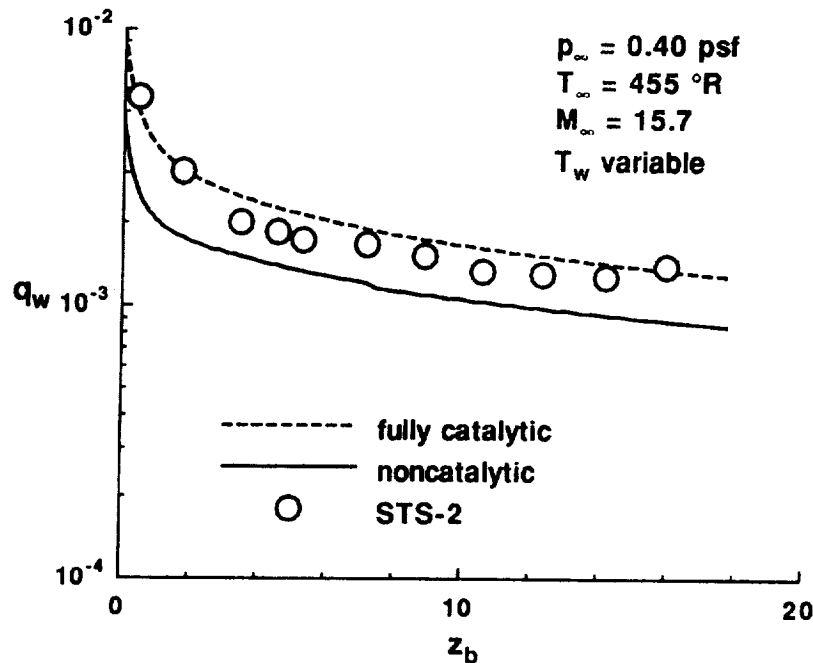
Figure 9.116. Heat transfer calculations for $42.75°$ hyperboloid, $R_{nose} = 4.489$ *ft.*

Case 3

In the past, hyperboloids have been used to model the windward symmetry plane of the Shuttle at angle of attack (see Ref. [74], for example). As a final case, the present method is used to calculate the Mach 15.7 flow over a $42.75°$ hyperboloid, which approximates the windward symmetry plane of the Shuttle at an angle of attack of $42°$. The nose radius is $R_{nose} = 4.489$ *ft* and the solution is computed for a body length of $s_{b_{end}} = 25$. The freestream conditions for an altitude of 60.56 *km* are $p_\infty = 0.00276$ *psi* and $T_\infty = 455°R$, with a variable wall temperature input. Solutions are calculated for noncatalytic and fully-catalytic wall conditions. Figure 9.116 compares the two heating rate distributions with Shuttle windward centerline measurements from STS-2 [31]. As expected these two calculations bracket the measured values. Note that the flight data is closest to the fully-catalytic result. Results presented in Ref. [74] also show the flight data falls closer to the fully-catalytic solution. Those results are for a hyperboloid geometry as well, and the solution is calculated from VSL method of Ref. [8].

10   Conclusions

A new approximate VSL approach to solving hypersonic flowfields about axisymmetric blunt bodies has been developed. The method is applied to sphere-cones and hyperboloids, over a freestream Mach number range of 10 to 25. The shock layer profiles, when compared to VSL solutions, are seen to be smooth and accurate for perfect gas and reacting flows. This is an improvement over the results of Grantz [27], and can be at least partially attributed to differences in the transformation variable for the normal direction.

Using Maslen's pressure relation in lieu of numerically integrating the normal momentum equation is shown to give accurate pressure profiles outside of the pressure overexpansion/recompression region. As a result, predicted body pressures are generally within five percent of the VSL values. Not surprisingly, computing the normal component of velocity from the continuity equation, instead of using the approximate relation of Ref. [29], is shown to yield profiles which are more consistent with a full VSL solution. Because this component is small relative to the tangential velocity, the impact of the approximate normal velocity expression on the tangential velocity profiles is minimal except in the near-wall region.

Turning to heat transfer calculations for perfect gas flows, excellent agreement between the VSL and approximate approaches is seen in the nose region. Within the pressure overexpansion/recompression region, the Grantz [29] and present methods yield comparable results which deviate from the VSL solution. Further downstream, as the sharp-cone limit is approached, the present technique shows good agreement with the VSL solution, while the results of Ref. [29] are higher. This deviation appears to be due to the normal velocity inaccuracies (mentioned above) having an effect on the near-wall enthalpy profiles. For reacting flows, both equilibrium and nonequilibrium, results from the present approach consistently exhibit good agreement with VSL solutions. The Reynolds analogy relates the heating rate to the skin friction, so it is not surprising to see that the skin friction results from the present and VSL approaches are in good agreement in those regions where the heating results agree well.

In the present method, a limiting form of the governing equations can be obtained for use on the stagnation line. A different approach is used in Ref. [29], with only limited success. As a direct result of the formulation used here, the surface properties calculated with the present method approach their stagnation values more smoothly than those of Ref. [29] or the VSL solution.

Run time comparisons between the present and VSL [9, 14] approaches for perfect gas and reacting flows show typically an order of magnitude reduction in overall CPU requirements. Further analysis shows that for a given shock shape and time interval, the present technique can process two to three times more grid points than

the VSL algorithm. Based on the accuracy of the computed surface properties, this new approach could be useful in the preliminary design environment. Alternately, it could be used to generate an initial shock shape for more exact methods which require starting solutions.

11 Recommendations

For this new approach to be most useful in the design environment, its extension to three-dimensional flows is required. The approximate approach of Ref. [29] does not provide the desired accuracy, so the transverse momentum equation (or an approximate form of it) probably would need to be included in the governing equation set. In addition, certain facets of the ongoing research by Riley and DeJarnette [69] concerning the inviscid solution of three-dimensional flows might be extended to viscous flows.

Run-time comparisons show the present technique is significantly faster than the VSL approach. However, especially for nonequilibrium flows, it is unclear whether this is due primarily to Maslen's approximate relation or to other techniques developed herein to increase computational efficiency. It would be interesting to see if the run time would be increased by a large amount with the normal momentum equation included. In this scenario, the full VSL equations would be solved in a shock-normal system.

The present method employs a marching procedure without global iterations in the region where the outer portion of the shock layer is supersonic. As a result, the physically correct phenomenon of information propagating upstream through the subsonic portion of the boundary layer is neglected. With the VSL approach, global passes followed by shock-shape smoothing allow information to propagate upstream. An investigation into the effect of this omission in the current approach is warranted.

Currently, calculations cannot be made for very blunt bodies (greater than approximately 45°). This limitation prevents the calculation of flowfields over many ASTV-type vehicles. The shock shape equation for the subsonic-transonic region would require modification before such computations could be performed.

As a final comment, a more sophisticated procedure for determining the streamwise step size in the marching region would yield significant improvements in overall computational requirements. Such improvements would be most noticeable in the pressure overexpansion/recompression region.

References

[1] J. D. Anderson, Jr. "A Survey of Modern Research in Hypersonic Aerodynamics". AIAA Paper 84-1578, June 1984.

[2] O. M. McWherter, R. W. Noack, and W. L. Oberkampf. "Evaluation of Inviscid/Boundary Layer and Parabolized Navier-Stokes Solutions for Design of Reentry Vehicles". AIAA Paper 84-0486, January 1984.

[3] P. A. Gnoffo. "An Upwind-Biased Point-Implicit Relaxation Algorithm for Viscous, Compressible Perfect-Gas Flows". NASA TP 2953, June 1990.

[4] W. S. Helliwell, R. P. Dickson, and S. C. Lubard. "Viscous Flow over Arbitrary Geometries at High Angles of Attack". *AIAA Journal*, Volume 19: pages 191–197, February 1981.

[5] P. A. Gnoffo. "Hypersonic Flows Over Biconics Using a Variable-Effective-Gamma, Parabolized Navier Stokes Code". AIAA Paper 83-1666, July 1983.

[6] S. L. Lawrence, D. S. Chaussee, and J. C. Tannehill. "Application of an Upwind Algorithm to the Three-Dimensional Parabolized Navier-Stokes Equations". AIAA Paper 87-1112-CP, June 1987.

[7] R. T. Davis. "Numerical Solution of the Hypersonic Viscous Shock Layer Equations". *AIAA Journal*, Volume 8(Number 5): pages 843–851, May 1970.

[8] J. N. Moss. "Reacting Viscous Shock-Layer Solutions with Multicomponent Diffusion and Mass Injection". NASA TR R-411, June 1974.

[9] A. L. Murray and C. H. Lewis. "Hypersonic Three-Dimensional Viscous Shock Layer Flows over Blunt Bodies". *AIAA Journal*, Volume 16: pages 1279–1286, December 1978.

[10] R. N. Gupta, P. A. Gnoffo, and R. W. MacCormack. "Viscous Shock-Layer Flowfield Analysis by an Explicit-Implicit Method". *AIAA Journal*, Volume 23: pages 723–732, May 1985.

[11] E. C. Anderson and J. N. Moss. "Viscous-Shock-Layer Solution for Turbulent Flow of Radiation Gas Mixtures in Chemcal Equilibrium". NASA TM-X 72764, August 1975.

[12] J. V. Rakich, D. A. Stewart, and M. J. Lanfranco. "Results of a Flight Experiment on the Catalytic Efficiency of the Space Shuttle Heat Shield". AIAA Paper 82-0944, June 1982.

[13] E. W. Miner and C. H. Lewis. "Hypersonic Ionizing Air Viscous Shock-Layer Flows Over Nonanalytic Blunt Bodies". NASA CR 2550, May 1975.

[14] S. Swaminathan, M. D. Kim, and C. H. Lewis. "Three-Dimensional Nonequilibrium Viscous Shock-Layer Flows Over Complex Geometries". AIAA Paper 83-0212, January 1983.

[15] F. G. Blottner. "Viscous Shock Layer at the Stagnation Point with Nonequilibrium Air Chemistry". *AIAA Journal*, Volume 7(Number 12): pages 2281–2288, December 1969.

[16] R. N. Gupta and A. L. Simmonds. "Hypersonic Low-Density Solutions of the Navier-Stokes Equations with Chemical Nonequilibrium and Multicomponent Surface Slip". AIAA Paper 86-1349, June 1986.

[17] B. A. Bhutta and C. H. Lewis. "Recent Improvements in the Nonequilibrium VSL Scheme for Hypersonic Blunt-Body Flows". AIAA Paper 91-0469, January 1991.

[18] S. H. Maslen. Inviscid hypersonic flow past smooth symmetric bodies. *AIAA Journal*, Volume 5: pages 1055–1061, June 1964.

[19] W. L. Grose. *An Approximate Solution to the Nonequilibrium Flow in the Inviscid Shock Layer about a Vehicle in Hypersonic Flight in an Arbitrary Atmosphere.* PhD thesis, Virginia Polytechnic Institute, June 1969.

[20] W. L. Grose. "A Thin-Shock-Layer Solution for Nonequilibrium, Inviscid Hypersonic Flows in Earth, Martian, and Venusian Atmospheres". NASA TN D-6529, December 1971.

[21] S. H. Maslen. "Asymmetric Hypersonic Flow". NASA CR 2133, September 1971.

[22] E. V. Zoby and R. A. Graves, Jr. "A Computer Program for Calculating the Perfect Gas Inviscid Flow Field About Blunt Axisymmetric Bodies at an Angle of Attack of 0 Degrees". NASA TM-X 2843, December 1973.

[23] S. K. Jackson. *The Viscous-Inviscid Hypersonic Flow of a Perfect Gas over Smooth Symmetric Bodies.* PhD thesis, University of Colorado, August 1966.

[24] E. V. Zoby and A. L. Simmonds. "Engineering Flowfield Method with Angle of Attack Applications,". *Journal of Spacecraft and Rockets*, Volume 22(Number 4): pages 398–404, July-August 1985.

[25] E. V. Zoby. "Approximate Heating Analysis for the Windward Plane of Shuttle-Like Bodies at Large angles of Attack". In T. E. Horton, editor, *Thermophysics*

of Atmospheric Entry; Progress in Astronautics and Aeronautics, volume Volume 82, pages 229–247. AIAA, New York, 1982.

[26] F. R. DeJarnette, H. H. Hamilton II, K. J. Weilmuenster, and F. M. Cheatwood. "A Review of Some Approximate Methods Used in Aerodynamic Heating Analyses". AIAA Paper 85-0906, June 1985.

[27] A. C. Grantz. *An Approximate Viscous Shock Layer Method for Calculating the Hypersonic Flow over Blunt-Nosed Bodies*. PhD thesis, North Carolina State University, 1989.

[28] A. C. Grantz, F. R. DeJarnette, and R. A. Thompson. "An Approximate Viscous Shock Layer Method for Calculating the Hypersonic Flow over Blunt-Nosed Bodies". AIAA Paper 89-1695, June 1989.

[29] A. C. Grantz, F. R. DeJarnette, and R. A. Thompson. "Approximate Viscous Shock-Layer Method for Hypersonic Flow over Blunt-Nosed Bodies". *Journal of Spacecraft and Rockets*, Volume 27(Number 6): pages 597–605, November-December 1990.

[30] F. M. Cheatwood and F. R. DeJarnette. "An Approximate Viscous Shock Layer Approach to Calculating Hypersonic Flows about Blunt-Nosed Bodies". AIAA Paper 91-1348, June 1991.

[31] D. A. Throckmorton. "Benchmark Determination of Shuttle Orbiter Entry Aerodynamic Heat-Transfer Data". *Journal of Spacecraft and Rockets*, Volume 20: pages 219–224, May-June 1983.

[32] F. M. White. *Viscous Fluid Flow*. McGraw-Hill Book Company, New York, 1974.

[33] E. W. Miner, E. C. Anderson, and C. H. Lewis. "A Computer Program for Two-Dimensional and Axisymmetric Nonreacting Perfect Gas and Equilibrium Chemically Reacting Laminar, Transitional, and/or Turbulent Boundary Layer Flows". Technical Report VPI-E-71-8, Virginia Polytechnical Institute, May 1971.

[34] N. B. Cohen. "Correlation Formulas and Tables of Density and Some Thermodynamic Properties of Equilibrium Dissociating Air for Use in Solutions of the Boundary-Layer Equations". NASA TN D-194, February 1960.

[35] C. F. Hansen. "Approximations for the Thermodynamic and Transport Properties of High Temperature Air". NASA TR R-50, 1959.

[36] C. H. Lewis. "VSLNOSE: A Three-Dimensional Viscous Shock-Layer Code for Arbitrary Nosetips". Technical Report Volume I: Engineering Analysis, January 1983.

[37] W. E. Moeckel and K. C. Weston. "Composition and Thermodynamic Properties of Air in Chemical Equilibrium". NACA TN 4265, 1958.

[38] W. L. Bade. "Simple Analytical Approximation to the Equation of State of Dissociated Air". *ARS Journal*, Volume 29(Number 4), April 1959.

[39] S. Srinivasan, J. C. Tannehill, and K. J. Weilmuenster. "Simplified Curve Fits for the Thermodynamic Properties of Equilibrium Air". NASA RP 1181, August 1987.

[40] S. Srinivasan and J. C. Tannehill. "Simplified Curve Fits for the Transport Properties of Equilibrium Air". NASA CR 178411, December 1987.

[41] E. C. Anderson and J. N. Moss. "Numerical Solution of the Hypersonic Viscous-Shock-Layer Equations for Laminar, Transitional, and Turbulent Flows of a Perfect Gas Over Blunt Axially Symmetric Bodies". NASA TN D-7865, February 1975.

[42] M. C. Frieders, , and C. H. Lewis. "Effects of Mass Transfer into Laminar and Turbulent Boundary Layers over Cones at Angle of Attack". Technical Report VPI-AERO-031, Virginia Polytechnical Institute, March 1975.

[43] R. R. Thareja, K. Y. Szema, and C. H. Lewis. "Chemical Equilibrium Laminar or Turbulent Three-Dimensional Viscous Shock-Layer Flows". *Journal of Spacecraft and Rockets*, Volume 20: pages 454–460, September-October 1983.

[44] R. N. Gupta, K. P. Lee, E. V. Zoby, J. N. Moss, and R. A. Thompson. "Hypersonic Viscous Shock-Layer Solutions over Long Slender Bodies–Part I: High Reynolds Number Flows". *Journal of Spacecraft and Rockets*, Volume 27(Number 2): pages 175–184, March-April 1990.

[45] T. Cebeci and A. M. O. Smith. "A Finite-Difference Solution to the Incompressible Turbulent Boundary Layer Equations by an Eddy Viscosity Concept". In *Computation of Turbulent Boundary Layers, Volume 1*, pages 346–355. AFOSR-IFP-Stanford Conference, Stanford University, 1968.

[46] T. Cebeci. "Behavior of Turbulent Flow near a Porous Wall with Pressure Gradient". *AIAA Journal*, Volume 8: pages 2152–2156, December 1970.

[47] T. Cebeci and A. M. O. Smith. "A Finite-Difference Method for Calculating Compressible Laminar and Turbulent Boundary Layers". *Journal of Basic Engineering*, pages 523–535, September 1970.

[48] B. S. Baldwin and H. Lomax. "Thin Layer Approximation and Algebraic Model for Separated Turbulent Flows". AIAA Paper 78-0257, January 1978.

[49] L. A. King and D. A. Johnson. "Separated Transonic Airfoil Flow Calculations with a Nonequilibrium Turbulence Model". NASA TM 86830, 1985.

[50] T. J. Coakley. "Turbulence Modeling Methods for the Compressible Navier-Stokes Equations". AIAA Paper 83-1693, July 1983.

[51] E. R. Van Driest. "On Turbulent Flow Near a Wall". *Journal of Aeronautical Sciences*, Volume 23(Number 11): pages 1007-1011, November 1956.

[52] F. H. Clauser. "The Turbulent Boundary Layer". In H. L. Dryden and T. von Karmen, editors, *Vol. IV of Advances in Applied Mechanics*, pages 1-15. Academic Press, New York, 1956.

[53] P. S. Klebanoff. "Characteristics of Turbulence in a Boundary Layer with Zero Pressure Gradient". NACA Report 1247, 1955.

[54] S. Dhawan and R. Narashima. "Some Properties of Boundary Layer Flow during Transition from Laminar to Turbulent Motion". *Journal of Fluid Mechanics*, Volume 1(Part 4): pages 418-436, January 1958.

[55] P. S. Klebanoff. "Characteristics of Turbulence in a Boundary Layer with Zero Pressure Gradient". NACA TN 3178, July 1954.

[56] R. A. Thompson, E. V. Zoby, K. E. Wurster, and P. A. Gnoffo. "An Aerothermodynamic Study of Slender Conical Vehicles". AIAA Paper 87-1475, June 1987.

[57] J. E. Harris. "Numerical Solutions of the Equations for Compressible Laminar, Transitional and Turbulent Boundary Layers and Comparisons with Experimental Data". NASA TR 368, 1971.

[58] F. G. Blottner. "Finite-Difference Methods of Solution of the Boundary-Layer Equations". *AIAA Journal*, Volume 8(Number 2): pages 193-206, February 1970.

[59] R. T. Davis. "Hypersonic Flow of a Chemically Reacting Binary Mixture Past a Blunt Body". AIAA Paper 70-805, July 1970.

[60] R. A. Thompson, K. P. Lee, and R. N. Gupta. "Computer Codes for the Evaluation of Thermodynamic Properties, Transport Properties, and Equilibrium Constants of an 11-Species Air Model". NASA TM 102602, February 1990.

[61] R. N. Gupta, J. M. Yos, R. A. Thompson, and K. P. Lee. "A Review of Reaction Rates and Thermodynamic and Transport Properties for an 11-Species Air Model for Chemical and Thermal Nonequilibrium Calculations to 30,000 K". NASA RP 1232, August 1990.

[62] B. F. Armaly and K. Sutton. "Viscosity of Multicomponent Partially Ionized Gas Mixtures". AIAA Paper 80-1495, July 1980.

[63] E. A. Mason and S. C. Saxena. "Approximate Formula for the Thermal Conductivity of Gas Mixtures". *The Physics of Fluids*, Volume 3(Number 5): pages 361–369, September-October 1958.

[64] M. D. Van Dyke and H. D. Gordon. "Supersonic Flow Past a Family of Blunt Axisymmetric Bodies". NASA TR R-1, 1959.

[65] F. G. Blottner. "Introduction to Computational Techniques for Boundary Layers". Sandia Laboratories Release SAND 79-0893, September 1979.

[66] R. D. Richtmyer. *Difference Methods for Initial-Value Problems*. Interscience Publishers, Inc., New York, 1957.

[67] C. J. Riley. "An Approximate Method for Calculating Inviscid Flowfields Over Three-Dimensional Blunt-Nosed Bodies in Hypersonic Flow". Master's thesis, North Carolina State University, May 1988.

[68] C. J. Riley and F. R. DeJarnette. "An Approximate Method for Calculating Hypersonic Three-Dimensional Inviscid Flow Fields". NASA TP 3018, August 1990.

[69] C. J. Riley and F. R. DeJarnette. "Engineering Calculations of Three-Dimensional Inviscid Hypersonic Flow Fields". AIAA Paper 91-0701, January 1991.

[70] R. A. Thompson and E. V. Zoby. "Flowfield and Vehicle Parameter Influence on Hypersonic Heat Transfer and Drag". *Journal of Spacecraft and Rockets*, Volume 27(Number 4): pages 361–368, July-August 1990.

[71] J. W. Cleary. "Effects of Angle of Attack and Bluntness on Laminar Heating-Rate Distributions on a 15 Degree Cone at a Mach Number of 10.6". NASA TN 5450, October 1969.

[72] P. C. Stainback, C. B. Johnson, L. B. Boney, and K. C. Wicker. "Comparison of Theoretical Predictions and Heat-Transfer Measurements for a Flight Experiment at Mach 20 (Reentry F)". NASA TM-X 2560, 1972.

[73] R. A. Thompson, E. V. Zoby, K. E. Wurster, and P. A. Gnoffo. "Aerothermodynamic Study of Slender Conical Vehicles". *Journal of Thermophysics and Heat Transfer*, Volume 3(Number 4): pages 361–367, October 1989.

[74] J. L. Shinn, J. N. Moss, and A. L. Simmonds. "Viscous-Shock-Layer Heating Analysis for the Shuttle Windward Plane with Surface Finite Catalytic Recombination Rates". AIAA Paper 82-0842, June 1982.

[75] D. A. Anderson, J. C. Tannehill, and R. H. Pletcher. *Computational Fluid Mechanics and Heat Transfer.* Hemisphere Publishing Corporation, New York, 1984.

[76] J. D. Anderson, Jr. *Modern Compressible Flow: with Historical Perspective.* McGraw-Hill Book Company, New York, 1982.

[77] J. D. Anderson, Jr. *Hypersonic and High Temperature Gas Dynamics.* McGraw-Hill Book Company, New York, 1989.

[78] W. G. Vincenti and C. H. Kruger, Jr. *Introduction to Physical Gas Dynamics.* John Wiley and Sons, Inc., 1965.

A Reference Quantities

The governing equations are nondimensionalized according to the following relations:

$$s = \frac{s^\star}{R^\star_{nose}} \qquad n = \frac{n^\star}{R^\star_{nose}} \qquad h_3 = \frac{h^\star_3}{R^\star_{nose}}$$

$$z = \frac{z^\star}{R^\star_{nose}} \qquad r = \frac{r^\star}{R^\star_{nose}} \qquad \kappa_s = \kappa^\star_s R^\star_{nose}$$

$$u = \frac{u^\star}{V^\star_\infty} \qquad v = \frac{v^\star}{V^\star_\infty} \qquad \rho = \frac{\rho^\star}{\rho^\star_\infty}$$

$$p = \frac{p^\star}{p^\star_{ref}} \qquad h = \frac{h^\star}{h^\star_{ref}} \qquad \mu = \frac{\mu^\star}{\mu^\star_{ref}}$$

$$q = \frac{q^\star}{q^\star_{ref}} \qquad k = \frac{k^\star}{k^\star_{ref}} \qquad T = \frac{T^\star}{T^\star_{ref}}$$

$$\check{\mathcal{R}} = \frac{\check{\mathcal{R}}^\star}{C^\star_{p\infty}} \qquad C_p = \frac{C^\star_p}{C^\star_{p\infty}} \qquad \mathcal{R}_u = \frac{\mathcal{R}^\star_u}{C^\star_{p\infty}}$$

$$\tau = \frac{\tau^\star}{\tau^\star_{ref}} \qquad \dot{w}_i = \frac{\dot{w}^\star_i}{\dot{w}^\star_{ref}} \qquad \mathcal{J}_i = \frac{\mathcal{J}^\star_i}{\mathcal{J}^\star_{ref}}$$

The reference quantities are

$$p^\star_{ref} = \rho^\star_\infty V^{\star 2}_\infty \qquad\qquad h^\star_{ref} = V^{\star 2}_\infty$$

$$T^\star_{ref} = \frac{V^{\star 2}_\infty}{C^\star_{p\infty}} \qquad\qquad k^\star_{ref} = \mu^\star_{ref} C^\star_{p\infty}$$

$$q^\star_{ref} = \rho^\star_\infty V^{\star 3}_\infty \qquad\qquad \dot{w}^\star_{ref} = \frac{\rho^\star_\infty V^\star_\infty}{R^\star_{nose}}$$

$$\tau^\star_{ref} = \frac{V^\star_\infty \mu^\star_{ref}}{R^\star_{nose}} \qquad\qquad \mathcal{J}^\star_{ref} = \frac{\mu^\star_{ref}}{R^\star_{nose}}$$

and $\mu^\star_{ref}$ is the coefficient of viscosity evaluated at $T^\star_{ref}$.
In addition, the following dimensionless parameters appear in the equations:

$$Re = \frac{\rho^\star u^\star R^\star_{nose}}{\mu^\star} \qquad\qquad Pr = \frac{\mu^\star C^\star_p}{k^\star}$$

$$Le_{12_i} = \frac{\rho^\star C^\star_{p_f} \mathcal{D}^\star_{i,m}}{k^\star} \qquad\qquad Le_{12} = \frac{\rho^\star C^\star_{p_f} \mathcal{D}^\star_{12}}{k^\star}$$

$$\epsilon^2 = \frac{\mu^\star_{ref}}{\rho^\star_\infty V^\star_\infty R^\star_{nose}}$$

Units for the dimensional quantities used above are

$$R^\star_{nose} = [ft] \qquad\qquad V^\star_\infty = \left[\frac{ft}{s}\right] \qquad\qquad \rho^\star_\infty = \left[\frac{slug}{ft^3}\right]$$

$$p^\star_{ref} = \left[\frac{lb}{ft^2}\right] \qquad\qquad h^\star_{ref} = \left[\frac{ft^2}{s^2}\right] \qquad\qquad \mu^\star_{ref} = \left[\frac{slug}{ft\text{-}s}\right]$$

$$q^\star_{ref} = \left[\frac{BTU}{ft^2\text{-}s}\right] \qquad\qquad k^\star_{ref} = \left[\frac{BTU}{ft\text{-}s\text{-}^oR}\right] \qquad\qquad T^\star_{ref} = [^oR]$$

$$\tau^\star_{ref} = \left[\frac{lb}{ft^2}\right] \qquad\qquad \dot{w}^\star_{ref} = \left[\frac{slug}{ft^3\text{-}s}\right] \qquad\qquad \mathcal{J}^\star_{ref} = \left[\frac{slug}{ft^2\text{-}s}\right]$$

$$C^\star_{p\infty} = \left[\frac{BTU}{slug\text{-}^oR}\right]$$

B   Fluid Equations

The development of the Navier-Stokes equations can be found in a variety of sources within the literature, so in the interest of brevity, this derivation is not repeated here. In particular, Ref. [75] presents the Navier-Stokes equations written in an orthogonal curvilinear coordinate system. Restricting ourselves to axisymmetric flow, these equations are written below in dimensional form.

continuity:

$$\frac{\partial}{\partial s^\star}\left(\rho^\star u^\star h_3^\star\right) + \frac{\partial}{\partial n^\star}\left(\rho^\star v^\star h_1 h_3^\star\right) = 0 \tag{B.1}$$

$s^\star$ - *momentum:*

$$\rho^\star\left(\frac{u^\star}{h_1}\frac{\partial u^\star}{\partial s^\star} + v^\star\frac{\partial u^\star}{\partial n^\star} + \frac{u^\star v^\star}{h_1}\frac{\partial h_1}{\partial n^\star}\right) + \frac{1}{h_1}\frac{\partial p^\star}{\partial s^\star} =$$

$$\frac{1}{h_1}\frac{\partial \tau_{ss}^\star}{\partial s^\star} + \frac{\partial \tau_{sn}^\star}{\partial n^\star} + \frac{\tau_{ss}^\star - \tau_{\phi\phi}^\star}{h_1 h_3^\star}\frac{\partial h_3^\star}{\partial s^\star} + \left(\frac{2}{h_1}\frac{\partial h_1}{\partial n^\star} + \frac{1}{h_3^\star}\frac{\partial h_3^\star}{\partial n^\star}\right)\tau_{sn}^\star \tag{B.2}$$

$n^\star$ - *momentum:*

$$\rho^\star\left(\frac{u^\star}{h_1}\frac{\partial v^\star}{\partial s^\star} + v^\star\frac{\partial v^\star}{\partial n^\star} - \frac{u^{\star 2}}{h_1}\frac{\partial h_1}{\partial n^\star}\right) + \frac{\partial p^\star}{\partial n^\star} = \tag{B.3}$$

$$\frac{1}{h_1}\frac{\partial \tau_{sn}^\star}{\partial s^\star} + \frac{\partial \tau_{nn}^\star}{\partial n^\star} + \frac{\tau_{sn}^\star}{h_1 h_3^\star}\frac{\partial h_3^\star}{\partial s^\star} + \left(\frac{1}{h_1}\frac{\partial h_1}{\partial n^\star} + \frac{1}{h_3^\star}\frac{\partial h_3^\star}{\partial n^\star}\right)\tau_{nn}^\star - \frac{\tau_{\phi\phi}^\star}{h_3^\star}\frac{\partial h_3^\star}{\partial n^\star} - \frac{\tau_{ss}^\star}{h_1}\frac{\partial h_1}{\partial n^\star}$$

energy:

$$\rho^\star\left(\frac{u^\star}{h_1}\frac{\partial h^\star}{\partial s^\star} + v^\star\frac{\partial h^\star}{\partial n^\star}\right) - \frac{u^\star}{h_1}\frac{\partial p^\star}{\partial s^\star} - v^\star\frac{\partial p^\star}{\partial n^\star} =$$

$$\frac{1}{h_1 h_3^\star}\left[\frac{\partial}{\partial s^\star}\left(\frac{h_3^\star}{h_1}\frac{\mu^\star}{Pr}\frac{\partial h^\star}{\partial s^\star}\right) + \frac{\partial}{\partial n^\star}\left(h_1 h_3^\star\frac{\mu^\star}{Pr}\frac{\partial h^\star}{\partial n^\star}\right)\right] + \frac{\tau_{ss}^\star}{h_1}\left[\frac{\partial u^\star}{\partial s^\star} + v^\star\frac{\partial h_1}{\partial n^\star}\right] \tag{B.4}$$

$$+ \frac{\tau_{sn}^\star}{h_1}\left[\frac{\partial v^\star}{\partial s^\star} - u^\star\frac{\partial h_1}{\partial n^\star}\right] + \tau_{sn}^\star\frac{\partial u^\star}{\partial n^\star} + \tau_{nn}^\star\frac{\partial v^\star}{\partial n^\star} + \frac{\tau_{\phi\phi}^\star}{h_3^\star}\left[\frac{u^\star}{h_1}\frac{\partial h_3^\star}{\partial s^\star} + v^\star\frac{\partial h_3^\star}{\partial n^\star}\right]$$

stress terms:

$$\tau_{ss}^\star = 2\mu^\star\left[\frac{1}{h_1}\frac{\partial u^\star}{\partial s^\star} + \frac{v^\star}{h_1}\frac{\partial h_1}{\partial n^\star}\right] - \frac{2}{3}\frac{\mu^\star}{h_1 h_3^\star}\left[\frac{\partial}{\partial s^\star}\left(h_3^\star u^\star\right) + \frac{\partial}{\partial n^\star}\left(h_1 h_3^\star v^\star\right)\right]$$

$$\tau_{nn}^\star = 2\mu^\star\frac{\partial v^\star}{\partial n^\star} - \frac{2}{3}\frac{\mu^\star}{h_1 h_3^\star}\left[\frac{\partial}{\partial s^\star}\left(h_3^\star u^\star\right) + \frac{\partial}{\partial n^\star}\left(h_1 h_3^\star v^\star\right)\right] \tag{B.5}$$

$$\tau_{\phi\phi}^\star = 2\mu^\star\left[\frac{v^\star}{h_3^\star}\frac{\partial h_3^\star}{\partial n^\star} + \frac{u^\star}{h_1 h_3^\star}\frac{\partial h_3^\star}{\partial s^\star}\right] - \frac{2}{3}\frac{\mu^\star}{h_1 h_3^\star}\left[\frac{\partial}{\partial s^\star}\left(h_3^\star u^\star\right) + \frac{\partial}{\partial n^\star}\left(h_1 h_3^\star v^\star\right)\right]$$

$$\tau_{sn}^{\star} = \mu^{\star} \left[\frac{1}{h_1} \frac{\partial v^{\star}}{\partial s^{\star}} + h_1 \frac{\partial}{\partial n^{\star}} \left(\frac{u^{\star}}{h_1} \right) \right]$$

Using the definitions of Appendix A, Eqs. (B.1) through (B.5) are rewritten below in nondimensional form.

continuity:

$$\frac{\partial}{\partial s} \left(\rho u h_3 \right) + \frac{\partial}{\partial n} \left(\rho v h_1 h_3 \right) = 0 \tag{B.6}$$

s - momentum:

$$\rho \left(\frac{u}{h_1} \frac{\partial u}{\partial s} + v \frac{\partial u}{\partial n} + \frac{uv}{h_1} \frac{\partial h_1}{\partial n} \right) + \frac{1}{h_1} \frac{\partial p}{\partial s} =$$

$$\epsilon^2 \left\{ \frac{1}{h_1} \frac{\partial \tau_{ss}}{\partial s} + \frac{\partial \tau_{sn}}{\partial n} + \frac{\tau_{ss} - \tau_{\phi\phi}}{h_1 h_3} \frac{\partial h_3}{\partial s} + \left(\frac{2}{h_1} \frac{\partial h_1}{\partial n} + \frac{1}{h_3} \frac{\partial h_3}{\partial n} \right) \tau_{sn} \right\} \tag{B.7}$$

n - momentum:

$$\rho \left(\frac{u}{h_1} \frac{\partial v}{\partial s} + v \frac{\partial v}{\partial n} - \frac{u^2}{h_1} \frac{\partial h_1}{\partial n} \right) + \frac{\partial p}{\partial n} = \tag{B.8}$$

$$\epsilon^2 \left\{ \frac{1}{h_1} \frac{\partial \tau_{sn}}{\partial s} + \frac{\partial \tau_{nn}}{\partial n} + \frac{\tau_{sn}}{h_1 h_3} \frac{\partial h_3}{\partial s} + \left(\frac{1}{h_1} \frac{\partial h_1}{\partial n} + \frac{1}{h_3} \frac{\partial h_3}{\partial n} \right) \tau_{nn} - \frac{\tau_{\phi\phi}}{h_3} \frac{\partial h_3}{\partial n} - \frac{\tau_{ss}}{h_1} \frac{\partial h_1}{\partial n} \right\}$$

energy:

$$\rho \left(\frac{u}{h_1} \frac{\partial h}{\partial s} + v \frac{\partial h}{\partial n} \right) - \frac{u}{h_1} \frac{\partial p}{\partial s} - v \frac{\partial p}{\partial n} =$$

$$\epsilon^2 \left\{ \frac{1}{h_1 h_3} \left[\frac{\partial}{\partial s} \left(\frac{h_3}{h_1} \frac{\mu}{Pr} \frac{\partial h}{\partial s} \right) + \frac{\partial}{\partial n} \left(h_1 h_3 \frac{\mu}{Pr} \frac{\partial h}{\partial n} \right) \right] + \frac{\tau_{ss}}{h_1} \left[\frac{\partial u}{\partial s} + v \frac{\partial h_1}{\partial n} \right] \right. \tag{B.9}$$

$$\left. + \frac{\tau_{sn}}{h_1} \left[\frac{\partial v}{\partial s} - u \frac{\partial h_1}{\partial n} \right] + \tau_{sn} \frac{\partial u}{\partial n} + \tau_{nn} \frac{\partial v}{\partial n} + \frac{\tau_{\phi\phi}}{h_3} \left[\frac{u}{h_1} \frac{\partial h_3}{\partial s} + v \frac{\partial h_3}{\partial n} \right] \right\}$$

stress terms:

$$\tau_{ss} = 2\mu \left[\frac{1}{h_1} \frac{\partial u}{\partial s} + \frac{v}{h_1} \frac{\partial h_1}{\partial n} \right] - \frac{2}{3} \frac{\mu}{h_1 h_3} \left[\frac{\partial}{\partial s} \left(h_3 u \right) + \frac{\partial}{\partial n} \left(h_1 h_3 v \right) \right]$$

$$\tau_{nn} = 2\mu \frac{\partial v}{\partial n} - \frac{2}{3} \frac{\mu}{h_1 h_3} \left[\frac{\partial}{\partial s} \left(h_3 u \right) + \frac{\partial}{\partial n} \left(h_1 h_3 v \right) \right] \tag{B.10}$$

$$\tau_{\phi\phi} = 2\mu \left[\frac{v}{h_3} \frac{\partial h_3}{\partial n} + \frac{u}{h_1 h_3} \frac{\partial h_3}{\partial s} \right] - \frac{2}{3} \frac{\mu}{h_1 h_3} \left[\frac{\partial}{\partial s} \left(h_3 u \right) + \frac{\partial}{\partial n} \left(h_1 h_3 v \right) \right]$$

$$\tau_{sn} = \mu \left[\frac{1}{h_1} \frac{\partial v}{\partial s} + h_1 \frac{\partial}{\partial n} \left(\frac{u}{h_1} \right) \right]$$

where

$$\epsilon^2 = \frac{\mu_{ref}^{\star}}{\rho_{\infty}^{\star} u_{\infty}^{\star} R_{nose}^{\star}}$$

By assuming that v and n are of the order of ϵ and neglecting terms of higher order than ϵ, the standard viscous shock-layer equations are obtained:

continuity:

$$\frac{\partial}{\partial s}(\rho u h_3) + \frac{\partial}{\partial n}(\rho v h_1 h_3) = 0 \qquad \text{(B.11)}$$

s - momentum:

$$\rho\left(\frac{u}{h_1}\frac{\partial u}{\partial s} + v\frac{\partial u}{\partial n} + \frac{uv}{h_1}\frac{\partial h_1}{\partial n}\right) + \frac{1}{h_1}\frac{\partial p}{\partial s} =$$

$$\epsilon^2\left\{\frac{\partial}{\partial n}\left[\mu\left(\frac{\partial u}{\partial n} - \frac{u}{h_1}\frac{\partial h_1}{\partial n}\right)\right] + \mu\left(\frac{2}{h_1}\frac{\partial h_1}{\partial n} + \frac{1}{h_3}\frac{\partial h_3}{\partial n}\right)\left(\frac{\partial u}{\partial n} - \frac{u}{h_1}\frac{\partial h_1}{\partial n}\right)\right\} \qquad \text{(B.12)}$$

n - momentum:

$$\rho\left(\frac{u}{h_1}\frac{\partial v}{\partial s} + v\frac{\partial v}{\partial n} - \frac{u^2}{h_1}\frac{\partial h_1}{\partial n}\right) + \frac{\partial p}{\partial n} = 0 \qquad \text{(B.13)}$$

energy:

$$\rho\left(\frac{u}{h_1}\frac{\partial h}{\partial s} + v\frac{\partial h}{\partial n}\right) - \frac{u}{h_1}\frac{\partial p}{\partial s} - v\frac{\partial p}{\partial n} =$$

$$\epsilon^2\left\{\frac{\partial}{\partial n}\left[\frac{\mu}{Pr}\frac{\partial h}{\partial n}\right] + \frac{\mu}{Pr}\frac{\partial h}{\partial n}\left(\frac{1}{h_1}\frac{\partial h_1}{\partial n} + \frac{1}{h_3}\frac{\partial h_3}{\partial n}\right)\right.$$

$$\left. +\mu\left(h_1\frac{\partial u}{\partial n} - u\frac{\partial h_1}{\partial n}\right)\left(\frac{1}{h_1}\frac{\partial u}{\partial n} - \frac{u}{h_1^2}\frac{\partial h_1}{\partial n}\right)\right\} \qquad \text{(B.14)}$$

Note: *In order to keep the equations parabolic in nature, the right-hand side of the n-momentum equation is only of order 1.*

C   Maslen's Method

Maslen's pressure relation is an approximate solution to the normal momentum equation. Briefly, some terms are observed to be negligible in certain regions, while others are assumed to deviate little from their shock values. The resulting closed-form expression for p is a function of shock properties and stream function. The details of this derivation are given below, since some of the intermediate results are used in the present method.

Recall from the continuity equation, Eq. (B.11), that

$$\frac{\partial}{\partial s}\left(\rho u h_3\right) + \frac{\partial}{\partial n}\left(\rho v h_1 h_3\right) = 0$$

This expression is satisfied by the stream function Ψ, where

$$\frac{\partial \Psi}{\partial s} = \rho v h_1 h_3 \qquad \frac{\partial \Psi}{\partial n} = -\rho u h_3$$

Maslen works in a (ξ, η) coordinate system, where

$$\xi = s \qquad\qquad \eta = \frac{\Psi}{\Psi_s} \qquad\qquad (C.1)$$

The chain rule of differentiation gives

$$\frac{\partial}{\partial s} = \frac{\partial \xi}{\partial s}\frac{\partial}{\partial \xi} + \frac{\partial \eta}{\partial s}\frac{\partial}{\partial \eta} \qquad\qquad \frac{\partial}{\partial n} = \frac{\partial \xi}{\partial n}\frac{\partial}{\partial \xi} + \frac{\partial \eta}{\partial n}\frac{\partial}{\partial \eta} \qquad (C.2)$$

From Eq. (C.1)

$$\frac{\partial \xi}{\partial s} = 1 \qquad\qquad \frac{\partial \eta}{\partial s} = \frac{1}{\Psi_s}\frac{\partial \Psi}{\partial s} - \frac{\eta}{\Psi_s}\frac{d\Psi_s}{ds}$$

$$\frac{\partial \xi}{\partial n} = 0 \qquad\qquad \frac{\partial \eta}{\partial n} = \frac{1}{\Psi_s}\frac{\partial \Psi}{\partial n}$$

For axisymmetric flow,

$$\Psi_s = \frac{r_s^2}{2} \qquad\qquad \frac{d\Psi_s}{ds} = r_s \sin \Gamma_s$$

Thus,

$$\frac{\partial}{\partial s} = \frac{\partial}{\partial \xi} + \frac{\partial \eta}{\partial s}\frac{\partial}{\partial \eta} \qquad\qquad \frac{\partial}{\partial n} = -\frac{\rho u h_3}{\Psi_s}\frac{\partial}{\partial \eta} \qquad (C.3)$$

where

$$\frac{\partial \eta}{\partial s} = \frac{1}{\Psi_s}\left[\rho v h_1 h_3 - \eta r_s \sin \Gamma_s\right] \qquad\qquad (C.4)$$

From Eq. (B.13), the normal momentum equation is

$$\rho \left(\frac{u}{h_1} \frac{\partial v}{\partial s} + v \frac{\partial v}{\partial n} - \frac{u^2}{h_1} \frac{\partial h_1}{\partial n} \right) + \frac{\partial p}{\partial n} = 0 \qquad (C.5)$$

Applying the transformations of Eq. (C.3) to Eq. (C.5), substituting

$$\frac{\partial h_1}{\partial n} = -\kappa_s$$

and rearranging gives the normal momentum equation in this coordinate system:

$$\frac{\partial p}{\partial \eta} = \frac{1}{h_1 h_3} \left\{ \Psi_s \left[\frac{\partial v}{\partial \xi} + u \kappa_s \right] - r_s \eta \sin \Gamma_s \frac{\partial v}{\partial \eta} \right\} \qquad (C.6)$$

Apply Eq. (C.3) to n to get

$$v = \frac{u}{h_1} \frac{\partial n}{\partial \xi} + \frac{\eta r_s \sin \Gamma_s}{\rho h_1 h_3} \qquad \frac{\partial n}{\partial \eta} = -\frac{\Psi_s}{\rho u h_3} \qquad (C.7)$$

Using the approximation

$$n = \left. \frac{\partial n}{\partial \eta} \right|_s (\eta - 1)$$

along with Eq. (C.7) gives

$$n = \frac{r_s}{2 \rho_s u_s} (1 - \eta)$$

Differentiate with respect to ξ to get

$$\frac{\partial n}{\partial \xi} = \frac{1 - \eta}{2} \left\{ \frac{v_s}{\cos \Gamma_s} \left[1 - \frac{\kappa_s r_s}{\cos \Gamma_s} \right] - \frac{n}{\rho_s} \frac{d\rho_s}{d\xi} \right\} \qquad (C.8)$$

Maslen neglects the last term in this expression to get

$$\frac{\partial n}{\partial \xi} = \frac{(1 - \eta)}{2} \frac{v_s}{\cos \Gamma_s} \left[1 - \frac{\kappa_s r_s}{\cos \Gamma_s} \right] \qquad (C.9)$$

By substituting this expression into Eq. (C.7) and evaluating the remaining dependent variables at the shock, the following relation for v is obtained

$$v = v_s + \frac{v_s}{2} \left[1 + \frac{\kappa_s r_s}{\cos \Gamma_s} \right] (\eta - 1) \qquad (C.10)$$

Differentiate with respect to η to get

$$\frac{\partial v}{\partial \eta} = \frac{v_s}{2} \left[1 + \frac{\kappa_s r_s}{\cos \Gamma_s} \right]$$

Substitute this expression into Eq. (C.6) and evaluate the remaining dependent variables at the shock so that

$$\frac{\partial p}{\partial \eta} \approx \frac{\kappa_s r_s u_s}{2} - \frac{v_s \sin \Gamma_s}{2} \left[1 + \frac{\kappa_s r_s}{\cos \Gamma_s} \right] \eta \tag{C.11}$$

where the partial derivative of v with respect to ξ has been neglected. Integrate this expression to get Maslen's second-order pressure equation:

$$p(\xi, \eta) = p_s + p_{M1} (\eta - 1) + p_{M2} \frac{(\eta^2 - 1)}{2} \tag{C.12}$$

where

$$p_{M1} = \frac{\kappa_s r_s u_s}{2}$$

and

$$p_{M2} = -\frac{v_s \sin \Gamma_s}{2} \left[1 + \frac{\kappa_s r_s}{\cos \Gamma_s} \right]$$

This result is essentially a truncated Taylor's series expansion of p about its shock value:

$$p(\xi, \eta) = p_0(\xi) + p_1(\xi)[\eta - 1] + p_2(\xi) \frac{[\eta - 1]^2}{2!} \tag{C.13}$$

where

$$p_0 = p_s \qquad\qquad p_1 = p_{M1} + p_{M2} \qquad\qquad p_2 = p_{M2}$$

The streamwise derivative of p along lines of constant η_n appears in the governing equations. Differentiating Eq. (C.12) with respect to ξ gives an expression for the streamwise derivative along lines of constant η:

$$\frac{\partial p}{\partial \xi} = \frac{dp_s}{d\xi} + \frac{\eta - 1}{2} \left\{ u_s \kappa_s \frac{dr_s}{d\xi} + u_s r_s \frac{d\kappa_s}{d\xi} + \kappa_s r_s \frac{du_s}{d\xi} \right\}$$

$$- \frac{\eta^2 - 1}{4} \left\{ v_s \sin \Gamma_s \left[\frac{r_s}{\cos \Gamma_s} \frac{d\kappa_s}{d\xi} + \frac{\kappa_s}{\cos \Gamma_s} \left(\frac{dr_s}{d\xi} - \frac{r_s}{\cos \Gamma_s} \frac{d\cos \Gamma_s}{d\xi} \right) \right] \right.$$

$$\left. + \left[1 + \frac{\kappa_s r_s}{\cos \Gamma_s} \right] \left[\sin \Gamma_s \frac{dv_s}{d\xi} + v_s \frac{d \sin \Gamma_s}{d\xi} \right] \right\} \tag{C.14}$$

Recall that

$$\frac{dr_s}{d\xi} = \sin \Gamma_s \qquad\qquad \frac{du_s}{d\xi} = \kappa_s \sin \Gamma_s \qquad\qquad \frac{\partial}{\partial \xi} (\sin \Gamma_s) = -\kappa_s \cos \Gamma_s$$

Make these substitutions to obtain

$$\left. \frac{\partial p}{\partial \xi} \right|_\eta = \frac{dp_s}{d\xi} + \frac{\eta - 1}{2} \left\{ u_s \kappa_s \sin \Gamma_s + u_s r_s \frac{d\kappa_s}{d\xi} + \kappa_s^2 r_s \sin \Gamma_s \right\}$$

$$-\frac{\eta^2 - 1}{4}\left\{\frac{v_s \sin\Gamma_s}{\cos\Gamma_s}\left[r_s\frac{d\kappa_s}{d\xi} + \kappa_s\sin\Gamma_s\left(1 - \frac{r_s}{\cos\Gamma_s}\kappa_s\right)\right]\right.$$

$$\left. + \left[1 + \frac{\kappa_s r_s}{\cos\Gamma_s}\right]\left[\sin\Gamma_s\frac{dv_s}{d\xi} - v_s\kappa_s\cos\Gamma_s\right]\right\} \tag{C.15}$$

Eq. (C.15) is the partial derivative of p along lines of constant η. However, the desired quantity is the partial derivative of p along lines of constant η_n. Recall from Eq. (C.3) that

$$\frac{\partial p}{\partial s} = \frac{\partial p}{\partial \xi}\bigg|_\eta + \frac{\partial \eta}{\partial s}\frac{\partial p}{\partial \eta} \qquad\qquad \frac{\partial p}{\partial n} = -\frac{\rho u h_3}{\Psi_s}\frac{\partial p}{\partial \eta}$$

and from Eq. (2.1.7)

$$\frac{\partial p}{\partial s} = \frac{\partial p}{\partial \xi}\bigg|_{\eta_n} - \frac{\eta_n - 1}{n_b}\frac{dn_b}{d\xi}\frac{\partial p}{\partial \eta_n} \qquad\qquad \frac{\partial p}{\partial n} = -\frac{1}{n_b}\frac{\partial p}{\partial \eta_n}$$

Equate these expressions to get

$$\frac{\partial p}{\partial \xi}\bigg|_{\eta_n} = \frac{\partial p}{\partial \xi}\bigg|_\eta + \frac{\partial \eta}{\partial s}\frac{\partial p}{\partial \eta} + \frac{\eta_n - 1}{n_b}\frac{dn_b}{d\xi}\frac{\partial p}{\partial \eta_n} \qquad\qquad \frac{\partial p}{\partial \eta_n} = \frac{\rho u h_3 n_b}{\Psi_s}\frac{\partial p}{\partial \eta}$$

It turns out that the expression for $\partial\eta/\partial s$, Eq. (C.4), is not well-behaved near the stagnation line. By making use of Eq. (C.7), this expression may be rewritten as

$$\frac{\partial \eta}{\partial s} = \frac{\rho u h_3}{\Psi_s}\frac{\partial n}{\partial \xi} \tag{C.16}$$

where $\partial n/\partial\xi$ is defined in Eq. (C.9). Equation Eq. (C.16) is well-behaved near the stagnation line so this form is used everywhere.

D   Shock Layer Thickness

With each iteration in the solution of the governing equations, a calculated value of the shock layer thickness, n_b, may be determined from the continuity equation. As explained in Chapters 7 and 8, this thickness is compared with the geometric thickness given by the shock and body equations. When these two values are in agreement, the solution is advanced to the next station. This appendix provides the expression for determining this calculated shock layer thickness. Inherently, this expression also provides the relationship between η and η_n.

The continuity equation, Eq. (2.1.10), can be rewritten as

$$\frac{\partial}{\partial \xi} \left(n_b \rho_s \bar{\rho} u_s \bar{u} h_3 \right) - \rho_s u_s \frac{dn_b}{d\xi} \frac{\partial}{\partial \eta_n} \left[(\eta_n - 1) \bar{\rho} \bar{u} h_3 \right] - \rho_s \frac{\partial}{\partial \eta_n} \left(\bar{\rho} v h_1 h_3 \right) = 0 \qquad \text{(D.1)}$$

Integrate across the shock layer to obtain

$$\left(\rho_s \bar{\rho} v h_1 h_3 \right)_s - \left(\rho_s \bar{\rho} v h_1 h_3 \right)_w + \rho_s u_s \frac{dn_b}{d\xi} \left\{ \left[(\eta_n - 1) \bar{\rho} \bar{u} h_3 \right]_s - \left[(\eta_n - 1) \bar{\rho} \bar{u} h_3 \right]_w \right\}$$

$$= \int_0^1 \frac{\partial}{\partial \xi} \left(n_b \rho_s \bar{\rho} u_s \bar{u} h_3 \right) d\eta_n \qquad \text{(D.2)}$$

Recall that

$$v_s = \frac{\sin \Gamma_s}{\rho_s} \qquad\qquad v_w = \bar{u}_w = 0 \qquad\qquad h_{1_s} = 1 \qquad\qquad h_{3_s} = r_s$$

Make these substitutions into Eq. (D.2) to get

$$\frac{\partial}{\partial \xi} \left[n_b \rho_s u_s \int_0^1 \bar{\rho} \bar{u} h_3 d\eta_n \right] = r_s \sin \Gamma_s \qquad \text{(D.3)}$$

Integrate with respect to ξ to obtain

$$n_b \rho_s u_s \int_0^1 \bar{\rho} \bar{u} h_3 d\eta_n = \int_0^\xi r_s \sin \Gamma_s d\xi = \int_0^{r_s} r_s \sin \Gamma_s \frac{d\xi}{dr_s} dr_s \qquad \text{(D.4)}$$

Since

$$\frac{dr_s}{d\xi} = \sin \Gamma_s \qquad \text{(D.5)}$$

this can be rewritten as

$$n_b \rho_s u_s \int_0^1 \bar{\rho} \bar{u} h_3 d\eta_n = \int_0^{r_s} r_s dr_s = \frac{r_s^2}{2} = \Psi_s \qquad \text{(D.6)}$$

Substitute for h_3 to get

$$n_b \rho_s u_s r_s \int_0^1 \bar{\rho}\bar{u}\, d\eta_n + n_b \rho_s u_s n_b \cos\Gamma_s \int_0^1 \bar{\rho}\bar{u}\,(\eta_n - 1)\, d\eta_n = \Psi_s \qquad \text{(D.7)}$$

This yields the following quadratic for n_b, the normal distance from the shock to the body:

$$n_b^2 \left[\rho_s u_s \cos\Gamma_s \int_0^1 \bar{\rho}\bar{u}\,(\eta_n - 1)\, d\eta_n \right] + n_b \left[\rho_s u_s r_s \int_0^1 \bar{\rho}\bar{u}\, d\eta_n \right] - \Psi_s = 0 \qquad \text{(D.8)}$$

An alternate approach for calculating the shock-layer thickness is given below. For a given station (where s is a constant), utilizing Eq. (C.3) gives

$$\frac{d\eta}{dn} = \frac{\partial\eta}{\partial n} = -\frac{\rho u h_3}{\Psi_s}$$

Similarly, Eq. (2.1.7) shows that along a given shock-normal line

$$\frac{d\eta}{dn} = \frac{\partial\eta}{\partial n} = -\frac{1}{n_b}\frac{\partial\eta}{\partial\eta_n} = -\frac{1}{n_b}\frac{d\eta}{d\eta_n}$$

Equate these relations to get

$$\Psi_s \frac{d\eta}{d\eta_n} = \rho u h_3 n_b = \rho_s \bar{\rho} u_s \bar{u} h_3 n_b$$

Integrate to obtain

$$\Psi_s \int_0^\eta d\eta = \rho_s u_s n_b \int_0^{\eta_n} \bar{\rho}\bar{u} h_3 \, d\eta_n$$

Substitute for h_3 to get

$$\Psi_s \eta = n_b^2 \left[\rho_s u_s^2 \int_0^{\eta_n} \bar{\rho}\bar{u}\,(\eta_n - 1)\, d\eta_n \right] + n_b \left[\rho_s u_s r_s \int_0^{\eta_n} \bar{\rho}\bar{u}\, d\eta_n \right] \qquad \text{(D.9)}$$

At the shock, $\eta = 1$ and $\eta_n = 1$ so that

$$\Psi_s = n_b^2 \left[\rho_s u_s^2 \int_0^1 \bar{\rho}\bar{u}\,(\eta_n - 1)\, d\eta_n \right] + n_b \left[\rho_s u_s r_s \int_0^1 \bar{\rho}\bar{u}\, d\eta_n \right] \qquad \text{(D.10)}$$

which is equivalent to Eq. (D.8). Eq. (D.9) defines the relationship between η and η_n. As a result, it must be used in conjunction with Maslen's pressure equation in order to find p for a given value of (ξ, η_n).

E   Geometric Limits

When the governing equations are applied on the stagnation line, their limiting forms (as $\xi \to 0$) are required. These limiting expressions contain fractions in indeterminant form which must be evaluated through the use of l'Hopital's rule. This appendix provides the finite, nonzero values of these quantities.

As $\xi \to 0$,

$$u_s = \cos \Gamma_s \to 0 \qquad\qquad r_s \to 0 \qquad\qquad \frac{dn_b}{d\xi} \to 0 \qquad (E.1)$$

and

$$\frac{du_s}{d\xi} = \frac{d\cos \Gamma_s}{d\xi} = \kappa_s \sin \Gamma_s \to \kappa_{s_0} \qquad\qquad \frac{dr_s}{d\xi} = \sin \Gamma_s \to 1 \qquad (E.2)$$

Thus,

$$\frac{u_s}{r_s} = \frac{\cos \Gamma_s}{r_s} \to \frac{0}{0}$$

Applying l'Hopital's rule,

$$\lim_{\xi \to 0} \left\{ \frac{\cos \Gamma_s}{r_s} \right\} = \lim_{\xi \to 0} \left\{ \frac{d\left(\cos \Gamma_s\right)/d\xi}{dr_s/d\xi} \right\} = \kappa_{s_0}$$

Since from Eq. (2.1.4)

$$h_3 = r_s \left(1 - n\frac{\cos \Gamma_s}{r_s} \right)$$

as $\xi \to 0$,

$$h_3 \to r_s \left(1 - n\kappa_{s_0} \right) = r_s h_1 \qquad (E.3)$$

In addition to these fundamental quantities, two other terms merit attention. The first appears in Eq. (2.4.12), the limiting form of the streamwise pressure derivative:

$$\lim_{\xi \to 0} \left\{ \frac{1}{u_s} \frac{\partial p}{\partial \xi} \bigg|_\eta \right\} = \lim_{\xi \to 0} \left\{ \frac{1}{u_s} \frac{dp_s}{d\xi} \right\} + \kappa_{s_0} (\eta - 1) \qquad (E.4)$$

$$-\frac{\eta^2 - 1}{4} \left\{ v_{s_0} \left[\frac{1}{\kappa_{s_0}} \lim_{\xi \to 0} \left\{ \frac{1}{u_s} \frac{d\kappa_s}{d\xi} \right\} + \kappa_{s_0} \lim_{\xi \to 0} \left\{ \frac{\cos \Gamma_s - r_s \kappa_s}{u_s^3} \right\} \right] \right.$$

$$\left. + 2 \left[\lim_{\xi \to 0} \left\{ \frac{1}{u_s} \frac{dv_s}{d\xi} \right\} - v_{s_0} \kappa_{s_0} \right] \right\}$$

Applying l'Hopital's rule:

$$\lim_{\xi \to 0} \left\{ \frac{\cos \Gamma_s - r_s \kappa_s}{u_s^3} \right\} = \lim_{\xi \to 0} \left\{ \frac{1}{3u_s^2 \kappa_s \sin \Gamma_s} \left[\kappa_s \sin \Gamma_s - r_s \frac{d\kappa_s}{d\xi} - \kappa_s \sin \Gamma_s \right] \right\}$$

so that

$$\lim_{\xi \to 0} \left\{ \frac{\cos \Gamma_s - r_s \kappa_s}{u_s^3} \right\} = \frac{1}{3\kappa_{s_0}^2} \lim_{\xi \to 0} \left\{ \frac{1}{u_s} \frac{d\kappa_s}{d\xi} \right\} \qquad (E.5)$$

Thus,

$$\lim_{\xi \to 0} \left\{ \frac{1}{u_s} \frac{\partial p}{\partial \xi} \bigg|_\eta \right\} = \lim_{\xi \to 0} \left\{ \frac{1}{u_s} \frac{dp_s}{d\xi} \right\} + \kappa_{s_0} (\eta - 1) \qquad (E.6)$$

$$-\frac{\eta^2 - 1}{2} \left\{ \frac{2v_{s_0}}{3\kappa_{s_0}} \lim_{\xi \to 0} \left\{ \frac{1}{u_s} \frac{d\kappa_s}{d\xi} \right\} + \lim_{\xi \to 0} \left\{ \frac{1}{u_s} \frac{dv_s}{d\xi} \right\} - v_{s_0} \kappa_{s_0} \right\}$$

A second term to be evaluated appears in Eq. (2.4.16), the limiting form of the streamwise derivative of n:

$$\lim_{\xi \to 0} \left\{ \frac{1}{r_s} \frac{\partial n}{\partial \xi} \bigg|_\eta \right\} = (1 - \eta) \frac{v_{s_0}}{2} \lim_{\xi \to 0} \left\{ \frac{\cos \Gamma_s - r_s \kappa_s}{u_s^2 r_s} \right\} \qquad (E.7)$$

Note that

$$\lim_{\xi \to 0} \left\{ \frac{\cos \Gamma_s - r_s \kappa_s}{u_s^2 r_s} \right\} = \lim_{\xi \to 0} \left\{ \frac{\cos \Gamma_s}{r_s} \right\} \lim_{\xi \to 0} \left\{ \frac{\cos \Gamma_s - r_s \kappa_s}{u_s^3} \right\} = \frac{1}{3\kappa_{s_0}} \lim_{\xi \to 0} \left\{ \frac{1}{u_s} \frac{d\kappa_s}{d\xi} \right\}$$

so that

$$\lim_{\xi \to 0} \left\{ \frac{1}{r_s} \frac{\partial n}{\partial \xi} \bigg|_\eta \right\} = \frac{(\eta - 1) v_{s_0}}{6\kappa_{s_0}} \lim_{\xi \to 0} \left\{ \frac{1}{u_s} \frac{d\kappa_s}{d\xi} \right\} \qquad (E.8)$$

F   Shock Properties

Boundary conditions along the body and at the shock wave (in the form of jump conditions) are required for the solution of the governing equations. The jump conditions across the shock vary according to the chemical nature of the flowfield. This appendix provides the jump conditions for perfect gas, equilibrium, and nonequilibrium flows.

In the shock-normal system

$$v_\infty^\star = V_\infty^\star \sin \Gamma_s \qquad\qquad u_\infty^\star = u_s^\star = V_\infty^\star \cos \Gamma_s$$

From the conservation equation

$$\rho_\infty^\star v_\infty^\star = \rho_s^\star v_s^\star$$

From the momentum equation

$$p_\infty^\star + \rho_\infty^\star v_\infty^{\star 2} = p_s^\star + \rho_s^\star v_s^{\star 2} = p_s^\star + \rho_\infty^\star v_\infty^\star v_s^\star$$

From the energy equation

$$h_\infty^\star + \frac{v_\infty^{\star 2}}{2} = h_s^\star + \frac{v_s^{\star 2}}{2}$$

Writing these equations in nondimensional form (see Appendix A) yields

$$u_s = \cos \Gamma_s \tag{F.1}$$

$$\rho_s v_s = \sin \Gamma_s \tag{F.2}$$

$$p_s + v_s \sin \Gamma_s = p_\infty + \sin^2 \Gamma_s \tag{F.3}$$

$$h_s + \frac{v_s^2}{2} = h_\infty + \frac{\sin^2 \Gamma_s}{2} \tag{F.4}$$

Substituting Eq. (F.2) into Eq. (F.3) gives

$$p_s = p_\infty + \sin^2 \Gamma_s \left(1 - \frac{1}{\rho_s}\right) \tag{F.5}$$

Substituting Eq. (F.2) into Eq. (F.4) gives

$$h_s = h_\infty + \frac{\sin^2 \Gamma_s}{2} \left(1 - \frac{1}{\rho_s^2}\right) \tag{F.6}$$

The derivative of the u_s with respect to ξ appears in the streamwise momentum equation, while Maslen's relation for the streamwise pressure gradient requires the

ξ-derivatives of p_s and v_s. First, differentiate Eqs. (F.1), (F.2), (F.3), and (F.4) with respect to ξ to obtain

$$\frac{du_s}{d\xi} = \kappa_s \sin \Gamma_s \qquad (F.7)$$

$$\frac{dv_s}{d\xi} = -\frac{1}{\rho_s}\left[\kappa_s \cos \Gamma_s + v_s \frac{d\rho_s}{d\xi}\right] \qquad (F.8)$$

$$\frac{dp_s}{d\xi} = -2\kappa_s \sin \Gamma_s \cos \Gamma_s + v_s \kappa_s \cos \Gamma_s - \sin \Gamma_s \frac{dv_s}{d\xi} \qquad (F.9)$$

and

$$\frac{dh_s}{d\xi} = -\kappa_s \sin \Gamma_s \cos \Gamma_s - v_s \frac{dv_s}{d\xi} \qquad (F.10)$$

respectively.

The closure of the above two sets of equations requires the use of the equation of state and the definition of enthalpy. It is advantageous to use different forms of these two expressions for various flowfield regimes. Thus, at this point the discussion branches into three such areas: perfect, thermally perfect, and chemically reacting gases.

F.1 Perfect Gas

For a perfect gas, the specific heats are constant so that enthalpy can be expressed as

$$h_s^\star = C_{ps}{}^\star T_s^\star$$

which gives

$$h_s = C_{ps} T_s = T_s \qquad (F.11)$$

From the equation of state

$$p_s = \rho_s \check{\mathcal{R}}_{air} T_s \qquad (F.12)$$

where

$$\check{\mathcal{R}}_{air} = \frac{\check{\mathcal{R}}_{air}^\star}{C_{p\infty}^\star}$$

Eqs. (F.2), (F.3), (F.4), (F.11), and (F.12) provide five equations for five unknowns. They may be solved algebraically (see [76] for details) to get

$$p_s = \frac{2\sin^2 \Gamma_s}{\gamma + 1} - \frac{\gamma - 1}{\gamma (\gamma + 1) M_\infty^2} \qquad (F.13)$$

$$\rho_s = \frac{(\gamma + 1) M_\infty^2 \sin^2 \Gamma_s}{2 + (\gamma - 1) M_\infty^2 \sin^2 \Gamma_s} \qquad (F.14)$$

$$T_s = \frac{p_s}{\rho_s}\frac{\gamma}{\gamma - 1} \qquad (F.15)$$

$$v_s = \frac{\sin \Gamma_s}{\rho_s} \tag{F.16}$$

Further, since differentiating Eq. (F.14) with respect to ξ gives

$$\frac{d\rho_s}{d\xi} = \frac{-4\kappa_s \rho_s^2 \cos \Gamma_s}{(\gamma + 1) M_\infty^2 \sin^3 \Gamma_s} \tag{F.17}$$

equations Eqs. (F.8) and (F.9) become

$$\frac{dv_s}{d\xi} = \kappa_s \cos \Gamma_s \left[\frac{4}{(\gamma + 1) M_\infty^2 \sin^2 \Gamma_s} - \frac{1}{\rho_s} \right] \tag{F.18}$$

$$\frac{dp_s}{d\xi} = -\frac{4}{\gamma + 1} \kappa_s \sin \Gamma_s \cos \Gamma_s = -\frac{4\kappa_s \sin \Gamma_s \cos \Gamma_s}{\gamma + 1} \tag{F.19}$$

F.2   Nonequilibrium Flow

As noted in Chapter 5, for a chemically reacting mixture, the enthalpy is given by

$$h = \sum_{i=1}^{N_s} c_i h_i \qquad \qquad .$$

so that

$$dh = C_{p_f} dT + \sum_{i=1}^{N_s} h_i dc_i$$

For nonequilibrium flowfield calculations, it is assumed that the flow is chemically frozen *through* the shock wave. Thus, behind the shock

$$dc_i = 0$$

so that

$$dh_s = C_{p_s} dT_s \tag{F.20}$$

where

$$C_{p_s} = c_{O_2 \infty} C_{p_{O_2}}(T_s) + c_{N_2 \infty} C_{p_{N_2}}(T_s)$$

In addition,

$$h_s = c_{O_2 \infty} h_{O_2}(T_s) + c_{N_2 \infty} h_{N_2}(T_s)$$

From the equation of state

$$p_s = \rho_s \frac{\mathcal{R}_u}{\mathcal{M}_{air}} T_s \tag{F.21}$$

where

$$\mathcal{R}_u = \frac{\mathcal{R}_u^\star}{C_{p\infty}^\star}$$

Differentiating Eqs. (F.20) and (F.21) with respect to ξ gives

$$\frac{dh_s}{d\xi} = C_{ps}\frac{dT_s}{d\xi} \tag{F.22}$$

$$\frac{dp_s}{d\xi} = \frac{\mathcal{R}_u}{\mathcal{M}_{air}}\left[\rho_s\frac{dT_s}{d\xi} + T_s\frac{d\rho_s}{d\xi}\right] \tag{F.23}$$

Combining Eqs. (F.22) and (F.10), substituting the result into Eq. (F.23), and using that expression with Eq. (F.8) gives

$$\frac{d\rho_s}{d\xi} = \frac{\dfrac{\mathcal{M}_{air}}{\mathcal{R}_u}\dfrac{dp_s}{d\xi} - \dfrac{\kappa_s}{C_{ps}}\cos\Gamma_s\left(v_s - \rho_s\sin\Gamma_s\right)}{T_s + \dfrac{v_s^2}{C_{ps}}} \tag{F.24}$$

Substituting Eq. (F.8) into Eq. (F.9) yields

$$\frac{d\rho_s}{d\xi} = \frac{1}{v_s^2}\left\{\frac{dp_s}{d\xi} - 2\kappa_s\cos\Gamma_s\left[v_s - \sin\Gamma_s\right]\right\} \tag{F.25}$$

Equating Eqs. (F.24) and (F.25) gives

$$\frac{dp_s}{d\xi} = \frac{\kappa_s\cos\Gamma_s\left\{\dfrac{(v_s - \rho_s\sin\Gamma_s)}{C_{ps}} - 2\left[\dfrac{T_s}{v_s^2} + \dfrac{1}{C_{ps}}\right](v_s - \sin\Gamma_s)\right\}}{\dfrac{\mathcal{M}_{air}}{\mathcal{R}_u} - \left(\dfrac{T_s}{v_s^2} + \dfrac{1}{C_{ps}}\right)} \tag{F.26}$$

Substituting Eq. (F.25) into Eq. (F.8) gives

$$\frac{dv_s}{d\xi} = 2\kappa_s\cos\Gamma_s\left(\frac{1}{\rho_s} - 1\right) - \frac{1}{\rho_s}\left[\kappa_s\cos\Gamma_s + \frac{1}{v_s}\frac{dp_s}{d\xi}\right] \tag{F.27}$$

F.3 Equilibrium Flow

For an equilibrium chemically reacting mixture of perfect gases, the definition of enthalpy is

$$h_s = h_s(p_s, T_s)$$

Typically, equilibrium air models must be employed in the form of "table look-up" or "curve fit" procedures. Since the energy equation is cast in terms of h, the model used here is of the form

$$T_s = T_s(p_s, h_s) \qquad\qquad Z_s = Z_s(p_s, h_s) \tag{F.28}$$

From the equation of state

$$p_s = \rho_s Z_s \tilde{\mathcal{R}}_{air}T_s \tag{F.29}$$

In general, algebraic expressions for the derivatives of p_s and v_s with respect to ξ are difficult to obtain in the manner applied in the previous two regimes. The approach taken in this work is detailed in Section 4.3.

G   Chemically Reacting Flows

The governing equations as presented in Appendix B may be applied to equilibrium flows, as will be discussed later in this appendix. For chemical nonequilibrium flows, expressing the energy equation in terms of T, rather than h is beneficial since the chemical finite rate equations are dependent on T. First, rewrite Eq. (B.14) as

$$\rho \left(\frac{u}{h_1} \frac{\partial h}{\partial s} + v \frac{\partial h}{\partial n} \right) - \frac{u}{h_1} \frac{\partial p}{\partial s} - v \frac{\partial p}{\partial n} = \tag{G.1}$$

$$-\frac{\partial q}{\partial n} + \epsilon^2 \left\{ -q \left(\frac{1}{h_1} \frac{\partial h_1}{\partial n} + \frac{1}{h_3} \frac{\partial h_3}{\partial n} \right) + \mu \left(\frac{\partial u}{\partial n} - \frac{u}{h_1} \frac{\partial h_1}{\partial n} \right)^2 \right\}$$

For perfect gas flow, the heat flux in the n-direction is

$$q^\star = -k^\star \frac{\partial T^\star}{\partial n^\star} = q_c^\star \tag{G.2}$$

so that in nondimensional form (see Appendix A),

$$q = -\epsilon^2 k \frac{\partial T}{\partial n} = q_c \tag{G.3}$$

where the subscript c denotes the energy flux due to conduction in the normal direction. Since

$$dh = C_p dT$$

this may be written as

$$q = q_c = -\epsilon^2 \frac{\mu}{Pr} \frac{\partial h}{\partial n} \tag{G.4}$$

which is the representation used in Eq. (B.14).

For chemically reacting flow, the effect of diffusion must be included. Thus,

$$q^\star = q_c^\star + q_d^\star \tag{G.5}$$

where $q_d^\star$ is the energy flux due to diffusion in the normal direction. This term can be expressed as

$$q_d^\star = -\rho^\star \sum_{i=1}^{N_s} \mathcal{D}_{i,m}^\star h_i^\star \frac{\partial c_i}{\partial n^\star} \tag{G.6}$$

where $\mathcal{D}_{i,m}^\star$ is the multicomponent diffusion coefficient, N_s is the number of species present in the mixture, and c_i is the mass fraction of species i. Define the Lewis number, which is the ratio of the mass diffusivity to the thermal diffusivity, as

$$Le_{i,m} = \frac{\rho^\star C_{p_f}{}^\star \mathcal{D}_{i,m}^\star}{k^\star} \tag{G.7}$$

Now Eq. (G.6) may be rewritten as

$$q_d^\star = -\sum_{i=1}^{N_s} \frac{k^\star Le_{i,m}}{C_{p_f}^\star} h_i^\star \frac{\partial c_i}{\partial n^\star} \qquad (G.8)$$

Written in nondimensional form,

$$q = q_c + q_d \qquad (G.9)$$

and

$$q_d = -\epsilon^2 \sum_{i=1}^{N_s} \frac{k Le_{i,m}}{C_{p_f}} h_i \frac{\partial c_i}{\partial n} \qquad (G.10)$$

In the case of equilibrium flow, the conduction and diffusion quantities are combined through the following procedure. From Eqs. (G.4), (G.9), and (G.10),

$$q = -\epsilon^2 \left\{ k \frac{\partial T}{\partial n} + \sum_{i=1}^{N_s} \frac{k Le_{i,m}}{C_{p_f}} h_i \frac{\partial c_i}{\partial n} \right\} \qquad (G.11)$$

For a gas in local chemical equilibrium,

$$dc_i = \left. \frac{\partial c_i}{\partial T} \right|_p dT + \left. \frac{\partial c_i}{\partial p} \right|_T dp \qquad (G.12)$$

and

$$dh = \left. \frac{\partial h}{\partial T} \right|_p dT + \left. \frac{\partial h}{\partial p} \right|_T dp \qquad (G.13)$$

where the subscripts p and T denote constant pressure and temperature, respectively. Assuming constant pressure in the normal direction gives

$$\frac{\partial c_i}{\partial n} = \frac{\partial c_i}{\partial T} \frac{\partial T}{\partial n} \qquad (G.14)$$

$$\frac{\partial h}{\partial n} = \frac{\partial h}{\partial T} \frac{\partial T}{\partial n} = C_p \frac{\partial T}{\partial n} \qquad (G.15)$$

and Eq. (G.11) can be rewritten as

$$q = -\epsilon^2 \left\{ k \frac{\partial T}{\partial n} + \sum_{i=1}^{N_s} \frac{k Le_{i,m}}{C_{p_f}} h_i \frac{\partial T}{\partial n} \frac{\partial c_i}{\partial T} \right\} \qquad (G.16)$$

or

$$q = -\epsilon^2 \left\{ k \frac{\partial T}{\partial n} + k_r \frac{\partial T}{\partial n} \right\} = -\epsilon^2 k_T \frac{\partial T}{\partial n} \qquad (G.17)$$

where the reaction conductivity (due to diffusion) is

$$k_r = \sum_{i=1}^{N_s} \frac{k Le_{i,m}}{C_{p_f}} h_i \frac{\partial c_i}{\partial T} \tag{G.18}$$

This definition of *total* conductivity (k_T) can be used to define an *equilibrium* Prandtl number:

$$Pr_{eq} = \frac{\mu C_p}{k_T} \tag{G.19}$$

This quantity is also referred to as the total or *reactive* Prandtl number. Substituting into Eq. (G.16) gives

$$q = -\epsilon^2 \frac{\mu C_p}{Pr_{eq}} \frac{\partial T}{\partial n} = -\epsilon^2 \frac{\mu}{Pr_{eq}} \frac{\partial h}{\partial n} \tag{G.20}$$

By combining Eqs. (G.20) and (G.1), it is seen that Eq. (B.14) can be used for both perfect gas and equilibrium flows (provided Pr_{eq} is used).

For nonequilibrium flows, substituting Eq. (G.11) into Eq. (G.1) gives

$$\rho \left(\frac{u}{h_1} \frac{\partial h}{\partial s} + v \frac{\partial h}{\partial n} \right) - \frac{u}{h_1} \frac{\partial p}{\partial s} - v \frac{\partial p}{\partial n} =$$

$$\epsilon^2 \left\{ \frac{\partial}{\partial n} \left[k \frac{\partial T}{\partial n} \right] + k \frac{\partial T}{\partial n} \left(\frac{1}{h_1} \frac{\partial h_1}{\partial n} + \frac{1}{h_3} \frac{\partial h_3}{\partial n} \right) + \mu \left(\frac{\partial u}{\partial n} - \frac{u}{h_1} \frac{\partial h_1}{\partial n} \right)^2 \right. \tag{G.21}$$

$$\left. + \frac{\partial}{\partial n} \left[\sum_{i=1}^{N_s} \frac{k Le_{i,m}}{C_{p_f}} h_i \frac{\partial c_i}{\partial n} \right] + \sum_{i=1}^{N_s} \frac{k Le_{i,m}}{C_{p_f}} h_i \frac{\partial c_i}{\partial n} \left(\frac{1}{h_1} \frac{\partial h_1}{\partial n} + \frac{1}{h_3} \frac{\partial h_3}{\partial n} \right) \right\}$$

The variable h still appears on the left hand side of the above equation. Note that for a mixture of thermally perfect gases

$$h = h(c_i, T) = \sum_{i=1}^{N_s} c_i h_i(T)$$

Therefore,

$$dh = \sum_{i=1}^{N_s} c_i dh_i + \sum_{i=1}^{N_s} h_i dc_i = \sum_{i=1}^{N_s} c_i \frac{dh_i}{dT} dT + \sum_{i=1}^{N_s} h_i dc_i$$

Thus,

$$\frac{\partial h}{\partial s} = \frac{\partial T}{\partial s} \sum_{i=1}^{N_s} c_i C_{p_i} + \sum_{i=1}^{N_s} h_i \frac{\partial c_i}{\partial s}$$

Since the frozen specific heat is given by

$$C_{p_f} = \sum_{i=1}^{N_s} c_i C_{p_i}$$

this can be written as

$$\frac{\partial h}{\partial s} = C_{p_f}\frac{\partial T}{\partial s} + \sum_{i=1}^{N_s} h_i \frac{\partial c_i}{\partial s}$$

Similarly,

$$\frac{\partial h}{\partial n} = C_{p_f}\frac{\partial T}{\partial n} + \sum_{i=1}^{N_s} h_i \frac{\partial c_i}{\partial n}$$

Substituting into Eq. (G.21) gives

$$\rho\left(\frac{u}{h_1}\left[C_{p_f}\frac{\partial T}{\partial s} + \sum_{i=1}^{N_s} h_i \frac{\partial c_i}{\partial s}\right] + v\left[C_{p_f}\frac{\partial T}{\partial n} + \sum_{i=1}^{N_s} h_i \frac{\partial c_i}{\partial n}\right]\right) - \frac{u}{h_1}\frac{\partial p}{\partial s} - v\frac{\partial p}{\partial n} =$$

$$\epsilon^2\left\{\frac{\partial}{\partial n}\left[k\frac{\partial T}{\partial n}\right] + k\frac{\partial T}{\partial n}\left(\frac{1}{h_1}\frac{\partial h_1}{\partial n} + \frac{1}{h_3}\frac{\partial h_3}{\partial n}\right) + \mu\left(\frac{\partial u}{\partial n} - \frac{u}{h_1}\frac{\partial h_1}{\partial n}\right)^2\right. \qquad \text{(G.22)}$$

$$\left. + \frac{\partial}{\partial n}\left[\sum_{i=1}^{N_s}\frac{kLe_{i,m}}{C_{p_f}}h_i\frac{\partial c_i}{\partial n}\right] + \sum_{i=1}^{N_s}\frac{kLe_{i,m}}{C_{p_f}}h_i\frac{\partial c_i}{\partial n}\left(\frac{1}{h_1}\frac{\partial h_1}{\partial n} + \frac{1}{h_3}\frac{\partial h_3}{\partial n}\right)\right\}$$

If the assumption of binary diffusion is made,

$$\rho\left(\frac{u}{h_1}\left[C_{p_f}\frac{\partial T}{\partial s} + \sum_{i=1}^{N_s} h_i \frac{\partial c_i}{\partial s}\right] + v\left[C_{p_f}\frac{\partial T}{\partial n} + \sum_{i=1}^{N_s} h_i \frac{\partial c_i}{\partial n}\right]\right) - \frac{u}{h_1}\frac{\partial p}{\partial s} - v\frac{\partial p}{\partial n} =$$

$$\epsilon^2\left\{\frac{\partial}{\partial n}\left[k\frac{\partial T}{\partial n}\right] + k\frac{\partial T}{\partial n}\left(\frac{1}{h_1}\frac{\partial h_1}{\partial n} + \frac{1}{h_3}\frac{\partial h_3}{\partial n}\right) + \mu\left(\frac{\partial u}{\partial n} - \frac{u}{h_1}\frac{\partial h_1}{\partial n}\right)^2\right. \qquad \text{(G.23)}$$

$$\left. + \frac{\partial}{\partial n}\left[\sum_{i=1}^{N_s}\frac{kLe_{12}}{C_{p_f}}h_i\frac{\partial c_i}{\partial n}\right] + \sum_{i=1}^{N_s}\frac{kLe_{12}}{C_{p_f}}h_i\frac{\partial c_i}{\partial n}\left(\frac{1}{h_1}\frac{\partial h_1}{\partial n} + \frac{1}{h_3}\frac{\partial h_3}{\partial n}\right)\right\}$$

Based on the binary mass diffusivity, $\mathcal{D}_{12}^\star$, the definition of the binary Lewis number is

$$Le_{12} = \frac{\rho^\star C_{p_f}{}^\star \mathcal{D}_{12}^\star}{k^\star} \qquad \text{(G.24)}$$

In addition to modifications to the energy equation, calculating flowfields with finite-rate chemistry requires the solution of the species conservation equation for each chemical species in the mixture. An excellent derivation of this equation is presented in [77]. The final result is repeated here:

$$\rho^\star\left(\frac{u^\star}{h_1}\frac{\partial c_i}{\partial s^\star} + v^\star\frac{\partial c_i}{\partial n^\star}\right) = \dot{w}_i^\star - \frac{\partial \mathcal{J}_i^\star}{\partial n^\star} - \mathcal{J}_i^\star\left(\frac{1}{h_1}\frac{\partial h_1}{\partial n^\star} + \frac{1}{h_3^\star}\frac{\partial h_3^\star}{\partial n^\star}\right) \qquad \text{(G.25)}$$

where $\dot{w}_i^\star$ is the rate of production term for species i and $\mathcal{J}_i^\star$ is the diffusion mass flux term of species i. This binary diffusion mass flux term is defined by Fick's law to be

$$\mathcal{J}_i^\star = -\rho^\star \mathcal{D}_{12}^\star \frac{\partial c_i}{\partial n^\star} \qquad \text{(G.26)}$$

which can be written as

$$\mathcal{J}_i^{\star} = -\frac{k^{\star}}{C_{p_f}^{\star}} Le_{12} \frac{\partial c_i}{\partial n^{\star}} = -\frac{\mu^{\star}}{Pr} Le_{12} \frac{\partial c_i}{\partial n^{\star}} \tag{G.27}$$

Using the definitions of Appendix A, Eq. (G.25) is rewritten below in nondimensional form:

$$\rho \left(\frac{u}{h_1} \frac{\partial c_i}{\partial s} + v \frac{\partial c_i}{\partial n} \right) = \dot{w}_i - \epsilon^2 \left\{ \frac{\partial \mathcal{J}_i}{\partial n} + \mathcal{J}_i \left(\frac{1}{h_1} \frac{\partial h_1}{\partial n} + \frac{1}{h_3} \frac{\partial h_3}{\partial n} \right) \right\} \tag{G.28}$$

where

$$\mathcal{J}_i = -\frac{k}{C_{p_f}} Le_{12} \frac{\partial c_i}{\partial n} \tag{G.29}$$

Substituting Eq. (G.29) into Eq. (G.23) and rearranging yields

$$\rho C_{p_f} \left(\frac{u}{h_1} \frac{\partial T}{\partial s} + v \frac{\partial T}{\partial n} \right) - \frac{u}{h_1} \frac{\partial p}{\partial s} - v \frac{\partial p}{\partial n} + \sum_{i=1}^{N_s} h_i \left[\rho \left(\frac{u}{h_1} \frac{\partial c_i}{\partial s} + v \frac{\partial c_i}{\partial n} \right) \right] =$$

$$\epsilon^2 \left\{ \frac{\partial}{\partial n} \left[k \frac{\partial T}{\partial n} \right] + k \frac{\partial T}{\partial n} \left(\frac{1}{h_1} \frac{\partial h_1}{\partial n} + \frac{1}{h_3} \frac{\partial h_3}{\partial n} \right) + \mu \left(\frac{\partial u}{\partial n} - \frac{u}{h_1} \frac{\partial h_1}{\partial n} \right)^2 \right\} \tag{G.30}$$

$$-\sum_{i=1}^{N_s} h_i \epsilon^2 \left\{ \frac{\partial \mathcal{J}_i}{\partial n} + \mathcal{J}_i \left(\frac{1}{h_1} \frac{\partial h_1}{\partial n} + \frac{1}{h_3} \frac{\partial h_3}{\partial n} \right) \right\} - \epsilon^2 \sum_{i=1}^{N_s} \mathcal{J}_i C_{p_i} \frac{\partial T}{\partial n}$$

Combining Eq. (G.28) and Eq. (G.30) gives

$$\rho C_{p_f} \left(\frac{u}{h_1} \frac{\partial T}{\partial s} + v \frac{\partial T}{\partial n} \right) - \frac{u}{h_1} \frac{\partial p}{\partial s} - v \frac{\partial p}{\partial n} =$$

$$\epsilon^2 \left\{ \frac{\partial}{\partial n} \left[k \frac{\partial T}{\partial n} \right] + k \frac{\partial T}{\partial n} \left(\frac{1}{h_1} \frac{\partial h_1}{\partial n} + \frac{1}{h_3} \frac{\partial h_3}{\partial n} \right) + \mu \left(\frac{\partial u}{\partial n} - \frac{u}{h_1} \frac{\partial h_1}{\partial n} \right)^2 \right\} \tag{G.31}$$

$$-\epsilon^2 \sum_{i=1}^{N_s} \mathcal{J}_i C_{p_i} \frac{\partial T}{\partial n} - \sum_{i=1}^{N_s} h_i \dot{w}_i$$

H   Reaction Rates

In nonequilibrium flows, the chemical reactions proceed at a finite rate. The production terms ($\dot{w}_i$ for each species i in the mixture) appear in the energy equation (when formulated in terms of temperature) and in the species continuity equations. A discussion of these production terms is presented below.

Consider as an example, the dissociation of diatomic oxygen:

$$O_2 + M_r \xrightarrow{k_f^\star} 2O + M_r \tag{H.1}$$

where M_r is a collision partner (or catalytic third body). Catalytic bodies are those collision partners which do not undergo a chemical change during the reaction. From empirical results, the rate of *formation* of O can be written as

$$\frac{d}{dt^\star}[O] = 2k_f^\star[O_2][M_r] \tag{H.2}$$

where $k_f^\star$ is the forward reaction rate coefficient which is a function of $T^\star$ only, and each bracketed term represents the concentration of that substance (in $moles/cm^3$). The reverse (backward) reaction is

$$O_2 + M_r \xleftarrow{k_b^\star} 2O + M_r \tag{H.3}$$

so that the rate of *reduction* of O is

$$\frac{d}{dt^\star}[O] = -2k_b^\star[O]^2[M_r] \tag{H.4}$$

Combining these two elements gives

$$O_2 + M_r \rightleftharpoons 2O + M_r \tag{H.5}$$

so that the net rate of O formation is

$$\frac{d}{dt^\star}[O] = 2k_f^\star[O_2][M_r] - 2k_b^\star[O]^2[M_r] \tag{H.6}$$

For the more general case of a multicomponent gas with N_s distinct reacting chemical species and N_r simultaneous chemical reactions, the stoichiometric relations for the overall change from reactants to products are:

$$\sum_{i=1}^{N_t} \alpha_{i,r} X_i^\star \rightleftharpoons \sum_{i=1}^{N_t} \beta_{i,r} X_i^\star \tag{H.7}$$

where $r = 1, 2, ..., N_r$ and N_t is equal to the total number of the reacting species (N_s) and catalytic third bodies (N_c). The quantities $\alpha_{i,r}$ and $\beta_{i,r}$ are the stoichiometric coefficients for reactants and products, respectively. The variable $X_i^\star$ denotes the concentration of species i (or catalytic third body $i - N_s$):

$$X_i^\star = \rho_i^\star \frac{c_i}{\mathcal{M}_i} \quad , \quad \left[\frac{moles}{cm^3}\right] \tag{H.8}$$

In the above example,

$$\alpha_{O_2} = 1 \qquad\qquad \alpha_O = 0 \qquad\qquad \alpha_{M_r} = 1$$
$$\beta_{O_2} = 0 \qquad\qquad \beta_O = 2 \qquad\qquad \beta_{M_r} = 1$$

For the r-th reaction of Eq. (H.7), the forward rate of production is

$$\left(\frac{dX_i^\star}{dt^\star}\right)_r = (\beta_{i,r} - \alpha_{i,r})\, k_{f_r}^\star \prod_{i=1}^{N_c} (\gamma_i \rho^\star)^{\alpha_{i,r}} \tag{H.9}$$

while the backward rate is

$$\left(\frac{dX_i^\star}{dt^\star}\right)_r = -(\beta_{i,r} - \alpha_{i,r})\, k_{b_r}^\star \prod_{i=1}^{N_c} (\gamma_i \rho^\star)^{\beta_{i,r}} \tag{H.10}$$

so that the net rate of production [78] is

$$\left(\frac{\dot{w}_i^\star}{\mathcal{M}_i}\right)_r = \left(\frac{dX_i^\star}{dt^\star}\right)_r = (\beta_{i,r} - \alpha_{i,r}) \left[k_{f_r}^\star \prod_{i=1}^{N_c} (\gamma_i \rho^\star)^{\alpha_{i,r}} - k_{b_r}^\star \prod_{i=1}^{N_c} (\gamma_i \rho^\star)^{\beta_{i,r}} \right] \tag{H.11}$$

where $\rho^\star$ is in gm/cm^3. The net mass rate of production of the i-th species may be obtained by summing (Eq. H.11) over all the reactions N_r:

$$\dot{w}_i^\star = \rho^\star \frac{\partial c_i}{\partial t^\star} = \sum_{r=1}^{N_r} \left(\frac{d\rho_i^\star}{dt^\star}\right)_r = \mathcal{M}_i \sum_{r=1}^{N_r} \left(\frac{dX_i^\star}{dt^\star}\right)_r \quad , \quad \left[\frac{gm}{cm^3\text{-}s}\right] \tag{H.12}$$

or

$$\frac{\dot{w}_i^\star}{\rho^\star} = \mathcal{M}_i \sum_{r=1}^{N_r} (\beta_{i,r} - \alpha_{i,r}) \left(R_{f,r}^\star - R_{b,r}^\star\right) \tag{H.13}$$

where

$$R_{f,r}^\star = \frac{k_{f_r}^\star}{\rho^\star} \prod_{i=1}^{N_c} (\gamma_i \rho^\star)^{\alpha_{i,r}} = k_{f_r}^\star \rho^{\star \alpha_r} \prod_{i=1}^{N_c} (\gamma_i)^{\alpha_{i,r}}$$

$$R_{b,r}^\star = \frac{k_{b_r}^\star}{\rho^\star} \prod_{i=1}^{N_c} (\gamma_i \rho^\star)^{\beta_{i,r}} = k_{b_r}^\star \rho^{\star \beta_r} \prod_{i=1}^{N_c} (\gamma_i)^{\beta_{i,r}}$$

$$\alpha_r = \sum_{i=1}^{N_c} \alpha_{i,r} - 1$$

Table H.1. Chemical Reactions

r	Reaction	M_r
1	$O_2 + M_1 \rightleftharpoons 2O + M_1$	N_2, O_2, O, NO, N
2	$N_2 + M_2 \rightleftharpoons 2N + M_2$	N_2, O_2, O, NO
3	$N_2 + M_3 \rightleftharpoons 2N + M_3$	N
4	$NO + M_4 \rightleftharpoons N + O + M_4$	N_2, O_2, O, NO, N
5	$NO + O \rightleftharpoons O_2 + N$	
6	$N_2 + O \rightleftharpoons NO + N$	
7	$N + O \rightleftharpoons NO^+ + e^-$	

$$\beta_r = \sum_{i=1}^{N_c} \beta_{i,r} - 1$$

The mole-mass ratio (or mole number), γ_i, is defined as

$$\gamma_i = \begin{cases} \dfrac{c_i}{\mathcal{M}_i} = \dfrac{X_i^\star}{\rho^\star} & , \text{ for } i = 1, 2, ..., N_s \\[3mm] \displaystyle\sum_{n=1}^{N_s} Z_{i-N_s, n} \gamma_n & , \text{ for } i = N_s + 1, ..., N_t \end{cases} \qquad (\text{H.14})$$

where $Z_{i-N_s, n}$ is the catalytic efficiency of third body M_{i-N_s} for specie n. Written in modified Arrhenius form, the reaction rates are

$$k_{f_r}^\star = A_{f,r} T^{\star B_{f,r}} \exp(-T_{D_{f,r}}^\star / T^\star) \quad , \quad \left[\frac{1}{s} \left(\frac{cm^3}{mole} \right)^{\alpha_r} \right] \qquad (\text{H.15})$$

$$k_{b_r}^\star = A_{b,r} T^{\star B_{b,r}} \exp(-T_{D_{b,r}}^\star / T^\star) \quad , \quad \left[\frac{1}{s} \left(\frac{cm^3}{mole} \right)^{\beta_r} \right] \qquad (\text{H.16})$$

where $T^\star$ is in K.

In this study, a seven-species model [15] for air is used. Table H.1 lists the reactions and third bodies which are considered. The efficiencies of the catalytic third bodies are given in Table H.2 for the various reactions. Finally, the forward and backward rate coefficients are presented in Table H.3.

Table H.2. Third Body Efficiencies Relative to Argon

Catalytic Bodies	$i - N_s$	Efficiencies					
		N_2 $i = 1$	O_2 $i = 2$	N $i = 3$	O $i = 4$	NO $i = 5$	NO^+ $i = 6$
M_1	1	2	9	1	25	1	0
M_2	2	2.5	1	0	1	1	0
M_4	3	1	1	20	20	20	0
e^-	4	0	0	0	0	0	1

Table H.3. Chemical Rate Coefficients

r	$k^*_{f_r}$ $[cm^3/mole\text{-}sec]$	$k^*_{b_r}$ $[cm^3/mole\text{-}sec]$ or $[cm^6/mole^2\text{-}sec]$
1	$3.61 \times 10^{18} T^{-1.0} \exp(\ -5.94 \times 10^4/T)$	$3.01 \times 10^{15} T^{-0.5}$
2	$1.92 \times 10^{17} T^{-0.5} \exp(-1.131 \times 10^5/T)$	$1.09 \times 10^{16} T^{-0.5}$
3	$4.15 \times 10^{22} T^{-1.5} \exp(-1.131 \times 10^5/T)$	$2.32 \times 10^{21} T^{-1.5}$
4	$3.97 \times 10^{20} T^{-1.5} \exp(\ -7.56 \times 10^4/T)$	$1.01 \times 10^{20} T^{-1.5}$
5	$3.18 \times 10^9\ T^{1.0}\ \exp(\ -1.97 \times 10^4/T)$	$9.63 \times 10^{11} T^{0.5}\ \exp(-3.6 \times 10^3/T)$
6	$6.75 \times 10^{13}\ \ \ \ \exp(\ -3.75 \times 10^4/T)$	1.50×10^{13}
7	$9.03 \times 10^9\ T^{0.5}\ \exp(\ -3.24 \times 10^4/T)$	$1.80 \times 10^{19} T^{-1.0}$

I Species Thermodynamic Properties

For nonequilibrium flows, species thermodynamic properties are required for each species present in the fluid. Ref. [60] has provided curve fits for $C_{p_i}^{\star}$ and $h_i^{\star}$ for the temperature range of $300K \leq T^{\star} \leq 30000K$:

specific heat:

$$\frac{C_{p_i}^{\star}}{\mathcal{R}_u{}^{\star}} = \mathcal{A}_1 + \mathcal{A}_2 T^{\star} + \mathcal{A}_3 T^{\star 2} + \mathcal{A}_4 T^{\star 3} + \mathcal{A}_5 T^{\star 4} \qquad (I.1)$$

static enthalpy:

$$\frac{h_{i_{298.15}}^{\star}}{\mathcal{R}_u{}^{\star} T^{\star}} = \mathcal{A}_1 + \frac{\mathcal{A}_2 T^{\star}}{2} + \frac{\mathcal{A}_3 T^{\star 2}}{3} + \frac{\mathcal{A}_4 T^{\star 3}}{4} + \frac{\mathcal{A}_5 T^{\star 4}}{5} + \frac{\mathcal{A}_6}{T^{\star}} \qquad (I.2)$$

The subscript i denotes the i-th species as given in Table 5.1. The temperature range cited has been divided into five sub-ranges with each sub-range curve fit with the above polynomials. Coefficients $\mathcal{A}_1$ through $\mathcal{A}_5$ are presented in Table I.1, grouped according to these sub-ranges. The $\mathcal{A}_6$ coefficients are related to the heats of formation of their respective species (and therefore invariant with temperature). They are located in Table I.2, along with the species heats of formation.

Note that the enthalpy from Eq. (I.2) is referenced to a temperature of $298.15K$. The specific enthalpy for a reference temperature of $0K$ is desired. This can be calculated using the relation

$$h_i^{\star} = h_{i_0}^{\star} = h_{i_{298.15}}^{\star} + \Delta h_{i_0}^{\star} - \Delta h_{i_{298.15}}^{\star} + 298.15\, C_{p_{i_{pg}}}^{\star} \qquad (I.3)$$

where the first term on the right hand side is obtained from the above curve fits. The second and third terms (which are the heats of formation at $0K$ and $298.15K$, respectively) are provided in Table I.2, while the perfect gas values of $C_{p_i}^{\star}$ are presented in Table 5.1.

Table I.1. Constants for Polynomial Curve-fits of Thermodynamic Properties

Species	$\mathcal{A}_1$	$\mathcal{A}_2$	$\mathcal{A}_3$	$\mathcal{A}_4$	$\mathcal{A}_5$
$300K \leq T^* \leq 1000K$					
N_2	$.36748 \times 10^1$	$-.12081 \times 10^{-2}$	$.23240 \times 10^{-5}$	$-.63218 \times 10^{-9}$	$-.22577 \times 10^{-12}$
O_2	$.36146 \times 10^1$	$-.18598 \times 10^{-2}$	$.70814 \times 10^{-5}$	$-.68070 \times 10^{-8}$	$.21628 \times 10^{-11}$
N	$.25031 \times 10^1$	$-.21800 \times 10^{-4}$	$.54205 \times 10^{-7}$	$-.56476 \times 10^{-10}$	$.20999 \times 10^{-13}$
O	$.28236 \times 10^1$	$-.89478 \times 10^{-3}$	$.83060 \times 10^{-6}$	$-.16837 \times 10^{-9}$	$-.73205 \times 10^{-13}$
NO	$.35887 \times 10^1$	$-.12479 \times 10^{-2}$	$.39786 \times 10^{-5}$	$-.28651 \times 10^{-8}$	$.63015 \times 10^{-12}$
NO^+	$.35294 \times 10^1$	$-.30342 \times 10^{-3}$	$.38544 \times 10^{-6}$	$.10519 \times 10^{-8}$	$-.72777 \times 10^{-12}$
e^-	$.25000 \times 10^1$	$.00000 \times 10^0$	$.00000 \times 10^0$	$.00000 \times 10^0$	$.00000 \times 10^0$
$1000K \leq T^* \leq 6000K$					
N_2	$.32125 \times 10^1$	$.10137 \times 10^{-2}$	$-.30467 \times 10^{-6}$	$.41091 \times 10^{-10}$	$-.20170 \times 10^{-14}$
O_2	$.35949 \times 10^1$	$.75213 \times 10^{-3}$	$-.18732 \times 10^{-6}$	$.27913 \times 10^{-10}$	$-.15774 \times 10^{-14}$
N	$.24820 \times 10^1$	$.69258 \times 10^{-4}$	$-.63065 \times 10^{-7}$	$.18387 \times 10^{-10}$	$-.11747 \times 10^{-14}$
O	$.25421 \times 10^1$	$-.27551 \times 10^{-4}$	$-.31028 \times 10^{-8}$	$.45511 \times 10^{-11}$	$-.43681 \times 10^{-15}$
NO	$.32047 \times 10^1$	$.12705 \times 10^{-2}$	$-.46603 \times 10^{-6}$	$.75007 \times 10^{-10}$	$-.42314 \times 10^{-14}$
NO^+	$.32152 \times 10^1$	$.99742 \times 10^{-3}$	$-.29030 \times 10^{-6}$	$.36925 \times 10^{-10}$	$-.15994 \times 10^{-14}$
e^-	$.25000 \times 10^1$	$.00000 \times 10^0$	$.00000 \times 10^0$	$.00000 \times 10^0$	$.00000 \times 10^0$
$6000K \leq T^* \leq 15000K$					
N_2	$.31811 \times 10^1$	$.89745 \times 10^{-3}$	$-.20216 \times 10^{-6}$	$.18266 \times 10^{-10}$	$-.50334 \times 10^{-15}$
O_2	$.38599 \times 10^1$	$.32510 \times 10^{-3}$	$-.92131 \times 10^{-8}$	$-.78684 \times 10^{-12}$	$.29426 \times 10^{-16}$
N	$.27480 \times 10^1$	$-.39090 \times 10^{-3}$	$.13380 \times 10^{-6}$	$-.11910 \times 10^{-10}$	$.33690 \times 10^{-15}$
O	$.25460 \times 10^1$	$-.59520 \times 10^{-4}$	$.27010 \times 10^{-7}$	$-.27980 \times 10^{-11}$	$.93800 \times 10^{-16}$
NO	$.38543 \times 10^1$	$.23409 \times 10^{-3}$	$-.21354 \times 10^{-7}$	$.16689 \times 10^{-11}$	$-.49070 \times 10^{-16}$
NO^+	$.26896 \times 10^1$	$.13796 \times 10^{-2}$	$-.33985 \times 10^{-6}$	$.33776 \times 10^{-10}$	$-.10427 \times 10^{-14}$
e^-	$.25000 \times 10^1$	$.00000 \times 10^0$	$.00000 \times 10^0$	$.00000 \times 10^0$	$.00000 \times 10^0$
$15000K \leq T^* \leq 25000K$					
N_2	$.96377 \times 10^1$	$-.25728 \times 10^{-2}$	$.33020 \times 10^{-6}$	$-.14315 \times 10^{-10}$	$.20333 \times 10^{-15}$
O_2	$.34867 \times 10^1$	$.52384 \times 10^{-3}$	$-.39123 \times 10^{-7}$	$.10094 \times 10^{-11}$	$-.88718 \times 10^{-17}$
N	$-.12280 \times 10^1$	$.19268 \times 10^{-2}$	$-.24370 \times 10^{-6}$	$.12193 \times 10^{-10}$	$-.19918 \times 10^{-15}$
O	$-.97871 \times 10^{-2}$	$.12450 \times 10^{-2}$	$-.16154 \times 10^{-6}$	$.80380 \times 10^{-11}$	$-.12624 \times 10^{-15}$
NO	$.43309 \times 10^1$	$-.58086 \times 10^{-4}$	$.28059 \times 10^{-7}$	$-.15694 \times 10^{-11}$	$.24104 \times 10^{-16}$
NO^+	$.59346 \times 10^1$	$-.13178 \times 10^{-2}$	$.23297 \times 10^{-6}$	$-.11733 \times 10^{-10}$	$.18402 \times 10^{-15}$
e^-	$.25000 \times 10^1$	$.00000 \times 10^0$	$.00000 \times 10^0$	$.00000 \times 10^0$	$.00000 \times 10^0$
$25000K \leq T^* \leq 30000K$					
N_2	$-.51681 \times 10^1$	$.23337 \times 10^{-2}$	$-.12953 \times 10^{-6}$	$.27872 \times 10^{-11}$	$-.21360 \times 10^{-16}$
O_2	$.39620 \times 10^1$	$.39446 \times 10^{-3}$	$-.29506 \times 10^{-7}$	$.73975 \times 10^{-12}$	$-.64209 \times 10^{-17}$
N	$.15520 \times 10^2$	$-.38858 \times 10^{-2}$	$.32288 \times 10^{-6}$	$-.96053 \times 10^{-11}$	$.95472 \times 10^{-16}$
O	$.16428 \times 10^2$	$-.39313 \times 10^{-2}$	$.29840 \times 10^{-6}$	$-.81613 \times 10^{-11}$	$.75004 \times 10^{-16}$
NO	$.23507 \times 10^1$	$.58643 \times 10^{-3}$	$-.31316 \times 10^{-7}$	$.60495 \times 10^{-12}$	$-.40557 \times 10^{-17}$
NO^+	$-.51595 \times 10^1$	$.26290 \times 10^{-2}$	$-.16254 \times 10^{-6}$	$.39381 \times 10^{-11}$	$-.34311 \times 10^{-16}$
e^-	$.25000 \times 10^1$	$.00000 \times 10^0$	$.00000 \times 10^0$	$.00000 \times 10^0$	$.00000 \times 10^0$

Table I.2. Heats of Formation

Species	$\Delta h^\star_{i_{298.15}}$	$\Delta h^\star_{i_0}$	$\mathcal{A}_6$
	[kcal/gm-mole]		
N_2	0.0	0.0	$-.10430 \times 10^4$
O_2	0.0	0.0	$-.10440 \times 10^4$
N	112.973	112.529	$.56130 \times 10^5$
O	59.553	58.984	$.29150 \times 10^5$
NO	21.580	21.457	$.97640 \times 10^4$
NO^+	236.660	235.180	$.11840 \times 10^6$
e^-	0.0	0.0	$-.74542 \times 10^3$

J   Species Transport Properties

For nonequilibrium flows, species transport properties are required for each species present in the fluid. For the temperature range of $1000K \leq T^\star \leq 30000K$, the species transport properties are defined by the curve fits of Ref. [60]. The expression for viscosity is

$$\mu_i^\star = e^{\left[C_{\mu_i}\right]} T^{\star\left[A_{\mu_i} \ln T^\star + B_{\mu_i}\right]} \quad , \quad [gm/cm\text{-}s] \tag{J.1}$$

where the species coefficients are given in Table J.1. The frozen thermal conductivity is given by

$$k_i^\star = e^{\left[E_{k_i}\right]} T^{\star\left[A_{k_i}(\ln T^\star)^3 + B_{k_i}(\ln T^\star)^2 + C_{k_i}\ln T^\star + D_{k_i}\right]} \quad , \quad [cal/cm\text{-}s\text{-}K] \tag{J.2}$$

with the species coefficients located in Table J.2.

The ionic species viscosities and frozen thermal conductivities as defined by the tabulated coefficients are for the limiting electron pressure, which is defined as

$$p_{el_{max}}^\star = .0975 \left(\frac{T^\star}{1000}\right)^4 \quad , \quad [atm] \tag{J.3}$$

These values should be corrected by employing the following formula [61]:

$$\frac{\mu_i\left(p_{el}^\star\right)}{\mu_i\left(p_{el_{max}}^\star\right)} = \frac{k_i\left(p_{el}^\star\right)}{k_i\left(p_{el_{max}}^\star\right)} = \frac{2}{\ln\left[.0209\left(\dfrac{T^\star}{1000p_{el}^{\star\,.25}}\right)^4 + 1.52\left(\dfrac{T^\star}{1000p_{el}^{\star\,.25}}\right)^{8/3}\right]} \tag{J.4}$$

The local electron pressure is

$$p_{el}^\star = N_e K_B T^\star \quad , \quad [atm] \tag{J.5}$$

Table J.1. Constants for Viscosity Curve-Fits

Species	A_μ	B_μ	C_μ
N_2	0.0203	0.4329	-11.8153
O_2	0.0484	-0.1455	-8.9231
N	0.0120	0.5930	-12.3805
O	0.0205	0.4257	-11.5803
NO	0.0452	-0.0609	-9.4596
NO^+	0.0	2.5	-32.0453
e^-	0.0	2.5	-37.4475

Table J.2. Constants for Frozen Thermal Conductivity Curve-Fits

Species	A_k	B_k	C_k	D_k	E_k
N_2	0.03607	-1.07503	11.95029	-57.90063	93.21782
O_2	0.07987	-2.58428	31.25959	-166.76267	321.69820
N	0.0	0.0	0.01619	0.55022	-12.92190
O	0.0	0.0	0.03310	0.22834	-11.58116
NO	0.02792	-0.87133	10.17967	-52.03466	88.67060
NO^+	-0.06836	2.57829	-35.72737	219.09215	-519.00261
e^-	0.0	0.0	0.00032	2.49375	-27.89805

where N_c is the electron number density and K_B is Boltzmann's constant. In the present work, an electron pressure of 1 atm is assumed everywhere so that the above correction reduces to

$$\frac{\mu_i}{\mu_i\left(p^\star_{el_{max}}\right)} = \frac{k_i}{k_i\left(p^\star_{el_{max}}\right)} = \frac{2}{\ln\left[.0209\left(\frac{T^\star}{1000}\right)^4 + 1.52\left(\frac{T^\star}{1000}\right)^{8/3}\right]} \qquad (J.6)$$

K   Conic Shock Shape

Define the shock shape with a conic equation:

$$r_s^2 = 2C_s z_s - b_s z_s^2 \tag{K.1}$$

Differentiating Eq. (K.1) with respect to ξ gives

$$\frac{dr_s}{d\xi} = (C_s - b_s z_s)\frac{\cos\Gamma_s}{r_s} = \sin\Gamma_s \tag{K.2}$$

Differentiate Eq. (K.2) with respect to ξ and rearrange to get

$$\frac{\kappa_s r_s}{\cos\Gamma_s} = \sin^2\Gamma_s + b_s\cos^2\Gamma_s \tag{K.3}$$

Now differentiate Eq. (K.3) with respect to ξ to get

$$\frac{d}{d\xi}\left(\frac{\kappa_s r_s}{\cos\Gamma_s}\right) = 2\kappa_s\sin\Gamma_s\cos\Gamma_s\,(b_s - 1) \tag{K.4}$$

Utilizing the product rule of differentiation,

$$\frac{d}{d\xi}\left(\frac{\kappa_s r_s}{\cos\Gamma_s}\right) = \kappa_s\frac{d}{d\xi}\left(\frac{r_s}{\cos\Gamma_s}\right) + \frac{r_s}{\cos\Gamma_s}\frac{d\kappa_s}{d\xi} \tag{K.5}$$

so that

$$\frac{d\kappa_s}{d\xi} = \frac{\cos\Gamma_s}{r_s}\left[2\kappa_s\sin\Gamma_s\cos\Gamma_s\,(b_s - 1) - \kappa_s\left(\tan\Gamma_s - \frac{r_s}{\cos^2\Gamma_s}\kappa_s\sin\Gamma_s\right)\right]$$

That is,

$$\frac{d\kappa_s}{d\xi} = \kappa_s\left[2\sin\Gamma_s\frac{\cos^2\Gamma_s}{r_s}\,(b_s - 1) - \frac{\sin\Gamma_s}{r_s}\left(1 - \frac{\kappa_s r_s}{\cos^2\Gamma_s}\right)\right] \tag{K.6}$$

Substituting Eq. (K.3) and rearranging gives

$$\frac{d\kappa_s}{d\xi} = 3\kappa_s\sin\Gamma_s\frac{\cos^2\Gamma_s}{r_s}\,(b_s - 1) \tag{K.7}$$

On the stagnation line, Eq. (K.7) has the following limiting form:

$$\lim_{\xi\to 0}\left\{\frac{1}{\cos\Gamma_s}\frac{d\kappa_s}{d\xi}\right\} = 3\kappa_{s_0}{}^2\,(b_s - 1) \tag{K.8}$$

L Cubic Shock Shape

Define the shock shape in the region between the previous and current marching stations with the following cubic equation:

$$r_s = \tilde{r}_0 + \tilde{r}_1 (\Delta z_s) + \frac{\tilde{r}_2}{2!} (\Delta z_s)^2 + \frac{\tilde{r}_3}{3!} (\Delta z_s)^3 \qquad (L.1)$$

where

$$\Delta z_s = z_s - z_{s_{k-1}}$$

The axial position of the current station is $z_s = z_{s_k}$, while the previous station is at $z_s = z_{s_{k-1}}$. Differentiating Eq. (L.1) with respect to z_s gives the shock slope:

$$\frac{dr_s}{dz_s} = \tilde{r}_1 + \tilde{r}_2 (\Delta z_s) + \frac{\tilde{r}_3}{2} (\Delta z_s)^2 = \tan \Gamma_s \qquad (L.2)$$

Differentiating Eq. (L.2) with respect to z_s gives

$$\frac{d^2 r_s}{dz_s^2} = \tilde{r}_2 + \tilde{r}_3 (\Delta z_s) = -\kappa_s \cos^{-3} \Gamma_s \qquad (L.3)$$

One more differentiation yields

$$\frac{d^3 r_s}{dz_s^3} = \tilde{r}_3 \qquad (L.4)$$

Now focus on the previous station $(k-1)$, where this current shock segment meets the previous segment (between stations $k-2$ and $k-1$). The shock geometry here was determined from this previous segment. Requiring a continuous position, slope, and curvature across this juncture (where $z_s = z_{s_{k-1}}$) gives

$$\tilde{r}_0 = r_{s_{k-1}} \qquad \tilde{r}_1 = \left. \frac{dr_s}{dz_s} \right|_{k-1} \qquad \tilde{r}_2 = \left. \frac{d^2 r_s}{dz_s^2} \right|_{k-1}$$

However, from Eq. (L.4), note that the curvature derivative is not continuous between shock segments. In fact, the derivative's value is invariant along the length of a given segment.

Eq. (L.3) can be rewritten as

$$\tilde{r}_3 = \frac{1}{\Delta z_s} \left[\frac{d^2 r_s}{dz_s^2} - \left. \frac{d^2 r_s}{dz_s^2} \right|_{k-1} \right] \qquad (L.5)$$

so that Eq. (L.4) becomes

$$\frac{d^3 r_s}{dz_s^3} = \frac{1}{\Delta z_s} \left[\frac{d^2 r_s}{dz_s^2} - \left. \frac{d^2 r_s}{dz_s^2} \right|_{k-1} \right] \qquad (L.6)$$

which is simply a two-point backward difference representation of d^2r_s/dz_s^2. Substitute this definition of $\ddot{r}_3$ into Eq. (L.1) to get

$$r_s = r_{s_{k-1}} + \Delta z_s \left.\frac{dr_s}{dz_s}\right|_{k-1} + \frac{\Delta z_s^2}{6}\left[2\left.\frac{d^2r_s}{dz_s^2}\right|_{k-1} + \frac{d^2r_s}{dz_s^2}\right] \tag{L.7}$$

which defines the shock segment in terms of values at the previous station. Similarly, Eq. (L.2) can be written as

$$\frac{dr_s}{dz_s} = \left.\frac{dr_s}{dz_s}\right|_{k-1} + \frac{\Delta z_s}{2}\left[\left.\frac{d^2r_s}{dz_s^2}\right|_{k-1} + \frac{d^2r_s}{dz_s^2}\right] \tag{L.8}$$

to yield an expression for the shock slope between stations $k-1$ and k.

Report Documentation Page

1. Report No.	2. Government Accession No.	3. Recipient's Catalog No.
NASA CR-187617		

4. Title and Subtitle	5. Report Date
An Approximate Viscous Shock Layer Technique for Calculating Chemically Reacting Hypersonic Flows About Blunt-Nosed Bodies	August 1991
	6. Performing Organization Code

7. Author(s)	8. Performing Organization Report No.
F. McNeil Cheatwood	
	10. Work Unit No.
	506-40-91-02

9. Performing Organization Name and Address	11. Contract or Grant No.
North Carolina State University Raleigh, NC 27695-7910	NCC1-100
	13. Type of Report and Period Covered

12. Sponsoring Agency Name and Address	Contractor Report
NASA Langley Research Center Hampton, VA 23665-5225	14. Sponsoring Agency Code

15. Supplementary Notes

Langley Technical Monitor: E. Vincent Zoby

16. Abstract

An approximate axisymmetric method has been developed which can reliably calculate fully viscous hypersonic flows over blunt-nosed bodies. By substituting Maslen's second-order pressure expression for the normal momentum equation, a simplified form of the viscous shock layer (VSL) equations is obtained. This approach can solve both the subsonic and supersonic regions of the shock layer without a starting solution for the shock shape. The approach is applicable to perfect gas, equilibrium, and nonequilibrium flowfields. Since the method is fully viscous, the problems associated with coupling a boundary-layer solution with an inviscid-layer solution are avoided. This procedure is significantly faster than the parabolized Navier-Stokes (PNS) or VSL solvers and would be useful in a preliminary design environment. Problems associated with a previously developed approximate VSL technique are addressed before extending the method to nonequilibrium calculations. Perfect gas (laminar and turbulent), equilibrium, and nonequilibrium solutions have been generated for air flows over several analytic body shapes. Surface heat transfer, skin friction, and pressure predictions are comparable to VSL results. In addition, computed heating rates are in good agreement with experimental data. The present technique generates its own shock shape as part of its solution, and therefore could be used to provide more accurate initial shock shapes for higher-order procedures which require starting solutions.

17. Key Words (Suggested by Author(s))	18. Distribution Statement
CFD Flow Field VSL Analysis Reacting chemistry	Unclassified-Unlimited Subject Category 34

19. Security Classif. (of this report)	20. Security Classif. (of this page)	21. No. of pages	22. Price
Unclassified	Unclassified	194	A09